Study of accreting neutron stars, massive black holes and cosmological forecasts for SRG/eROSITA

Sergei Bykov

München 2023

Study of accreting neutron stars, massive black holes and cosmological forecasts for SRG/eROSITA

Sergei Bykov

Dissertation
der Fakultät für Physik
der Ludwig-Maximilians-Universität
München

vorgelegt von
Sergei Bykov
aus Samara, Russland

München, den 16.11.2023

Erstgutachter: Prof. Dr. Rashid Sunyaev
Zweitgutachter: Prof. Dr. Jochen Weller
Tag der mündlichen Prüfung: 25.01.2024

Contents

List of Figures

List of Tables

Zusammenfassung

Diese Arbeit widmet sich einem breiten Spektrum von Akkretionsproblemen. Es werden zwei Arten von Objekten untersucht: aktive galaktische Kerne (Active galactic nuclei, AGN, auf Englisch) - akkretierende massive Schwarze Löcher in den Zentren von Galaxien und Röntgenpulsare - akkretierende Neutronensterne mit extrem hohen Magnetfeldern.

Im ersten Teil dieser Arbeit untersuchen wir massive Schwarze Löcher (SL), die in den Zentren fast aller massereichen Galaxien leben. Die Masse der SLs korreliert mit der Bulge-Masse ihrer Wirtsgalaxien, was diese Objekte zu einem wichtigen Faktor für die Galaxienentwicklung macht. Einige BHs emittieren aufgrund der Akkretion von Materie große Mengen an Strahlung - sie werden aktive galaktische Kerne (AGN) genannt. Himmelsdurchmusterungen bei Röntgenwellenlängen sind wirksam bei der Entdeckung von AGNs und der Untersuchung ihrer Entwicklung. Die räumliche Verteilung von AGNs dient als effektiver Indikator für die großräumige Struktur (large-scale structure, LSS, auf Englisch) des Universums. Wir konzentrieren uns auf die Röntgendurchmusterung des SRG/eROSITA-Teleskops, das bereits fast ~drei Millionen AGNs entdeckt hat.

Wir bewerten die Aussichten für kosmologische Messungen mit eROSITA auf der Grundlage der LSS von AGNs und Galaxienhaufen. Wir finden, dass die marginalisierten Fehler der kosmologischen Parameter (Energiedichte der dunklen und baryonischen Materie, Hubble-Konstante) eine Genauigkeit von $1 - 10\%$ erreichen. Die vorhergesagte Genauigkeit der kosmologischen Einschränkungen, die von der SRG/eROSITA-Gesamtdurchmusterung erwartet werden, ist konkurrenzfähig mit den Einschränkungen von aktuellen und geplanten kosmologischen Durchmusterungen und Missionen.

Wir stellen eine Methode zur Identifizierung von eROSITA-Röntgenquellen in Himmelsdurchmusterungen in optischen Bändern vor. Diese Aufgabe ist für die Abschätzung der Rotverschiebung von Röntgenquellen von entscheidender Bedeutung. Wir kombinieren maschinelle Lerntechniken mit einem Bayes'schen Ansatz, um die Quellen aus dem Röntgenkatalog von eROSITA im Lockman-Loch mit optischen Quellen abzugleichen. Die Genauigkeit erreicht 94% für den gesamten Röntgenkatalog.

Wir suchen mit eROSITA-Daten nach aktiven Kernen von Zwerggalaxien (mit geringer Masse). Es wird erwartet, dass Zwerggalaxien zentrale Schwarze Löcher beherbergen, die im Vergleich zum Großteil der AGNs eine geringere Masse haben. Man geht davon aus, dass diese SLs die Relikte der ersten Schwarzen Löcher sind, und sie sind wichtig, um die Szenarien der Entstehung von Schwarzen Löchern einzugrenzen. Wir erstellen einen Katalog von 82 Zwerggalaxien mit nuklearer Röntgenaktivität - ein eindeutiger Indikator für ein massereiches akkretierendes SL. Wir berechnen den Anteil der Zwerggalaxienpopulation, die ein aktives Schwarzes Loch beherbergen, als Funktion der Röntgenleuchtkraft und der stellaren Masse der Galaxie. Der Anteil aktiver Zwerge ist bei geringer Röntgenleuchtkraft bis zu 2% groß und sinkt bei höheren Leuchtkräften. Wir entdecken zufällig eine Gezeitenstörung eines Sterns durch ein zentrales BH in einer Zwerggalaxie und demonstrieren die Fähigkeit von Gezeiteneruptionen, die Population von ruhenden Schwarzen Löchern aufzudecken.

Im zweiten Teil dieser Arbeit befassen wir uns mit der Untersuchung von Röntgenpulsaren - entstehenden Neutronensternen (NS) in stellaren Doppelsternsystemen. Das Material wird

durch das Magnetfeld eingefangen und zu einem NS gelenkt, wo reichlich Röntgenemission erzeugt wird. Die Geometrie der Akkretionsströme ist komplex und hängt von einer Reihe von Parametern ab, wie etwa der Stärke des Magnetfelds. Wir verwenden eine neuartige Technik, um die Geometrie von Systemen zu untersuchen, bei denen die Röntgenemission eines NS von der umgebenden Materie aufgearbeitet wird. Wir analysieren zwei Pulsare, V0332+53 und Swift J0243.6+6124. Letzterer ist ein extrem leuchtstarkes Objekt (ultrahelle Röntgenquelle).

Wir untersuchen die Pulsationen der wiederaufbereiteten Emission in beiden Pulsaren. Wir zeigen, dass in J0243 die wiederaufbereitete Emission über die Rotationsphase des Pulsars schwach variabel ist und die direkte Emission größere Pulsationen zeigt. Wir vermuten, dass sich der Pulsar im Zentrum einer Vertiefung befindet, die von einer geometrisch dicken Akkretionsscheibe gebildet wird, die durch das Magnetfeld abgeschnitten ist. Die Innenseiten der Senke werden vom Pulsar beleuchtet und erzeugen reflektierte Emission. Wir schätzen den Magnetfeldwert eines Pulsars, indem wir die Dopplerverbreiterung der Eisenlinie messen.

In V0332 pulsieren die Absorptionstiefe der Eisen-K-Kante und die Intensität der K_α-Linie. Der Fluss als Funktion der Rotationsphase zeigt zwei Einbrüche von identischer Form, die um 180 Grad voneinander getrennt sind. Die Absorptionskante ist während der Einbrüche am stärksten, aber ihre Tiefe kann nicht durch die Absorption von Röntgenstrahlen durch das einfallende Material verursacht werden. Wir kommen zu dem Schluss, dass die Daten nicht mit einfachen Modellen der Emissionsrezessionen durch die umgebende Materie erklärt werden können, was die Bedeutung weiterer Studien solcher Objekte für die Bestimmung der Geometrie von Akkretionsströmen unterstreicht.

Abstract

This thesis is dedicated to a broad range of problems related to accretion. Two types of objects are studied: active galactic nuclei (AGN) - accreting massive black holes at the centres of galaxies, and X-ray pulsars - accreting neutron stars with extremely high magnetic fields.

In the first part of this thesis, we investigate massive black holes (BH) dwelling at the centres of almost all massive galaxies. The mass of BHs correlates with the bulge mass of their host galaxies, making these objects an important asset for galaxy evolution. Some BHs emit copious amounts of radiation due to the accretion of matter — they are called active galactic nuclei (AGN). Sky surveys in X-ray wavelengths are effective at discovering AGNs and studying their evolution. The spatial distribution of AGNs serves as an effective tracer of the Large-Scale structure (LSS) of the Universe. We focus on the all-sky X-ray survey performed by the SRG/eROSITA telescope, which has already discovered close to ~three million AGNs.

We assess the prospects of cosmological measurements with eROSITA based on the LSS of AGNs and galaxy clusters. We find that the marginalised errors on cosmological parameters (energy density of dark and baryon matter, Hubble constant) achieve precision $1 - 10\%$. The predicted precision of cosmological constraints expected from the SRG/eROSITA all-sky survey is competitive with the constraints from current and planned cosmological surveys and missions.

We present a method for identifying eROSITA X-ray sources in sky surveys in optical bands. This task is paramount for estimating redshifts of X-ray sources. We combine machine learning techniques with a Bayesian approach to match the sources from the X-ray catalogue of eROSITA in the Lockman hole with optical sources. The accuracy achieves 94% for the entire X-ray catalogue.

We perform the search for active nuclei of dwarf (low-mass) galaxies using eROSITA data. Dwarf galaxies are expected to host central black holes of lower mass compared to the bulk of AGNs. These BHs are thought to be the relics of the first black holes and are important to constrain the black hole seeding scenarios. We construct a catalogue of 82 dwarf galaxies with nuclear X-ray activity – an unambiguous indicator of a massive accreting BH. We calculate the fraction of the dwarf galaxy population hosting an active black hole as a function of X-ray luminosity and galaxy stellar mass. The fraction of active dwarfs is as large as 2% for low X-ray luminosity and drops for higher luminosities. We serendipitously discover a tidal disruption of a star by a central BH in a dwarf galaxy and demonstrate the ability of tidal flares to uncover the population of *dormant* black holes.

In the second part of this work, we focus on the study of X-ray pulsars–accreting neutron stars (NS) in stellar binary systems. The material is captured by the magnetic field and directed to a NS, where ample X-ray emission is produced. The geometry of accretion flows is complex and depends on a number of parameters, such as magnetic field strength. We use a novel technique to study the geometry of systems with X-ray emission of a NS reprocessed by surrounding matter. We analyse two pulsars, V0332+53 and Swift J0243.6+6124. The latter is an extremely luminous object (ultra-luminous X-ray source).

We study pulsations of the reprocessed emission in both pulsars. We show that in J0243 the reprocessed emission is weakly variable over the pulsar rotational phase and direct emission shows larger pulsations. We conjecture that the pulsar is located at the centre of a well, formed

by a geometrically thick accretion disc truncated by the magnetic field. The inner sides of the well are illuminated by the pulsar and produce reflected emission. We estimate the magnetic field value of a pulsar by measuring the Doppler broadening of the iron line.

In V0332 the iron K-edge absorption depth and K_α line intensity pulsate. Flux as a function of the rotational phase shows two dips of identical shape separated by 180°. The absorption edge is the strongest during the dips, but its depth cannot be caused by the absorption of X-rays by the infalling material. We conclude that the data can not be explained with simple models of emission reprocession by surrounding matter, emphasising the importance of further studies of such objects for pinpointing the geometry of accretion flows.

CHAPTER 1

Introduction

In this thesis, we consider **accretion** - one of the most important mechanisms of energy release in the Universe. The basic motivation for studying accretion and its observational appearance are discussed in sect. 1.1. The topic will be elaborated further into the introduction of several extreme cosmic phenomena studied in this thesis - Active Galactic Nuclei (AGN) and X-ray pulsars, both powered by the accretion of matter. For X-ray pulsars (in sect. 1.2), we touch on their origin and physics, observational properties and how observations can be connected to the physics of accretion. For the AGNs (in sect. 1.3), we consider the main model for this kind of object and their population properties (X-ray luminosity functions, clustering studies). Section 1.4 is devoted to one of the main instruments we use in this thesis to study extreme objects - SRG/eROSITA. The final section (1.5) outlines the structure of this thesis.

1.1 Accretion

Following Frank et al. (2002), let us consider a body of mass M, radius R in an empty space. If a blob of matter with mass m falls on it from infinity, the release of potential energy would be

$$E_{\rm acc} = GMm/R,$$

where G is the gravitation constant (6.67×10^{-8} dyn cm^2 g^{-2}). This is the energy release of the accretion process.

In nature, different combinations of mass and radius are possible, and the accretion energy output depends on the M/R ratio. For instance, a consequence of a stellar explosion, a neutron star (NS), will have $R \sim 10$ km and $M \sim M_\odot$ (one solar mass, $\sim 2 \times 10^{33}$ g). This leads to the energy release of 1.4×10^{20} erg ($\sim 10^{13}$ J) for each accreted gram. It is illustrative to compare this value to the output of thermonuclear reactions occurring in stellar cores when from one gram of mass one can extract

$$E_{\rm nuc} = 0.007[1\ {\rm g}]c^2 \sim 6.3 \times 10^{18}\ {\rm erg}$$

($c = 3 \times 10^{10}$ cm s^{-1} is the speed of light). For a neutron star, $E_{\rm acc}$ is by a factor of 20 larger $E_{\rm nuc}$, rendering accretion a very efficient mechanism of energy extraction for objects with large M/R.

Another type of compact object is a black hole (BH). For BHs, the so-called gravitational radius is roughly the radius where energy release may take place. For a BH with mass M, it is calculated with the formula $R = \frac{2GM}{c^2}$. For $10M_\odot$ black hole the gravitational radius is ~ 30 km. M/R ratio does not depend on the black hole mass, meaning the accretion efficiency is expected to be equal for $10M_\odot$ and $10^9 M_\odot$ black holes. The efficiency of accretion onto black holes is

also very high, as seen from its M/R[1]. The black holes can be of very different masses. Black holes born in the explosion of massive stars can be as massive as 10-100 suns ($M \sim 10...100 M_\odot$). On the other hand, black holes dwelling at the centres of galaxies can be as massive as $10^9 M_\odot$ (Supermassive black holes, SMBH, see sect. 1.3). Nonetheless, 1 g of material accreted on both small and large black holes will produce the same amount of energy. The amount of energy released per unit of time depends on the **mass accretion rate** $\dot{M} = \frac{\mathrm{d}M}{\mathrm{d}t}$. Part of this energy will be radiated away and detected as electromagnetic waves by telescopes.

If the luminosity is very high, the radiation created by accretion will start to affect the accreting material itself, regulating the whole process. If the luminosity exceeds a certain threshold, the accretion will be prevented, effectively stopping the rise of luminosity. Assuming that the accreting matter is fully ionised hydrogen, the blob of matter may be deemed as a large number of bound electron-proton pairs which are affected by both gravity (mainly protons) and radiation force (mainly electrons). Suppose the object's luminosity (energy output in a unit of time) is L. Gravity attracts protons (and electrons bound to them) with a force $F_\mathrm{g} = GMm_\mathrm{p}/r^2$ ($m_\mathrm{p} = 1.7 \times 10^{-24}$ g is a proton mass) for a distance r. The light puts outward pressure on electrons by means of Thomson scattering. If the flux of radiation energy per unit area at the same distance r is $S = \frac{L}{4\pi r^2}$ erg s^{-1} cm^{-2}[2], the outward force is $F_\mathrm{rad} = \sigma_\mathrm{T} S/c$ (where $\sigma_\mathrm{T} = 6.7 \times 10^{-25}$ cm^2 is the electron scattering cross-section). The two forces F_rad and F_g are balanced for a luminosity L_Edd which does not depend on distance and equals to

$$L_\mathrm{Edd} = \frac{4\pi G M m_\mathrm{p} c}{\sigma_\mathrm{T}} \approx 1.3 \times 10^{38} \left(\frac{M}{M_\odot}\right) \text{ erg s}^{-1}.$$

This luminosity is called **Eddington Luminosity** and depends linearly on the mass of the object matter accretes onto. We assumed spherical symmetry of the problem, which probably does not hold in the majority of astrophysical situations, but it is a useful order-of-magnitude estimate of the maximum attainable luminosity.

The accretion luminosity L_acc is usually expressed through the mass accretion rate $\dot{M}$ as

$$L_\mathrm{acc} = \frac{GM\dot{M}}{R},$$

where R is the radius of an object. Part of this energy is released via an accretion disc, and the rest is released on the surface of an accretor (or is not released for a black hole), see Shakura, Sunyaev (1988); Sibgatullin, Sunyaev (2000)

Next, we briefly describe what kind of accretion flow is expected in the majority of sources (from White Dwarfs to the most massive quasars). We touch on the distribution of radiation intensity in different wavelengths and how it depends on the compact object.

It is now well established that significant energy release in accreting systems occurs via the viscous **accretion disc** (Lynden-Bell, 1969; Shakura, Sunyaev, 1973; Pringle, 1981). The

[1] In black holes, the energy release occurs mostly on radii a few times larger than the gravitational radius (Shakura, Sunyaev, 1973). The efficiency of black hole accretion is around 0.1 of rest mass, and for neutron stars, it is 0.15 of rest mass. Nuclear fusion has the efficiency of 0.007 of rest mass.

[2] radiation flux will be referred to as F for all other chapters of the thesis.

current standard model is the so-called α-discs proposed by Shakura, Sunyaev - optically thick, geometrically thin discs[3]. Radiation forms from half of the energy of accretion. The angular velocity of rotation $\Omega(r)$ is Keplerian

$$\Omega(r) = \Omega_{\rm K}(r) = \left(\frac{GM}{r^3}\right)^{1/2},$$

where M, as above, is the mass of an accretor. The energy release occurs from the friction due to the differential rotation of matter.

The temperature of the disk depends on the distance to the accretor r and the mass accretion rate $\dot{M}$

$$T(r) = \left[\frac{3GM\dot{M}}{8\pi r^3\sigma_{\rm SB}}\left[1-\sqrt{R/r}\right]\right]^{1/4},$$

where $\sigma_{\rm SB}$ is the Stefan-Boltzmann constant. The maximum of the temperature $0.488T_*$ is achieved on a radius $\frac{49}{36}R$, with

$$T_* = \left(\frac{3GM\dot{M}}{8\pi R^3\sigma_{\rm SB}}\right)^{1/4}.$$

We note a few interesting consequences of this equation: (i) For a stellar mass BH or a NS the expected temperature is $\sim 10^7$ K (i.e. $k_{\rm B}T \sim 1$ keV, where $k_{\rm B} = 1.38\times10^{-16}$ erg K^{-1} is a Boltzmann constant) (ii) For BHs, the temperature scales as $M^{-1/4}\left(\frac{\dot{M}}{\dot{M}_{\rm Edd}}\right)^{1/4}$ - for a constant accretion rate (in terms of Eddington Luminosity), less massive black holes have higher temperatures.

The fate of matter after achieving the inner regions of the disc depends on the nature of the accretor. For white dwarfs and neutron stars, there is a surface to fall onto, but for BHs there is only an event horizon. We will discuss the difference later.

The emitted spectrum of a disc can be crudely presented as the sum of black body rings emitting radiation with different temperatures (Shakura, Sunyaev, 1973). The effective shape of the spectrum is a power law with the exponential decay (the Wien tail) at the energies corresponding to the largest disc temperature. The outer disc temperature dictates the shape of the spectrum on longer wavelengths. In massive black holes (with masses over $10^5 M_\odot$) the temperature of the disc falls into the UV region of the spectrum; whilst for stellar mass BHs or neutron stars the temperature is in the X-ray regime.

However, observations show that another component of the accretion disc emission is present in accreting BH (from stellar mass BHs to SMBH). This component possesses much higher photon energies than the disc emission and is related to the presence of hot plasma in the vicinity of accreting matter, called **corona** (Galeev et al., 1979; Haardt, Maraschi, 1991, 1993). Corona is believed to be quite compact, extending at most by a few tens of gravitational radii from the accretor. This material is hot ($\sim 10^9$ K) and optically thin (electron scattering optical depth

[3]For systems with low accretion rate, the disc may not be geometrically thin and optically thick, see Narayan, Yi (1995); Yuan, Narayan (2014). We, however, focus on relatively bright systems and α-discs.

$\tau \lesssim 1$). Corona intercepts some part of the disc emission and reprocesses it. The process of inverse Compton scattering transfers energy from the hot electrons of the corona to the less energetic photons from an accretion disc, effectively creating a power-law distribution of intensity in wavelengths. The exponential cutoff at high energies (> 100 keV) is also observed and related to the temperature of corona (Sunyaev, Truemper, 1979; Sunyaev, Titarchuk, 1980; Titarchuk, 1994). In both stellar mass and massive BHs comptonized spectrum falls into the hard X-ray regime (energies > a few keV).

Some scattered photons are directed towards the accretion disc when they are reprocessed again. Some are reflected back to the observer and the reflection component of the energy spectrum is detected (Pounds et al., 1990; George, Fabian, 1991; Magdziarz, Zdziarski, 1995; Ross, Fabian, 2005). The shape of reflection is dictated by the physical conditions of the disc and its geometry, generally having a hump-shaped spectrum peaking around 30 keV with emission lines imposed on it (Basko et al., 1974; Fabian et al., 1989). Reflection of hard radiation plays an important role in X-ray pulsars and is the primary method of investigation in Chapters 5 and 6 of this thesis.

The schematic view of the accretion flows and radiation in a stellar black hole binary is shown in Fig 1.1.

In the next two sections, we describe the basic properties of X-ray pulsars (sect. 1.2) and Active Galactic Nuclei (sect. 1.3).

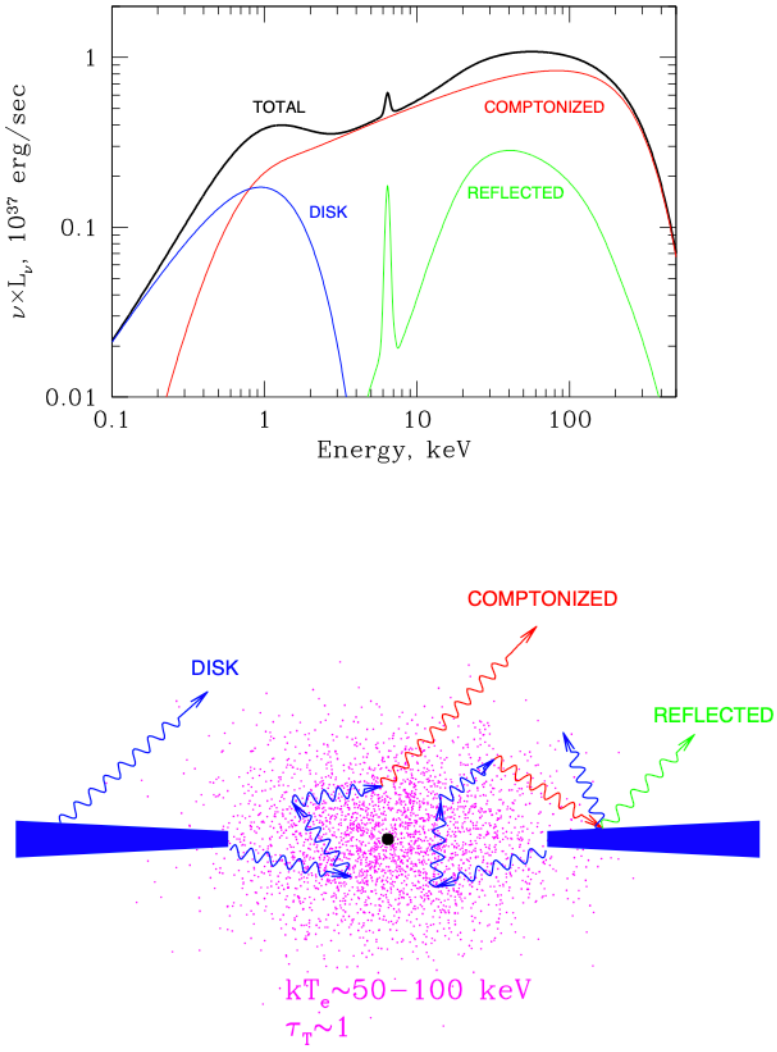

Figure 1.1: Main components of X-ray emission from an accreting black hole with stellar mass. The top panel shows the emitted spectrum (by different components), bottom panel shows the plausible geometry of the accretion flows. The picture is similar for accreting massive black holes (at the centres of galaxies) but with much lower disc temperatures. From Gilfanov (2010).

1.2 Accretion onto neutron stars and X-ray pulsars

Stars with a stellar mass $M_* > 8M_\odot$ end their lives in a spectacular explosion called core-collapse supernova (Bethe, Wilson, 1985; Carroll, Ostlie, 1996; Woosley, Janka, 2005; Sukhbold et al., 2016). A neutron star or a black hole appears as a result of this dramatic event. When a star runs out of thermonuclear fusion, the force of gravity can no longer be negated by the pressure of gas or radiation, and the catastrophic collapse of the star ensues. In very massive stars ($M_* > 20-30M_\odot$) the result of the collapse yields a **black hole**.

In the less massive stars, a very dense object of small radius is born - a **neutron star**, with the mass in the range $1.4 - 2.2M_\odot$ and radius $10 - 20$ km (Cerda-Duran, Elias-Rosa, 2018). Neutron stars tend to have very large magnetic fields and angular momentum due to the conservation of the respective quantities. Typical values for magnetic field lie between $10^9 - 10^{14}$ G, and the rotation frequency can be as fast as one hundred times in a second. Another way to create a neutron star is the explosion of white dwarfs (WD), a product of the evolution of low-mass stars, see Canal, Gutiérrez 1997; Yungelson, Kuranov 2016. White dwarfs accreting material in a binary star system may eventually achieve its mass limit of $1.4M_\odot$ (called Chandrasekhar limit), collapse on itself and leave a neutron star as a result. Two white dwarfs merging with each other also may create a neutron star.

Neutron stars (also stellar mass black holes and white dwarfs) are frequently found in a binary star system - when they are paired with a normal star (Remillard, McClintock, 2006). When a companion star has low mass ($\leq M_\odot$), such systems are dubbed a Low-mass X-ray binary (LMXB). If the companion star is massive, they are classified as a High-mass X-ray binary. Accretion in such systems is very common due to the constant flux of matter onto the compact object (due to the Roche lobe overflow or stellar wind, see Frank et al. 2002; Remillard, McClintock 2006). HMXB and LMXB can be very bright and achieve luminosities of 10^{38} erg s^{-1} or more. A particular type of HMXB studied in this thesis is the so-called **Be/X-ray binaries (BeXRBs)**. They harbour a neutron star and a fast-rotating star of O or B class with an equatorial circumstellar disc (Reig, 2011; Coe, Kirk, 2015). They frequently show outbursts of X-ray radiation related to the processes of accretion onto the neutron star (Okazaki, Negueruela, 2001; Okazaki et al., 2002). A more complete introduction to BeXRBs may be found in Chapter 5.

During the accretion onto an object with a hard surface, accreted material forms a boundary layer which emits half of the accretion energy (luminosity) if the rotation of an object is much slower than the Keplerian velocity (Shakura, Sunyaev, 1988; Frank et al., 2002). However, in pulsars, a phenomenon investigated in Chapters 5 and 6, the disc does not extend towards the surface of a compact object (neutron star).

When an accretor (a white dwarf or a neutron star) has a strong magnetic field, the accretion disc changes its structure dramatically. The magnetic field disrupts the innermost regions of the disc because the magnetic pressure starts to control the disc's dynamics (Ghosh, Lamb, 1979). The characteristic radius is the so-called **Alfven radius**, on which the pressure of falling matter and magnetic field are equal in an idealised case of spherical accretion on a magnetised object (assuming dipole filed). In this section, we will focus solely on neutron star accretion. Alfven

radius can be calculated with the formula (Ghosh, Lamb, 1979; Frank et al., 2002; Mushtukov et al., 2017)

$$r_{\rm M} = 2.9 \times 10^8 L_{37}^{-2/7} (M/M_\odot)^{-1/7} \mu_{30}^{4/7} R_6^{-2/7} {\rm cm}\ ,$$

where $r_{\rm M}$ is the Alfven radius, L_{37} is the luminosity in units of 10^{37} erg s^{-1}, M is the mass of a neutron star, μ_{30} is the magnetic moment in units G cm^{-3}, R_6 is the radius of a neutron star in units of 10^6 cm. For a typical accreting neutron star the numerical factors are all of the order of unity, and the Alfven radius is around 3000 km. In the accretion from the disc, the inner side of the disc is expected to be smaller than the Alfven radius by a factor of a few (Ghosh, Lamb, 1979).

What happens with matter at radii less than Alfven radius, is dictated by magnetic field. If the inner disc radius is larger than the co-rotation radius (the radius when the angular Keplerian velocity equals the spin velocity of a NS) the accretion is inhibited by centrifugal forces, leading to the decrease in accretion rate - so-called propeller effect (Illarionov, Sunyaev, 1975).

Otherwise, the accretion flow follows the magnetic field which accumulates matter onto the poles of a neutron star (in a dipole configuration). The so-called hot spot is formed by decelerated particles. In some cases, an accretion column appears (see below). Due to the rotation of the neutron star, if the magnetic axis and the rotation axis are misaligned, the emission from the hot spot columns will be modulated with the rotation of the neutron star. Such pulsating emission gave a name to such a phenomenon - Pulsar. Because we focus on the X-ray emission, the objects of interest in this thesis emit mostly X-rays and are called **X-ray pulsars** (see Mushtukov, Tsygankov, 2022, for a comprehensive review). The general illustration of accretion flows is shown in Fig. 1.2. Those objects are unique laboratories suited for studying the extremes of astrophysics (Mushtukov, Tsygankov, 2022): general relativity and quantum effects, extreme magnetic fields, extreme accretion luminosity and temperature, plasma and radiation physics under conditions unattainable on Earth.

The observed spectra of X-ray pulsars are usually described with a power law emission with exponential decay at large energies ($> 20 - 30$ keV) and features superimposed on it. The most common features are the iron emission line (from reflection), and the cyclotron absorption features (CRSF, related to the presence of Landau levels in the electron distribution). Basko, Sunyaev (1976); Lyubarskii, Syunyaev (1982) proposed the model of accretion columns to explain the basic properties of X-ray pulsars. In the low-$\dot{M}$ regime, the matter reaches the NS surface freely and transfers energy to the pulsar's atmosphere - a hot spot is formed. As the accretion rate rises, the shock wave is formed and the falling plasma releases its energy through radiation (Compton scattering of hot spot emission). When the accretion rate is above a critical threshold, the accretion column height is large and the emission escapes the column from the sides (Gnedin, Sunyaev, 1973; Mushtukov et al., 2015a, 2017). The emission diagram is called a 'fan-beam' when the radiation escapes through the sides, and a 'pencil-beam' when it escapes through the top of the column (Schönherr et al., 2007). The illustration is shown in Fig. 1.3. The rotation of the emission region coupled with the variable observer's line of sight through the column creates a very wide variety of observed X-rays from pulsars. The variability of the spectrum is also very prominent - the spectrum of an X-ray pulsar may change very dramatically with the phase

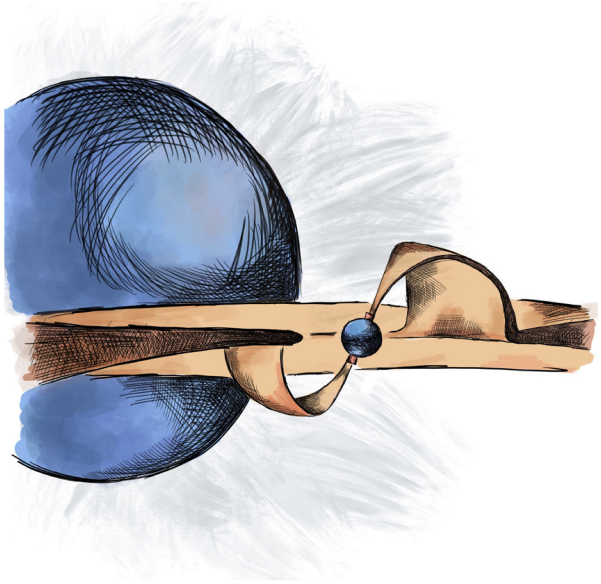

Figure 1.2: Schematic of an X-ray pulsar and the accretion flows around. From Tsygankov et al. (2022); Mushtukov, Tsygankov (2022).

of rotation (method of phase-resolved spectroscopy, extensively used in Chapters 5 and 6), but aperiodic variations are also ubiquitous. More elaborate discussion of the energy spectra and variability can be found in different sections of Chapters 5 and 6 references therein, for a recent review of theory and observations see Mushtukov, Tsygankov (2022).

The theory of accretion columns outlined above allows one to crudely (qualitatively at best) describe the observed intensity profile of pulsations (e.g. single- or double-peaked profiles). There are no self-consistent models able to explain the wealth of observational data, see the review by Mushtukov, Tsygankov. In the respective chapters of the thesis, elaborate discussion can be found on the possible mechanisms for spectral and temporal variability, and the interpretation of those with the models of accretion column and accretion flows around the accretor.

In this thesis (Chapters 5 and 6) we focus our attention on the geometrical configuration of the accretion flows around X-ray pulsars. For that, we used one of the readily available methods sensitive to the geometry of the system – reflected spectrum (see the aforementioned chapters and references therein for discussion). A new avenue for the studies of geometry is the studies of polarisation of X-ray emission (Basko, Sunyaev, 1975). Recent advances in X-ray polarimetry with the advent of IXPE satellite (Weisskopf et al., 2016) allowed researchers to put first constraints on the polarisation properties of magnetised neutron stars. Turned out that the emission was significantly less polarised than expected, and it is tentatively related to the processes of reprocessing of emission by accretion flows, disc or companion star (see Tsygankov et al. (2022) for discussion).

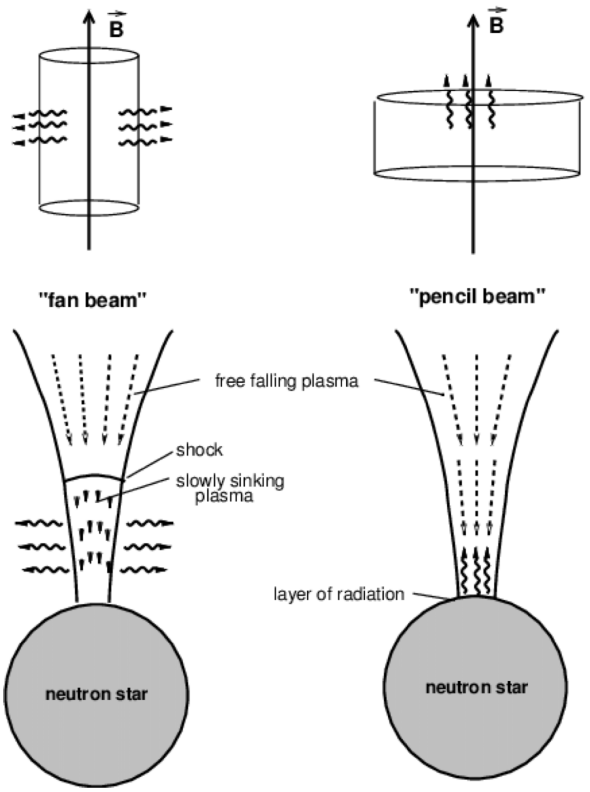

Figure 1.3: Schematic of accretion columns. The left panel shows the case for fan beam emission from under the shock wave. The right panel illustrates the pencil beam emission at lower accretion rates. From Schönherr et al. (2007).

1.3 Active Galactic Nuclei

It is now well known that most (almost all) massive galaxies host a **supermassive black hole (SMBH)** with masses $M > 10^6 M_\odot$ at their cores (Kormendy, Ho, 2013; Heckman, Best, 2014). These black holes gather mass during the episodes of intense accretion of matter from the surroundings. While accreting, the core of a galaxy becomes very bright and usually outshines the galaxy it is located in. Such objects are thus called the **Active galactic nuclei, or AGN** (Padovani et al., 2017). A **Quasar** is a very luminous sub-type of an AGN where the central machine is so bright that the galaxy hosting it cannot be discerned. The accretion power of AGN allows them to be detected at very large distances (high redshifts[4]).

AGN and quasars emit light in a wide spectrum of energies, from radio to X-rays and γ-rays (Frank et al., 2002; Padovani et al., 2017). **X-ray emission** is one of the least biased ways to detect AGNs (see below) and is a primary means of study in this thesis. The typical emission of an accretion disc in an AGN has a peak in the ultraviolet-optical wavelengths (Yuan, Narayan, 2014), but the reprocessed emission in the disc corona and galactic material far away from the black hole have its signatures in the emitted spectrum on larger and smaller wavelengths. There are numerous observed classes of AGNs (AGN zoo, see Padovani et al. 2017 for review), usually classified by their spectra in optical wavelength (e.g. the width of emission lines, the shape of the continuum, etc). It is now clear that a large part of the variability in classes is attributed mainly to the orientation effects (e.g. orientation of the system with respect to an observer). Studies are complicated further due to the variability of AGN emission over a wide range of timescales.

The **unification scheme of AGN** strives to unite the different manifestations of active nuclei under the framework of accretion onto BH and how the surrounding galaxy affects the observable radiation (Antonucci, 1993; Urry, Padovani, 1995; Netzer, 2015; Padovani et al., 2017; Hickox, Alexander, 2018). It is currently believed that the black hole and its accretion disc are surrounded by a torus of dusty and molecular material capable of blocking and reprocessing radiation emanating from an accretion disc. The inner regions of an AGN produce emission from accretion disc, corona, jet (if present) and the ionised gas responsible for broad emission lines. In regions near or behind the torus, a narrow line region is located. The torus itself reprocesses emission from an accretion disc and radiates it away in the infrared wavelengths. The ionised gas responsible for broad lines, broad line region (BLR), is located within the sphere of influence of a black hole and has typical broadening corresponding to velocities of $10^{3..4}$ km/s. The narrow line region (NLR) is located farther from the black hole and its dynamics is dictated by the host galaxy, with a typical broadening of $100 - 500$ km/s (Hickox, Alexander, 2018). BLR may be blocked by the torus and is usually not detected in obscured sources. The schematic structure of an AGN surroundings is shown in Fig. 1.4. The example of Spectral Energy Distribution (SED) coming from different components is shown in Fig. 1.5. Overall, the majority of energy release occurs in the central regions of an AGN. The X-ray emission originates almost exclusively in the very central regions, therefore probing the most energetic part of the accretion flow.

[4]Redshift (z) is a cosmological term for 'distance' in this thesis. Redshift is an increase on the observed wavelength $\lambda_{\rm obs}$ due to the expansion of space in comparison with the emitted (rest-frame) wavelength $\lambda_{\rm rest}$: $z = \frac{\lambda_{\rm obs}}{\lambda_{\rm rest}} - 1$. Hence, the energy of photons becomes smaller by a factor of $1 + z$ for a distant observer.

X-ray spectrum of a generic AGN is a **power-law** to a first-order approximation. Its intensity is written as $F(E) \propto E^{-(\Gamma-1)}$, with F is the flux of energy [keV (photons s^{-1} cm^{-2} keV^{-1})] and Γ is a photon index. Energy flux in a narrow energy band $[E, E + dE]$ is $F(E)dE$. If $\Gamma = 2$, the energy spectrum $EF(E)$ is flat, if $\Gamma < 2$, the spectrum is hard and has higher energy output in larger energies, and vice versa if $\Gamma > 2$. The typical value for photon index for X-ray selected non-absorbed AGN is $\Gamma \sim 1.9$ although with large dispersion (Ge et al., 2022; Liu et al., 2022a). The emission is believed to be related to the process of inverse Compton scattering of disc photons in the corona and is described in sect. 1.1. The high energy data shows the exponential cut-off of the spectrum due to the temperature of the corona.

The spectrum has sometimes additional modifications. X-ray **reflection** is prominent in some sources and manifests itself in the form of iron line emission at ~ 6.4 keV and reflection hump (as also described in sect. 1.1). The spectral shape and temporal variability of reflected emission is a useful tool to study the innermost regions of the accretion flow and the properties of a black hole (e.g. Reynolds, Fabian, 2008; Reynolds, 2014). Recently, X-ray polarimetry studies provided insights into the geometry of the X-ray-producing corona (Gianolli et al., 2023).

At energies smaller than the onset of corona emission (~ 1 keV), sometimes an excess of X-ray emission is observed, and it has unclear origin (Gierliński, Done, 2004; Crummy et al., 2006; Done, 2010; Done et al., 2012). It is usually called **'soft excess'** and has temperatures of $0.1 - 0.2$ keV independent of BH mass, in contrast to what is expected from an accretion disc. Possible explanations involve additional warm corona or modified emission from the disc (see references above).

Absorption of X-ray emission is possible by interstellar material in the host galaxy and in our Galaxy. Flux suppression in soft X-ray range ($E \lesssim 1 - 2$ keV) can be accounted for by using the tabulated abundances and cross-sections of interstellar gas, red-shifted if necessary (Done, 2010). The absorption strength depends on the line-of-sight (LOS) hydrogen column density ($N_{\rm H}$, measured in units of cm^{-2}). The LOS hydrogen column density for *absorption in our Galaxy* depends on the part of Milky Way we are looking through and is smallest far from the galactic disc (typical value is $N_{\rm H} \sim 10^{21}$ cm^{-2}). *Intrinsic absorption* related to the host galaxy, however, has a range of possible values, from small absorption ($N_{\rm H} \lesssim 10^{21}$ cm^{-2}) up to regime when $N_{\rm H} \sim 10^{24}$ cm^{-2} (the electron-scattering optical depth is around unity). AGNs with small intrinsic absorption are called **unobscured** (or type-1 AGN), and those with moderate or high column densities are called **obscured** (type-2 AGN). **Compton-thick AGNs** are AGNs with absorption column densities $N_{\rm H} \gtrsim 10^{24}$ cm^{-2} (roughly the inverse of electron scattering cross-section). In the heavily obscured case, soft X-ray emission of the central machine may be completely absent – only the reflected part is usually detectable. In general, obscuration affects different wavelengths differently, and here we focus only on the X-ray emission. For a review of obscured AGNs, see Hickox, Alexander (2018).

AGN signatures at the galactic core usually unambiguously indicate that there is indeed a black hole at the galactic centre. A black hole can also be detected if this black hole is dormant (not an AGN). One opportunity relevant to this thesis is a **Tidal Disruption Event** (Hills, 1975; Rees, 1988) - a process of disruption of a star when it passes too close to a black hole. Tidal forces experienced by a star in the vicinity of a black hole may exceed a star's self-gravity, leading

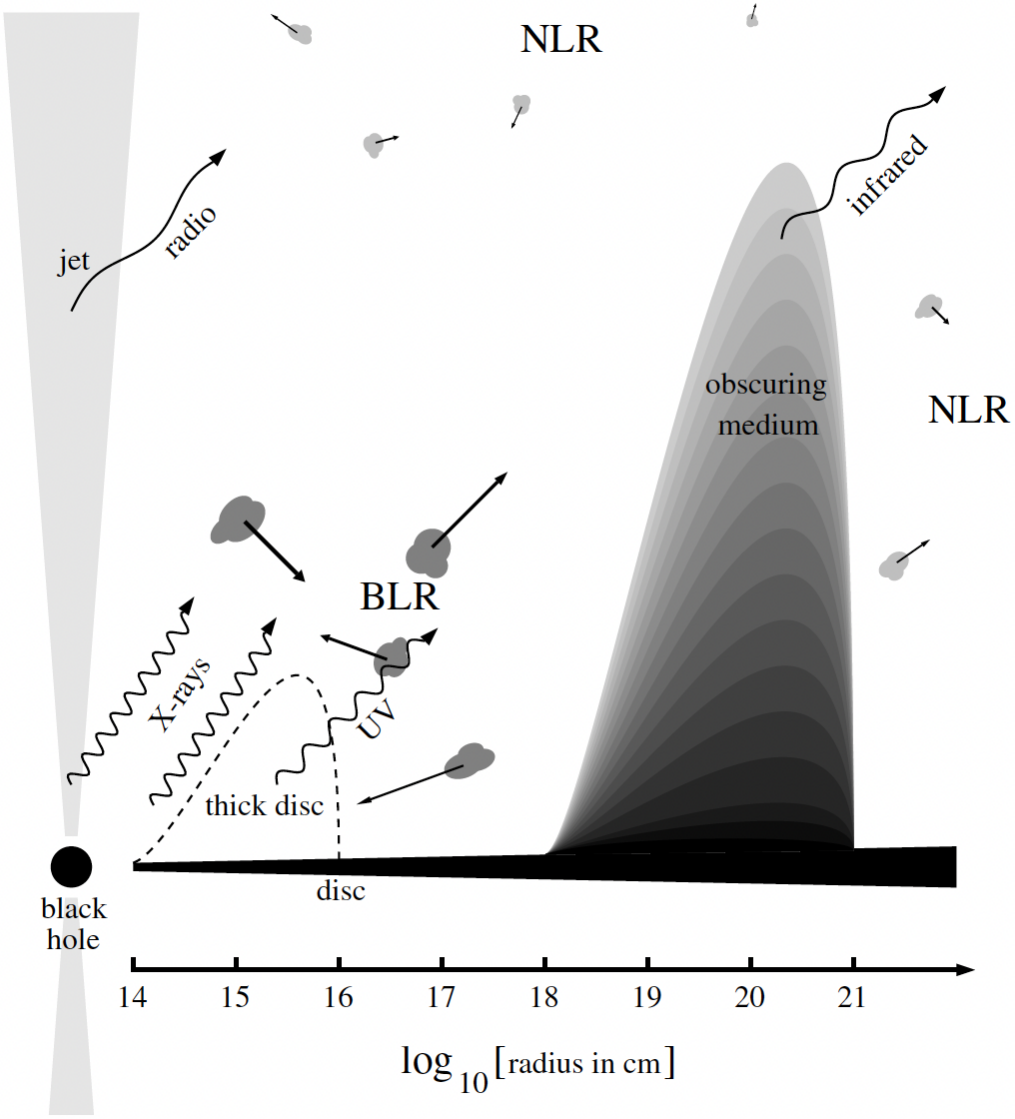

Figure 1.4: Visual scheme for a unified model of AGN. The central regions near the black hole produce radio (if the jet is present), X-ray (corona) and UV (disc) radiation. The dusty torus (obscuring medium) blocks the central regions (if the observer is on the right side of the picture) and reprocesses the radiation into IR emission. Clouds responsible for broad (BLR) and narrow (NLR) lines are also shown. The thick disc is a possible accretion flow configuration for high-luminosity systems. From Frank et al. (2002). 1 parsec is $\approx 3 \times 10^{18}$ cm.

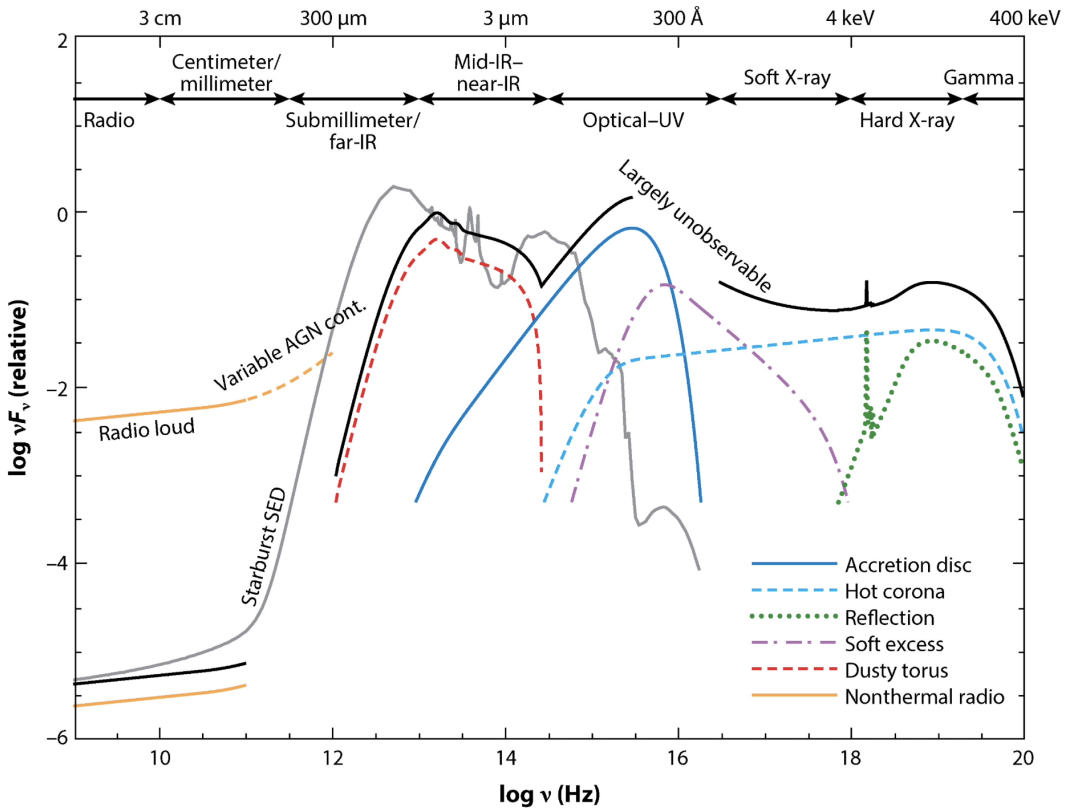

Figure 1.5: Schematic view of the AGN SED - energy spectral distribution coming from different components of an AGN (marked in the legend of a plot). Spectra of a galaxy with active star formation is shown in grey. From Hickox, Alexander (2018) originally adopted from Harrison (2014).

to the disruption of stellar material. A radius at which a TDE occurs is the so-called tidal radius:

$$r_{\rm t} = R_{\rm star} \left(\frac{M_{\rm BH}}{M_{\rm star}} \right)^{\frac{1}{3}} .$$

For a $1 M_\odot$ star and a $10^6 M_\odot$ black hole, this radius is around 1 a.u. (7×10^7 km). If the tidal radius is smaller than the BH's gravitational radius, the star is swallowed as a whole without a tidal disruption. The accretion of the disrupted material leads to the luminosity decaying in time (after initial peak) as a power-law function (Rees, 1988), $\dot{M} \propto t^{-5/3}$ with a peak effective temperature of $k_{\rm B}T \sim 30$ eV for $M_{\rm BH} = 10^6 M_\odot$. Emission of TDE may frequently be identified with X-ray observations of a galaxy when the central black hole changes its brightness according to the power-law explained above. For a review of TDE, see Gezari (2021). In this thesis, a TDE is a subject of investigation in Chapter 4, specifically in section 4.5.1.

Next, we will make a short introduction to the AGNs[5] as a population and how it is studied.

1.3.1 AGN population studies in X-ray

The census of accreting black holes over a wide range of cosmic time allows for studying the processes of their formation and evolution. It is known that the properties of SMBH are tightly correlated with the properties of their host galaxies notwithstanding a very small sphere of influence of a BH (Ferrarese, Merritt, 2000; Di Matteo et al., 2005; Hopkins et al., 2006, 2008; Fanidakis et al., 2012; McConnell, Ma, 2013; Kormendy, Ho, 2013; Heckman, Best, 2014; Harrison et al., 2018). The exact mechanism of this relationship (called **'AGN feedback'**, see Lagos et al. 2008; Alexander, Hickox 2012 and references above) is not known but it is certain that the growth of SMBH through accretion and the process of galaxy evolution are related (almost every galaxy is an AGN in some part of its life).

AGNs are quite numerous - millions of such sources are known from surveys in different wavelengths, from radio to γ-rays. It is long known that the population of AGNs is not static: currently, the spatial density of AGNs is not as large as it once used to be (cosmic evolution). This behaviour is seen in AGN surveys in radio, optical and X-ray bands and discussed below in more detail. The AGNs are also not distributed uniformly in space - they are clustered, and this non-uniformity has been measured in different bands of electromagnetic radiation. Studying the properties of the population helps to understand the growth of SMBHs and what environment AGN primarily occupy.

X-ray surveys reveal AGN activity in a less biased way compared to surveys at longer wavelengths (see Brandt, Hasinger (2005); Brandt, Alexander (2015) and also Fig. 1.6). In the last decades, a multitude of X-ray surveys of both deep[6] and shallow[7] types were performed. Almost all data come from X-ray surveys performed by *ROSAT*[8] (Truemper, 1982), *Chandra X-ray observatory* (Weisskopf et al., 2002), *XMM-Newton*[9] (Jansen et al., 2001), *Neil Gherels Swift*

[5] AGNs (plural form) will also be referred to as simply AGN in this thesis

[6] deep X-ray exposure and small sky area, so-called pencil beam surveys

[7] shallow X-ray exposure and large sky area

[8] Roentgensatellit

[9] X-ray Multi-Mirror Mission

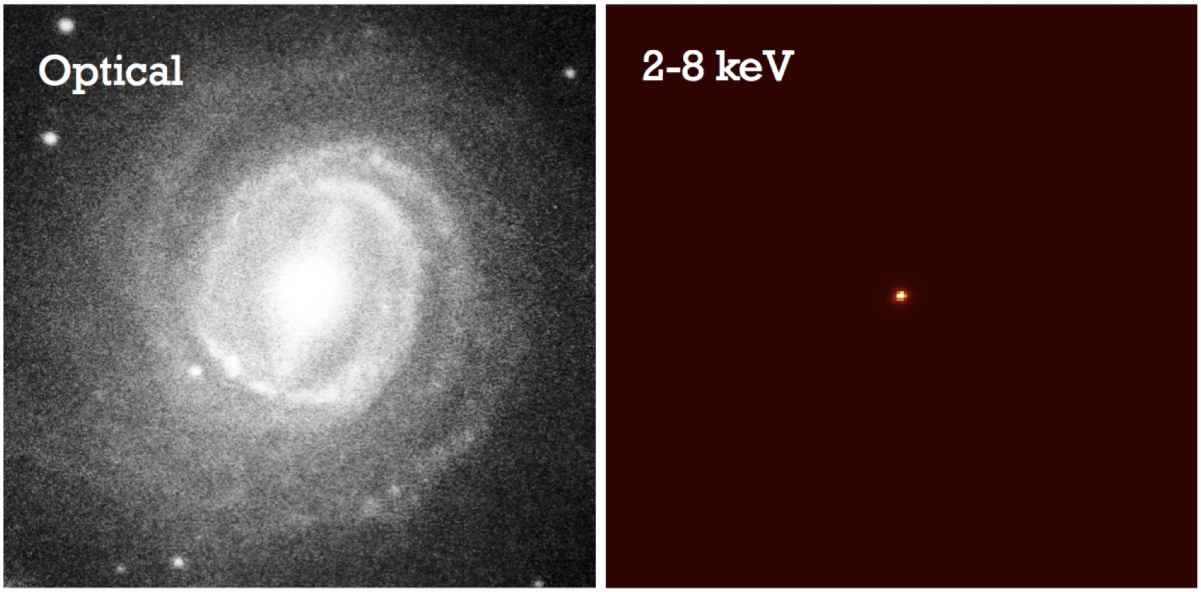

Figure 1.6: Active galaxy NGC 3783 in the optical (left) and X-ray (right, Chandra 2-8 keV) light. The emission of an accreting massive black hole is unambiguously identified from an X-ray image, whereas the optical data is contaminated by the host galaxy. From Brandt, Alexander (2015).

Observatory (Gehrels et al., 2004), *NuSTAR*[10] (Harrison et al., 2013), and recently ***SRG/eROSITA*** (Predehl et al. (2021), extensively used in this thesis as described in sect. 1.4). The plot of limiting X-ray flux – survey area corresponding to major X-ray surveys is shown in Fig. 1.7. In this figure, deep surveys have a small area but the best sensitivity, whereas shallow surveys cover a much larger area but have worse sensitivity. SRG/eROSITA telescope extensively used in this thesis is a wide-angle survey. We note that AGNs form the majority of X-ray detected sources down to the flux limits of $\sim 10^{-17}$ erg s^{-1} cm^{-2} (Lehmer et al., 2012). In fact, the AGN angular density achieves $\sim 10^4$ sources per degree squared (Luo et al., 2017), and deep surveys show that the AGNs are responsible for $\sim 90\%$ of the so-called extragalactic Cosmic X-ray background (CXB, Gilli et al. 2007; Moretti et al. 2012; Cappelluti et al. 2017).

These surveys allowed the precise measurements of AGN spatial density and the history of SMBH growth (as a function of redshift, luminosity and intrinsic absorption) up to large redshifts ($z \lesssim 6$), with an incomplete list of essential papers: Miyaji et al. (2000); Ueda et al. (2003); Hasinger et al. (2005); Brusa et al. (2009); Aird et al. (2010); Vito et al. (2014); Ueda et al. (2014); Aird et al. (2015); Buchner et al. (2015); Georgakakis et al. (2015); Miyaji et al. (2015); Ranalli et al. (2016); Fotopoulou et al. (2016); Ananna et al. (2019); Wolf et al. (2021). The study of spatial density is performed with the construction of **X-ray luminosity functions (XLF)**.

XLFs ϕ encode the number of objects dN per unit comoving volume dV and (log[11]) X-ray

[10] Nuclear Spectroscopic Telescope Array

[11] in this thesis, log operator will mean the decimal logarithm of a quantity

luminosity $\mathrm{d}\log L_\mathrm{X}$:

$$\phi(\log L_\mathrm{X}, z) = \frac{\mathrm{d}N}{\mathrm{d}V \mathrm{d}\log L_\mathrm{X}}.$$

The estimation of the XLF in a bin (assuming negligible evolution within the bin) may be performed with this formula (Page, Carrera, 2000):

$$\phi_\mathrm{bin} = \frac{N}{\int\int \Omega(\log L_\mathrm{X}, z) \frac{\mathrm{d}V}{\mathrm{d}z} \mathrm{d}z \mathrm{d}\log L_\mathrm{X}},$$

where N is the number of (observed) objects in a bin, $\frac{\mathrm{d}V}{\mathrm{d}z}$ is the differential comoving volume, and $\Omega(\log L_\mathrm{X}, z)$ is the area of a given survey for sources with a particular luminosity and redshift (so-called selection function). In the simplest case of a flux-limited survey, the survey area is the geometrical area of a survey for fluxes above the flux limit and zero otherwise. More thorough analysis involving simulations or analytical computations is usually needed to assess the available sky area of a survey (hence probed volume) as a function of flux (Georgakakis et al., 2008; Liu et al., 2022b).

Currently, more elaborated techniques are frequently used to make an *unbinned* estimation of XLF for an assumed functional dependency of XLF on luminosity and redshift (Georgakakis et al., 2015; Aird et al., 2015; Fotopoulou et al., 2016). The benefit of that approach is that the likelihood calculations may take full advantage of the fact that neither X-ray flux (luminosity) nor redshift are measured precisely and have uncertainties for each source. Non-parametric forms of XLF are also constructed (Buchner et al., 2015). The addition of a new dimension - intrinsic hydrogen absorption N_H, allows to also take into account that unabsorbed sources are over-represented in soft X-ray surveys. In fact, it is currently accepted that obscured AGNs constitute the majority of the AGN population (Ueda et al., 2014; Aird et al., 2015; Buchner et al., 2015; Ananna et al., 2019), see also Hickox, Alexander (2018, sect. 3) for review. The obscured portion of the AGN population depends on the luminosity and redshift (see references above). One of the peculiar results on the growth of the SMBH is that the peak abundance of low-luminosity AGNs occurs later in cosmic time (smaller redshift) than the peak of high-luminosity quasars, as illustrated in Fig. 1.8 and is called 'AGN downsizing'. Those facts are important to reconcile the growth of SMBH and their host galaxies (Alexander, Hickox, 2012; Fanidakis et al., 2012; Harrison et al., 2018).

In this thesis, we construct the X-ray luminosity function of a specific kind of active galaxies, AGNs located in galaxies of small mass (dwarf galaxies). We use a similar approach to that outlined above, but instead of volume density, we calculate the incidence of AGN in a parent population of dwarf galaxies in the Sloan Digital Sky Survey (SDSS). For more information, see Chapter 4 and specifically sect. 4.4.4.

Another important tool to study the environment and triggering mechanism of (X-ray) AGNs is the study of their distribution in space (**clustering studies**), see Gilli et al. (2005, 2009); Cappelluti et al. (2010); Hickox et al. (2011); Krumpe et al. (2012, 2018). Numerical simulations show that the growth of structures (structure formation) in the Universe is driven mainly by dark matter and structures experience hierarchical growth from the primordial density fluctuations (Springel et al., 2005). Galaxies (including AGNs) are believed to live in dark matter halos

(DMH) - large-scale agglomeration of dark matter which serves as a building block of the **Large-Scale Structure (LSS)** of the Universe (Navarro et al., 1996, 1997). Galaxies (and AGNs) are therefore tracers of the LSS, but, in a way, biased – galaxies do not form in every DMH, they occupy the most pronounced density peaks. In turn, AGNs are also a quite rare type of galaxy, therefore they have a bias of their own. The clustering properties of the AGN population may give hints about the environment they occupy, mainly via the estimated mass of the dark matter halos which is directly related to the clustering strength and its evolution with redshift.

Currently, it is estimated that the X-ray selected AGNs predominantly occupy halos with a mass similar to that of a group of galaxies ($M_{\rm DMH} \sim 10^{13}\ M_{\odot}$), see Allevato et al. (2011, 2016, 2019); Viitanen et al. (2023). It hints to a scenario of AGN triggering via mergers of galaxies is subdominant in comparison to secular processes (such as disc instabilities), but the dominant fuelling mechanism may depend on luminosity (Hopkins et al., 2006, 2008). See Cappelluti et al. 2012 for the review of X-ray clustering of AGNs. The clustering of obscured and unobscured AGNs is also studied in attempts to check whether the obscuration is a geometrical effect or whether those AGNs live in different environments. The majority of works do not report very significant differences between the clustering of type-1 and type-2 AGNs (Ebrero et al., 2009; Coil et al., 2009; Mountrichas, Georgakakis, 2012; Powell et al., 2018), but the matters are complicated due to the different definitions of obscured AGNs used by different authors (e.g. via the hardness ratio or the measured hydrogen column density, see Viitanen et al. 2023). Some, on the other hand, claim the difference in the clustering (thus environment) between two types of AGNs (Elyiv et al., 2012; Koutoulidis et al., 2018; Viitanen et al., 2023). Overall, the progress in understanding the dependence of the clustering strength of AGNs on luminosity, redshift or type is somewhat hampered by the relatively small sample sizes used to derive the correlation function. The advent of SRG/eROSITA with a clean sample of a few million X-ray AGNs will provide a new window into the studies of the LSS of X-ray AGNs and quasars (Kolodzig et al., 2013a).

From the point of view of data analysis, the clustering studies are performed with the help of **correlation functions**. Briefly, a two-point autocorrelation function (ACF, $\xi(r)$) is a two-point statistic which estimates the probability $\mathrm{d}P$ of finding a pair of objects at a given separation in small volume elements: $\mathrm{d}P = n^2[1 + \xi(r)]\mathrm{d}V_1\mathrm{d}V_2$, where n is the density of objects, $\mathrm{d}V_{1,2}$ is the volume element. ACF is estimated from the data using the randomly generated catalogues with similar selection functions as in a real catalogue, but uniform distribution of sources in space. Clustering studies may be performed in 3D (spatial) or in 2D (angular) space. For a review of the clustering measurement techniques, see Cappelluti et al. (2012) and also Chapter 2. The models of bias factors of X-ray AGNs[12] and how it can be translated into measurable correlation functions is described extensively in Chapter 2, sect. 2.3. In the same chapter, we discuss how the overall shape of the correlation function depends on the cosmological parameters (the history of the growth of primordial density fluctuations) and show that the SRG/eROSITA sample of AGNs will be able to pinpoint the values of cosmological parameters.

[12] i.e. the increase of clustering amplitude of their 3D power spectra with respect to the underlying dark matter fluctuation power spectra

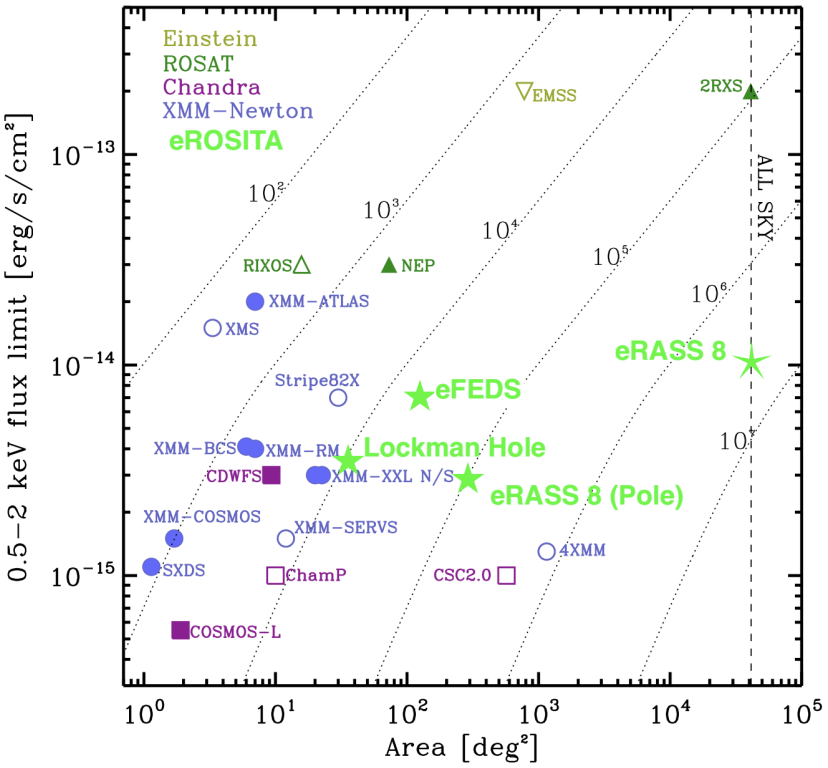

Figure 1.7: Limiting flux - area curve for various X-ray surveys and SRG/eROSITA. Original image from Brunner et al. (2022a) with the addition of eROSITA surveys: eFEDS (Brunner et al., 2022a), Lockman hole (Gilfanov et al., in prep + see Chapter 3), eRASS 8 (full-sky average and poles). The dotted lines show the contours of a constant number of detected sources using number counts from Mateos et al. (2008).

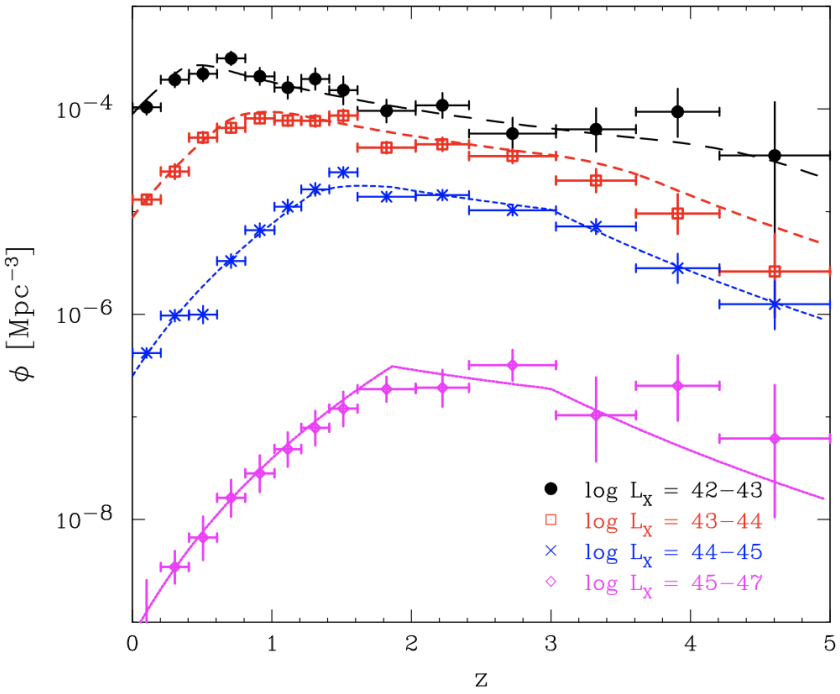

Figure 1.8: Co-moving number density of AGNs as a function of redshift. Colours encode the (log) X-ray luminosity. AGN downsizing is evident - less luminous objects peak later in time than more powerful AGNs. Adapted from Brandt, Alexander (2015), originally from Ueda et al. (2014).

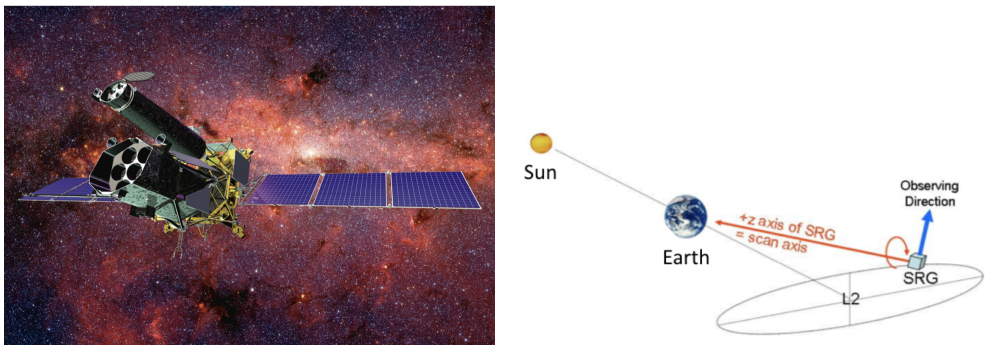

Figure 1.9: Left: artist's impression of SRG in space. ART-XC is on the top, eROSITA is at the bottom, and both are mounted on a platform 'Navigator'. Right: Schematics of an orbit of the observatory, arrow shows the rotation of the spacecraft during the all-sky scanning mode. Distance to Earth is around 1.5 million km. Both figures from Sunyaev et al. (2021).

1.4 SRG/eROSITA X-ray telescope

As demonstrated above, X-ray surveys are the most direct way to find and study active galactic nuclei. AGN science is one of the main drivers for SRG/eROSITA telescope (Merloni et al., 2012). eROSITA stands for "**extended ROentgen Survey with an Imaging Telescope Array**", and SRG is an abbreviation of "Spektr-RG" (Spectrum + Roentgen + Gamma).

SRG (Sunyaev et al., 2021) is a Russian-German astrophysical space observatory launched on 13 July 2019 from Baikonur Cosmodrome. It hosts two X-ray telescopes - eROSITA (Predehl et al., 2021) and ART-XC (Pavlinsky et al., 2021). eROSITA is sensitive to X-rays with energies 0.2–9 keV and was developed by the Max Planck Institute for Extraterrestrial Physics (MPE). ART-XC (Mikhail Pavlinsky Astronomical Roentgen Telescope - X-ray Concentrator) is a hard X-ray telescope with sensitivity in the 4–30 keV energy range, developed by Space Research Institute (IKI). The main view of the observatory and its orbit to perform scans is shown in Fig. 1.9. The observatory is located in the second Lagrange point of the Earth-Sun system on the so-called halo orbit (Sunyaev et al., 2021).

eROSITA is the second telescope (after ROSAT, Truemper (1982); Voges et al. (1999)) to perform the survey of the sky in soft X-ray wavelengths. The main scientific drivers for the mission are problems related to **galaxy clusters and AGN population studies**. The population of galaxy clusters (namely, their distribution in mass, redshifts and clustering properties) are sensitive to the cosmological parameters such as matter density $\Omega_{\rm m}$ and total rms fluctuation power σ_8 (Vikhlinin et al., 2009a,b; Allen et al., 2011), see Chapter 2. In comparison to ROSAT, eROSITA is by a factor of $\sim$ 20 more sensitive to soft X-rays, allowing the production of an unprecedented number of detected AGNs and galaxy clusters, and pushing further **AGN population studies** including X-ray luminosity functions, clustering and even cosmological measurements (Kolodzig et al., 2013b,a; Hütsi et al., 2014; Comparat et al., 2019). eROSITA performed a few auxiliary surveys during the performance verification phase of the mission. One survey is called eFEDS (**eROSITA final equatorial depth survey**, Brunner et al. 2022b) and the **deep survey of Lockman Hole** (Gilfanov et al., in prep). eFEDS has an area of approximately 140 squared degrees and has

limiting sensitivity close to what is expected from the eROSITA's final all-sky survey sensitivity in the ecliptic equator (around 10^{-14} erg s^{-1} cm^{-2}). Lockman Hole survey has an area of around 30 square degrees and has sensitivity by a factor of a few better (around 3×10^{-15} erg s^{-1} cm^{-2}). Both surveys are shown in Fig. 1.7. In this thesis, we use the data from the all-sky survey of eROSITA (eRASS) in Chapter 4 and the data from Lockman Hole in Chapter 3.

eROSITA's technical description is provided by Predehl et al.. The instrument consists of seven identical mirror assemblies (MA, 54 paraboloid/hyperboloid nickel shells with Wolter-I geometry and gold covering) and camera assemblies (CA, charge-coupled devices with 384×384 pixels, with around 1-degree field of view corresponding to approx 10 arcsec pixel resolution on a sky). Each pair of MA/CA make one of seven co-aligned telescope modules called TM1...TM7. The average on-axis point source response of MAs is 16.1" half-energy width (HEW) at the energy of 1.5 keV, but the average over the field of view (FoV) is worse – 26". The resolution degrades with the increase of the off-axis angle. The **effective area** of eROSITA measures its ability to collect X-rays in the working energy range and depends strongly on the energy of incident photons. Since the main mode of operation of SRG is an X-ray survey, the important characteristic is the effective area in a given energy (averaged over FoV) multiplied by the field of view – a value called **grasp**. Grasp measures the ability to perform X-ray surveys and is useful to compare eROSITA with more sensitive telescopes (e.g. Chandra, XMM) having a smaller FoV. The grasp of eROSITA is shown in Fig. 1.10 and is so far unparalleled in comparison to Chandra, ROSAT and XMM (in the 0.3–2.3 keV energy range).

In the **all-sky survey mode**, SRG observatory rotates around the survey axis, making one rotation in four hours, therefore making a map of the sky with the width of $\sim$ 1 deg (FoV size) and height of 360 deg. One all-sky scan therefore takes around half a year to complete. The planned duration of the mission is four years with 8 full all-sky scans (eRASS1...8). So far eROSITA completed four all-sky surveys and 40% of the fifth. Due to the orbit shape, all scans intersect in two poles of ecliptic orbit - the exposure here is the greatest (over 1 ks per point in one all-sky scan), and falls down at smaller longitudes - the expected exposure is around 300 seconds in the ecliptic equator in a single all-sky scan.

The eROSITA data and properties are extensively used in this thesis (in Chapters 2, 3, 4).

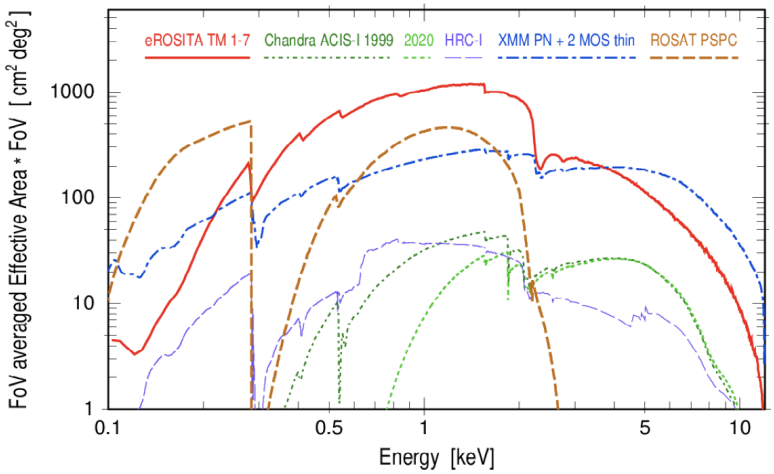

Figure 1.10: Grasp of eROSITA (red) - the product of the field of view and the effective area at a given energy. The grasp of other X-ray observatories is shown in different colours according to the legend. From Predehl et al. (2021).

1.5 Thesis outline

The main results of this work are reported in several published papers (**Bykov** et al., 2021, 2022b,a, 2023, 2024). Part one of the thesis (Chapters 2,3 and 4) is devoted to the studies of AGNs and cosmology. Part two of the thesis (Chapters 5 and 6) is related to X-ray pulsars.

In Chapter 2 we explore the prospects of SRG/eROSITA sample of AGN and galaxy clusters for cosmological measurements. As a cosmological probe, we use the clustering properties of both populations. We assume the presence of photometric redshift estimates of the distances and examine its effect on the quality of the forecast. We also consider how the survey parameters such as area and depth affect the cosmological constraints.

In Chapter 3 we develop a method for the search of *optical* counterparts of *X-ray* sources using SRG/eROSITA catalogue in the Lockman Hole as an example. We apply machine learning techniques and Bayesian statistics to use the photometric properties of optical objects to select the most probable counterparts to eROSITA sources.

In Chapter 4 we perform a search for active nuclei in low-mass (so-called dwarf) galaxies. To identify the accreting black holes, we use X-ray data from SRG/eROSITA. We estimate the fraction of the active dwarf galaxy population and its dependence on the X-ray luminosity and stellar mass of the host. We discovered several sources with interesting properties from the point of view of AGN triggering and BH population.

In Chapter 5 and 6 we study the geometry of accretion flows in two X-ray pulsars. For that, we use X-ray emission of a neutron star reprocessed by surrounding matter. We perform time-resolved analysis of X-ray emission spectra and speculate on the possible configuration of accretion flows.

In Chapter 7 we summarise the main findings of this thesis.

The thesis is the report of my doctoral projects supervised by Prof. Dr. Rashid Sunyaev and Dr. Marat Gilfanov at the Max Planck Institute for Astrophysics.

List of publications upon which this thesis is based (in chronological order):

1. *"Pulsating iron spectral features in the emission of X-ray pulsar V 0332+53", **Bykov** et al. 2021, Monthly Notices of the Royal Astronomical Society, Volume 506, Issue 2, pp.2156-2169*

2. *"ULX pulsar Swift J0243.6+6124 observations with NuSTAR: dominance of reflected emission in the super-Eddington state", **Bykov** et al. 2022b, Monthly Notices of the Royal Astronomical Society, Volume 516, Issue 2, pp.1601-1611*

3. *"Optical Cross-Match of SRG/eROSITA X-ray Sources Using the Deep Lockman Hole Survey as an Example", **Bykov** et al. 2022a, Astronomy Letters, Volume 48, Issue 11, p.653-664*

4. *"Forecasts for cosmological measurements based on the angular power spectra of AGN and clusters of galaxies in the SRG/eROSITA all-sky survey", **Bykov** et al. 2023, Astronomy & Astrophysics, Volume 669, id.A61, 15 pp.*

5. *"SRG/eROSITA catalogue of X-ray active SDSS dwarf galaxies", **Bykov** et al. 2024, Monthly Notices of the Royal Astronomical Society, Volume 527, Issue 2, pp.1962–1981*

Part I

Accreting massive black holes and cosmological forecast

CHAPTER 2

Forecasts for cosmological measurements based on the angular power spectra of AGN and clusters of galaxies in the SRG/eROSITA all-sky survey

The contents of this chapter are based on the manuscript originally published in ***Bykov*** *et al. (2023). My contribution to that paper was the main idea for the project, calculations of all relevant quantities (X-ray luminosity function, angular power spectra, etc.), discussion of the results in the context of modern cosmological missions and writing. Other authors (especially M. Gilfanov) contributed to the discussion of calculations and writing.*

Abstract

The eROSITA X-ray telescope aboard the Spectrum-Roentgen-Gamma (SRG) orbital observatory, in the course of its all-sky survey, is expected to detect about three million active galactic nuclei (AGNs) and approximately one hundred thousand clusters and groups of galaxies. Such a sample, clean and uniform, complemented with redshift information, will open a new window into the studies of the large-scale structure (LSS) of the Universe and the determination of its cosmological parameters. The purpose of this work is to assess the prospects of cosmological measurements with the eROSITA sample of AGNs and clusters of galaxies. We assumed the availability of photometric redshift measurements for eROSITA sources and explored the impact of their quality on our forecasts. As the LSS probe, we use the redshift-resolved angular power spectrum of the density fluctuations of objects. We employed a Fisher-matrix formalism and assumed flat ΛCDM cosmology to forecast the constraining power of eROSITA samples of AGNs and clusters of galaxies. We computed the LSS-relevant characteristics of AGNs and clusters in the framework of the halo model and their X-ray luminosity functions. As the baseline scenario, we considered the full four-year all-sky survey and investigated the impact of reducing the survey length to two years. We find that the accuracy of photometric redshift estimates has a more profound effect on cosmological measurements than the fraction of catastrophic errors. Under realistic assumptions about the photometric redshift quality, the marginalised errors on the cosmological parameters achieve $1-10\%$ accuracy depending on the cosmological priors used from other experiments. The statistical significance of Baryon acoustic oscillation detection in angular power spectra of AGNs and clusters of galaxies considered individually achieves $5-6\sigma$. Our results demonstrate that the eROSITA sample of AGNs and clusters of galaxies used in combination with currently available photometric redshift estimates will provide cosmological constraints on a par with dedicated optical LSS surveys.

2.1 Introduction

The distribution of matter in the Universe is not uniform. Galaxies form the so-called cosmic web, comprising filaments, walls, and voids, which make up the large-scale structure (LSS) of the Universe (Dodelson, 2003; Eisenstein et al., 2005; Beutler et al., 2011; Alam et al., 2017). Mapping the LSS yields a wealth of important information about cosmological parameters, the evolution of density perturbations, the growth of structures, and the mass-energy content of the Universe (Tegmark et al., 2004; Percival et al., 2010; Blake et al., 2011; Padmanabhan et al., 2012; Abbott et al., 2022a,b). The LSS is traced not only by normal galaxies but also by active galactic nuclei (AGNs) and clusters of galaxies.

The large-scale structure has been probed by several wide-angle optical galaxy surveys such as SDSS (Sloan Digital Sky Survey)[1], DES (Dark Energy Survey[2]), 2dF (2dF Galaxy Redshift Survey[3]). Using spectroscopic or photometric redshifts of the objects, such surveys unveil the 3D distribution of visible matter in the Universe, permitting us to measure its power spectrum and to detect and quantify various cosmologically significant effects such as baryon acoustic oscillations (BAOs, Sunyaev, Zeldovich, 1970; Peebles, Yu, 1970) and redshift-space distortions (RSD, Kaiser, 1987). These data allow one to measure cosmological parameters (Cole et al., 2005; Eisenstein et al., 2005; Abbott et al., 2022a,b; Alam et al., 2021). Planned space missions and ground-based facilities, such as Euclid[4], the Vera Rubin observatory[5], the Dark Energy Spectroscopic Instrument[6], and the Nancy Grace Roman Telescope[7] will dramatically increase the number of objects available for cosmological studies, potentially increasing the accuracy of cosmological measurements.

To date, all cosmologically significant large-scale structure surveys have been conducted in visible light. However, the selection of galaxies and quasars in optical wavelengths is complicated by a number of effects, such as contamination by stars and nearby galaxies, absorption, and several others. On the contrary, X-ray surveys represent an efficient tool for identifying accreting supermassive black holes – indeed, AGNs constitute the majority of sources detected in extragalactic X-ray surveys (e.g. Brandt, Hasinger, 2005; Sunyaev et al., 2021). Deep (but relatively narrow, up to $\sim$ 25 sq. degrees) X-ray surveys performed by XMM-Newton and Chandra observatories demonstrated the feasibility and usefulness of studying the clustering of X-ray-selected AGNs (Allevato et al., 2011; Mountrichas et al., 2016; Kolodzig et al., 2017, 2018; Allevato et al., 2019). Furthermore, hot intracluster medium shines in X-rays by which means one can detect a cluster of galaxies without actually registering individual galaxies. X-ray data allow the determination of cluster mass and temperature, quantities essential for astrophysics and cosmology (e.g. Vikhlinin et al., 2009a,b; Allen et al., 2011). Thus, X-ray-selected samples present a reasonably clean and complete flux-limited census of extragalactic objects – AGNs and clusters of galaxies - for which

[1] http://sdss.org
[2] https://www.darkenergysurvey.org
[3] http://www.2dfgrs.net
[4] https://sci.esa.int/web/euclid
[5] https://www.lsst.org
[6] https://www.desi.lbl.gov
[7] https://roman.gsfc.nasa.gov

number density is sufficient to study the LSS.

The SRG orbital X-ray observatory (Sunyaev et al., 2021) was launched into the halo orbit around the Sun-Earth Lagrangian L2 point on July 13, 2019, and on December 12, 2019, an all-sky survey began, which was planned to continue for four years, until December 2023. So far, the eROSITA telescope has completed 4.4 full sky surveys and currently is in safe mode. The SRG observatory continues science observations in the interests of the Mikhail Pavlinsky ART-XC telescope – the second science instrument aboard the SRG observatory.

In the course of the full four-year all-sky survey, the eROSITA telescope (Predehl et al., 2021) aboard SRG is expected to detect, in the $0.5 - 2$ keV energy range, ~ 3 million AGNs with a median redshift of $z \sim 1$ (Kolodzig et al., 2013b) and $\sim 10^5$ clusters of galaxies with a median redshift of $z \sim 0.4$ (Merloni et al., 2012; Pillepich et al., 2012). Cosmological measurements and the nature of dark energy are the main scientific drivers of the mission (Sunyaev et al., 2021). To this end, a significant role will be played by the measurements of the mass function of clusters of galaxies based on their X-ray properties. Cosmological studies can be also conducted using the 3D distribution of quasars and clusters of galaxies. The enormous size of the X-ray-selected AGN sample makes their study especially meaningful in this context; as shown earlier, BAOs will be clearly detectable in the eROSITA AGN sample (Hütsi et al., 2014; Kolodzig et al., 2013a). Prospects of cosmological studies with clusters of galaxies have been previously investigated by Pillepich et al. (2012); however, the potential role of AGNs remained unexplored.

The purpose of the present chapter is to fill this gap and to forecast the accuracy of cosmological measurements based on AGN samples detected in the SRG/eROSITA all-sky survey. To facilitate the comparison with AGNs and previous works and to investigate the power of combined AGN-cluster estimates, we also present results of similar calculations for clusters of galaxies. In our calculations, we used the characteristics of eROSITA performance measured in-flight during the first two years of the survey, and realistic, already achieved parameters of the photometric redshift estimates of AGNs and clusters of galaxies.

The chapter is structured as follows. We assess the usefulness of AGNs and clusters for large-scale structure studies in the presence of photometric redshift errors in Section 2.2. In Section 2.3, we describe the calculations of redshift distributions and linear bias factors of both tracers, as well as the model for photo-z scatter in distance measurements. We explain formalism for computing the two-point correlation function and Fisher matrix forecasts in Sect. 2.4. Sect. 2.5 presents our forecast for BAO detectability and cosmological precision. We discuss our findings and place the results in the context of current cosmological probes in Sect. 2.6. We conclude in Section 2.7. In Appendix A, we justify the usage of the Fisher matrix method by comparing its predictions with the posterior distribution calculated with the Markov chain Monte Carlo algorithm. In appendix B we describe a set of simulations of the small-scale clustering measurements of AGN in a narrow X-ray survey.

We use decimal logarithms throughout the chapter and assume fiducial cosmological parameters, $H_0 = 70$ km s^{-1} Mpc^{-1}, $\Omega_\mathrm{m} = 0.3$, $\Omega_b = 0.05$, $\sigma_8 = 0.8$, and $n_\mathrm{s} = 0.96$ for flat ΛCDM cosmology. Mass is in units of M_{500c}. Cosmological calculations of distances, halo model, biases, and so on are done in the Core Cosmology Library (CCL[8], Chisari et al., 2019). Unless stated

[8] https://ccl.readthedocs.io/en/latest/

otherwise, angular power spectra are calculated with the Code for Anisotropies in the Microwave Background (CAMB[9], Lewis, Challinor, 2011).

2.2 Initial feasibility study

The 3D distribution of matter is usually analysed with two-point statistics. A common choice is the power spectrum, which shows the amplitude of density fluctuation on a given co-moving scale, and its errors are directly related to the ability of the survey to sample the LSS. Hütsi et al. (2014) showed that the density of AGNs in the eROSITA survey would provide sufficient signal-to-noise ratio at the median redshift of $z = 1$.

The capability of a survey to probe the LSS depends on the volume of the Universe observed given the power spectrum of tracer objects and their redshift distribution. This is quantified by the effective volume of a survey, $V_{\rm eff}$ (Eisenstein et al., 2005):

$$V_{\rm eff}(k) = \Omega \int_{z_{\rm min}}^{z_{\rm max}} \left(\frac{\mathcal{N}(z) P_{\rm tr}(k,z)}{\mathcal{N}(z) P_{\rm tr}(k,z) + 1} \right)^2 \frac{{\rm d}V(z)}{{\rm d}z} {\rm d}z,$$

where Ω is a solid angle of a survey, $\mathcal{N}(z)$ is the spatial number density, $P_{\rm tr}(k)$ is the tracer power spectrum, and $\frac{{\rm d}V(z)}{{\rm d}z}$ is the differential co-moving volume. Differential volume is calculated with the formula $\frac{{\rm d}V(z)}{{\rm d}z} = cr(z)^2/H(z)$ [Mpc^3 sr^{-1}], where r is the co-moving radial distance, $H(z)$ is a Hubble parameter, and c is the speed of light. The details of the calculation of redshift distribution and power spectrum are in the next section. The error on the power spectrum is proportional to the $V_{\rm eff}^{-\frac{1}{2}}$ assuming Gaussian statistics and independent bins in k space. The effective volume for the spectroscopic eROSITA sample of AGNs was calculated in Kolodzig et al. (2013a) and shown to be larger than those of some of the optical surveys. In the present chapter, we go one step further and include clusters of galaxies and the effects of photometric redshift errors.

We utilised the model of Hütsi (2010) to take into account the power suppression on small scales due to the photo-z errors. The power spectrum of tracers is found as

$$P(k,z)_{\rm tr} = b^2(z) P(k,z)_{\rm CDM} \times \frac{\sqrt{\pi}}{2\sigma k} \, {\rm erf}(\sigma k),$$

where $b(z)$ is the linear bias factor, $P(k,z)_{\rm CDM}$ is the power spectrum of dark matter, and spatial suppression scale $\sigma = \frac{c}{H(z)} \sigma_z$ (c is the speed of light, $H(z)$ is the Hubble constant at given z, and $\sigma_z = \sigma_0(1 + z_{\rm eff})$ is the photometric redshift error). $z_{\rm eff}$ is taken as 1 for AGNs and 0.4 for clusters. σ_0 is a free parameter that depends on the quality of the optical follow-up. We restrict $0.5 < z < 2.5$ and $0.1 < z < 0.8$ for AGNs and clusters, respectively, assuming 65% of the sky used in the analysis. Photo-z scatter, σ_0, is varied between 0 and 0.05.

We show the results in Fig. 2.1. The effective volume for an AGN sample drops from ~ 50 to less than ~ 2 h^{-3}Gpc^3 between $k = 0.01$ and $k = 0.2$ h Mpc^{-1}. For clusters, the figures are ~ 4

[9] https://camb.readthedocs.io/en/latest/index.html

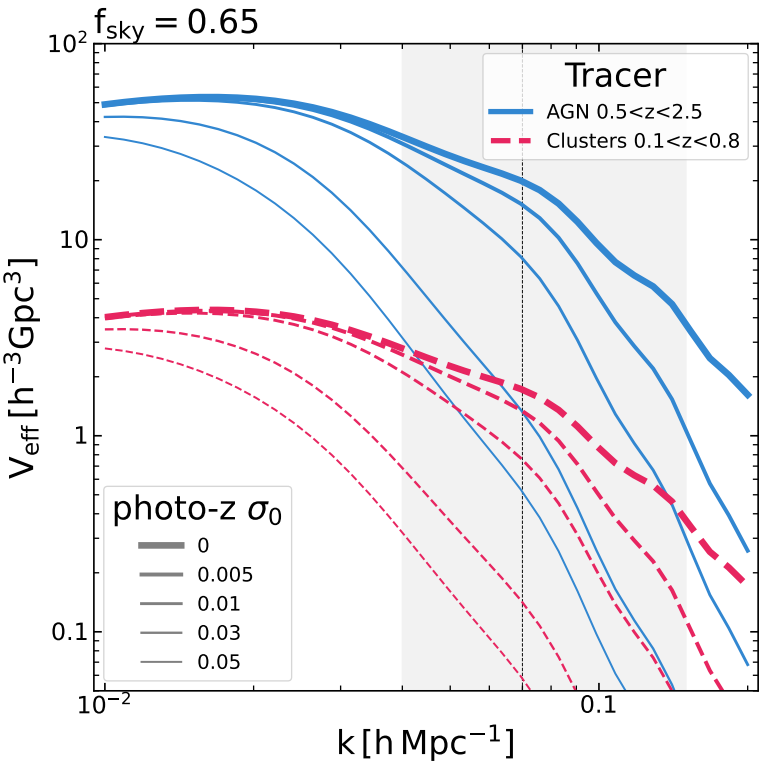

Figure 2.1: Effective volume as a function of co-moving scale probed by AGNs and clusters (solid and dashed lines, respectively) in the eROSITA all-sky survey. The thicker the line, the better the quality of photo z. The grey band illustrates the scales where the BAO feature is prominent, and the vertical dashed line shows the position of the first peak.

and $\sim 0.2\ h^{-3}Gpc^3$. It can be seen that on very large scales (small k) the AGN sample is more efficient than clusters, even when the photo-z errors are large. In the area of moderate scales ($k = 0.05 - 0.2$), the relative performance of both tracers depends significantly on the quality of photo-z. For instance, even though AGNs are much more numerous (2 mil), with the $\sigma_0 = 0.05$ they would be outperformed by a much smaller number of clusters (90k) with $\sigma_0 < 0.005$. Typically one may expect $\sigma_0 = 0.03$ for AGNs and 0.01 for clusters. In this configuration, the effective volumes at BAO scales are comparable.

We, therefore, expect that both tracers suffer significantly from the loss of the photometric redshift precision and that the AGN and cluster samples would provide roughly comparable results and complement each other.

2.3 Modelling details

In this section, we illustrate our calculations of redshift distributions and number counts (sect. 2.3.1), linear bias factors (sect. 2.3.2), and the model for photometric redshift (Sect. 2.3.3).

2.3.1 X-ray luminosity functions

To the power spectrum shape, we need to know the space number densities of AGNs and clusters. With the knowledge of the X-ray luminosity function (XLF) of AGN $\phi(\log L, z)$ and the flux limit of the survey, we calculated the distribution of AGNs with redshift. We used the XLF measured in Hasinger et al. (2005) with an exponential cutoff for $z > 2.7$ (Brusa et al., 2009); for details of calculations, see Kolodzig et al. (2013b).

The shape of the AGN XLF is the following:

$$\phi(L, z) = K_0 \left[\left(\frac{L}{L_*} \right)^{\gamma_1} + \left(\frac{L}{L_*} \right)^{\gamma_2} \right]^{-1} \times e(L, z),$$

where factor

$$e(L, z) = \begin{cases} (1+z)^{p_1}, z \leq z_c(L) \\ (1+z_c(L))^{p_1} \left(\frac{1+z}{1+z_c(L)} \right)^{p_2}, z > z_c(L), \end{cases} \tag{2.1}$$

and cutoff redshift

$$z_c(L) = \begin{cases} z_{c,0} \left(\frac{L}{L_\alpha} \right)^{\alpha}, L \leq L_\alpha \\ z_{c,0}, L > L_\alpha. \end{cases} \tag{2.2}$$

All parameters were taken from Hasinger et al. (2005), Table 5, LDDE model. The cutoff over redshift 2.7 is done as in Kolodzig et al. (2013b), i.e. $\phi(L, z) \rightarrow \phi(L, 2.7) \times 10^{0.43(2.7-z)}$ for $z > 2.7$.

The redshift distribution $n(z)$, per deg^2, is found as

$$n(z) = \frac{\mathrm{d}V(z)}{\mathrm{d}z} \int_{\log L_{\min}(S,z)}^{48} \phi(\log L, z) \mathrm{d} \log L,$$

where $\frac{\mathrm{d}V(z)}{\mathrm{d}z}$ is the differential co-moving volume, S is the flux limit of the survey (we adopt 10^{-14} erg s^{-1} cm^{-2}), and the smallest observed luminosity $L_{\min}$ at given redshift z is found as $L_{\min} = 4\pi S r_{\mathrm{L}}^2$ (r_{L} is the luminosity distance). The k correction was done assuming a photon index of $\Gamma = 1.9$ and no absorption.We multiply the XLF by a factor of 1.3 to match the predicted sky number density of AGNs at a flux limit of 10^{-14} erg s^{-1} cm^{-2} with observations (i.e. ~ 90 AGN/deg^2; see e.g. Georgakakis et al. (2008).

The resulting AGN distribution is shown in Fig. 2.2 (panel A). The distribution peaks at $z \approx 1$ and yields ≈ 2474000 AGN on 65.8% of the sky. This sky fraction corresponds to the extragalactic sky $|b| > 15$ deg. During the calculations of the effective volume in the previous section, the spatial number density of objects was found as $\mathcal{N}(z) = \frac{n(z)}{\mathrm{d}V/\mathrm{d}z}$.

To calculate the distribution of clusters of galaxies, we invoke the halo model approach. We start from the halo mass function $n(M, z)$ of Tinker et al. (2008) and the fixed mass-luminosity relation of X-ray clusters calibrated in Vikhlinin et al. (2009a, eq. 22)[10]. We used k correction assuming the thermal plasma model APEC with temperature from Vikhlinin et al. (2009a, Table 3, free slope). The minimum mass for integration is taken as $5 \times 10^{13}\ h^{-1}\ M_\odot$ [11] since the ML relation is not well-known for lower masses. The redshift distribution is then found as

$$n(z) = \frac{\mathrm{d}V(z)}{\mathrm{d}z} \int_{M_{\rm min}(S,z)}^{M_{\rm max}} n(M, z)\mathrm{d}M,$$

where, as before, $M_{\rm min}(S, z)$ is the minimum observable mass at a given redshift, and $M_{\rm max}$ is the maximum mass considered ($10^{16}\ h^{-1}\ M_\odot$). As the limiting flux, we assume 4.4×10^{-14} erg s^{-1} cm^{-2} (for extended source detection, see Pillepich et al. (2012, fig. 4).

Such a flux limit produces the redshift distribution shown in panel B in Fig. 2.2, with the break at $z \approx 0.3$ due to the minimum mass cut. On 65.8% of the sky, one would detect ≈93400 clusters, with ≈ 900 of them at $z > 1$. Approximately 52200 would have masses of $M > 10^{14}$ $h^{-1}\ M_\odot$, and 3100 clusters with $M > 3 \times 10^{14}\ h^{-1}\ M_\odot$.

2.3.2 Linear bias factors

Active galactic nuclei and clusters live in dark matter halos. Halos are biased tracers of the underlying dark matter distribution, and they are more clustered.

The bias factors of X-ray-selected AGNs at different redshifts were measured with XMM-Newton data (Allevato et al., 2011) and were found to be consistent with the biasing of dark matter halos with the mass similar to that of the galaxy group, $M_{\rm DMH} \sim 10^{13}\ h^{-1}\ M_\odot$. We, therefore, used the model (fitting formulae) of Tinker et al. (2010) for the bias $b_{\rm eff}(z)$ of dark matter halos with a mass of $2 \times 10^{13}\ h^{-1}\ M_\odot$. The bias is shown in panel C of Fig. 2.2.

For X-ray clusters, we used the halo model with effective bias given by the average bias of halos weighed with their number density:

$$b_{\rm eff}(z) = \frac{\int_{M_{\rm min}(S,z)}^{M_{\rm max}} b(M, z)n(M, z)\mathrm{d}M}{n(z)}.$$

We show the effective bias of the cluster population in Fig. 2.2, panel C. At the peak redshift of the sample, the bias factor is ~ 3. This is consistent with the bias measurements with the two-point correlation functions of ∼ 200 X-ray-selected galaxy clusters from the XMM-Newton XXL survey (Marulli et al., 2018). We limited our calculations for clusters of galaxies by a redshift of 0.8, as explained in Section 4. Correspondingly, we do need to construct a bias model for clusters beyond this redshift value.

[10] We ignore the scatter in this relation for simplicity, but uncertainties in this relation have a profound effect on the cosmological analysis, see Pillepich et al. (2012).

[11] $5 \times 10^{13}\ h^{-1}\ M_\odot = 7.14 \times 10^{13} M_\odot$ in our fiducial cosmology

2.3.3 Photometric redshift model

Photometric redshifts have poorer accuracy than redshifts based on spectroscopic data. However, it is compensated by the possibility of estimating redshifts for a much larger number of objects. A common approach to analysing photometric-redshift data sets is to bin objects in the redshift space so that one 'integrates out' the effects of photo-z errors. The width of the bins is chosen to be a few times the photo-z scatter at a given z. The true underlying distribution of redshifts (spec-z) would be smoothed in those bins by random errors (i.e. scatter $z_{\rm spec} - z_{\rm phot}$). We used the model of Hütsi et al. (2014) for Gaussian photometric redshift errors (see their Eq. 7) with two parameters: σ_0, which controls the scatter, and $f_{\rm fail}$ - the catastrophic errors fraction. The smoothed shape of the i-th redshift bin $n^{(i)}$ ($z_{p_1}^{(i)} < z < z_{p_2}^{(i)}$) is given by

$$n^{(i)}(z) = n(z) \left[(1 - f_{\rm fail}\,) \frac{\mathrm{erf}\left(\frac{z_{\rm p_2}^{\rm (i)} - z}{\sqrt{2}\sigma(z)}\right) - \mathrm{erf}\left(\frac{z_{\rm p_1}^{\rm (i)} - z}{\sqrt{2}\sigma(z)}\right)}{1 + \mathrm{erf}\left(\frac{z}{\sqrt{2}\sigma(z)}\right)} + f_{\rm fail}\,\frac{z_{p_2}^{(i)} - z_{p_1}^{(i)}}{z_p^{\rm max}} \right],$$

where $\sigma(z) = \sigma_0(1+z)$ is the scatter and $z_p^{\rm max}$ is the maximum redshift of the sample.

The diluted bins of the photometric redshift selection of AGNs or clusters for fiducial values of parameters σ_0 and $f_{\rm fail}$ are shown in Fig. 2.2 on panels A and B with coloured solid lines. The coloured vertical strips correspond to the bin's borders in photo-z space, and the solid line of the respective colour shows the true underlying distribution in spec-z space. As the redshift bin width, we use $\Delta z = \sigma(z)$ at a given redshift if not stated otherwise. We illustrate the effect of photometric redshift errors in Fig. 2.3, where we plot the dilution of a redshift bin for various values of σ_0.

Multi-wavelength data and the availability of rich spectroscopic information for large samples of objects allow efficient training of the models for source classification and photo-z evaluation. The SRGz machine learning system for classification and photometric redshift estimation is being developed by the Russian eROSITA consortium (Meshcheryakov et al., in prep; see also Borisov et al. (2021); Belvedersky et al. (2022b)). SRGz is capable of determining photometric redshift probability density distribution of individual X-ray-selected AGNs with an accuracy better than $\sigma_0 \sim 0.05$ and the outlier fraction better than $\sim 10\%$. The accuracy of photo-z for galaxy clusters is nearly an order of magnitude better. In our analysis, we assumed that the photometric redshift error and fraction of catastrophic failures are known. These quantities and their redshift dependence are usually provided by the photometric redshift estimation code, based on the analysis of verification samples of objects whose redshifts are measured in spectroscopic observations. Our approach is similar, for example, to that used in Sereno et al. (2015). In the calculations below, we assumed the photo-z accuracy that is within the reach of the current version of the SRGz system.

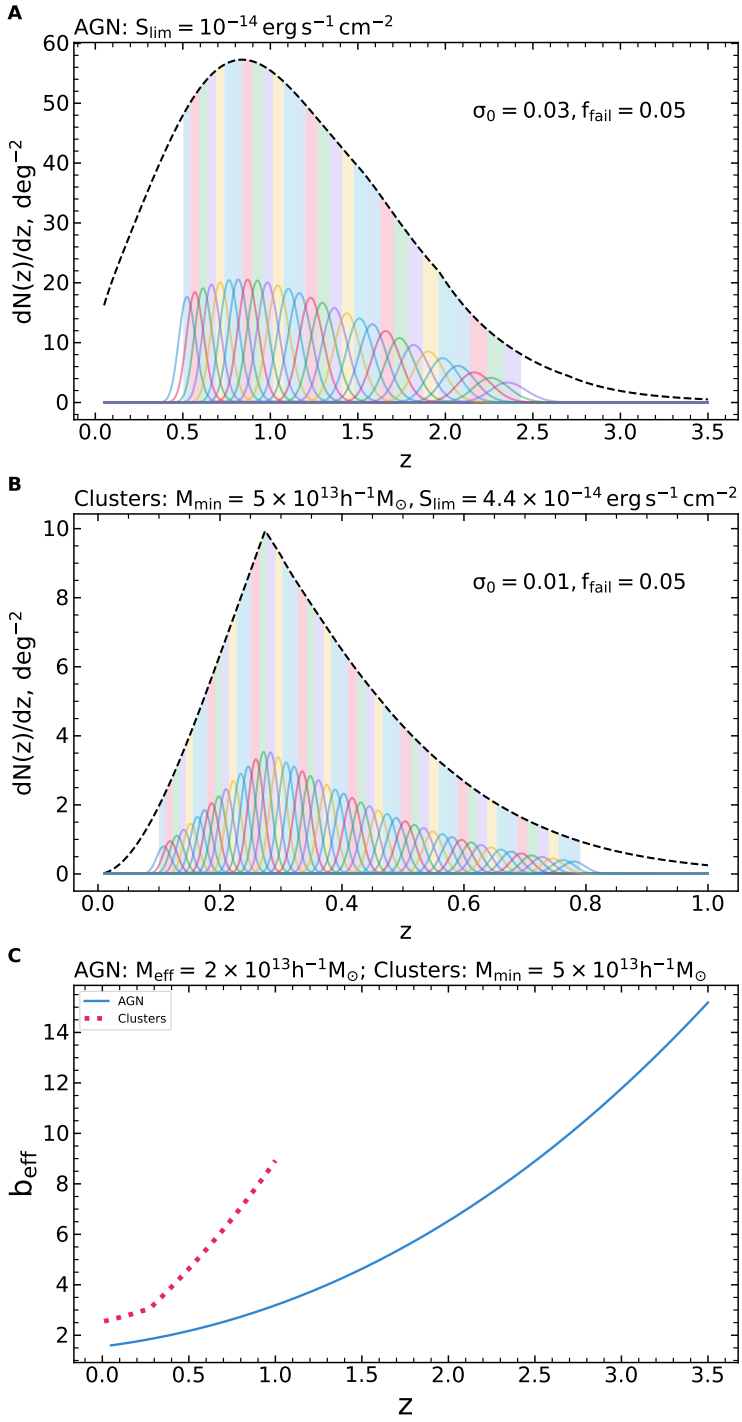

Figure 2.2: Panels A and B: Redshift distributions of AGN and cluster tracers. The black dashed line in each panel shows the total distribution of objects, while solid lines show the distributions of objects in photo-z bins (the corresponding vertical stripes show the boundaries of the bins in the photo-z space). The parameters for the photometric redshift scatter are shown in each panel. Panel C: Effective linear bias factors of tracer populations as a function of z.

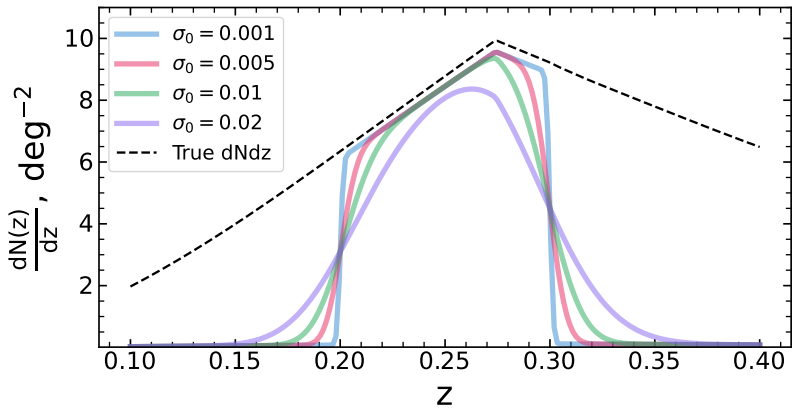

Figure 2.3: Effect of photometric redshift errors on the redshift distribution of clusters of galaxies. The black dashed line shows the true distribution of clusters of galaxies over redshift. Thick solid lines show the observed distribution of clusters from the redshift bin $0.2 < z < 0.3$ over photometric redshift for various values of σ_0. The value of $f_{\rm fail}$ is fixed at 0.05.

2.4 Angular power spectrum and Fisher matrices

In this section, we describe the computation of angular power spectra (sect. 2.4.1) and the calculation of Fisher matrices (sect. 2.4.2).

2.4.1 Angular power spectrum

The angular power spectrum (APS) is a Fourier counterpart of the two-point angular correlation function. The benefit of using angular correlations is that one does not assume fiducial cosmology to analyse data.

The angular power spectrum of sources in i and j-th redshift bins is calculated as follows:

$$\mathbf{C}_\ell^{ij} = \frac{2}{\pi} \int P(k, z=0) W_\ell^i(k) W_\ell^j(k) k^2 \mathrm{d}k$$

where $P(k, z = 0)$ is the matter 3d power spectrum at present time and $W_\ell^i(k)$ is a projection kernel of bin i. Secondly, we use

$$W_\ell^i(k) = \int j_\ell(kr) f^{(i)}(r) g(r) b_{\rm eff}(r) \mathrm{d}r$$

where r is a comoving radial distance, j_ℓ is the spherical Bessel function of order ℓ, $f^{(i)}$ is the normalised redshift distribution of i-th bin, and g and $b_{\rm eff}$ are linear growth and bias factors, respectively.

Calculations of angular power spectra are done in CAMB and include the effects of redshift space distortions. The matter power spectrum is calculated by CAMB in the linear regime, while

bias factors and redshift distributions are found as described in Section 2.3. We applied the Limber approximation (Simon, 2007) at $\ell > 110$ for both tracers. We used logarithmic bins in ℓ. A minimum multipole number, $\ell = 10$, is used in all calculations due to the effects of the sky mask at lower multipoles. To not include non-linear effects in our analysis, we restricted $\ell < 500$ (150) for AGN (cluster) samples (Kolodzig et al., 2013a; Hütsi et al., 2014). For the same reason, we used 0.5 (0.1) as the minimum redshift of a cosmological sample of AGN (clusters), whilst the maximum is 2.5 (0.8) due to the scarcity of objects at higher redshifts.

We used the following analytical formula for the Gaussian covariance matrix of angular power spectra:

$$\mathrm{Cov}_\ell(\mathbf{C}_\ell^{ij}\mathbf{C}_\ell^{mn}) = \frac{1}{(2\ell+1)f_{\mathrm{sky}}}\left(\mathbf{C}_\ell^{im}\mathbf{C}_\ell^{jn} + \mathbf{C}_\ell^{in}\mathbf{C}_\ell^{jm}\right),$$

with f_{sky} being the fraction of the sky observed and $\mathbf{C}^{ij}$ including the shot noise ($1/N$, where N is a surface density in the bin) if $i = j$. We treated partial sky coverage lightly with the factor f_{sky}, whereas in reality the covariance between different modes would be introduced, especially for sky masks of complex shapes. In the case of extragalactic sky $|b| > 15°$ considered here, this effect can be neglected in this calculation.

To accelerate computations, we ignored cross-correlation between the bins that are spaced far apart (more than $3\sigma(z)$). We remind the reader that the width of the redshift bin Δz is adjusted so that $\Delta z = \sigma_0(1+z)$ for given photo-z scatter parameter σ_0 unless stated otherwise.

2.4.2 Fisher matrix

We made use of the angular power spectra to derive errors in the determination of cosmological parameters with the Fisher matrix formalism.

Fisher matrices approximate the posterior distribution of the parameters of interest with multidimensional Gaussian distribution (Tegmark, 1997; Tegmark et al., 1997; Dodelson, 2003). We used the following formula for a Fisher matrix, assuming a Gaussian distribution of data points and constant covariance:

$$F_{i,j} = \frac{\partial \mathbf{C}_\ell^T}{\partial\theta_i}\mathrm{Cov}_\ell^{-1}\frac{\partial \mathbf{C}_\ell}{\partial\theta_j},$$

where $F_{i,j}$ is a Fisher matrix, i, j are the indices of cosmological parameters of interest, $\mathbf{C}_\ell$ is a data vector, and Cov_ℓ is data covariance. Our model includes all five cosmological parameters of flat ΛCDM: dark matter density fraction Ω_c, baryon density fraction Ω_b, reduced Hubble constant h, the slope of the primordial power spectrum n_{s}, and the amplitude parameter σ_8. Derivatives and covariance matrices were calculated in fiducial cosmology. We transformed the Fisher matrices so that instead of dark matter density Ω_{c}, we used matter density $\Omega_{\mathrm{m}} = \Omega_{\mathrm{c}} + \Omega_b$, and we added priors to the matrix if needed (Coe, 2009).

We found derivatives numerically using NUMDIFFTOOLS library[12] with the jacobian of data vector calculated with step 5×10^{-4} and two-point central finite difference.

[12] https://github.com/pbrod/numdifftools

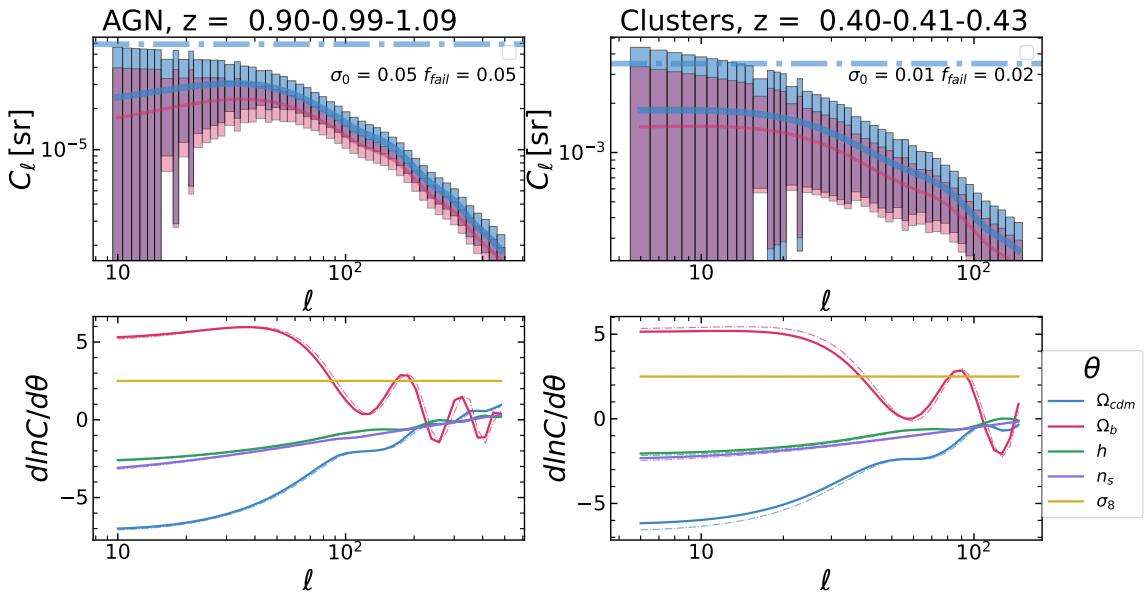

Figure 2.4: Example of angular power spectra of AGNs (left panels) and clusters (right panels). In the top panels, the auto-spectrum of the first redshift bin is shown in blue (bin 0.9<z<0.99 for AGNs and 0.40<z<0.41 for clusters), and the cross-spectra of the first redshift bin with the second bin (0.99<z<1.09 for AGNs and 0.41<z<0.43 for clusters) in red. Horizontal lines show the level of Poisson noise for auto-spectra. In the bottom panels, the derivatives of those power spectra (solid and dashed lines, respectively) are shown with respect to parameters in the plot's legend. Parameters of photometric redshift errors are $\sigma_0 = 0.05$ and 0.01, $f_{\rm fail} = 0.05$ and 0.02 for AGNs and clusters, respectively.

We do not include uncertainties of the redshift distribution $n(z)$, bias $b_{\rm eff}(z)$, or M-L relation for clusters of galaxies in our simulations. We assumed that these quantities would be measured from the eROSITA all-sky survey with sufficient accuracy. In particular, as it was demonstrated in Kolodzig et al. (2013b); Comparat et al. (2019), the AGN XLF and bias $b(z)$ will be accurately measured from the all-sky survey data. The M-L relation for clusters of galaxies also plays an important role in cosmological measurements with clusters (e.g. Pillepich et al. 2012). To this end, eROSITA is planned to measure this relation with high precision in the dedicated pointed phase after the all-sky survey ends.

After the Fisher matrix $F_{i,j}$ is calculated, its inverse can be used as the covariance matrix of the parameters, from which one obtains marginalised errors (Tegmark et al., 1997; Coe, 2009). In Appendix A, we compare the marginalised errors and credibility contours returned by the Fisher analysis and by the Markov chain Monte Carlo (MCMC) algorithm of posterior sampling and demonstrate that they produce consistent results.

In Fig. 2.4, we show the angular power spectrum examples for AGNs and clusters. In addition, we show logarithmic derivatives with respect to all cosmological parameters.

2.5 Forecast results

In the following section, we describe the main results of the chapter: the significance of BAO detection in AGN and cluster distributions (Sect. 2.5.1) and the forecast on the cosmological constraining power of SRG/eROSITA samples of AGN and clusters of galaxies (Sect. 2.5.2).

To investigate the impact of photo-z errors, we used a grid of parameters, σ_0 and $f_{\rm fail}$: $\sigma_0 = 0.005, 0.01, 0.015, 0.02, 0.03, 0.05, 0.07, 0.1, 0.2, 0.3$ and $f_{\rm fail} = 0.01, 0.02, 0.05, 0.1, 0.2$ for clusters, and we did the same for AGNs, except for the AGNs we did not do calculations for: $\sigma_0 = 0.005$ and 0.01. Redshift bin sizes are $\Delta z = \sigma_0(1+z)$ except for the case of $\sigma_0 = 0.005$, where we used redshift bins $\Delta z = 1.3 \times \sigma_0(1+z)$ to reduce the size of the matrices involved. We assumed the sky survey of $f_{\rm sky} = 0.658$ down to fluxes of 10^{-14} erg s^{-1} cm^{-2}(4.4×10^{-14} erg s^{-1} cm^{-2}) and used objects in the redshift range of $0.5 < z < 2.5$ ($0.1 < z < 0.8$) for AGNs (clusters). The total cosmological sample size would be $\approx$ 1.97 million AGNs and $\approx$ 88000 clusters.

2.5.1 Baryon acoustic oscillations

We start from the question of whether BAOs would be detectable in the distribution of AGNs and clusters depending on the quality of photo-z. A similar task was done in Hütsi et al. (2014) for the AGN population.

For BAO detection, we used the following technique: given the smooth model for the 3D matter power spectrum (template without BAO wiggles, NW superscript) we find the χ^2 difference between data vectors $\mathbf{C}_\ell$ for a model with and without BAOs (i.e. confidence in units of σ):

$$S/N = \sqrt{(\mathbf{C}_\ell - \mathbf{C}_\ell^{\rm NW})^T {\rm Cov}_\ell^{-1} (\mathbf{C}_\ell - \mathbf{C}_\ell^{\rm NW})},$$

As for the calculations of BAO significance, we used angular power spectra calculated by the CCL library (in contrast to the CAMB calculations done in the remainder of the chapter) and compared the APS obtained with the matter power spectrum of Eisenstein and Hu, with and without wiggles (Eisenstein, Hu, 1998) in Limber approximation.

The results of the exercise are presented in Fig. 2.5. We show contours of the significance of BAO detection as a function of both σ_0 and $f_{\rm fail}$, along with cross-sections of such a surface with planes of constant σ_0 or $f_{\rm fail}$.

One can immediately see that in our regime for both tracers the photo-z scatter parameter has a greater impact on the performance (BAO detectability) than the catastrophic error fraction. Namely, the decrease of σ_0 from 0.1 to 0.03 leads to the increase in the significance of BAO detection from $\sim 3\sigma$ to $\sim 6\sigma$ (assuming $f_{\rm fail} = 0.01$ for the AGN sample). Our results are in line with the work of (Hütsi et al., 2014); see their Fig. 7), notwithstanding the difference in implementation. For the AGN sample, the BAO significance achieves $\sim 7-8\sigma$ if $\sigma_0 = 0.015$ (1.5%), but for a more realistic $\sigma = 0.03$ (3%) the figure is $\sim 5-6\sigma$ with little dependence on $f_{\rm fail}$. For clusters with $\sigma_0 = 0.005$ (0.5%, which is quite a reasonable accuracy level of photo-z for clusters), the significance is $\sim 4-5\sigma$.

Overall, we conclude that the detection of BAOs with photometric-quality z is plausible for both AGNs and clusters. The comparable statistical significance of BAO detection in both samples is also consistent with our expectation from the preliminary analysis based on effective volumes (Sect. 2.2).

2.5.2 Cosmological parameters

For each configuration of the photo-z quality, we calculated the Fisher matrix F of the cosmological parameters and the information content number called the figure of merit (FoM):

$$\mathrm{FoM} = \log \frac{\pi}{\sqrt{\det(F^{-1})}}.$$

Hence, for every pair $\sigma_0, f_{\mathrm{fail}}$, one obtains a Fisher matrix and the FoM.

Before we proceed with the effects of photo-z quality on the forecast, we show one example for the case $\sigma_0 = 0.03, 0.005$ and $f_{\mathrm{fail}} = 0.1, 0.01$ for AGNs and clusters, respectively (see Fig. 2.6). We added a relatively weak Gaussian prior (0.1) to parameter h for this illustration. The value in parentheses is the standard deviation of the prior distribution and is indicated for other priors in the rest of the chapter.

We show expected error ellipses from the analysis of both samples separately and combined (i.e. adding two Fisher matrices). The figure also shows the table with the expected marginalised error percentages. Both AGNs and cluster samples give comparable errors on all the cosmological parameters. More importantly, the combination of AGN with clusters increases the FoM of the former by 0.6. This is due to the partial alleviation of the parameter degeneracy.

The parameter σ_8 is well constrained because the error on the amplitude of the signal directly yields the constraints on the amplitude of fluctuations σ_8. Parameters Ω_{c} and n_{s} have a level of accuracy better than $\sim 5\%$ because they control the overall shape of the matter power spectrum and the prior added to h, which lifted the degeneracy with n_{s} and Ω_{c}. Ω_b is not well constrained since the significance of baryonic effects on the angular power spectrum is limited.

We made such a forecast for each combination of photo-z precision parameters and condensed the result in Fig. 2.7 using FoM as the proxy for the quality of the forecast. We assumed no priors for this calculation.

As with BAOs, photo-z scatter σ_0 affects the analysis quality dramatically, while f_{fail} has a less profound influence on the result. For instance, a decrease of σ_0 from 0.1 to 0.03 increases the FoM from ~ 8.5 to ~ 10 for AGNs with $f_{\mathrm{fail}} = 0.01$. For clusters FoM ~ 6.5 with $\sigma_0 = 0.05$ and FoM ~ 9 if $\sigma_0 = 0.005$. We conclude that the quality of cosmological analysis pivots on the σ_0 parameter.

Table 2.1 shows the quality of the forecast for several cases of photometric redshift parameters. For a 'conservative' case, we chose the following parameters: $\sigma_0 = 0.01, 0.05$ and $f_{\mathrm{fail}} = 0.02, 0.1$ for clusters and AGNs, respectively. For an 'optimistic' case, we choose $\sigma_0 = 0.005, 0.03$ and $f_{\mathrm{fail}} = 0.01, 0.1$. We show options without prior information, with a wide prior on the reduced Hubble constant h (0.1) and, in particular, the prior knowledge of parameters h (0.0054) and n_{s} (0.0042) derived from the Planck CMB experiment data (CMB+lensing, see table 1 in Planck Collaboration et al. (2020), last column). This demonstrates that the combination of the LSS

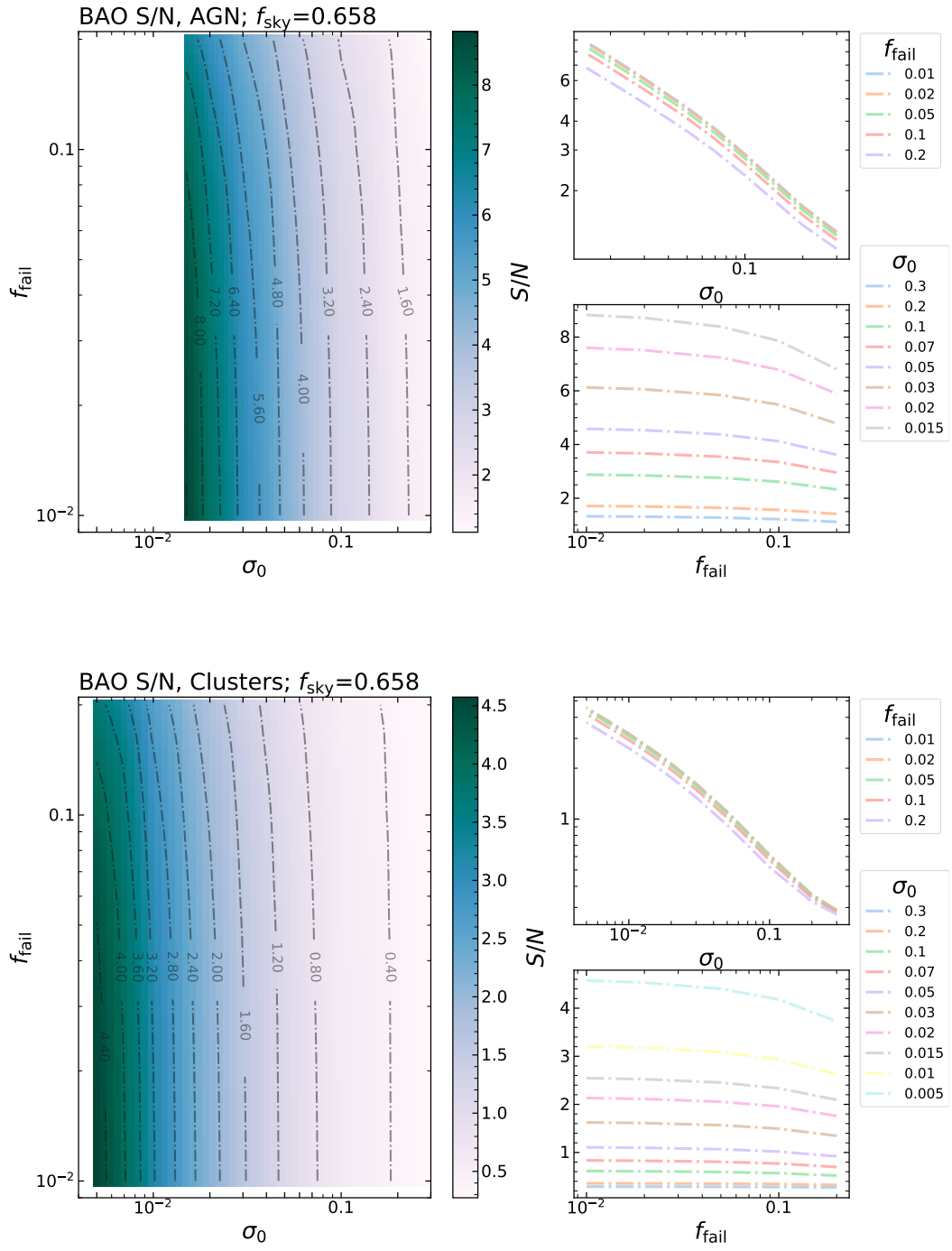

Figure 2.5: Significance of BAO detection (S/N) in the sample of AGNs (top sub-figure) and clusters (bottom). In the left panel, the contours of significance are shown as a function of photo-z accuracy for parameters σ_0 and $f_{\rm fail}$. In the right panels, the cross-sections with constant $f_{\rm fail}$ (top) and σ_0 (bottom) are shown.

Photo-z (σ_0, $f_{\rm fail}$)	Priors	Tracer	$\Omega_{\rm m}$	$\Omega_{\rm b}$	h	$n_{\rm s}$	σ_8	FoM
Clusters(0.01,0.02); AGN(0.05,0.1)	no prior	Clusters	15.9%	81.4%	72.4%	36.0%	1.4%	8.43
		AGN	10.3%	45.9%	40.4%	18.6%	1.2%	9.25
		combination	7.0%	38.0%	33.8%	15.5%	0.8%	9.77
	h prior (0.1)	Clusters	11.7%	22.2%	14.0%	11.5%	1.1%	9.14
		AGN	9.8%	20.4%	13.5%	8.6%	1.0%	9.72
		combination	6.3%	14.5%	9.7%	6.3%	0.7%	10.31
	h, $n_{\rm s}$ Planck prior	Clusters	5.4%	15.8%	0.8%	0.4%	0.9%	11.73
		AGN	5.1%	14.2%	0.8%	0.4%	0.6%	12.13
		combination	3.6%	10.0%	0.5%	0.3%	0.5%	12.74
Clusters(0.005,0.01); AGN(0.03,0.1)	no prior	Clusters	13.1%	61.5%	54.8%	28.3%	1.0%	9.05
		AGN	8.1%	35.3%	30.6%	14.5%	1.0%	9.82
		combination	5.3%	27.6%	24.5%	11.3%	0.6%	10.38
	h prior (0.1)	Clusters	8.9%	19.1%	13.8%	9.9%	0.8%	9.65
		AGN	7.5%	17.7%	12.9%	7.5%	0.8%	10.19
		combination	4.8%	12.5%	9.3%	5.4%	0.5%	10.80
	h, $n_{\rm s}$ Planck prior	Clusters	3.9%	11.3%	0.8%	0.4%	0.6%	12.11
		AGN	3.9%	10.5%	0.8%	0.4%	0.5%	12.47
		combination	2.6%	7.3%	0.5%	0.3%	0.4%	13.10

Table 2.1: SRG/eROSITA forecasts. Fisher marginalised errors for cosmological parameters (in % of the fiducial value) and FoM values for two cases of photometric redshift quality and different priors added to the Fisher information. Results are shown for AGNs and clusters of galaxies separately and combined (see text for details).

probed by eROSITA and the independent data from other experiments may significantly enhance the resulting constraints.

2.6 Discussion

2.6.1 Comparison with dedicated cosmological surveys

BAO

In Sect. 2.5.1, we predict that assuming realistic accuracy of photo-z determination – $\sigma_0 = 0.03$ and 0.005 for AGNs and clusters, respectively, significant baryonic oscillations would be detected in the SRG/eROSITA all-sky survey in the distribution AGNs (redshift range of $0.5 < z < 2.5$, about 2 million sources) and clusters of galaxies (redshift range $0.1 < z < 0.8$, about 90000 sources). Those figures are to be compared with the progress made so far in detecting the baryonic features at other wavelengths and using other LSS tracers.

Baryon acoustic oscillation peaks in galaxy distribution were detected for the first time in SDSS data (Eisenstein et al., 2005; Hütsi, 2006) and have been routinely observed ever since (Ross et al., 2015; Alam et al., 2021).

There are many detections of BAOs with spectroscopic quality information at different redshifts. SDSS galaxies observed in the Baryon Oscillation Spectroscopic Survey (BOSS[13]) provide BAO detection in the redshift range of $0.2 < z < 0.75$ from the sample of 1.2 million galaxies

[13] https://www.sdss.org/surveys/boss/

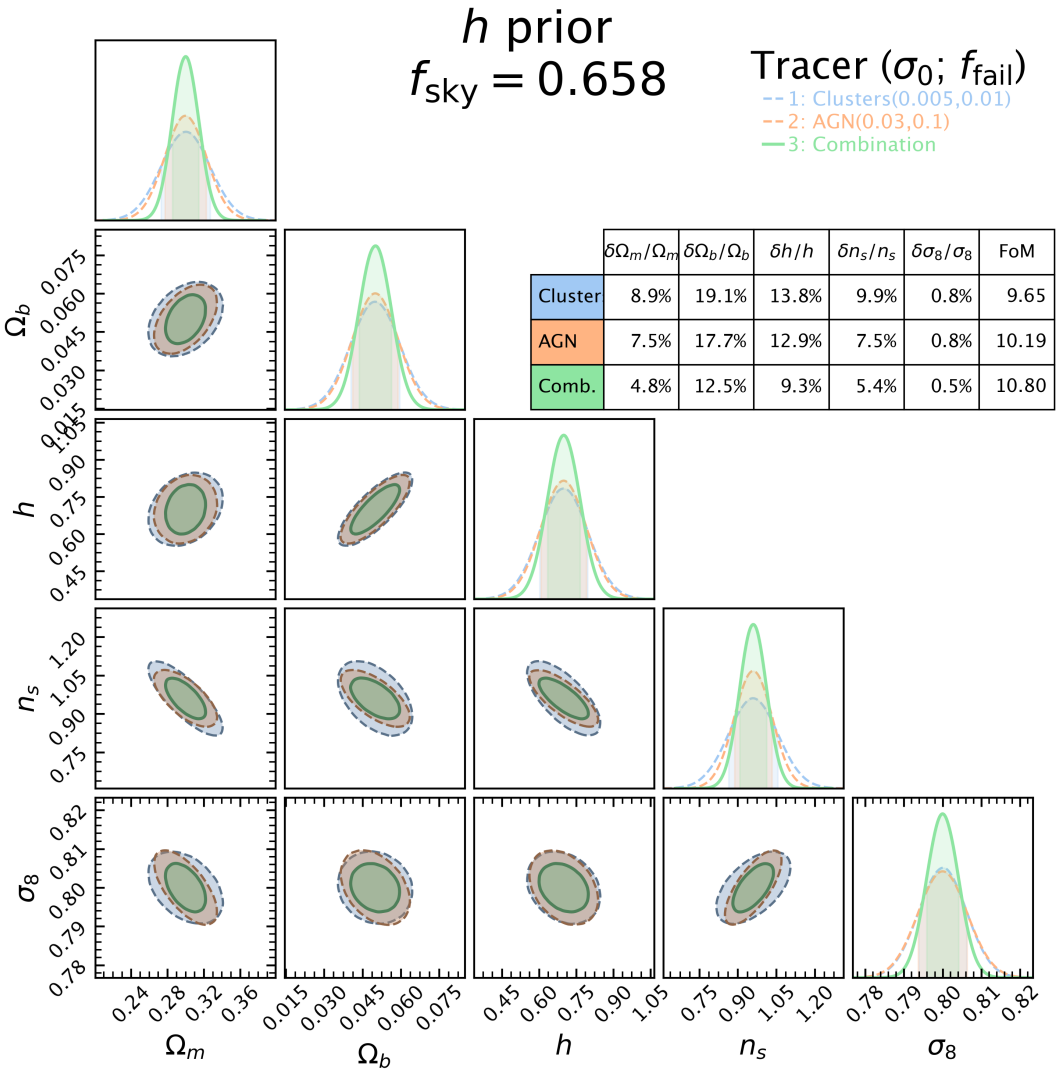

	$\delta\Omega_m/\Omega_m$	$\delta\Omega_b/\Omega_b$	$\delta h/h$	$\delta n_s/n_s$	$\delta\sigma_8/\sigma_8$	FoM
Cluster	8.9%	19.1%	13.8%	9.9%	0.8%	9.65
AGN	7.5%	17.7%	12.9%	7.5%	0.8%	10.19
Comb.	4.8%	12.5%	9.3%	5.4%	0.5%	10.80

Figure 2.6: Expected error ellipses of cosmological parameters from the analysis of AGNs and galaxy clusters in the complete eROSITA all-sky survey. Photometric redshift quality $\sigma_0 = 0.03, 0.005$ and $f_{\rm fail} = 0.1, 0.01$ for AGNs and clusters, respectively. Prior 0.1 on h is added to the Fisher matrix. The corner plot shows the results derived from the Fisher matrix of clusters (blue), AGNs (orange), and combined (green) samples. The table shows the percentage errors on the parameters and the value for the FoM.

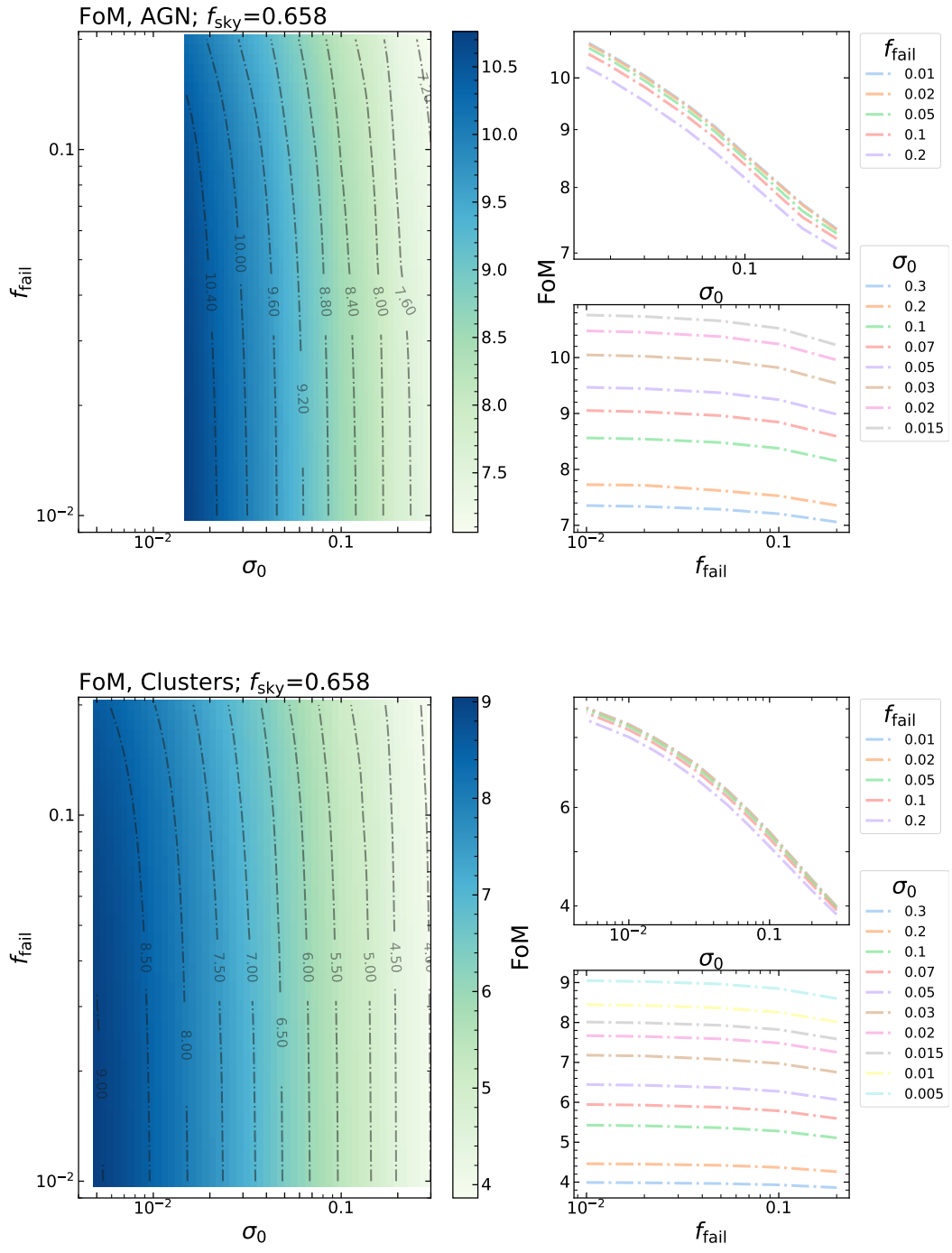

Figure 2.7: Quality of cosmological constraints (FoM) in the sample of AGNs (top sub-figure) and clusters (bottom). In the left panel, the contours of quality are shown as a function of photo-z parameters σ_0 and $f_{\rm fail}$. In the right panels, the cross-sections with constant $f_{\rm fail}$ (top) and σ_0 (bottom) are shown.

(Alam et al., 2017). The extended BOSS programme (eBOSS[14]) pushed the redshift range further, $0.6 < z < 1.1$, with $\sim$ 400k luminous red galaxies and $\sim$ 200k emission line galaxies (Gil-Marín et al., 2020; Raichoor et al., 2021; Bautista et al., 2021; de Mattia et al., 2021). The SDSS observed the BAOs in the distribution of quasar ($0.8 < z < 2.2$ with $\sim$ 350k objects) and Ly$-\alpha$ systems (210k quasars at $z > 2.1$), see Neveux et al. (2020); du Mas des Bourboux et al. (2020); Hou et al. (2021).

Photometric data samples include the BAO detection in SDSS photometric catalogues ($0.2 < z < 0.6$, $\sim$ 600k galaxies) (Padmanabhan et al., 2007; Crocce et al., 2011; Seo et al., 2012). Recent results from the Dark Energy Survey provide evidence for baryonic wiggles in the distribution of $\sim$ 7 million galaxies with photo-z quality $\sigma_0 = 0.03$ in redshift range $0.6 < z < 1.1$ (Abbott et al., 2022b).

For clusters, BAO were tentatively ($\sim 2\sigma$) detected in SDSS photometric cluster catalogue with some $\sim$ 10000 objects at $z < 0.3$ (Estrada et al., 2009; Hütsi, 2010) for the first time. The significance of the detection has increased with the advent of better data, that is, $\sim 3.7\sigma$ detection with $\sim$ 80k SDSS clusters at $z < 0.5$ with spectroscopic redshifts in the work of Hong et al. (2016); see also Moresco et al. (2021).

Considering all of the above, it is clear that the SRG/eROSITA sample of AGNs and clusters would provide sufficiently precise measurements of BAO (and the corresponding sound horizon scales) to expand and complement current experiments, and to provide a cross-check of clustering measurements. It may not be as efficient as SDSS or DES galaxies at a low-redshift regime ($z < 0.6 - 0.7$), but due to the satisfactory density of high-redshift objects, it may compete with BAO findings in eBOSS emission line galaxies and quasar distribution (see also Fig. 9 in Kolodzig et al. 2013a).

For clusters of galaxies, the SRG/eROSITA sample of X-ray-selected clusters would provide clear detection of BAO even with photometric quality redshifts with significance comparable to or exceeding the current statistical power of spectroscopic sample of clusters from SDSS.

Cosmological parameters

In Section 2.5.2, we forecast the precision of determination of cosmological parameters from the angular clustering of AGNs and clusters in the all-sky eROSITA survey. We show that under realistic assumptions about the accuracy of the photo-z, one can achieve $\sim 1 - 20\%$ marginalised errors on the cosmological parameters. The errors can be further reduced by a factor of $\sim 2 - 3$ if using prior information from other experiments.

In Table 2.2 we compare SRG/eROSITA forecasts with other cosmological probes. In addition to the cosmological parameters discussed earlier, to ease comparison with other LSS surveys, we calculate uncertainty on the parameter of clustering amplitude $S_8 = \sigma_8(\Omega_m/0.3)^{0.5}$. For comparison, in the two top lines of the table, we repeat the eROSITA combined AGN and clusters of galaxies forecast from the second half of Table 2.1. We show both forecasts made with and without the Planck priors h (0.0054) and n_s (0.0042) (Planck Collaboration et al., 2020). The accuracy of cosmological parameter determination from the Planck data is shown in the third line

[14] https://www.sdss.org/surveys/eboss/

of the table. Notably, the combined eROSITA sample in combination with Planck priors leads to improvement in the precision of determination for h, n_s, and σ_8 compared to Planck-only data.

Some of the LSS experiments use different LSS tracers (Alam et al., 2021). For example, Loureiro et al. (2019) used spectroscopic SDSS BOSS data of ~ 1.3 million galaxies ($0.15 < z < 0.8$). The results (their Table 4) are listed in the fourth line in Table 2.2. X-ray samples, used without Planck priors, would have tighter errors on the parameter Ω_m and S_8, approximately similar uncertainty on Ω_b and larger error margins for h and n_s.

The ongoing Dark Energy Survey (DES) measures the shapes and positions of millions of galaxies. DES uses cosmic shear and clustering of galaxies as the effective cosmological probe of the matter fluctuation amplitude and density. We show their results (Y3, Table II in Abbott et al. 2022a) for flat ΛCDM from the DES data alone and with a combination of BAO and RSD measurements, supernovae, and CMB data. We see that SRG data alone provide better constraints on the matter density and perform worse for σ_8 (we note in our forecast we that did not fix the other three parameters of the model). If compared with the combination of the DES and other probes, it is seen that the combination of eROSITA data and Planck prior for two parameters would perform comparably, having similar errors on h, and n_s, larger errors on Ω_m, Ω_b, and S_8, and a slightly smaller error on σ_8. We also show the forecast results (Euclid Collaboration et al., 2020) for the *Euclid* probe for the case of photometric galaxy clustering and weak lensing (their Table 9, optimistic settings for GC_{ph}+WL). As expected, Euclid will outperform eROSITA constraints without priors.

The above comparison demonstrates that samples of AGNs and clusters of galaxies from the SRG/eROSITA all-sky survey combined with the currently available photo-z estimates provide a sufficiently powerful cosmological LSS probe. They compete in statistical power with those derived from the dedicated cosmological large-scale structure surveys in the optical band. The statistical power of the eROSITA X-ray-selected samples will increase further if and when the accuracy of redshift determination achieves spectroscopic quality. This appears to be feasible, in principle, for clusters of galaxies that require the acquisition of $\sim 10^5$ optical spectra. For AGNs, where $\sim 10^6$ new optical spectra need to be obtained, this may be a more difficult task for the more distant future.

The calculations for cluster mass function were performed in Pillepich et al. (2012). We used the results for the fixed M-L relation for clusters of galaxies. They took the accuracy of photo-z into account by setting the redshift bin width at $0.05(1 + z)$ and the assumed sky coverage of $f_{sky} = 0.658$, and they also used the Fisher matrix formalism. Comparing the last row of Table 2.2 with the first two rows and with Table 2.1, one can conclude that the cluster mass function is an equally important cosmological tool. When both are used without any priors, the mass-function-based measurement would be ~ 5 times more accurate in measuring Ω_m than the LSS-based one (which is to be expected). However, all other cosmological parameters are determined more accurately, by a factor of $\sim 1.5 - 3.5$ in the LSS-based measurement (Clusters+AGN). Expressed in terms of the FoM, the cluster-mass function is expected to achieve FoM≈ 10.1, which should be compared with FoM$\approx 9.8 - 10.4$ for an LSS-based measurement (Table 2.1). The power of the cluster-mass-function method increases significantly when combined with the Planck priors.

Finally, it should be noted that the cluster-mass function is prone to systematic errors in mass determination, whereas the LSS-based measurement does not include systematic uncertainties

Experiment	$\Delta\Omega_m$	$\Delta\Omega_b$	Δh	Δn_s	$\Delta\sigma_8$	ΔS_8
SRG/eRosita[1]	±0.016	±0.014	±0.172	±0.108	±0.005	±0.019
SRG/eRosita[1] h, n_s Planck prior	±0.008	±0.004	±0.004	±0.003	±0.003	±0.012
Planck (CMB+lensing)[2]	±0.0074	±0.0007	±0.0054	±0.0042	±0.0061	±0.013
SDSS BOSS[3]	$^{+0.034}_{-0.033}$	$^{+0.010}_{-0.009}$	$^{+0.088}_{-0.069}$	$^{+0.064}_{-0.045}$	-	$^{+0.072}_{-0.064}$
DES 3×2pt[4]	$^{+0.032}_{-0.031}$	-	-	-	$^{+0.039}_{-0.049}$	$^{+0.017}_{-0.017}$
DES 3×2pt +BAO+RSD+SNIa+CMB[4]	$^{+0.004}_{-0.005}$	$^{+0.0005}_{-0.0004}$	$^{+0.004}_{-0.003}$	$^{+0.004}_{-0.003}$	$^{+0.008}_{-0.005}$	$^{+0.008}_{-0.008}$
SRG/eRosita cluster mass function[5]	±0.0031	±0.0492	±0.364	±0.143	±0.003	-
Euclid[6]	±0.0038	±0.046	±0.020	±0.0037	±0.0017	-

Table 2.2: Comparison of SRG/eROSITA forecasts with other cosmological probes. Forecast Fisher marginalised errors for cosmological parameters in the flat ΛCDM model. SRG/eROSITA results are for the combined data of AGNs and clusters of galaxies, with and without Planck priors.
References: [1]: this work; [2]: Planck Collaboration et al. (2020); [3]: Loureiro et al. (2019); [4]: Abbott et al. (2022a); [5]: Pillepich et al. (2012); [6]: Euclid Collaboration et al. (2020)

of comparable amplitude (at least for AGNs) and therefore should be more robust. As discussed in Pillepich et al. (2012), the FoM of cosmological analysis degrades dramatically when the uncertainty in the M-L relation is included.

2.6.2 Dependence on the parameters of the all-sky survey.

The SRG satellite performs a full scan of the sky in six months (Sunyaev et al., 2021), and it is planned to conduct eight all-sky surveys in the course of the mission. After the 4.4 already completed surveys, eROSITA achieved the record all-sky sensitivity of ~ 15 times better than that reached in the previous all-sky survey performed by the ROSAT satellite in 1990 (Truemper, 1982; Voges et al., 1999). It is therefore interesting to assess the quality of cosmological measurements that can be achieved before the completion of the full survey.

To this end, we reran our calculations, changing the limiting flux of the survey to the values corresponding to two years of the survey (named eRASS4) and to three years (eRASS6). For point sources, these values are 1.45×10^{-14} (eRASS4) and 1.25×10^{-14} (eRASS6) erg s^{-1} cm^{-2}, see (Kolodzig et al., 2013b). Changing the limiting flux affects the redshift distribution of tracer objects and, more importantly, their number density within redshifts of interest. For eRASS4,6,8 the number of sources is 1 051 773, 1 346 620, and 1 914 915, respectively ($0.5 < z < 2.5$). In Table 2.3, the forecast (with a wide prior in h and photo-z parameters $\sigma_0 = 0.03$ and $f_{\rm fail} = 0.1$) is shown for these limiting fluxes. FoM values between eRASS4 and eRASS8 differ by 0.8, and the errors on the cosmological parameters increase by a factor of $\sim 1.5 - 2$.

We also investigated the impact of the survey area on the forecast. We started by considering the case when only data from half of the extragalactic sky is used in calculations. We neglected the effects of the mode coupling in angular power spectra of half-sky masked data and simply changed the sky area surveyed by a factor of two. In addition, we present a forecast for the survey with the area of 9000 deg^2, which approximately corresponds to the footprint of the SDSS survey where the model of photo z would be better calibrated (at least for the AGN sample).

The scaling of Fisher matrices with $f_{\rm sky}$ is trivial, $F_{i,j} \propto f_{\rm sky}$, hence the marginalised errors scale as the inverse square root of the sky area. We illustrate in Table 2.3 the results for the fiducial eRASS8 AGN setup and show errors on cosmological parameters obtained for different sky areas used in the analysis. It can be seen that for the one half of the extragalactic sky $f_{\rm sky} = \frac{0.658}{2}$ the results differ from the all-extragalactic case by a factor of $\sqrt{2}$, and the FoM differs by 0.75, whereas for the 9k deg^2 case the errors are larger by approximately a factor of two, and the FoM value is smaller by 1.2.

2.6.3 Predictions for small-scale clustering of AGN

This section was not included in the original paper.

The analysis of the whole AGN or Cluster samples would be an arduous task due to the difficulties in obtaining source identification, classification and photometric redshifts estimation uniformly for millions of objects (see sect. 2.3.3). Smaller eROSITA data samples may be useful for the first attempts to perform LSS studies and XLF analysis. During its performance verification (PV) phase, eROSITA surveyed a few extragalactic fields with depth and solid angles

	Ω_m	Ω_b	h	n_s	σ_8	FoM
eRASS4	11.4%	22.4%	13.7%	9.7%	1.1%	9.39
eRASS6	9.6%	20.1%	13.5%	8.6%	1.0%	9.72
eRASS8	7.5%	17.7%	12.9%	7.5%	0.8%	10.19
eRASS8, half extragal.	10.7%	25.1%	18.3%	10.7%	1.1%	9.44
eRASS8, 9000 deg^2	13.1%	30.7%	22.4%	13.1%	1.4%	9.00

Table 2.3: SRG/eROSITA forecasts for different survey parameters. Forecast Fisher marginalised errors (in % of fiducial value) on AGN clustering depending on the survey parameters (survey depth and solid angle). eRASS4, 6 and 8 correspond to two, three, and four years of the all-sky survey. Photo-z accuracy parameters are $\sigma_0 = 0.03$ and $f_{\rm fail} = 0.1$ (see Section 2.6.2 for further details.)

comparable to those of XMM-Newton or Chandra. Namely, the eROSITA final depth equatorial survey (eFEDS, Brunner et al. 2022a) and the survey of the Lockman Hole (LH) region (Gilfanov et al. 2023, submitted.). The former has the area ~ 140 deg^2 and sensitivity (in $0.5-2$ keV) down to fluxes $\sim 7\times10^{-15}$ erg s^{-1} cm^{-2}, whilst for the latter the figures are ~ 20 deg^2 and $\sim 2\times10^{-15}$ erg s^{-1} cm^{-2}. There are $\sim$ 22 thousand AGN in eFEDS (Liu et al., 2021) and $\sim$ 8500 AGN in Lockman Hole (in prep.). The clustering of AGN has been studied in similar surveys with relatively small footprints and high source densities, e.g. XMM-XXL survey (Elyiv et al., 2012; Plionis et al., 2018). We therefore envision that a tangible clustering signal should be detected in the distribution of AGN in eFEDS and LH fields. To substantiate we perform a set of HEALPIX simulations of extragalactic fields (described in appendix B) with coverage and survey depth similar to eFEDS and LH surveys. We modelled the precision of determination of the angular correlation function of AGN in two redshift bins: $0.1 < z < 3.0$ (almost no z-information) and $1.0 < z < 1.5$ (wide photometric bin).

The result of the simulation for both fields and redshift ranges are shown in Fig. 2.8. In the angular scales between 0.03 deg and $\sim$ 1 deg the achieved signal-to-noise ratio (in both bins) of $\sim 5-6\sigma$ in LH and $\sim 7\sigma$ in eFEDS. The actual figures would depend on the survey geometry and telescope sensitivity variations across the field. With our simplistic modelling, we can conclude that the clustering of AGN in eFEDS and LH surveys should be detectable with photometric-quality information about distances to the AGN sources. Complemented with the higher quality photo-z and/or a sensible number of spectroscopic redshift measurements one may study the dependence of clustering signal on the redshift range or object type. The further discussion of the forecast of small-scale clustering measurements and its implications is beyond the scope of this chapter.

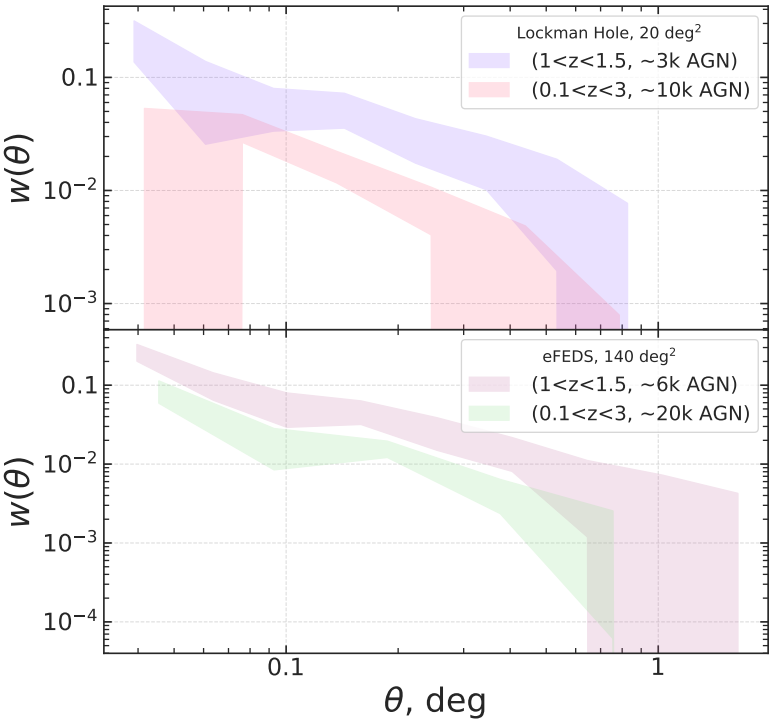

Figure 2.8: The results of the simulations of the measurements of the angular correlation function (ACF) $w(\theta)$ in a survey similar to the eROSITA the survey of Lockman hole (LH, top panel) and eROSITA final depth equatorial survey (eFEDS, bottom panel). On both graphs, the shaded line on the top represents the value and standard error of the ACF measured in wide redshift bin $1.0 < z < 1.5$, and the bottom line represents ACF of very wide bin $0.1 < z < 3.0$. The signal-to-noise ratio of above 5 for all displayed ACF. In the legend, we also specify the number of simulated sources used in the analysis of angular correlations.

2.7 Conclusion

We investigated the potential of X-ray-selected samples of AGNs and clusters of galaxies (to be) detected in the SRG/eROSITA all-sky survey to serve as a cosmological probe. We focused on the ability to detect BAOs and to constrain cosmological parameters under the assumption of the availability of photometric redshifts of realistically achievable quality. Our main results are given in Sect. 2.5.1 and 2.5.2.

Using the model of Hütsi et al. (2014) of photometric redshift scatter, we show that for both BAOs and the cosmological forecast, the redshift scatter parameter σ_0 has more influence on the quality of cosmological constraints than the fraction of catastrophic errors $f_{\rm fail}$ (Fig.2.5, 2.7)

We demonstrate that under reasonable assumptions regarding the quality of photo z ($\sigma_0 = 0.03$ and 0.005 for AGNs and clusters of galaxies, respectively), it is possible to detect BAOs with a significance level of $\sim 5-6\sigma$ and $\sim 4-5\sigma$ in the distribution of AGNs and clusters, respectively. This is comparable with the BAO detections in large-scale structure surveys for galaxies and clusters (Sect. 2.6.1).

A Fisher matrix analysis of angular power spectra under the same assumptions yields the following: (i) a joint analysis of AGNs and cluster data alleviates some of the degeneracies and reduces errors on the cosmological parameters by a factor of $\sim$ 1.5 (Fig. 2.6); (ii) solely X-ray data constrain cosmological parameters with the accuracy in the $\sim 5-25\%$ range without priors and in the $\sim 0.5-10\%$ range with Planck priors (Table 2.1); (iii) X-ray-selected samples of SRG/eROSITA AGNs, and clusters of galaxies used alone or in combination with other data provide a powerful cosmological probe that represents stiff competition for the dedicated cosmological surveys such as SDSS or DES (sect. 2.6.1 and Table 2.2).

Comparing with the results of Pillepich et al. (2012), we conclude that cosmological measurements based on the mass function of clusters of galaxies are expected to provide an ~ 5 times more accurate measurement of $\Omega_{\rm m}$ than the LSS-based one. However, all other cosmological parameters are determined by a factor of $\sim 1.5-3.5$ more accurately in the clustering-based measurement of AGNs and clusters of galaxies. Both methods give comparable values of the FoM (Table 2.1, 2.2).

We investigated the dependence of our forecasts on the survey parameters – its area and depth (sect. 2.6.2, Table 2.3). We demonstrate that even with incomplete sky coverage or limited exposure SRG/eROSITA all-sky survey data still produce competitive results.

Our simulations of small-scale clustering measurements of AGN show that it is possible to detect clustering of the AGN distribution in small-area surveys like eFEDS and Lockman Hole.

In the next chapter, we will explore one of the problems related to the analysis of the AGNs (and other objects) population – given an *X-ray source*, how do we decide which *optical object* is emitting X-ray that we see? This task is essential because the identification of an X-ray source in the optical band is the only way to establish its redshift (via spectral analysis) or estimate photometric redshift (via magnitudes and colour analysis).

CHAPTER 3

Optical identification of X-ray sources in the SRG/eROSITA Survey of Lockman Hole

The contents of this chapter are based on the manuscript originally published in ***Bykov*** *et al. (2022a). My contribution to that paper was the main idea for the project, data collection (from Chandra, XMM, DESI LIS), the process of identification with machine-learned photometric priors, and writing. Other authors contributed to the discussion and writing (M. Gilfanov, M. Belvedersky).*

Abstract

We present a method for the optical identification of sources detected in wide-field X-ray sky surveys. We have constructed and trained a neural network model to characterise the photometric attributes of the populations of optical counterparts of X-ray sources and optical field objects. The photometric information processing result is used for the probabilistic cross-match of X-ray sources with optical DESI Legacy Imaging Surveys sources. The efficiency of the method is illustrated using the SRG/eROSITA Survey of Lockman Hole. To estimate the accuracy of the method, we have produced a validation sample based on the Chandra and XMM-Newton catalogues of X-ray sources. The cross-match precision in our method reaches 94% for the entire X-ray catalogue and 97% for sources with a flux $F_{\mathrm{x},0.5-2} > 10^{-14}$ erg/s/cm^2. We discuss the further development of the optical identification model and the steps needed for its application to the SRG/eROSITA all-sky survey data.

3.1 Introduction

The SRG orbital X-ray observatory SRG (Sunyaev et al., 2021) was launched in July 2019 and began the all-sky survey in December 2019. There are two instruments onboard the observatory: the X-ray telescope SRG/eROSITA (Predehl et al., 2021) sensitive in the 0.3–9.0 keV energy band and the Mikhail Pavlinsky SRG/ART-XC telescope (Pavlinsky et al., 2021) operating in the 6–30 keV energy band. It is expected that based on the results of its four-year sky survey, SRG/eROSITA will discover of the order of three million active galactic nuclei, about one hundred thousand clusters and groups of galaxies, and many X-ray bright stars and galaxies (Prokopenko, Gilfanov, 2009; Merloni et al., 2012; Pillepich et al., 2012; Kolodzig et al., 2013b,a).

For a complete use of the X-ray sky survey results it is necessary to determine the properties of objects not only in X-rays but also in other wavelengths. First of all, we are talking about the determination of the object type and distance. The problem is solved by the identification of

X-ray sources with known objects in the optical (predominantly) and other spectral ranges. This problem is known as cross-match (Sutherland, Saunders, 1992; Budavári, Loredo, 2015; Pineau et al., 2017). In this chapter, we consider the problem of searching for optical counterparts of X-ray sources. We will call the X-ray sources "sources" and the candidates for optical counterparts "objects." A peculiarity of the problem is that the positional error of X-ray sources is larger than the positional error of optical objects approximately by an order of magnitude. In addition, because of the high density of optical objects, there may be several candidates for optical counterparts in in X-ray source positional uncertainty region. In this case, it is often difficult to determine which of the optical candidates is the true counterpart (or that there is no counterpart at all). Additional data, for example, the magnitudes or colours of objects, need to be used to solve this problem. This chapter is devoted to solving this problem using the SRG/eROSITA data as an example.

One of the earliest approaches to the inclusion of additional information was demonstrated in Sutherland, Saunders (1992) using the likelihood ratio method (LR). The method takes into account the positions of sources in the catalogues (including the errors), their angular number density, and the magnitude distribution. Subsequently, this method was developed further in Budavári, Szalay (2008); Naylor et al. (2013); Budavári, Loredo (2015); Pineau et al. (2017); Salvato et al. (2018) with a generalisation to the cross-correlation of more than two catalogues and the construction of a probabilistic (Bayesian) model to take into account the set of measurements of any type.

The history of applying various methods of searching for counterparts to X-ray surveys (predominantly the Chandra and XMM-Newton surveys) is extensive (Brusa et al., 2007; Luo et al., 2010; Naylor et al., 2013; Marchesi et al., 2016; Ananna et al., 2017; Luo et al., 2017; Pineau et al., 2017; Salvato et al., 2018; Chen et al., 2018; Belvedersky et al., 2022b; Salvato et al., 2022). In the broad sense, different methods use similar approaches to the problem. In the first step, the distributions of magnitudes (and, sometimes, also colours or other attributes) are calculated for the optical counterparts and field objects, and in the second step, this information is combined with the information about the relative positions of the sources from different catalogues and their positional errors. The achieved cross-match accuracy depends on the specific method of including the photometric information and the quality of the X-ray and optical catalogues, their depth and positional uncertainties.

The aim of this chapter is to solve the problem of the optical cross-match of X-ray sources for the parameters of the SRG/eROSITA all-sky survey (see also Belvedersky et al., 2022b). In this chapter, we describe the cross-match method and its application to the deep Lockman Hole survey data and estimate the accuracy of the proposed method using a validation sample. Our main goal is to present and validate the method of cross-matching SRG/eROSITA X-ray sources. The characteristics of the X-ray observations, the catalogue of sources, and the results of their optical cross-match and classification are presented in the accompanying papers of the series of publications devoted to the deep SRG/eROSITA Lockman Hole survey (Gilfanov et al. 2023, in press; Belvedersky et al. 2022a).

The chapter is structured as follows. In Section 3.2 we describe the data used. In Section 3.3 we construct the cross-match model and produce the training and validation samples of objects. In Section 3.4 we discuss the results and conclude.

3.2 Data

3.2.1 X-ray data

The Lockman Hole is the area of low interstellar absorption (Lockman et al., 1986) on the sky that was studied by eROSITA within the performance verification phase of SRG telescopes in the fall of 2019. A relatively deep survey of this region was carried out in November 2019. The survey footprint is $5^\circ \times 3.7^\circ$ in size with an area 18.5 square degree (for the flux limit of $\sim 5 \times 10^{-15}$ erg/s/cm^2). The exposure depth was 8 ks per point; the sensitivity in the 0.3–2.3 keV energy band is $\sim 3 \times 10^{-15}$ erg/s/cm^2 . The centre of the region has approximate coordinates RA $= 162^\circ$; Dec $= 58^\circ$. Further details of the observations, the X-ray data, and the catalogue of sources are given in Gilfanov et al. (2023).

The optical cross-match model was developed and tested on the catalogue of medium- and high-brightness eROSITA Lockman Hole X-ray sources (Gilfanov et al. 2023). Point sources with a detection likelihood DL > 10 were included in this catalogue (DL > 10 roughly corresponds to significance $\approx 4\sigma$,). The catalogue includes 6885 X-ray sources.

For the construction and validation of the optical identification model, we used data from the Chandra and XMM-Newton X-ray observatories. We took the Chandra data from the Chandra Source Catalogue 2.0, CSC (Evans et al., 2010), and the XMM-Newton data from the 4XMM DR10 catalogue (Webb et al., 2020). These catalogues were filtered by detection quality flags to minimise the number of spurious X-ray sources[1]. In the SRG/eROSITA Lockman Hole survey footprint, we found 2029 and 1316 Chandra and XMM sources, respectively. The data of these observatories cover about 20% of the footprint area. The positions of the SRG/eROSITA, Chandra, and XMM-Newton sources in the Lockman Hole field are shown in Gilfanov et al. (2023).

3.2.2 Optical data

We chose the photometric DESI Legacy Imaging Survey (DESI LIS, Dey et al., 2019) as a catalogue of optical sources among which we will search for counterparts to SRG/eROSITA sources. DESI LIS has sufficient sensitivity and large area[2]. The catalogue is produced from the data of three telescopes: BASS (g, r), MzLS (z), and DECaLS (g, r, z). These three telescopes have different limiting sensitivities in different filters. DECaLS provides data at Dec $< 32^\circ$. Hence, for the Lockman Hole (Dec $\approx 58^\circ$) and our study of the photometric attributes we used the BASS and MzLS data. In addition, the DESI LIS catalogue provides data on the infrared fluxes in four WISE filters. All magnitudes were dereddened.

The DESI data were used in the entire Lockman Hole field (with a mean density of objects $\sim$ 58000 sources per degree squared) to identify the eROSITA sources. For training the

[1]Filters for CSC: conf_flag, extent_flag, sat_src_flag, pileup_flag, dither_warning_flag are all false, likelihood > 10. 4XMM DR10 filtering: sc_sum_flag=0 or 1, also sc_var_flag, sc_extent and confused equal to false, sc_det_ml> 10.

[2]`https://www.legacysurvey.org`

photometric model, we used all DESI objects around the CSC 2.0 sources in the sky with Dec > 32° (see Subsection 3.3.1).

For all DESI objects, we calculated the signal-to-noise ratio (S/N) for the measurements in all filters (g,r,z,w1,w2,w3,w4). If the measurement in some filters had S/N less than 3, then we assumed that the measurement in this filter was absent.

3.3 Model

In this section, we describe the photometric model for the selection of candidates for optical identification and its application to the eROSITA data. We describe the photometric model in Subsection 3.3.1 or, more specifically, the training sample in Subsection 3.3.1 and the photometric neural network classifier in Subsection 3.3.1. We discuss the validation sample in the Lockman Hole field in Subsection 3.3.2 and the application of the Bayesian approach to the cross-match problem and its results for the eROSITA sources in Subsection 3.3.3.

3.3.1 Photometric model

In this part, we study the photometric attributes of two populations:

1. the DESI LIS objects that are the true counterparts of X-ray sources (in our case, Chandra sources)
2. the DESI LIS objects that are not the counterparts of X-ray sources, the so-called field optical sources.

This division of the optical objects into two classes is motivated by the fact that the X-ray sources are a fairly rare and peculiar type of objects so their optical counterparts have attributes different from those of field objects.

For the selection of optical objects into the first class, we used unambiguous optical counterparts of X-ray sources from the Chandra catalogue (which has high positional accuracy). The procedure for the selection of sources with unambiguous optical counterparts will be described below.

Training sample

We used the CSC 2.0 data in the extragalactic sky ($|b| > 20°$) within the DESI LIS coverage zone, excluding the Lockman Hole area. The produced sample of 157958 Chandra sources was cross-correlated with the DESI catalogue with a search radius of 30 arcsec. Thus, we selected $\sim$ 3 million DESI objects. For each Chandra source, we determined the local density of optical objects $\rho_{\rm desi}$ based on their number in a 10–30 arcsec ring. To control the frequency of random chance associations between CSC and DESI, for each X-ray source we calculated the chance identification radius $r_{\rm false}$ from the formula

$$r_{\rm false} = \sqrt{-\frac{\ln(1 - f_{\rm lim})}{\pi \rho_{\rm desi}}}$$

where $f_{\rm lim}$ is the probability of finding one or more optical objects at a distance $r < r_{\rm false}$ from the X-ray source (Belvedersky et al., 2022b). The quantity $r_{\rm false}$ was calculated by assuming a homogeneous distribution of optical objects with a density $\rho_{\rm desi}$. As a threshold probability, we chose $f_{\rm lim} = 0.03$. For each source from the Chandra catalogue, we also calculate the positional uncertainty r_{98} corresponding to the radius within which the true X-ray source position is located with a 98% probability.

Our further selection of reliable optical counterparts was made as follows: if only one DESI LIS object was found within $r_{\rm false}$ from the X-ray source, with the separation between the two being smaller than r_{98}, then this object was deemed *a reliable optical counterpart of the Chandra source*. We also left only reliable Chandra sources (see Subsection 3.2.1). We found 71993 such Chandra– DESI pairs.

For the selection of *reliable field sources* we found all DESI objects in a 10–30 arcsec ring from the Chandra source. The number of field objects was 2 135 168.

In the next step, in the sample of reliable counterparts, we left only those objects for which the $0.5-2$ keV X-ray flux from the Chandra source was larger than 3×10^{-15} erg/s/cm^2, corresponding to the approximate eROSITA limiting flux in the Lockman Hole field. Note that this is a very important step since the training and validation samples must be equivalent in their properties to the X-ray catalogue for which the optical identification will be made. For example, if we included all Chandra sources in the sample of reliable counterparts, then their photometric attributes would be biased toward numerous faint sources inaccessible to SRG/eROSITA (Salvato et al., 2018).

Finally, we selected only reliable counterparts and field objects located at Dec $> 32^\circ$ (see Subsection 3.2.2). From the field sources obtained in this way, we randomly selected only half, since the total number of objects turned out to be large.

As a result of this selection procedure, the size of the sample of reliable counterparts was 12 452, while the size of the sample of reliable field objects was 244 008.

In Fig. 3.1 we show the distribution of the sources from these two samples in DESI LIS g filter apparent magnitude. It can be seen that, on average, the counterparts of the X-ray sources are brighter than the field sources. In the absence of additional information, this fact can be used to determine more preferable optical counterparts to eROSITA sources (for a discussion, see below).

The limiting S/N in the training sample (see Subsection 3.2.2) was changed from 3 to 4.

Photometric classifier

The problem of classification is to determine whether a source is more likely the counterpart of an X-ray source or more likely a field source based on a set of photometric information. Such problems are efficiently solved with machine learning algorithms.

As attributes for the model, we used the g, r, z, w1, and w2 magnitudes and the appropriate colours. We did not use the magnitudes w3 and w4, since these measurements are lacking for 95 and 90% of the sources in the Lockman Hole, respectively. In addition, for some of the X-ray sources, there are no measurements in the g, r, z, w1, and w2 filters (18, 12, 6, 35, and 60%, respectively). For this reason, we introduced three models: the first model uses only the attributes (magnitudes and colours) pertaining to the g, r, and z filters, the second model uses the g, r, z,

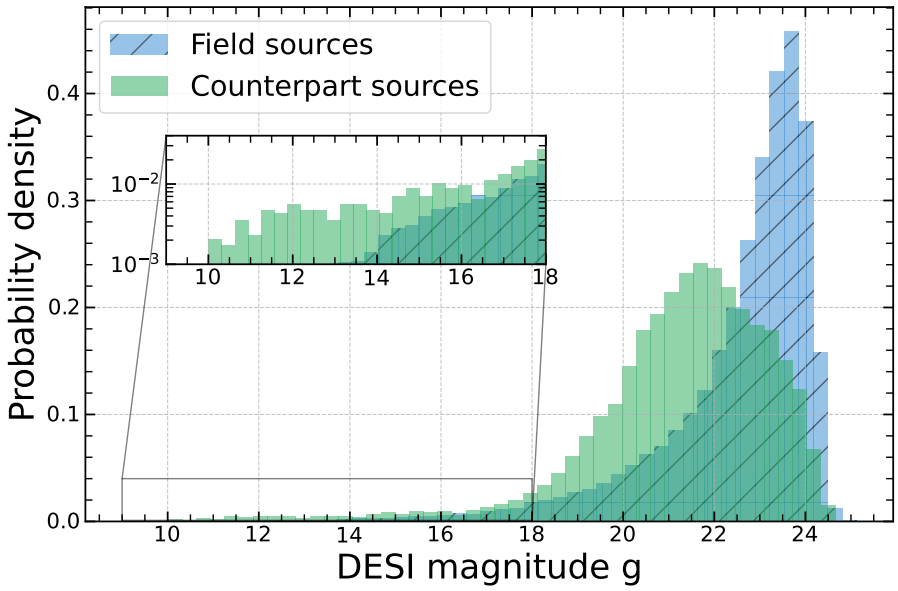

Figure 3.1: The distribution of apparent g magnitude for the DESI objects that fell into the samples of counterparts (green histogram) and field sources (blue histogram with dashes). The inset shows the region of bright objects on a logarithmic scale along the y-axis.

and w1 filters, and the third model uses g, r, z, w1, and w2.

As a classifier we used a neural network, with the corresponding attributes as input and a number between 0 and 1 that we called nnmag as output; 1 and 0 were assigned to counterparts and field objects, respectively. Below we will describe the model based on all attributes: g, r, z, w1, and w2.

We constructed a neural network with tanh activation function in which there were 4 layers of 8 neurons each. After each layer, we added a dropout layer with a probability of 0.1 to prevent over-fitting. At the output of the neural network, we added a layer with one neuron with logistic activation. As a loss function, we used binary cross-entropy. The number of sources of the "counterpart" and "field" classes was 10 480 and 55 636, respectively; we used 30% of the data as a test sample, 20% for cross-validation, and the remainder as a training sample. Keras[3] package was used to train the classifiers.

Figure 3.2 (upper panel) illustrates a histogram of the neural network output (nnmag) on the test sample (the data that were not used for training) for both classes of objects. It can be seen that the objects of class 1 (counterparts) have nnmag closer to 1, while the objects of class 0 (field sources) have nnmag closer to 0. This histogram can be compared with Fig. 3.1, where the separation in g magnitude is not so obvious. The lower panel in Fig. 3.2 also shows two model quality metrics for different nnmag thresholds: recall and precision. At a given nnmag the sources are designated as a counterpart (field) if their nnmag is larger (smaller) than the threshold[4]. As an

[3] https://keras.io

[4] The recall is calculated from the formula $TP/(TP+FN)$, while the precision is calculated as $TP/(TP+FP)$,

Model	Features	Sample size[1]	Network structure	Overall quality[2]
nnmag_grzw1w2	g,r,z, w1, w2 g-r,r-z,g-z z-w1, r-w1, w1-w2	1: 10480 0: 55636	4 layers with 8 neurons Dropout rate: 0.1	0.67
nnmag_grzw1	g,r,z, w1 g-r,r-z,g-z, z-w1	1: 10814 0: 89670	4 layers with 8 neurons Dropout rate: 0.1	0.61
nnmag_grz	g,r,z g-r,r-z,g-z	1: 11092 0: 141845	2 layers with 13 neurons Dropout rate: 0.0	0.38

Table 3.1: Description of the photometric models. For each model, we show the used photometric features, sample sizes, neural network structure and the overall quality of a model. 1: Class 1 and class 0 refer to the counterparts and field sources, respectively. 2: The recall at the point of intersection of the recall and precision curves (see Subsection 3.3.1).

overall model quality metric we used the precision at the point of intersection of the two curves; for the g,r,z,w1,w2 model this number is 0.67. Note that at the point of intersection of the two curves the recall and the precision are equal.

Important parameters for all three models are described in Table 1: the attributes used as input features, sample sizes, neural network structure, and the overall model quality. The drop in the model precision with the loss of data from the infrared is worth noting— the grzw1w2, grzw1, and grz models have an overall precision of 0.67, 0.61, and only 0.38, respectively.

3.3.2 Validation sample in the Lockman Hole

To estimate the optical identification quality, we need to have a sample of eROSITA sources with known optical counterparts. For this we invoke the Chandra and XMM-Newton data in the Lockman Hole. We used an approach similar to that in Belvedersky et al. (2022b).

The selection procedure is as follows:

1. We cross-correlated the complete Chandra (XMM) catalogues[5] with the eROSITA catalogue with a search radius of 30 arcsec and wrote out the unique eROSITA–Chandra (XMM) pairs, leaving only the reliable Chandra/XMM detections from them. 461 (646) such pairs were obtained.

2. For each Chandra (XMM) source we found all DESI LIS objects within 15 arcsec and chose those from them that (i) lay within $1.1 \times r_{98}$ from the X-ray source and are the only optical object within this radius and (ii) lay within $r_{\rm false}$. We found 310 (383) Chandra (XMM)–DESI pair (for the definition of the quantities, see Subsection 3.3.1). As $r_{\rm false}$ we chose a radius of 1.47" from the average DESI sky density in the Lockman Hole.

where TP (true positive) is the number of correctly assigned counterparts, FN (false negative) is the number of counterparts assigned as field ones, and FP (false positive) is the number of field sources assigned as counterparts

[5]Without a quality filter, see Subsection 3.2.1

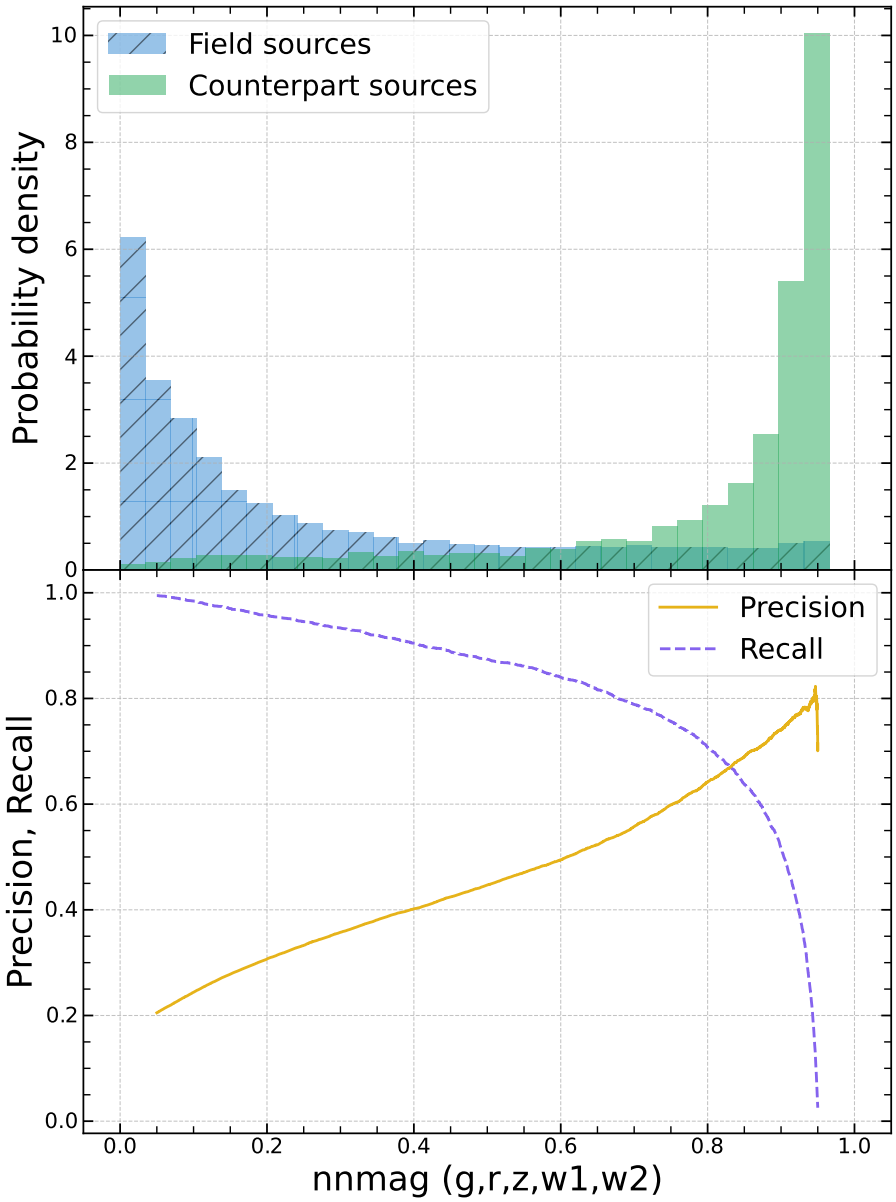

Figure 3.2: Upper panel: the distribution of neural network output (nnmag) for the DESI objects that fell into the test samples of field sources (blue histogram with dashes) and counterparts (green histogram). Lower panel: the recall (dashed line) and precision (solid line) curves for the counterparts as a function of nnmag threshold.

3. Thereafter, from the Chandra (XMM)–DESI pairs we excluded those in which the 0.5– 2 keV fluxes from the eROSITA and Chandra/XMM data differed by more than a factor of 5 (Belvedersky et al., 2022b)— 235 (374) sources remained.

4. The two catalogues (eROSITA–Chandra–DESI and eROSITA–XMM–DESI) were combined, while the duplicates were removed. We obtained a catalogue consisting of 548 eROSITA–Chandra (XMM)–DESI triples. From it, we removed the cases where there was one reliable XMM/Chandra source and two or more Chandra/XMM sources that did not pass the detection quality filter. 529 eROSITA–Chandra (XMM)– DESI triples remained.

This allowed us to determine the correspondence between an eROSITA X-ray source and a DESI optical object. This catalogue will be used below to estimate the optical identification quality.

We also produced a catalogue of eROSITA sources that have no optical counterpart in the DESI LIS catalogue—these are the so-called hostless sources. In the second step, we changed the search criterion by requiring that there was no DESI optical object within $2\times r_{98}$ and $2\times r_{\rm false}$. The remaining steps were not changed. The final number of hostless eROSITA sources in the validation sample was 30.

3.3.3 NWAY and the Identification of X-ray Sources in the Lockman Hole

The information about astrometry and photometric properties was combined with the NWAY code[6] (Salvato et al., 2018), which uses the Bayesian approach to calculate the probabilities of different candidates to be a true counterpart. Two catalogues, eROSITA and DESI, are fed to the input of this code. Initially, the match probability for each possible pair is calculated based only on the astrometric positions, their errors, and the density of sources in both catalogues. Subsequently, the probabilities are refined using additional information (hereafter, photometric priors). In this case, the refinement is based on the ratio of the prior probability densities for the counterparts and field sources. At the output with each eROSITA object, we associate the number $p_{\rm any}$ characterising the presence of an optical counterpart and with each candidate DESI source we associate the number $p_{\rm i}$ characterising its probability to be the counterpart. The closer the number to 1, the more reliable the corresponding assertion.

As a photometric prior we used nnmag obtained by the neural network—photometric classifier (Subsection 3.3.1, see also the example in Fig. 3.2). The photometric model (Table 1) was chosen, depending on which attributes were available for a particular DESI LIS object. At the same time, we made sure that there was no "leak" of information: for each optical object, we used only one photometric prior to the model with the greatest precision available for this object (Table 1). If, however, the photometric information about the object was not sufficient for any of the models in Table 1 (for example, there was no measurement in the z filter), then as a prior we used any available information (magnitudes and colours) calibrated based on the sample from Subsection 3.3.1, for example, as illustrated in Fig. 3.1.

[6] https://github.com/JohannesBuchner/nway

As 1σ[7] positional errors we used the corresponding calibrated positional error from the eROSITA catalogue of X-ray sources (Gilfanov et al. 2023) and a fixed error of 0.1" for the DESI LIS sources.

With NWAY we calculated the parameter $p_{\rm any}$ for each eROSITA source and $p_{\rm i}$ for each optical object within 30 arcsec from the X-ray source. The candidate with the greatest $p_{\rm i}$ was designated as the most probable counterpart. The X-ray sources with $p_{\rm any}$ below the threshold $p_{\rm any,0} = 0.12$ were deemed hostless. The choice of the threshold $p_{\rm any,0}$ is discussed in the next section.

3.4 Results and discussion

In this section, we present the results of the optical identification of eROSITA X-ray sources in the Lockman Hole. We provide the overall statistics on the number of identifications in Subsection 3.4.1, describe the calibration of the positional errors of the X-ray catalogue based on the validation sample in Subsection 3.4.2, and describe the estimation of the precision (purity), recall (completeness) of the catalogue of counterparts in Subsection 3.4.3. In Subsection 3.4.4 we discuss a generalisation of the model to the entire sky and the changes in the procedure needed for this.

3.4.1 Identification results

As a result of applying the cross-match procedure described above, 6346 (92%) and 4360 (63%) of the 6885 eROSITA sources in the Lockman Hole field have $p_{\rm any} > 0.12$ and $p_{\rm any} > 0.8$, respectively. For 5866 and 1019 X-ray sources the nearest and not nearest DESI LIS object, respectively, was assigned a counterpart. For 6458 and 427 X-ray sources, the most probable optical counterpart lies at angular separations sep $< r_{98}$ and sep $> r_{98}$, respectively. For 443 (6%) eROSITA sources we found two or more candidates with similar values of $p_{\rm i}$ (within a factor of 2). For 5919 (86%) eROSITA sources one of the optical objects has $p_{\rm i} > 0.8$.

3.4.2 Positional Errors of eROSITA X-ray Sources

The 529 eROSITA–DESI LIS validation pairs allow us to check the validity of the positional error for the X-ray sources. If the errors were calibrated correctly, then the distribution of $\frac{\rm sep}{\sigma}$ (where sep is the separation between the observed position of the X-ray source and its true position, and σ is the X-ray positional error) is expected to follow the Rayleigh distribution (Watson et al., 2009; Chen et al., 2018; Brunner et al., 2022a; Belvedersky et al., 2022b).

The results are presented in Fig. 3.3, where the distribution of this quantity from the validation catalogue is shown. As the true position of an X-ray source, we used the position of its optical counterpart that is known with an accuracy better than fractions of arcsec, whilst the typical positional accuracy of X-ray sources is $\sim 3 - 20$ arcsec. Figure 3.3 presents the distributions for the complete catalogue in which the detection likelihood DL > 10 and for the sources with

[7]Corresponds to a probability of 39% for a bivariate normal distribution.

DL > 15 (corresponding to a significance level $\approx 5\sigma$). The higher the threshold, the fewer the number of spurious sources. The expected Rayleigh distribution is also shown.

As can be seen from Fig. 3.3, the observed distributions follow well the Rayleigh distribution. For the complete validation sample including the sources up to DL = 10 we can see two sources at large deviations sep $\gtrsim 5\sigma$. A visual inspection of these sources revealed no obvious anomalies in the X-ray or optical data. The appearance of these two sources is the result of a chance superposition of unrelated eROSITA and Chandra sources; some of the eROSITA sources may be false (i.e., the result of statistical fluctuations in the X-ray image), as may be suggested by their comparatively low statistical significance ($< 5\sigma$). Note that at the 4σ significance threshold, we expect $\sim 10-20$ false sources in the Lockman Hole (for a more detailed discussion, see Gilfanov et al. 2023). There is no such a tail in the distribution of high-significance (DL> 15) sources—it agrees well with the Rayleigh distribution.

Thus, the positional errors given in the catalogue of eROSITA sources adequately describe the uncertainties in the positions of the X-ray sources, justifying their use in calculating the Bayesian source cross-match probabilities in the NWAY code.

3.4.3 Optical Identification Precision and Recall

It is necessary to estimate the quality of our identification model, to compare it with the algorithm for a trivial choice of the nearest optical object as a counterpart, and to calibrate the $p_{\rm any}$ threshold. We use the validation sample and compare the counterparts selected by our model and the true counterparts found using the Chandra/XMM data.

To interpret the results of our cross-match model, we apply the following algorithm. Using the preselected threshold $p_{\rm any,0}$, we classify the eROSITA sources with $p_{\rm any} < p_{\rm any,0}$ as hostless. For the sources with $p_{\rm any} > p_{\rm any,0}$ we choose the object with the maximum value of $p_{\rm i}$ as a counterpart. In this case, the following outcomes are possible:

- It was correctly determined that the source has a counterpart and the counterpart was chosen correctly. We denote this number by A.
- It was correctly determined that the source has a counterpart, but the counterpart itself was chosen incorrectly (B). This is the identification error.
- The hostless source was incorrectly classified as a source with a counterpart (C). This is the classification error of the hostless source.
- The source with a counterpart was incorrectly classified as a hostless one (D). This is the classification error of the source with a counterpart.
- It was correctly determined that the source is hostless (E).

Several examples of sources from the validation catalogue and their optical surroundings are given in Fig. 3.4. The positions of X-ray sources (eROSITA, Chandra, XMM) and optical objects are marked. We also specify the identification parameters ($p_{\rm any}$, $p_{\rm i}$) and the true counterpart. We show three examples of correct matches and one example of incorrect matches.

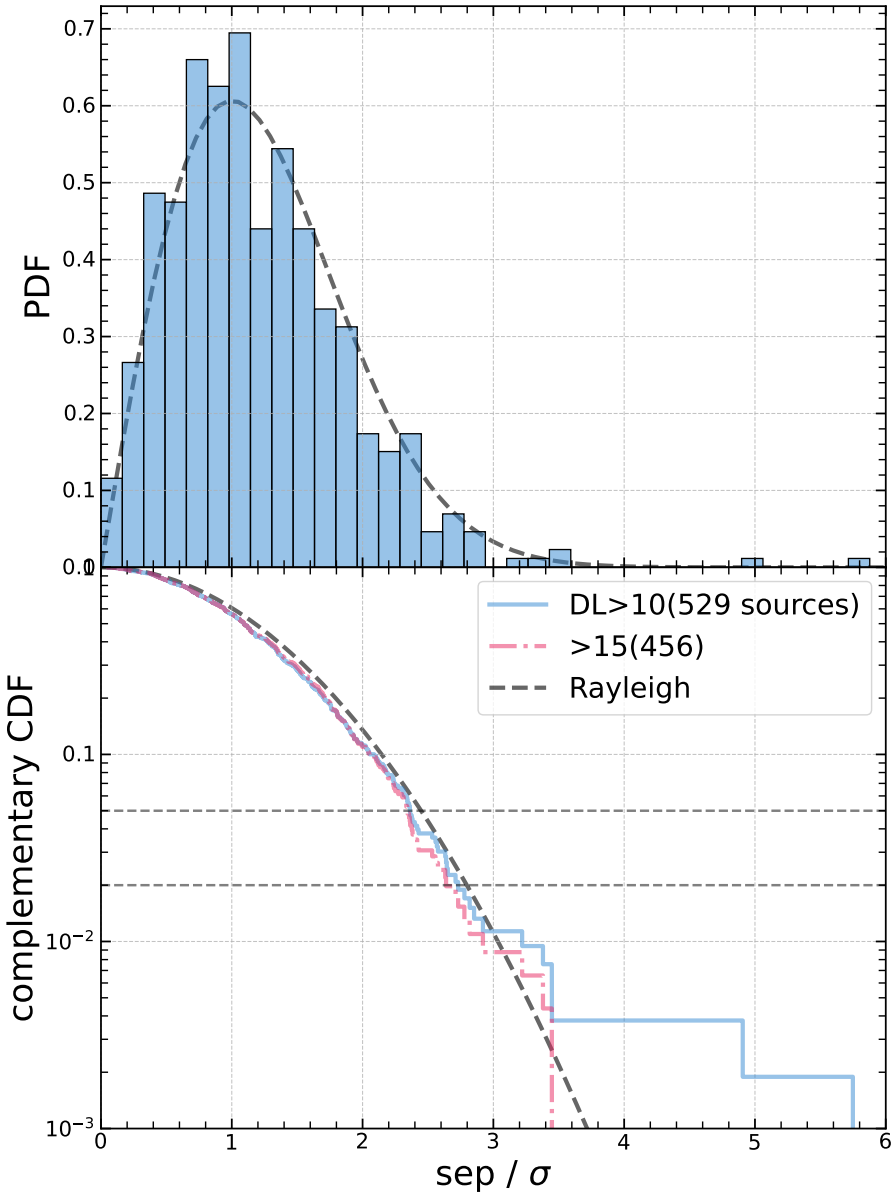

Figure 3.3: Distributions in offsets of the X-ray sources from their optical counterpart position in the validation sample. Upper panel: blue histogram shows the probability distribution of $\frac{\text{sep}}{\sigma}$. Lower panel: cumulative distribution of the same quantity for two selections of X-ray sources by detection likelihood DL (DL> 10— blue solid line, DL> 15— red dash–dotted line). On both panels, the black dashed line indicates the expected Rayleigh distribution. On the lower panel, the horizontal lines indicate 95 and 98% probability levels.

In the validation sample, there are $N_c = 529$ sources with counterparts and $N_h = 30$ hostless sources. We specify the following quality metrics (Belvedersky et al., 2022b):

- overall metric $Q = \frac{A+E}{N_c+N_h}$
- counterpart identification recall (completeness) $C_c = \frac{A}{N_c}$
- hostless identification recall $C_h = \frac{E}{N_h}$
- counterpart identification precision (purity) $P_c = \frac{A}{A+B+C}$
- hostless identification precision $P_h = \frac{E}{D+E}$

Figure 3.5 shows the behaviour of the metrics for three versions of the identification model: the complete model using the photometric and positional information, the positional model (the nearest optical object is chosen as a counterpart), and the complete model applied to bright sources (with a 0.5-2 keV energy range flux $F_X > 10^{-14}$erg/s/cm^2).

The point of intersection of the counterpart selection recall and precision curves is located at $p_{\rm any} = 0.12$, with a precision and recall reaching 94–95%. For the hostless sources intersection occurs at $p_{\rm any} \approx 0.15$ with a precision and recall of 80%. At $p_{\rm any} = 0.12$ the overall precision of our identification model reaches Q = 94%. $p_{\rm any}$ threshold must be chosen, depending on the specific scientific problem for which the optical cross-match is made. For the general X-ray source identification/classification problem threshold $p_{\rm any,0} = 0.12$ is a good choice.

In the case of a naive identification of an X-ray source with the nearest optical object from the DESI LIS catalogue, the counterpart selection curves intersect at $p_{\rm any} \approx 0.24$ with a precision and recall of 86– 87%, and $p_{\rm any}$ is the same with a precision and recall of 70% for the selection of hostless ones. The overall precision of the model is Q = 86%.

When bright sources (0.5–2 keV flux $F_{\rm X} > 10^{-14}$ erg/s/cm^2) are identified, the precision and recall reach $\sim$ 98% for $p_{\rm any,0} \approx 0.12$. Note that with this X-ray flux filter, there are only three hostless sources in the validation sample. Therefore, metrics for hostless sources were not calibrated.

Table 2 presents the results of the quality estimation in the corresponding cases.

There is an increase in the identification quality when adding the photometric information—the overall cross-match quality Q increases by 8%. Interestingly, however, the identification with the closest optical source provides a good accuracy per se. This is due to the relatively good eROSITA positional accuracy and the density of optical objects at the DESI LIS sensitivity level in the Lockman Hole. The density of DESI objects in the Lockman Hole corresponds to roughly one object in a 10" circle which is approximately the positional accuracy of SRG/eROSITA. For this reason, the identification of eROSITA sources with the nearest optical object in many cases leads to the correct result.

3.4.4 Further Steps for the All-Sky Survey

Lockman Hole Field was observed by eROSITA during the performance verification period of SRG observations. The X-ray exposure is distributed fairly uniformly over the survey area. In

Model	Companion is correct (A)	Companion is incorrect (B)	Companion assigned to hostless (C)	Source with companion assigned hostless (D)	Correct hostless (E)	Model quality
NWAY + nnmag $p_{\mathrm{any},0} = 0.12$	503	20	6	6	24	Q = 0.94
closest candidate $p_{\mathrm{any},0} = 0.24$	460	61	9	8	21	Q = 0.86
NWAY + nnmag (bright sources) $p_{\mathrm{any},0} = 0.11$	246	4	0	0	3	Q = 0.98

Table 3.2: The number of correctly or incorrectly determined counterparts of eROSITA sources for three versions of the cross-match model: the complete model, the selection of the nearest optical source, and the complete model applied to bright sources from the validation catalogue. Columns show the number of correct or incorrect identifications (see sect. 3.4.3), and the overall quality.

addition, the survey area is not too large, which allows us to ignore the interstellar absorption and DESI LIS depth variations. When the photometric model is extended to larger sky areas, it will be necessary to take into account these effects. DESI LIS does not cover the entire sky, and Pan-STARRS [8] or similar optical large area surveys can probably be used as a photometric catalogue.

In Subsection 3.3.1 we described a fairly flexible photometric model training procedure. First, in the training data, we placed emphasis on the X-ray survey depth 3×10^{-15} erg/s/cm^2, and the update of the procedure to the all-sky survey regime (where the X-ray depth varies) is fairly easy and consists of partitioning the models into X-ray flux bins. Second, emphasis in this chapter was put on extragalactic fields ($|b| > 20°$), and using a new training sample from the Galactic disk region will allow one to approach the problem of the optical identification of X-ray sources in densely populated fields in the ridge of our Galaxy ($|b| > 20°$).

A validation catalogue from the all-sky data will allow us to calibrate more accurately the positional errors of X-ray sources (see Subsection 3.4.2) through a noticeable increase in the sample size. It will probably also be possible to take into account the subtler effects associated with the dependence of the positional error on the X-ray flux, the detection likelihood (Belvedersky et al., 2022b), the position in the sky, etc. A large validation catalogue will help to estimate more accurately the recall and purity curves of the cross-match algorithm and its dependence on the detection parameters, including the position in the sky.

[8] https://outerspace.stsci.edu/display/PANSTARRS/

3.5 Conclusion

In this chapter, we constructed a model for the optical identification of sources discovered by eROSITA using the eROSITA catalogue of X-ray sources in the Lockman Hole as an example and estimated its precision and recall. As a source of optical information, we used DESI LIS data. The models were trained and validated using Chandra and XMM X-ray data.

We presented a photometric model based on neural networks to separate the photometric attributes of the optical counterparts of X-ray sources and field sources. The model transforms the entire set of available photometric data into one number that we call nnmag and allows these two classes to be separated with a precision/recall of 40–70%, depending on the available data.

We describe the construction of a sample of eROSITA sources with reliably determined optical counterparts. Such a sample allows the precision and recall of any cross-match model to be characterised and, if necessary, is easily constructed in larger sky fields. In the Lockman Hole field, this allowed us to pinpoint the optical counterpart for 559 of the 6885 eROSITA. The validation sample allowed us to check the accuracy of the positional errors for X-ray sources, as described in Subsection 3.4.2.

We applied a combination of the neural network classifier and the NWAY code to search for optical counterparts of SRG/eROSITA sources in the Lockman Hole.

The quality of the constructed optical identification model is discussed in Subsection 4.3. The model reaches a recall (completeness) and precision (purity) of 95% for the selection of counterparts and 80% for the selection of hostless sources, which exceeds the naive identification with the nearest optical source by 8%. For bright X-ray sources ($F_{0.5-2} > 10^{-14}$ erg/s/cm^2) the model reaches 98% purity/completeness. We give examples of identifications and detailed calibration curves. In conclusion, we discussed the necessary steps to apply the model to the SRG/eROSITA all-sky survey.

In the next chapter, we will explore the massive central black hole population in dwarf (low-mass) galaxies. This effort is motivated by the fact that low-mass galaxies are expected to host black holes which are less massive than that of a typical AGN or Quasar. A Census of actively accreting black holes in dwarf galaxies can shed light on the question of how the first black holes were born.

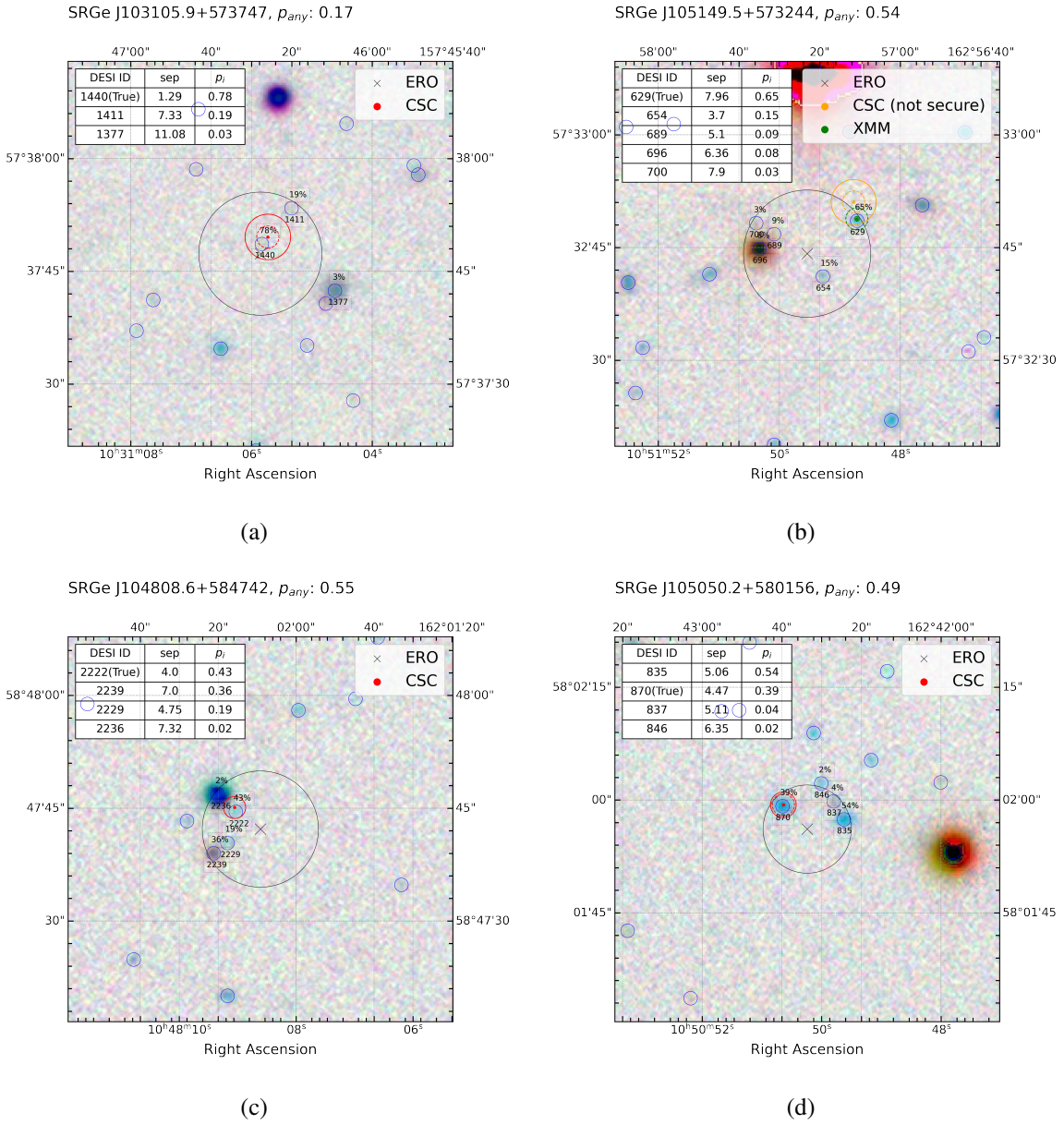

Figure 3.4: Examples of DESI LIS sky images in the vicinity of eROSITA sources. The cross and the black circle mark eROSITA source position and its positional uncertainty r_{98}. The source name and $p_{\rm any}$ are specified in the header. Small blue circles indicate the positions of the DESI LIS objects, the identifier and $p_{\rm i}$ in per cent are given below and above each circle, respectively. Candidates for counterparts with $p_{\rm i} > 0.01$, their identities, and the distance to the eROSITA source in arcsec are specified in tables in the insets. The positions of the Chandra(XMM) sources from the validation catalogue are indicated by red (green) circles. The dotted line indicates radius $r_{\rm false} = 1.47$" around Chandra/XMM. True counterpart is specified by a comment (True). The counterpart identification is correct in cases (a), (b), and (c) and incorrect in case (d), despite relatively large $p_{\rm any} > 0.12$.

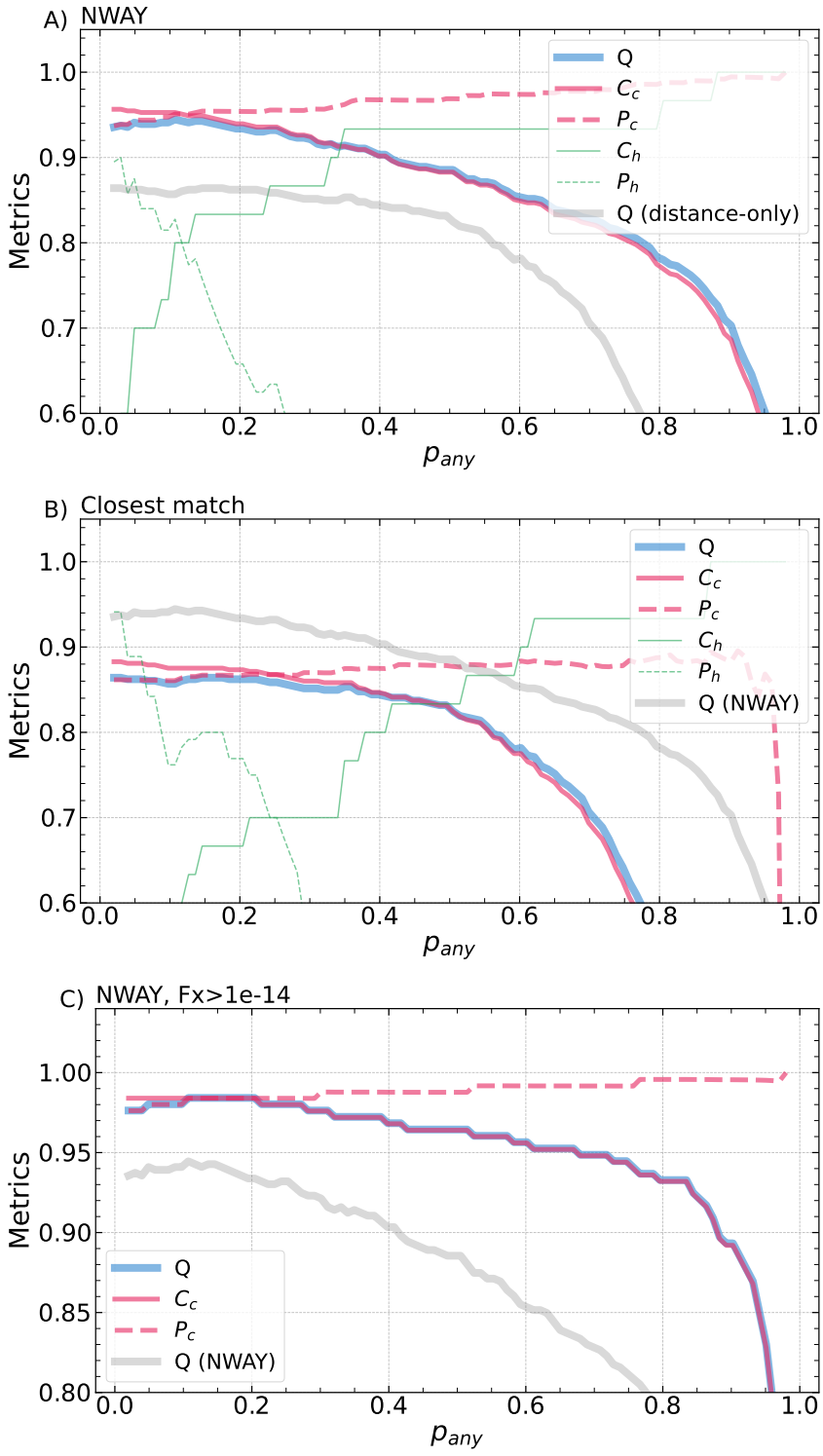

Figure 3.5: Cross-match model quality metrics versus threshold $p_{\mathrm{any},0}$. A solid thick blue line indicates the behaviour of metric Q. Medium-thickness red lines correspond to the selection of counterparts: the solid line is the recall C_c, dashed line is the precision P_c. Thin green lines indicate that for the selection of hostless sources: the solid line is recall P_h, dashed line is precision P_h. (A) complete identification model using the photometric and positional information; the grey line indicates metric Q for the selection of the nearest counterpart. (B) identification with the nearest optical object; the grey line indicates the metric Q of the photometric model. (C) complete cross-match model for bright sources ($F > 10^{-14}$ erg/s/cm^2); grey line indicates metric Q of the photometric model for the complete catalogue.

CHAPTER 4

SRG/eROSITA sample of X-ray active SDSS dwarf galaxies

The contents of this chapter are based on a manuscript published in ***Bykov*** *et al. (2024). My contribution to that paper was the main idea for the project, analysis of data, discussion of the results and writing. Other authors (especially M. Gilfanov) contributed to the discussion of the results and writing.*

Abstract

We present a sample of 99 dwarf galaxies ($M_* < 10^{9.5} M_\odot$) with X-ray activity in their central regions. The sample was obtained from a match of the SRG/eROSITA X-ray catalogue in the Eastern Galactic hemisphere with the MPA-JHU SDSS catalogue. The obtained matches were cleaned rigorously with the help of external optical catalogues to increase the purity of the sample. This work is the largest study of this kind – X-ray activity in ≈ 85 per cent of matched dwarfs was not reported before. The majority of X-ray active dwarfs are identified as star-forming galaxies. However, the X-ray luminosity of 82 objects cannot be explained by the collective emission of X-ray binaries, rendering them strong candidates for dwarf galaxies with an active accreting black hole in their centre. We find that the fraction of AGN among dwarf galaxies drops from $\sim 2 \cdot 10^{-2}$ at $L_X \sim 10^{39}$ erg/s to $\sim (2-4) \cdot 10^{-4}$ at $L_X \sim 10^{41}$ erg/s and increases with the stellar mass of the host galaxy. We serendipitously discovered sources with unexpected properties. We report on a tidal disruption event (TDE) candidate in a dwarf galaxy, a massive black hole in a dwarf galaxy with a soft thermal spectrum, a luminous dwarf galaxy with an obscured X-ray spectrum and a few other peculiar sources. We found three Ultra-luminous X-ray source (ULX) candidates and a sample of X-ray bright galaxy pairs, in four of which both members shine in X-rays.

4.1 Introduction

It is known that virtually every massive galaxy hosts a supermassive black hole (SMBH) in its core (Kormendy, Ho, 2013). The observed correlations between SMBH mass and galaxy bulge properties (such as velocity dispersion, luminosity, and mass) led to the belief that the evolution of SMBHs is intimately related to the evolution of host galaxies (Ferrarese, Merritt, 2000; McConnell, Ma, 2013). In less massive galaxies (stellar mass $M_* < 10^{9.5} M_\odot$, so-called dwarf galaxies) the demography of central black hole population is not so explicit because of the difficulties in the detection of nuclear activity (Greene et al., 2020; Reines, 2022). The role of a central black hole in dwarf galaxies might be the key to the solution to several cosmological and galaxy evolution problems. Examples include AGN feedback, outflows and suppression of

star formation in dwarfs (Calabrò et al., 2017; Barai, de Gouveia Dal Pino, 2019; Manzano-King et al., 2019; Ferré-Mateu et al., 2021), core-cusp problem and the reionisation of the Universe (Silk, 2017). Finally, the importance of dwarfs is emphasised simply by their sheer abundance - it is the most abundant type of galaxy in the Universe.

Additional consideration comes from the fact that the formation and evolution of SMBH is not yet understood, and theories are challenged by the presence of very massive quasars within the first Gyr after the Big Bang (Volonteri, 2010; Woods et al., 2019; Lusso et al., 2022). Possible scenarios for the birth of such SMBHs involve the seed black holes formed as the remnants of Population III stars (Madau, Rees, 2001), heavier seed such as the direct collapse of gas clouds (Loeb, Rasio, 1994), or other models (Mezcua, 2017). The less massive black holes at the centres of dwarfs (which may be of intermediate mass, IMBH) still have imprints of the precursor BHs formation and evolution (Volonteri, 2010). Moreover, dwarf galaxies can help the understanding of the seeding mechanism because they have relatively poor merger and accretion history, thus their BHs are the closest analogues of the seed BHs (Mezcua, 2017; Zubovas, 2019; Greene et al., 2020; Reines, 2022; Burke et al., 2023).

There are several ways to find black holes in dwarf (and massive) galaxies. The standard way is the analysis of optical emission line spectra for the signatures of an active (i.e. accreting) galactic nucleus (Reines et al., 2013; Chilingarian et al., 2018; Molina et al., 2021). Other possibilities are optical variability (Baldassare et al., 2020; Ward et al., 2022), radio (Reines et al., 2011, 2020), mid-infrared (Sartori et al., 2015; Marleau et al., 2017) and X-ray (Birchall et al., 2022; Zou et al., 2023) selections. All methods are prone to selection effects and contamination by non-AGN-related processes mimicking AGN signatures, such as supernovae and their remnants, star formation activity, and tidal disruption events (TDE) among others. The mentioned methods allow selection only of active black holes, whereas finding quiescent (dormant) black holes is much more difficult and addressed with dynamical methods, TDE detection or gravitational waves, see Reines (2022).

X-ray emission is a reliable indicator of accretion onto the central black hole if it is not confused with a TDE, aggregated X-ray binaries emission or a background AGN. X-ray selection allows picking up objects accreting at lower Eddington ratios compared to other search methods (Birchall et al., 2022). The usual approach is to take a stellar-mass selected sample of galaxies and search for X-ray emission. X-ray data from Chandra or XMM-Newton are often employed (Pardo et al., 2016; Lemons et al., 2015; Baldassare et al., 2017; Birchall et al., 2020; Mezcua et al., 2023), and recently – SRG/eROSITA (Latimer et al., 2021). The largest X-ray selected samples come from XMM-SERVS (73 candidates from Zou et al. 2023), 3XMM (61 candidates from Birchall et al. 2020) and Chandra COSMOS (40 candidates from Mezcua et al. 2018). Small-area X-ray surveys (COSMOS, XMM-SERVS) allow finding more distant and faint dwarfs AGN (up to redshift $z \sim 2.5$), whereas wide-angle surveys (3XMM) pick up the local population ($z \lesssim 0.3$) and more rare and luminous objects. Hard X-ray (>10 keV) selection proposes a method less prone to absorption biases and ULX/X-ray binaries contamination, but limited by shallow flux limits (e.g. Mereminskiy et al., 2023). Another example of X-ray data helping to find active dwarfs comes from the work of Chilingarian et al. (2018), who studied the properties of optical spectra to search for the IMBH candidates and only then invoked X-ray data to find 10 bona fide accreting IMBHs. If the contribution from X-ray binaries is subtracted properly and the selection

effects are taken into account, the occupation fraction of central BHs can be studied in detail with its dependencies on luminosity, stellar mass and redshift (Mezcua et al., 2018; Birchall et al., 2020; Zou et al., 2023).

This chapter focuses on the search for active nuclei in dwarf galaxies with the help of X-ray data from the SRG/eROSITA all-sky survey, eRASS. In section 4.2 we describe the data used to construct the sample: catalogue of dwarf galaxies from SDSS (subsect. 4.2.1) and eROSITA data (4.2.2). Section 4.3 explains the process of X-ray active dwarf catalogue construction and cleaning steps (4.3.1), analysis of X-ray data (4.3.2), and the estimation of the contamination from X-ray binaries and hot interstellar gas (4.3.3). We present the catalogue properties and the discussion of individual sources in sect. 4.4 and 4.5 respectively. In sect. 4.6 we conclude.

We use decimal logarithms in the chapter and assume fiducial cosmological parameters, $H_0 = 70$ km s^{-1} Mpc^{-1} ($h = 0.7$), $\Omega_m = 0.3$ for flat ΛCDM cosmology. Uncertainties are quoted on a 90% confidence interval unless stated otherwise. Masses are in units of solar mass $M_\odot$.

4.2 Data

4.2.1 Catalogue of dwarf galaxies

Our primary catalogue of galaxies is MPA-JHU[1] catalogue of galaxy properties for SDSS DR12 spectroscopic measurements (part of SDSS-IV, Alam et al. 2015). The catalogue description is provided in the link mentioned and the techniques used are based on the methods of Kauffmann et al. (2003b); Brinchmann et al. (2004); Tremonti et al. (2004). This catalogue covers approximately 9300 square degrees of the sky and contains 1472581 sources.

In the MPA-JHU catalogue, galaxy properties are obtained by fitting galactic spectra with templates of singular stellar populations from the population synthesis code of Bruzual, Charlot (2003) for different stellar ages and metallicities. The best-fitting model is chosen for a single metallicity and a combination of ten populations of a single age. The continuum is then subtracted from the data and the residual emission lines are fit with Gaussians. The result is a set of galaxy parameters, most notable for us are the stellar mass, star formation rate and BPT classification (Baldwin et al., 1981).

The stellar masses are measured with the assumption of the initial mass function of Kroupa (2001) within the SDSS fibre (3 arcsec diameter). The authors also calculate the total stellar mass from the model photometry, i.e. representative of the whole galaxy. We use the median of the total stellar mass estimate as the galaxy's stellar mass. We deem a galaxy as a dwarf candidate if the total stellar mass $M_* < 10^{9.5} M_\odot \approx 3 \times 10^9 M_\odot$. There are 65461 such sources[2]. Sources were numbered starting from 0 and this value is used as source ID. Only 'reliable' photometry is used (flag RELIABLE=1 from GALSPECINFO table). The typical mass uncertainty for this sample is 0.6 dex. Star formation rate is calculated alike: within the aperture and from the photometry (total star formation rate, following Salim et al. 2007). We use the median of the total rate of star formation.

[1] https://www.sdss4.org/dr12/spectro/galaxy_mpajhu/

[2] 39004 of which are on the eastern galactic hemisphere (eROSITA-RU)

In addition, when possible, we find redshift-independent distance estimation for MPA-JHU galaxies at low redshift ($z < 0.01$) from NASA/IPAC Extragalactic Database (NED[3]). Out of a sample of 178 dwarf candidates active in X-rays (see below), 64 have redshift $z < 0.01$, and for 29 of those we find the redshift-independent distance estimation in NED. For these galaxies, we use the median of all available measurements for a given galaxy. The aim of this exercise is to correct the redshift stated in the MPA-JHU catalogue for the proper motion of galaxies, which becomes important at $z < 5 \times 10^{-3}$ (1500 km/s) (Kauffmann et al., 2003b).

4.2.2 X-ray data

The SRG X-ray observatory (Sunyaev et al., 2021) is an X-ray mission launched in 2019. In December of that year, it started its all-sky survey which was put to a halt in 2022 after ≈ 4.4 all-sky scans (each scan takes 6 months to complete). The eROSITA X-ray telescope (Predehl et al., 2021) operates in the 0.2–9 keV energy range. We use SRG/*eROSITA* catalogue of X-ray sources in the Eastern Galactic hemisphere ($0 < l < 180°$) gathered after over two years of operations (four all-sky scans + 40% of the fifth all-sky scan). The catalogue was obtained by the X-ray catalogue science working group of the Russian consortium of the eROSITA telescope. Calibration of data, production of sky and exposure maps, and source detection were carried out using the eSASS software developed by the German SRG/eROSITA consortium (Brunner et al., 2022b) and the software developed by the Russian SRG/eROSITA consortium. The positional errors and astrometry are calibrated by the catalogue working group via cross-match with a large sample of optical quasars, resulting in the final and corrected X-ray positions and positional errors. For matching with MPA-JHU dwarf galaxies we used eROSITA X-ray source catalogue in the Eastern Galactic hemisphere constructed in the 0.3–2.3 keV energy range. For further analysis, we filtered the eROSITA catalogue to leave point sources having the 98% positional uncertainty (r_{98}) better than 20" and with detection likelihood DL > 15, approximately corresponding to $\approx 5\sigma$ significance for Gaussian distribution. We note that in the course of the astrometric correction and error calibration, the 98% positional errors are capped at the lower limit of 5". Since we are interested in AGN (which would always be a point source), extended objects are not considered in this work.

In the next section, we describe the procedure of matching the eROSITA X-ray catalogue to the sample of dwarf galaxies from MPA-JHU galaxies.

4.3 Catalogue of active dwarf galaxies

4.3.1 Matching eROSITA X-ray source catalogue with dwarf galaxies.

Initial cross-match and random-chance associations

We start with cross-matching the sample of 65461 SDSS dwarfs (39004 of which are in the eastern galactic hemisphere) with the eROSITA catalogue of sources. The area of MPA-JHU

[3] https://ned.ipac.caltech.edu/Library/Distances/

footprint located in the Eastern Galactic hemisphere is 5200 degrees squared. The match radius was chosen to equal 98% positional uncertainty of the eROSITA source position. Sources with negative redshifts in the MPA-JHU catalogue are discarded. We found 198 eROSITA-SDSS pairs, made of 198 unique MPA-JHU galaxies and 178 unique eROSITA sources.

To assess the number of random-chance associations between eROSITA and MPA-JHU dwarfs we performed a simple simulation. eROSITA sources were displaced in a random direction by 0.1 degree and the cross-match with the original dwarf catalogue was performed. All matches found after random shifts are not real and constitute chance alignments. By repeating the simulation 200 times we estimate that the number of random-chance associations between eROSITA and MPA-JHU dwarf is 33.7 ± 5.9 sources ($\sim$ 17 per cent, 1σ error). The amount of random-chance associations is quite significant due to the large number of eROSITA sources. False matches with X-ray active quasars could in principle be identified with the help of IR data to exclude quasars from matching pairs. Systematic implementation of this approach is deferred for future work. However, we note that some fraction of false matches will be removed from the sample in the course of the cleaning procedure described below.

Removing duplicates

Among the 198 MPA-JHU objects, there are duplicated pairs of coordinates (when the MPA-JHU have two objects with different IDs, but equal coordinates). We remove one MPA-JHU object from such pairs leaving the one with greater mass[4]. This removes 11 MPA-JHU sources.

There are still duplicated pairs when one eROSITA source is close to two MPA-JHU entries with different IDs/coordinates. From such pairs, we again remove the one with the smaller mass[5]. During the visual inspection, we confirmed that those 9 cases are, in fact, several close-by SDSS fibre positions measuring the same galaxy (hence the mass difference). This left 178 pairs, with 178 unique X-ray detections and 178 unique SDSS dwarf galaxies.

Thus those 178 galaxies are our candidate dwarfs with active nuclei. We significantly increased the purity of the catalogue as per the steps below, but all 178 objects are listed in the tables accompanying this chapter.

Cleaning the Quasars

The cleaning continues with the cross-match of the sample with the SDSS DR16 list of quasars (Lyke et al., 2020)[6]. We found 11 distant AGN/quasars within r_{98} of the eROSITA position and removed them from the active dwarf candidates. Three additional quasars are excluded with the help of Simbad database (Wenger et al., 2000). X-ray emission is much more likely to originate in a quasar rather than (any) galaxy for the eROSITA flux limit.

[4]maximum mass difference in a pair is 6%

[5]maximum mass difference is a factor of 10-500 in three sources, for 8 sources the figure is of the order of unity.

[6]`https://www.sdss4.org/dr17/algorithms/qso_catalog/`

Cleaning of massive galaxies

In the next step, we cross-correlate the X-ray positions with the whole MPA-JHU catalogue (not only dwarf galaxies) with a 40" radius. We find 19 cases when within r_{98} we can see a massive galaxy ($M_* > 10^{9.5} M_\odot$, independent of the reliability of photometry). We believe that this is an example when a galaxy (usually of a large size) is being measured by several fibres and one of them provides a total stellar mass in the dwarf regime incorrectly (so-called photometric fragmentation, see Sartori et al. 2015; Birchall et al. 2020). All 19 sources are excluded.

Based on the same arguments we cross-match the sample with NASA-Sloan Atlas of galaxies (NSA v1_0_1[7]) catalogue with 40" radius, and remove galaxies which have a massive $M_* > 10^{9.5+0.3} M_\odot$ neighbour within r_{98}. Note that we increase the dwarf mass limit by 0.3 dex (factor of 2) to conservatively accommodate the mass measurement uncertainty. 45 objects are excluded in this manner (all except a few sources are photometric fragmentation examples). Some of them also have a massive neighbour from SDSS (see step above).

Visual inspection

The final step in the cleanup is the visual inspection of each source and its surroundings using DESI LIS[8] cutouts. In this step, we excluded 16 sources. 15 cases were examples of photometric fragmentation or HII regions in large (12 objects) or dwarf (3 objects) galaxies outside of r_{98}, and one case of a stellar object (Simbad). This leaves us with 99 remaining and 79 excluded sources. Examples of AGN dwarf candidates are presented in Fig. 4.1, and examples of excluded sources due to different reasons are presented in Fig. C.1. In the attached tables, a comment is made on the reason for the exclusion of removed sources.

Even though we excluded almost half of eROSITA matches, the catalogue may not be 100% pure and extreme objects (e.g. in mass or luminosity) should be treated with caution. For example, we note that 9 out of 10 galaxies with extremely low stellar mass ($M_* < 10^7 M_\odot$) have counterparts in the NSA catalogue. Out of 9 such galaxies, 7 have a significantly more massive dwarf counterpart in NSA (e.g. for ID 28027 the mass from MPA-JHU is $\sim 10^6$ and from NSA $\sim 6 \times 10^8 M_\odot$), therefore properties of such sources should be used with care. For the overall consistency, we use only MPA-JHU masses in this work.

In what follows we will refer to the sources which passed the cleaning criteria unless stated otherwise.

4.3.2 X-ray variability and spectral analysis

For each source we extract data during each of four (five) eROSITA all-sky surveys (eRASS1...5) and the co-added data of all surveys. 61 sources have data from the fifth sky survey. For each scan (or added data) the source extraction region is a circle with a 60" radius centred on the position of an X-ray source from the added data. The background was estimated from an annulus with inner and outer radii of 120" and 300". From both regions, we exclude a 40" circle around any

[7] https://live-sdss4org-dr13.pantheonsite.io/manga/manga-target-selection/nsa/

[8] Dey et al. 2019, https://www.legacysurvey.org

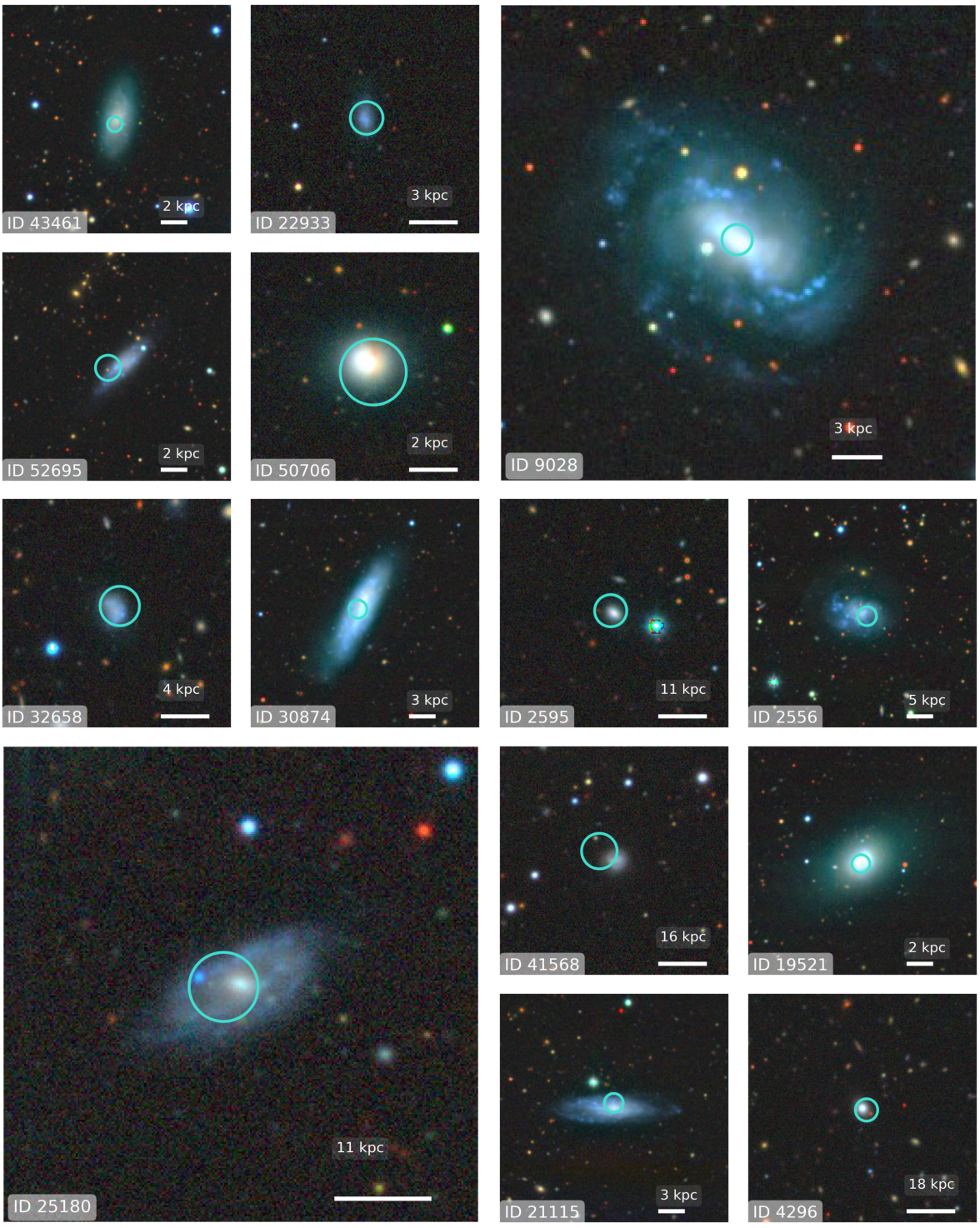

Figure 4.1: Examples of galaxies which passed the selection criteria. Each image is a DESI LIS cutout centred on the dwarf's position. eROSITA X-ray source position and positional uncertainty (r_{98}) shown as cyan circle. Each galaxy has an ID on the bottom left and the scale bar on the bottom right (20" in length).

source detected nearby (with the detection likelihood DL > 10). The spectra were rebinned to have at least three source counts per channel. The fitting is done in XSPEC (Arnaud, 1996) with Cash statistics (Cash, 1979) in the 0.3–8 keV energy range. Spectral models are not red-shifted due to the relatively small distances involved.

Spectral analysis and X-ray flux calculation

In order to characterise the range of spectral properties and to compute X-ray flux, we fit the X-ray spectra of all candidates with a simple power law model absorbed with the neutral hydrogen in our Galaxy. The hydrogen column density $N_{\rm H}$ is fixed for a given source on the value from the NH4PI map at the source's position (HI4PI Collaboration et al., 2016). Sources in our sample have a fairly low number of counts (the median of net source counts is ~ 20) and correspondingly large uncertainties in their spectral parameters. To avoid additional errors due to uncertainties in spectral parameters, for the flux calculation we used several models of fixed spectral shape chosen depending on the power law fit results, as described below.

86 out of 99 sources have photon indices consistent (within 90% confidence interval) with the canonical AGN values in the range $1.5 \lesssim \Gamma \lesssim 2.5$ (Ge et al., 2022; Liu et al., 2022a). For those sources, we used a fiducial spectral model of a power law with fixed photon index $\Gamma = 1.9$ for flux calculation. Three sources[9] are statistically significantly softer than this range, we used a black body model BBODYRAD with frozen best-fit temperature and with fixed Galactic absorption for them[10]. Spectra of ten sources are harder than the typical AGN spectrum with the 90% confidence interval for the photon index $\Gamma \lesssim 1.5$. Spectra of 8 of them[11] can be adequately described by the model of a mildly absorbed AGN with $\Gamma = 1.9$ and $N_{\rm H} = 5 \times 10^{21}$ cm^{-2} and we used this model for their flux calculation. Spectra of two remaining sources[12] are much harder and could not be fit with the mildly-absorbed $\Gamma = 1.9$ power law. For the flux calculation of these sources we used a power law with $\Gamma = 1.0$ and Galactic absorption. Examples of representative spectral shapes are shown in Fig. 4.2 for three relatively bright sources.

With the chosen fiducial models, the source's flux and luminosity were calculated in the 0.3–2, 0.5–2, and 2–8 keV energy ranges[13].

Variability

We analysed the light curve of each source by calculating flux in the 0.3–8 keV energy range for each scan. Flux (or its upper limit) was calculated using spectral models described above with the shape parameters fixed (e.g. Γ or black body temperature). 4 sources have only upper limits in all scans. Dwarfs were ranged by the ratio of the maximum measured flux to the minimal

[9] ID 10487, 33862 and 4296

[10] In X-ray spectra of ID 10487 and 4296 may have an additional power-law component as described in sect. 4.5.2 and 4.5.1 respectively.

[11] ID 52047, 51004, 50909, 45689, 27238, 5545, 20944 and 11124

[12] ID 15677 and 49241

[13] For ID 15677 and 25312 luminosity errors are quoted on 68% uncertainty level, since 90% errors formally give only upper limits.

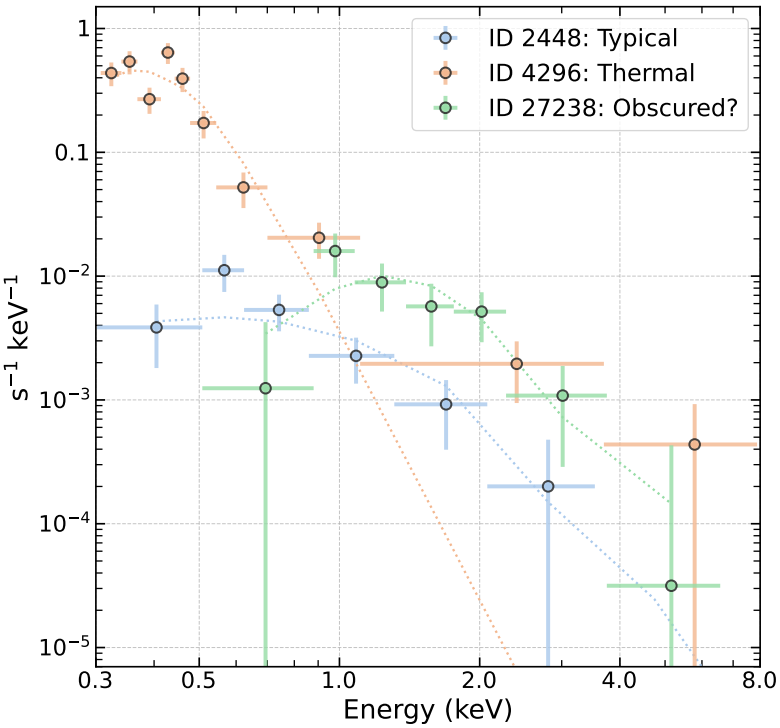

Figure 4.2: Representative X-ray spectra of dwarf galaxies as seen by eROSITA. Three sources are shown - an example of a 'typical' object (modelled with a power law, coloured blue), a thermal spectral shape (modelled with a black body model, orange), and a seemingly absorbed spectrum (modelled with a power law with additional absorption, green). Spectra were rebinned for plotting purposes. The model used to calculate fluxes is shown with dotted lines.

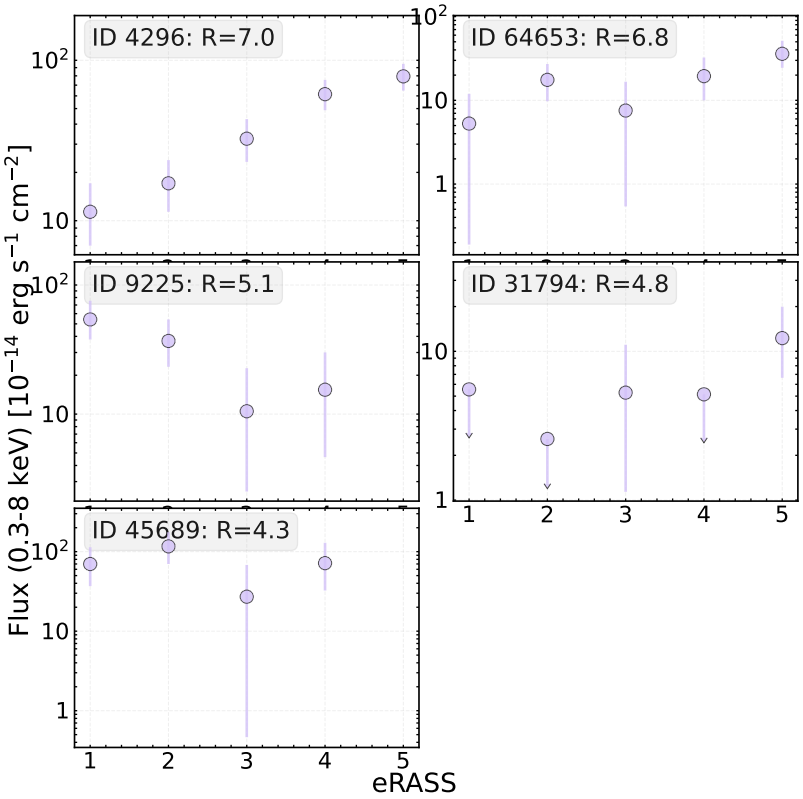

Figure 4.3: X-ray light curves of five dwarf galaxies with highest values of R. Each point shows the average flux registered in one all-sky survey.

flux/upper limit ignoring error bars. We call this ratio R and use it as an approximate variability indicator.

Out of 99 dwarf candidates, only 3 have $R > 5$, i.e. suspected significantly varying sources. Examples of light curves are shown in Fig. 4.3, where the top 5 variable sources are shown.

For more thorough techniques to search for variability suited for eROSITA (including upper limits and proper treatment of R uncertainties) see, e.g. Buchner et al. (2022); Medvedev et al. (2022). Using those, however, is deferred for future work.

4.3.3 Contribution of X-ray binaries and hot gas

X-ray emission in galaxies can come from a multitude of sources, but the primary contaminant for our study would be the X-ray emission from X-ray binaries and hot gas in the interstellar medium (ISM) (Mineo et al., 2012b; Gilfanov et al., 2022). The binary population consists of two types of sources, Low- and High-mass X-ray binaries (LMXB and HMXB), in which a black hole or a neutron star is paired with a normal star. LMXBs trace the old stellar population, whilst HMXB stalk young massive stars (Grimm et al., 2003; Lehmer et al., 2010; Mineo et al., 2012a,b;

Gilfanov et al., 2022).

The aggregated emission of both binaries populations and hot gas is tightly correlated with the main galaxy properties – stellar mass and star formation rate. Namely, the number and total luminosity of LMXB systems depend on the stellar mass, whereas that of HMXB depends on the star formation rate (SFR). The luminosity of hot gas is also proportional to the SFR. To predict the contributions of binaries populations for our dwarf candidates we use scaling relations from Lehmer et al. (2010) and Gilfanov et al. (2022)[14]. For hot gas, we use the relation from Mineo et al. (2012b)[15].

Out of 99 active dwarf candidates, 82 have the estimated XRB contribution ($L_{\rm X,XRB}$) far below the observed luminosity ($L_{\rm X,obs}$) in the 0.5–8 keV band, $\frac{L_{\rm X,obs}}{L_{\rm X,XRB}} > 3$. In all of those 82 sources the contribution of hot gas is also negligible compared to the observed luminosity in the 0.5–2 keV energy band. We conclude that the majority of our X-ray active dwarf galaxies are indeed powered by accretion onto a massive black hole. It is interesting to note that dwarf galaxies with $\frac{L_{\rm X,obs}}{L_{\rm X,XRB}} < 3$ do not show prominent X-ray variability, with the largest $R = 2.8$ for ID 39612.

4.4 Results & Discussion

4.4.1 The catalogue of X-ray active dwarf galaxies and candidates

In appendix C.1 we describe the catalogue of 99 X-ray active dwarf galaxies detected by eROSITA, and present a subset of its columns in table C.1 for dwarfs with $\frac{L_{\rm X,obs}}{L_{\rm X,XRB}} > 3$. The list of 76 eROSITA – MPA-JHU matches which were not included in the final catalogue is presented in appendix C.2 along with the reason for rejection for each case. DESI LIS images are available for all objects from the files attached to the chapter.

Fig. 4.4 shows the redshift – X-ray luminosity plane, with markers encoding the BPT classification of an object (see below) and the XRB contribution. The minimum luminosity is $\sim 10^{39}$ erg s^{-1}, the maximum is $\sim 10^{44}$ erg s^{-1}, median is 1.5×10^{41} erg s^{-1}. All sources except a few are on redshift $z < 0.1$, with the median of $z = 0.01$. The correlation between redshift and luminosity is expected for a flux-limited sample of eROSITA, but AGNs (according to the BPT classification) tend to be more luminous than SF galaxies.

4.4.2 Objects previously identified as AGN candidates

Before turning to the discussion of the results, we cross-correlated (5" match radius) our dwarf sample with some readily available active dwarf candidates catalogues mentioned in the introduction. First, the sample of 61 X-ray-selected active dwarfs from 3XMM-DR7 (Birchall et al., 2020) to find only 5 matches (IDs 11124, 20701, 34500, 49241, 53431). The study of Birchall et al., to our knowledge, used the largest publicly available X-ray survey with the area of $\sim$ 1000

[14] namely, we use formula (5) from Gilfanov et al. 2022 with luminosities in the 0.5–8 keV energy range and stellar mass/SFR from the MPA-JHU catalogue. $L_{\rm X,XRB} = \beta \times {\rm SFR} + \alpha \times M_*$, $\log \alpha = 29.25$, $\log \beta = 39.71$ (Lehmer et al., 2010)

[15] $L_{\rm gas} = 8.3 \times 10^{38} \times$SFR, with luminosities in the 0.5–2 keV range.

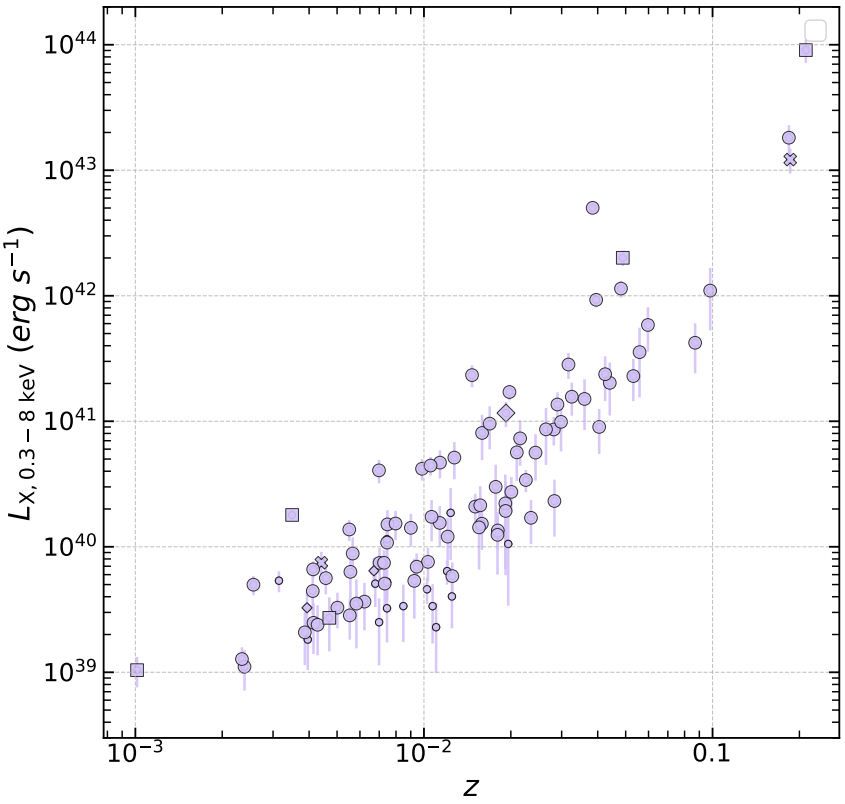

Figure 4.4: Redshift v. X-ray Luminosity plane for 99 dwarf galaxies detected by eROSITA. Larger-sized markers designate objects with $\frac{L_{\mathrm{X,obs}}}{L_{\mathrm{X,XRB}}} > 3$. Marker encodes dwarf's BPT classification from MPA-JHU (circle – star-forming, rhombus – composite, square – AGN, unclassified – X).

deg^2 – the closest one gets to eROSITA's power. We found four dwarf with AGN (ID 9225, 20701, 28027 and 49241) from 19 candidates of Lemons et al. (2015). Four optically-selected active dwarfs from Reines et al. (2013) may be found in our catalogue (ID 53431, 10487, 44628, 49241). Optical + mid-IR selection by Sartori et al. (2015) matched with the following 6 sources - ID 44628, 25337, 10487, 30754, 9028, 34500, 4296. Infrared selection of Marleau et al. (2017) coincided with our ID 10487, 44628, 20701, 20867, 11124, 49241. Finally, we searched for X-ray emission from 305 IMBH candidates of Chilingarian et al. 2018 to find three matches (ID 10487, 49241, 53431). From Greene, Ho (2007) we re-discovered only ID 10487.

Overall, 14 unique eROSITA-detected dwarfs were reported as (candidate) AGNs in low-mass galaxies before. Leaving our sample with $\sim$ 85 per cent new candidates discovered for the first time.

ID 6328, 19521, 20867, 33862 and 50706 are found in a sample of dwarf galaxies targeted for radio observation in Reines et al. (2020). They used high-resolution radio observations to establish that a large number of massive black holes in dwarfs are off-centred. Only ID 19521 and 20867 have compact radio sources near the galactic centre (offsets 0.3" and 0.6" whereas positional uncertainty is < 0.1", indicating offset from the centre). However both galaxies have radio properties consistent with star formation processes (see fig. 11 in Reines et al., our galaxies are their ID 49 and 62 respectively).

4.4.3 Sample properties

Stellar mass, SFR and the BPT-diagram

We start describing the catalogue of 99 selected dwarfs with the description of host properties. In the figures, data from MPA-JHU is shown with 1σ uncertainties. In Figure 4.5 we show the distribution of objects in M_*-SFR plane. For eROSITA dwarfs we show their BPT classification as different markers (see below). $\sim$ 80 per cent of the sample have stellar mass $M_* > 10^8 M_\odot$. The lowest mass is $10^6 M_\odot$. Star formation rate spans from 10^{-4} to 10 $M_\odot$ yr^{-1}. Medians are $7 \times 10^8 M_\odot$ and 0.15 $M_\odot$ yr^{-1} respectively. A large sample of dwarfs from MPA-JHU is also shown in the figure. KS-test for the distribution of masses show that the masses of eROSITA-selected objects and dwarf galaxies[16] are not drawn from the same distribution (p-value $\sim 10^{-4}$) - eROSITA objects have a slightly heavier low-mass tail. The same test for SFR values shows the p-value of 0.02, marginal consistency with the same distribution.

In Fig. 4.6 we show the BPT-diagram (Baldwin et al., 1981). It shows the ratio of two pairs of optical emission lines - $\frac{\mathrm{O_{III,5007}}}{\mathrm{H}_\beta}$ and $\frac{\mathrm{N_{II,6583}}}{\mathrm{H}_\alpha}$. The diagram is a diagnostics tool for the source of ionising radiation and is good in separating optical AGN and galaxies with active star formation. We plot the eROSITA sample, and samples of randomly selected dwarfs and massive galaxies from MPA-JHU, with all samples filtered to have the necessary line fluxes signal-to-noise larger than three (92 X-ray active dwarfs pass this criterion). For eROSITA sources their BPT classification from MPA-JHU (methodology of Brinchmann et al. 2004) is shown. Separation lines from Kewley et al. 2001; Kauffmann et al. 2003a between star-forming (SF), composite

[16] eastern galactic hemisphere

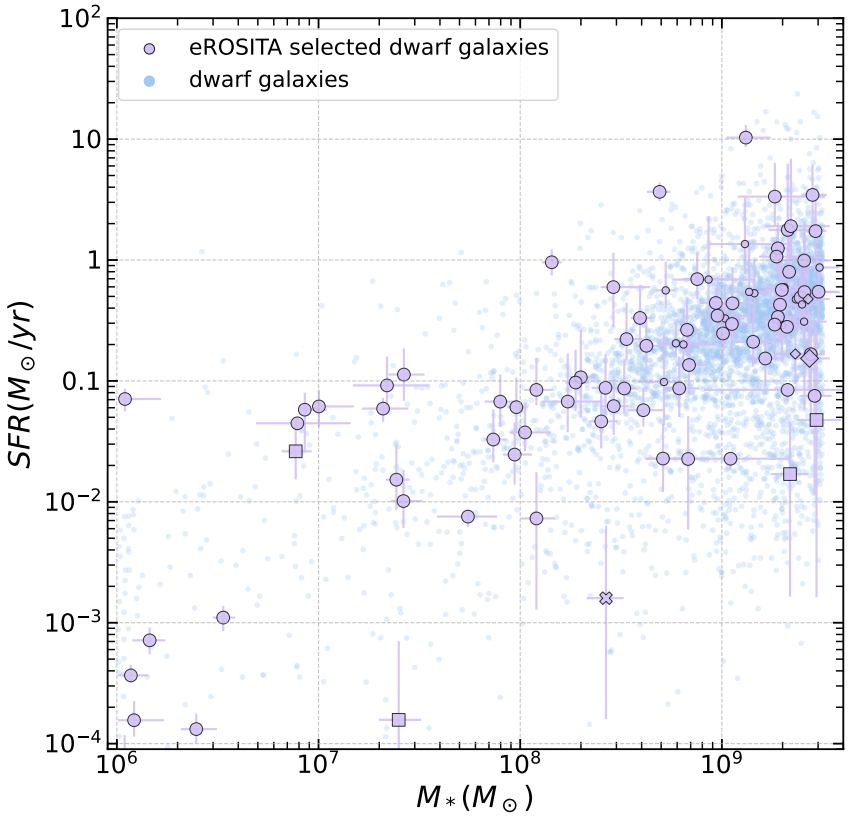

Figure 4.5: Position of 99 eROSITA-detected dwarf galaxies in the Stellar Mass v. Star Formation Rate plane (purple circles). Larger-sized markers designate objects with $\frac{L_{\rm X,obs}}{L_{\rm X,XRB}} > 3$. Marker encodes dwarf's BPT classification from MPA-JHU (circle – star-forming, rhombus – composite, square – AGN, unclassified – X). In addition, 5000 dwarf galaxies from MPA-JHU selected at random are shown as blue circles. Contours show iso-proportion density (inner – 20, 40, 60, 80% – outer) for 20k random dwarfs. It is apparent that eROSITA-selected dwarfs have more objects of lower mass than that expected from the contours of the parent population.

and active galaxies are shown. eROSITA sample has 89 SF galaxies, 5 AGN, 3 composite and 2 unclassified sources. Both eROSITA-selected and MPA-JHU dwarfs are dominated by SF galaxies, whereas massive objects are more dispersed in both SF and AGN branches. This plot shows that X-ray emission is able to pick up low-luminosity AGNs deep in the SF region of the BPT diagram, as explained in the introduction and consistent with previous X-ray studies (e.g. Birchall et al. 2020). Additional diagnostics can be performed based on the ratio of X-ray flux to the optical emission flux. For example the ratio of $O_{\rm III,5007}$ line to the hard X-ray luminosities is used to discern AGNs from TDE in eROSITA survey (Khorunzhev et al., 2022), or the ratio of the flux at 2500 angstrom to the flux at 2 keV (Birchall et al., 2020); but we do not attempt such diagnosis here.

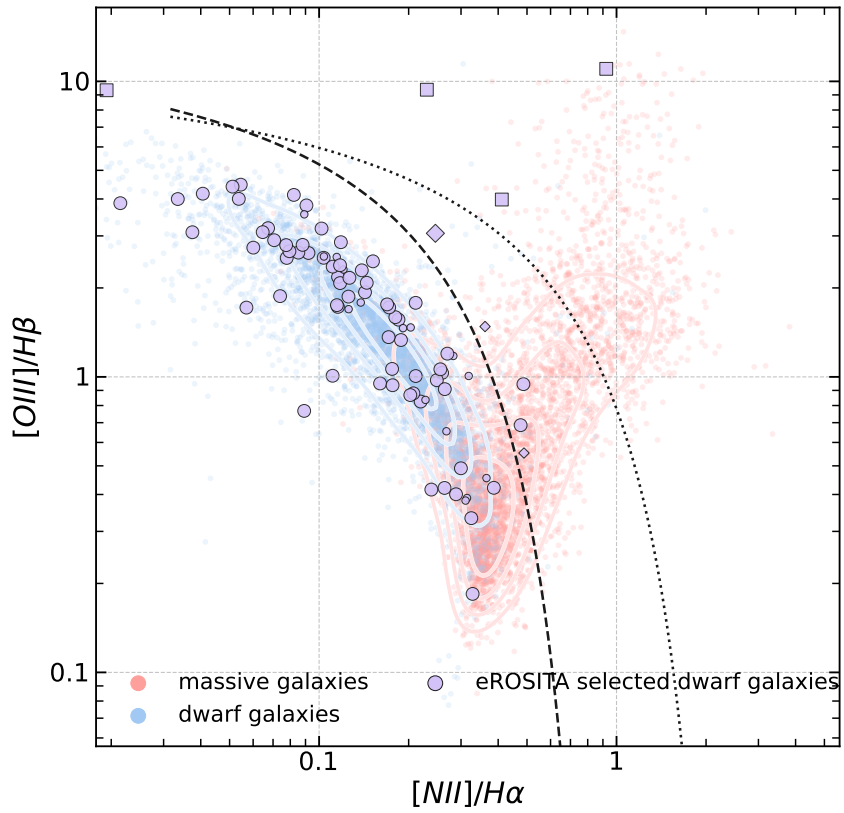

Figure 4.6: Position of eROSITA-selected dwarf galaxies in the BPT diagram. Colours and symbols are the same as in Fig. 4.5, but with added 5000 random massive (non-dwarf) galaxies from MPA-JHU (red). SF-Composite-AGN separation is shown as black dashed and dotted lines.

X-ray luminosity and Eddington ratio

Figure 4.7 shows the hard X-ray luminosity (2–8 keV) vs. host stellar mass. We plot lines of constant Eddington ratio $\lambda_{\rm Edd}$ (see Aird et al., 2012; Birchall et al., 2020, 2022; Zou et al., 2023) calculated as explained below.

We define

$$\lambda_{\rm Edd} = \frac{K \times L_{2-10\ \rm keV}}{1.3 \times 10^{38} M_{\rm BH}(M_*)}$$

where K is the bolometric correction (translates hard X-ray luminosity into bolometric luminosity), $M_{\rm BH}(M_*)$ is a mass of a central black hole expected for a given stellar mass. The coefficient in the denominator is the Eddington luminosity for unit mass. For an X-ray spectrum with photon index $\Gamma = 1.9$, the flux in the 2–10 keV band is 17% higher than in 2–8 keV. Given uncertainties in bolometric corrections and black hole masses, we ignore this difference and use measured 2–8 keV luminosities instead. No k-correction is made because redshifts are small.

AGN hard X-ray bolometric corrections are calibrated with respect to the bolometric luminosity, Eddington ratio and black hole mass in Duras et al. (2020). As we work in the low-mass regime, we use Eq. 7 from Duras et al. to calculate the bolometric correction for low BH masses. From their Fig. 9 and Eq. 7 one may estimate the $K \approx 16.7$ with the scatter of around 0.35 dex. Similar X-ray studies also use K in the range of 20-25 (Birchall et al., 2020; Latimer et al., 2021; Zou et al., 2023).

For black hole masses, we use scaling relations of Reines, Volonteri 2015 (their eq. 4, see also Suh et al. 2020) calibrated with AGN and galaxies in the local universe, including dwarf galaxies: $\log(M_{\rm BH}/M_\odot) = 7.45 + 1.05 \log \frac{M_*}{10^{11}\ M_\odot} \pm 0.55$. We note that according to such a relation, objects with $M_* < 3 \times 10^9 M_\odot$ are expected to host a BH of intermediate mass ($M_{\rm BH} < 10^6 M_\odot$).

Lines of constant $\lambda_{\rm Edd}$ are shown in Fig. 4.7. The majority of our sources have $\lambda_{\rm Edd} = 10^{-3}...10^{-1}$, with around $\sim 10-15$ sources seemingly accreting at the Eddington level or above, median $\lambda_{\rm Edd}$ is ~ 0.01. The median level is lower than that found in deep surveys such as Chandra (Mezcua et al., 2018) and XMM (Zou et al., 2023) with median values around $\sim 0.2-0.6$. This may be explained by the selection effects - in the distant Universe one has trouble detecting low-$\lambda_{\rm Edd}$ source due to them being under the flux limit. On the other hand, our median is higher than that of Birchall et al. (2020) with the median of ~ 0.001. The latter may be explained by the $M_{\rm BH}(M_*)$ relation adopted by Birchall et al. which predicts BH mass almost order of magnitude larger than the relation we adopt, our results are broadly consistent.

There are important caveats in interpreting the results. First, in the high $\lambda_{\rm Edd}$ regime the bolometric correction may change dramatically (Duras et al., 2020). Not only that, the spectral shape may be different from the expected power-law. In our sample two very bright sources ($L_{\rm X,0.3-2.0\ keV} \sim 10^{42}$) have thermal spectrum, therefore having negligible luminosity in the 2–8 keV regime. These two sources are basically missing in the calculations of $\lambda_{\rm Edd}$ presented here, but still even without bolometric correction they appear to have $\lambda_{\rm Edd} \sim 0.1$. One should also bear in mind that the correlation between the stellar and BH masses is highly uncertain in the low-mass regime (Suh et al., 2020; Mezcua et al., 2023). Very low-massive galaxies ($M_* < 10^7 M_\odot$), and sometimes normal dwarf galaxies may be prone to mass measurement errors (see sect. 4.3.1).

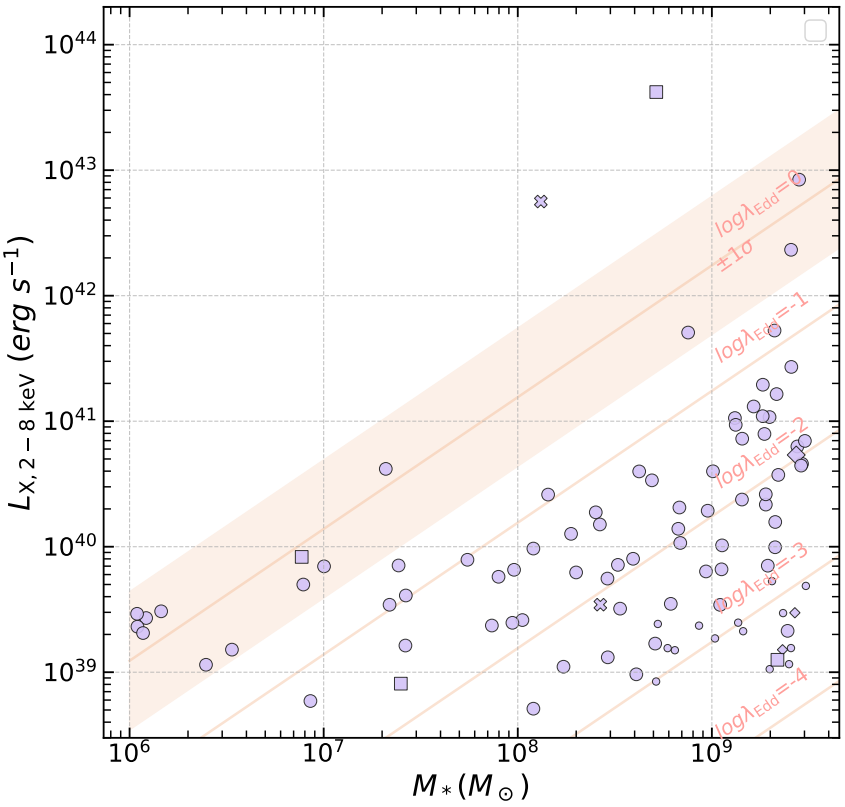

Figure 4.7: Mass v. X-ray Luminosity plane. Lines of constant Eddington ratio are shown with orange lines. For the $\lambda_{\rm Edd} = 1$ the expected scatter in $M_{\rm BH} - M_*$ relation is shown. Points above $\lambda_{\rm Edd} = 0.1$ should be interpreted with extreme care (see text).

4.4.4 AGN fraction and luminosity distribution

In order to compute the AGN fraction we need to take into account several incompleteness factors. The first one is the sensitivity of the eROSITA all-sky survey (varying across the sky) and the flux limit of its source catalogue. This factor is fully accountable for and will be corrected as described below. The second incompleteness factor is related to the incompleteness of the MPA-JHU SDSS catalogue at the faint (low mass, large redshift) end. We will attempt below several approaches to approximately correct for this effect and demonstrate that they all give consistent results.

Another incompleteness factor is related to the cleaning of the initial list of eROSITA – MPA-JHU matches. Our catalogue of X-ray active dwarf galaxies is constructed with the goal of being pure but not necessarily complete. Hence, we are likely to determine only the lower limit on the AGN fraction in dwarf galaxies. This factor is difficult to accurately correct. We note, however, that 96 sources out of 178 initial matches were excluded from the luminosity function calculation (after the cleaning procedure and the requirement of $\frac{L_{\rm X,obs}}{L_{\rm X,XRB}} > 3$). Therefore, the maximal uncertainty which can be introduced in this step is less than a factor of ~ 2; this should be taken into account when interpreting our results. Finally, an important question is how well the MPA-JHU catalogue represents the overall population of dwarf galaxies in the local Universe. This is discussed in more detail at the end of this section.

For calculating AGN fraction and luminosity distribution, only dwarfs with $\frac{L_{\rm X,obs}}{L_{\rm X,XRB}} > 3$ are used (82 objects). From MPA-JHU galaxies we removed galaxies duplicated in SPECOBJID or coordinates, and sources with non-reliable photometry. We limit the stellar mass to the range $8 < \log M_* < 9.5$ - the completeness limit is not well-defined for lower mass galaxies due to poor statistics.

To correct for the incompleteness of the X-ray detections we used a method similar to the approach used in the incompleteness correction of the $\log N - \log S$ flux distribution of X-ray sources (Shtykovskiy, Gilfanov, 2005; Voss et al., 2009). We use the eROSITA sensitivity map to compute the sensitivity curve $A(L_{\rm X}) = N(L_{\rm X,upper} < L_{\rm X})$ defined as the number of dwarf galaxies in the given mass-redshift range in the MPA-JHU catalogue where the eROSITA sensitivity is better than a given luminosity L_X. Next, for every eROSITA-detected dwarf galaxy with luminosity $L_{\rm X,k}$ we calculate the weight $w_{\rm k} = 1/A(L_{\rm X,k})$.

The binned estimate of XLF in a bin of luminosity would be then

$$\phi = \frac{{\rm d}N}{{\rm d}\log L_{\rm X}} = \frac{1}{\Delta \log L_{\rm X}} \sum_{\rm k \in bin} w_{\rm k}$$

and its error $\Delta\phi = \frac{1}{\Delta \log L_{\rm X}} \sqrt{\sum w_{\rm k}^2}$. For the cumulative XLF,

$$\Phi(L_{\rm X}) = \sum_{\rm k: L_{X,k} > L_X} w_{\rm k}$$

When no sources are detected in a bin/above a given luminosity, an upper limit of 95% is placed which for Poissonian distribution equals to three sources.

To control the possible completeness of the dwarf galaxy content of the MPA-JHU SDSS catalogue, we used three approaches. In the first approach, similar to Birchall et al. 2022, we

define the redshift-dependent stellar-mass limit of SDSS $M(z)$ as a mass above which lies 90% of galaxies in narrow redshift bins and use only galaxies with $M > M(z)$. In the second approach, we determine the mass-dependent redshift limit $z(M)$ below which lies 90% of galaxies in a narrow stellar mass bin and use only galaxies with $z < z(M)$. In the third approach, we use all objects in a given mass bin. The two selection curves are shown in Fig. 4.8 for $M_* > 10^8 M_\odot$.

To compare these three approaches, we calculate the cumulative fraction of X-ray active dwarf galaxies in a broad galaxy mass range $8 < \log M_* < 9.5$, shown in Fig. 4.9, panel A. The three curves virtually coincide up to the luminosity of $\sim 10^{40.5}$ and diverge notably at $L_X \geq 10^{41.5}$, where Poissonian errors start to dominate. For further analysis, we chose to use the results of the first method of incompleteness correction, $M(z)$.

The differential XLF of dwarf galaxies is shown in panel B of Fig. 4.9. Overall, the AGN fraction increases towards lower luminosities. The cumulative AGN fraction is $\sim 2.24 \pm 0.59$ per cent at $L_X > 10^{39}$ and decreases to $\sim 0.39 \pm 0.11$ per cent at $L_X > 10^{40}$. There is evidence of flattening of the differential XLF at the low luminosity end $L_X < 10^{38.5..39}$ (also seen in more narrow mass bins, see below), but further data is needed to confirm this finding. Some remaining systematic bias may be present at the low luminosity end of XLFs because of the contamination by X-ray binaries.

To investigate the mass dependence of the AGN fraction we separate the sample into two bins in stellar mass: $8 < \log M_* < 9$ and $9 < \log M_* < 9.5$. The results are shown in panels C and D of Fig. 4.9. For luminosity $L_X > 10^{39}$ the cumulative AGN fraction for the low mass bin is $\sim 1.85 \pm 0.61$ per cent, and $\sim 3.32 \pm 1.53$ per cent for the high mass bin. For luminosity $L_X > 10^{40}$ the AGN fraction is $\sim 0.17 \pm 0.09$ per cent (low mass bin) and $\sim 0.89 \pm 0.36$ per cent (high mass bin). The difference in AGN fraction is statistically significant for luminosity $L_X > 10^{40}$. This supports the picture of ubiquitous black hole occupation of massive galaxies which rises towards higher masses (Aird et al., 2012, 2018). The slope of XLF for the lower mass bin seems to be steeper than that of the higher mass. We checked that making 'volume-limited' samples of dwarfs by restricting redshifts to be below the redshift of the lowest mass limit in a given mass bin does not change these results significantly.

Differential XLF obtained in this chapter is slightly steeper than that of Birchall et al. 2020[17] for the high mass bin, but overall it is consistent in magnitude. The cumulative AGN fraction for $L_X > 10^{40}$ for low and high mass bins from Birchall et al. 2020 are roughly 0.5% and 1% respectively, slightly higher than the eROSITA results. The difference may arise from the selection criteria and our cleaning procedure, as discussed above. In this respect, we recall that Birchall et al. excluded only 15 out of 101 initial matches.

We did not find any statistically significant redshift evolution of the AGN fraction.

MPA-JHU galaxies (and SDSS galaxies in general) are rather luminous and relatively close by, therefore the catalogue of dwarfs may not be representative of the entire dwarf galaxy populations in the local Universe, especially at higher redshifts. We also found several obscured sources, against which eROSITA has strong bias due to the soft response. Obscured AGNs in dwarfs may or may not be a significant portion of the population, which we will likely miss. X-ray binaries may be problematic for a faint end of the luminosity function. One luminous X-ray binary is

[17] since they use band 8 of XMM for luminosities (0.2-12 keV), their luminosities are by ~ 0.5 dex larger than ours

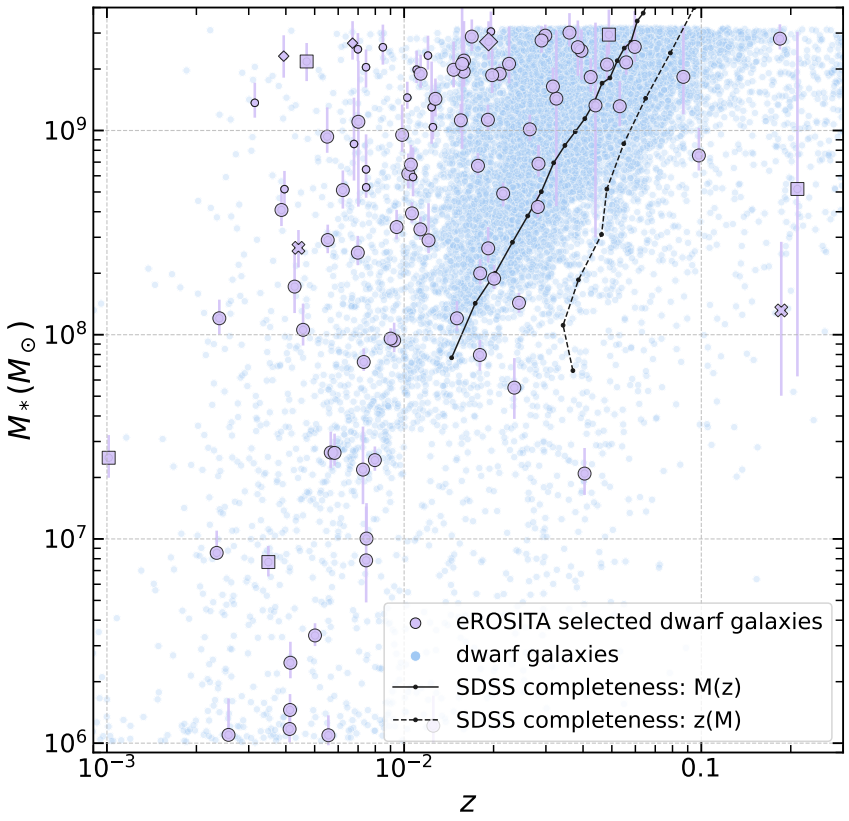

Figure 4.8: Mass v. redshift plane. The approximate SDSS mass completeness limit in redshift bins is shown as a black curve, and SDSS redshift completeness in mass bins in the black dashed curve. We calculate the fraction of active dwarfs in stellar bins highlighted by horizontal stripes.

enough to produce $L_X \sim 10^{38..39}$ erg s^{-1}which we can deem as an AGN.

In the conclusion of this section, we mention an exciting possibility to constrain the fraction of *dormant* black holes in dwarf galaxies using the data of wide angle and long time span surveys, like SRG/eROSITA all-sky survey. This possibility is given by the detection of TDEs in dwarf galaxies (for example discovered by eROSITA in ID 4296 in our sample, see discussion below). A TDE would be detected whether or not the host galaxy is classified as an AGN (in the case of ID 4296 it is a BPT-classified AGN). Detection of a TDE means that a star was disrupted by a black hole, leaving no doubt that the centre of a galaxy is inhabited by a massive BH. ID 4296 is a dwarf with stellar mass $\sim 3 \times 10^9 M_\odot$ and the corresponding BH mass of $\log M_{\rm BH} \sim 5.8$, redshift is $z = 0.048$. Detection of just one TDE places a rather weak lower limit on the fraction of dormant black holes in dwarf galaxies, roughly one in ~ 40000 galaxies. However, systematic wide-area sky surveys (also in optical, see Yao et al. 2023) will lead to an increase in the number of TDEs found in dwarf galaxies and will help to obtain more meaningful constraints.

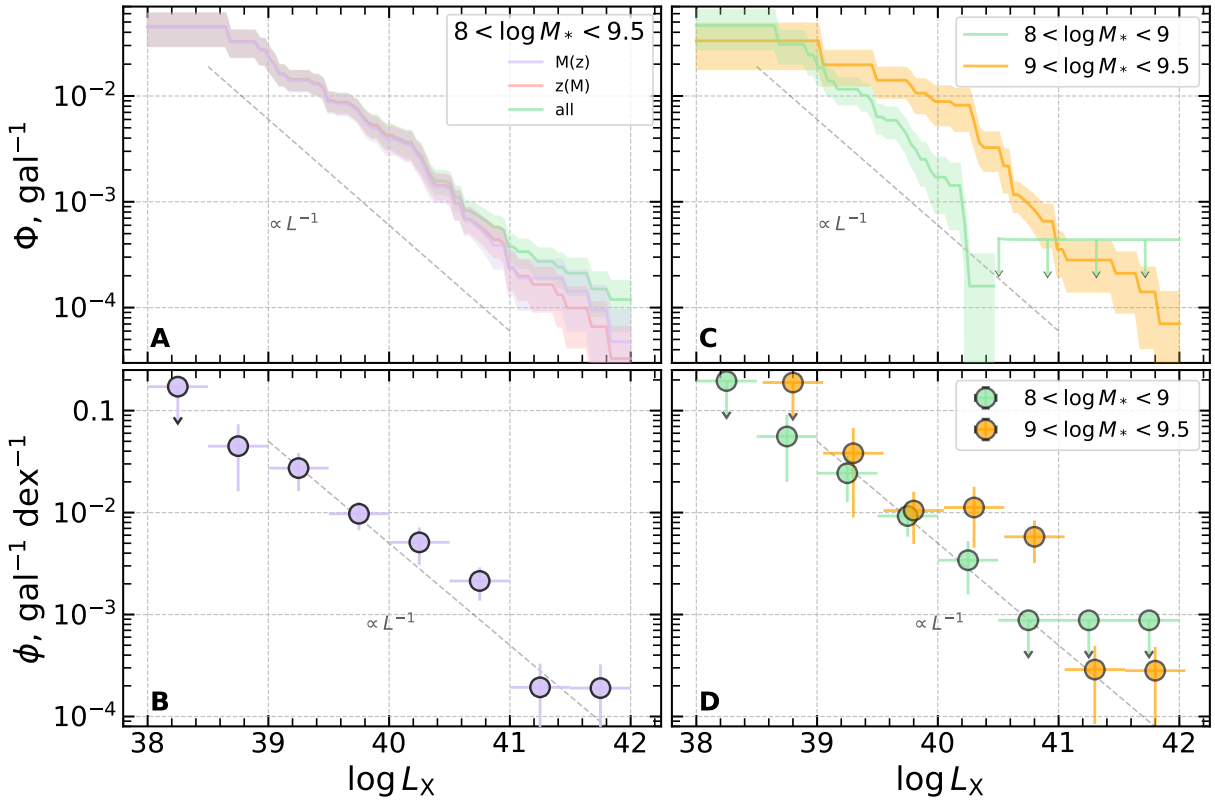

Figure 4.9: Results on the occupation fraction of AGN in dwarfs with $M_* > 10^8 M_\odot$. Panel A shows the cumulative XLF for the three cases of calculated mass-completeness limits of SDSS. Panel B shows the differential XLF for one completeness case. Panels C and D show cumulative and differential XLF for two samples of dwarf galaxies: with masses below or above $10^9 M_\odot$. All panels show the power law with a slope of -1 to guide the eye. X-ray luminosities are in the 0.5-2 keV energy band.

4.5 Individual objects

Based on the analysis of X-ray data, we selected several sources with interesting properties worth some further discussion. Among them a Tidal Disruption Event (TDE) candidate, a very soft and bright source but without significant variability, a luminous obscured AGN – the most distant and luminous source in the sample and an obscured and variable AGN. We also found several examples of X-ray active galaxy pairs and ultra-luminous X-ray source candidates. The objects discussed in this section are listed in Table 4.1.

4.5.1 ID 4296 – a possible Tidal Disruption Event in a dwarf galaxy

Object 4296 (SRGe J023346.8-010129, SDSS J023346.93-010128.3) is peculiar. It is classified as an AGN (not LINER) in MPA-JHU catalogue (the top right source in Fig. 4.6). 4296 has stellar mass $\sim 3 \times 10^9 M_\odot$ and the corresponding BH mass of $\log M_{\rm BH} \sim 5.8$ from the $M_* - M_{\rm BH}$ correlation. Redshift is $z = 0.048$ (distance of 203 Mpc).

It has the most variable X-ray light curve (top left in Fig. 4.3) constantly rising through eRASS1..5, and the softest spectrum ($\Gamma = 5.5 \pm 0.5$, Fig. 4.2). The DESI LIS image is shown in Fig. 4.1 in the bottom right. This object has a variable optical brightness and a transient event was discovered at that position in 2018 by Gaia Alerts Team (AT2018cqh[18]), but the event was not classified.

To track the evolution of the source's intensity we requested a Swift/XRT (Burrows et al., 2005) Target of Opportunity observations. ToO request ID is 19205 with 4355 s exposure in PC mode, performed on Aug 9, 2023. The data was processed using the standard Swift/XRT pipeline[19]. A source was detected in the given position with a significance over 3σ, and its coordinates were pinpointed with XRTCENTROID (position error $\sim$ 5"). The distance to the eROSITA position is 1.2", and to the SDSS dwarf is 2.5". The source extraction region was centred on the source position and had a 20-pixel radius, whilst the background region is an annulus with radii of 25 and 60 pixels. Spectrum was grouped to 1 count per channel and fit with Cash statistic.

Fit the co-added eROSITA data with the black body model gives the best-fitting temperature of 63 ± 7 eV and the size of the emitting area of $R \sim 1.9^{+0.8}_{-0.6} \times 10^{11}$ cm for 203 Mpc distance. No statistically significant temperature variations were detected between the individual sky surveys, although the statistical uncertainties in the first three surveys are fairly high. The Swift/XRT spectrum is similarly soft with the best-fitting temperature of 83 ± 25 eV, consistent with the eROSITA value. Both eROSITA and Swift/XRT data show evidence for the presence of a non-thermal hard tail which we model as a power law with a fixed photon index $\Gamma = 1.9$. For example, in eRASS 5 the C-statistic significantly improved from 31.67 (25 dof) to 17.34 (24 dof) with the added hard component, and it is responsible for $\sim$ 10 per cent of X-ray flux in the 0.3–2 keV energy band. For estimating flux evolution we, however, use a simpler model without the hard component (PHABS*BBODYRAD). For each scan (and the XRT observation) we use individual best-fitting temperature and normalisation to estimate unabsorbed flux in the 0.3–2 keV energy

[18] https://www.wis-tns.org/object/2018cqh
[19] https://www.swift.ac.uk/analysis/xrt/

range. We checked that the inclusion of the non-thermal component in the fit does not change the light curve discussed below significantly.

Zwicky Transient Facility (ZTF, Bellm et al. 2019) light curve provides almost continuous data for this object from mid 2018[20] and is shown in Fig. 4.10 along with X-ray light curve.

Optical data show a prominent flare which decayed to the quiescent state by the time of the first eROSITA observation. During this outburst, the galaxy became brighter by a least 1 mag (i.e. by a factor of 2.5) for at least 200 days, meaning that at the peak of its light curve, the optical transient event was $\sim$ 150 per cent of the galaxy luminosity. X-ray light curve of eROSITA shows a gradual rise by a factor of 10 from eRASS 1 (MJD 58800) to eRASS 4 (MJD 59500) and hints at a decrease in brightness between eRASS 4 and 5. With a new data point from SWIFT, we find that in the course of the 1.5-year observation gap, the source brightness decreased by a factor of $\sim 2-3$. The peak unabsorbed X-ray brightness corresponds to the $0.3-2$ keV luminosity of $\sim 5.5\times10^{42}$ erg s^{-1}and is delayed with respect to optical emission by at least two years (assuming optical and X-ray events are related). The X-ray to optical ratio computed between peak values in each band was $L_X/L_{\rm opt}\sim 0.3$.

Assuming the black hole mass quoted above ($\log M_{\rm BH}\sim 5.8$) and ignoring bolometric correction, we estimate that the source was accreting on at least $\sim$ 8 per cent of Eddington level. A bolometric correction in the X-ray band using the best fit black body spectrum increases this number by a factor of $\sim$ 5, to $\sim$ 40 per cent. The decay of the flux between eRASS4 and XRT observation roughly follows $\left(\frac{t-t_0}{\tau}\right)^{-5/3}$ trend expected for X-ray selected TDEs. We also did not find the 'infrared echo' from the NeoWISE light curve[21] – no increase in the W1 and W2 flux was detected.

The X-ray properties such as soft spectrum, large peak luminosity and flare-like light curve suggest that the source may be a Tidal Disruption event (TDE). The peak luminosity is less than that of usual X-ray-selected TDEs ($L_{\rm X}\gtrsim 10^{43}$ erg s^{-1}, Saxton et al. 2020; Sazonov et al. 2021) but still noticeably larger than other possibilities – a nova, supernova, flaring star, X-ray binary (inc. ULX), see Zabludoff et al. (2021) for discussion of 'impostors'. The main alternative scenario is an AGN flare (see Saxton et al. 2012; Auchettl et al. 2018; Neustadt et al. 2020; van Velzen et al. 2021b,a; Zabludoff et al. 2021), especially given that the galaxy has an active nucleus according to SDSS spectroscopy from 2001. However, a typical AGN flare observed by eROSITA has an AGN-like hard X-ray spectrum (Medvedev et al., 2022). This is in line with the conclusion of Auchettl et al. 2018, that X-ray selected TDEs have a drastically softer spectrum than AGN at $z<2$, and moreover, the spectrum is usually much less absorbed. We conclude that all the so far collected evidence strongly suggests that we caught a TDE.

Overall, several dozen TDEs active in X-rays have been identified so far, with only a handful of sources hosted by dwarf galaxies (Maksym et al., 2013; Donato et al., 2014; Maksym et al., 2014; Lin et al., 2017; He et al., 2021). Optical TDEs are also found in dwarf galaxies, the first candidate was discovered recently in Angus et al. 2022.

[20] `https://ztf.snad.space/dr17/view/401310100001492`, (Malanchev et al., 2023); translated into flux using the reference ZTF g filter wavelength (4783 angstrom) and AB system zero point 4.76×10^{-9} erg s^{-1} cm^{-2} per angstrom, see this url

[21] gathered with this python package, see Hwang, Zakamska (2020)

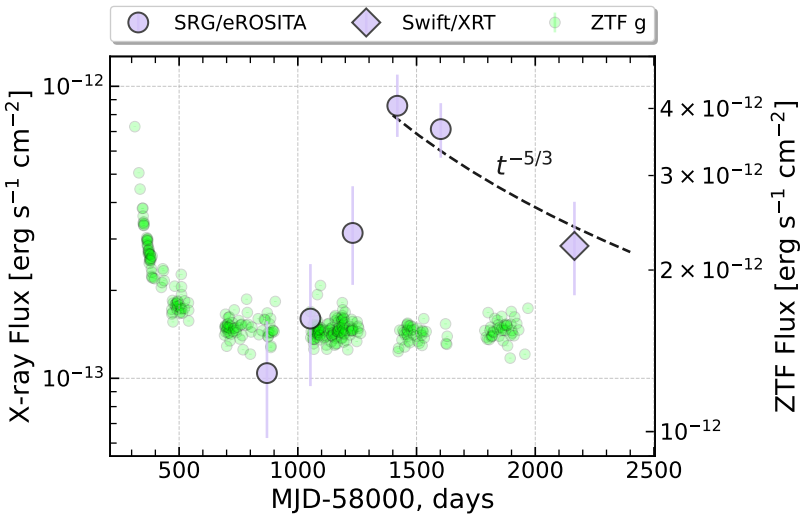

Figure 4.10: X-ray (0.3–2.0 keV) and ZTF light curve (g band) of ID 4296/AT2018cqh. The dashed line shows the expected $t^{-5/3}$ decline of X-ray luminosity expected from TDE.

There appears to be a dichotomy between X-ray bright and optically bright TDEs (Gilfanov et al., in preparation) with only some fraction, of the order of $\sim$ 20 per cent, of X-ray bright TDEs also showing significant optical activity. Many of those active in both bands typically show a time delay between the peaks of the optical and X-ray emission. Although the full multi-wavelength picture is still emerging, the delay in ID 4296 seems to be much longer than observed in other events. It remains to be seen whether the two-year-long delay is related to the properties of the host galaxy (dwarf with a low-mass black hole) or the parameters of the TDE itself.

The hard X-ray component may come either from the processes within the disrupted star remains, or be associated with the AGN in this dwarf (as per the SDSS BPT diagram, the galaxy was active long before eROSITA observations). eROSITA and XRT data are not sufficient to reliably establish the variability of the hard component.

4.5.2 ID 10487 - AGN with a thermal spectrum in a dwarf galaxy

eROSITA ID 10487 is also one of the three soft sources. It is located in a Seyfert galaxy RGG 123 at $z = 0.0395$ (168 Mpc), with mass $\sim 3 \times 10^9 M_\odot$. Chilingarian et al. 2018 has the black hole mass estimation of $M_{\rm BH} = 1.11 \pm 0.07 \times 10^5 M_\odot$. There is a Chandra detection at the position of the galaxy with $L_{\rm X} = 0.85 \times 10^{42}$ erg s^{-1}(Greene, Ho, 2007; Dong et al., 2012; Baldassare et al., 2017) but without sufficient number of photons to constrain the spectrum – only the photon index was estimated to be around 3 from the HR ratio (Baldassare et al., 2017). The Chandra data was taken in 2009-2010.

During eROSITA observations the source was quite bright (eROSITA detected 230 photons) and soft ($\Gamma = 3 \pm 0.5$). The spectrum is well-fit with a BBODYRAD model with interstellar absorption, eROSITA spectrum is shown in Fig. 4.11. The temperature is $\sim 160 \pm 15$ eV, the

emission radius is $1 \pm 0.3 \times 10^{10}$ cm, the luminosity (0.3–8 keV) is $0.9 \pm 0.1 \times 10^{42}$ erg s^{-1}, consistent with the cited works (bolometric correction is small). With the black hole mass quoted above, we estimate that the source is accreting at ~ 7 per cent of Eddington luminosity. The multi-colour black body disc model DISKBB also fits data well, with a temperature of $\sim 240 \pm 30$ eV and a smaller radius (by a factor of ~ 2, assuming inclination of 60°). The source has a marginally significant ($\sim 2.4\sigma$) hard power-law tail – spectral fit with only DISKBB component gives C-stat 55.38 for 60 dof; adding a power law with fixed slope $\Gamma = 1.9$ reduces C-stat to 49.86 for 59 dof. In further discussion we fit the data without a hard component, doing otherwise does not change the results within errors. Neither eROSITA nor ZTF[22] show evidence of brightness variability or flares. The apparent stability of luminosity between Chandra and eROSITA observations, and the lack of faster optical and X-ray variability suggest that this source is not a TDE.

The maximum temperature of the optically thick geometrically thin accretion disc is given by (Shakura, Sunyaev, 1973)

$$kT_{\rm max} = 11.5 \left(\frac{M_{\rm BH}}{10^8\ M_\odot} \right)^{-1/4} \dot{m}^{1/4} ({\rm eV})$$

where $\dot{m}$ is the accretion rate in terms of critical (Eddington) accretion rate. For the parameters of ID 10487 ($M_{\rm BH} = 10^5$, $\dot{m} = 0.07$), this formula gives the temperature of $kT = 30$ eV, which is several times smaller than the values quoted above. The decrease in BH mass by about an order of magnitude and account for spectral hardening (due to the Compton scattering) helps to explain the observed temperature.

To put this on a more quantitative footing we fit the data with the GRAD (General Relativistic Accretion Disk model around a Schwarzschild black hole, Ebisawa et al. 1991) model. Assuming the spectral hardening factor of $T_{\rm col}/T_{\rm eff} = 2$ and inclination angle of 60° we obtain the best-fitting value of the black hole mass $M_{\rm BH} = 1.0 \pm 0.3 \times 10^4\ M_\odot$ and the mass accretion rate of $2.9 \pm 0.5 \times 10^{22}$ g s^{-1}, giving the Eddington ratio of 1.5 ± 0.5 (accretion luminosity $L = 2 \pm 0.3 \times 10^{42}$ erg s^{-1}). The fit provided an adequate description of the data with the C-stat 54.11 for 60 dof.

To summarise, the soft thermal black body-like X-ray spectrum of this source suggests that we are observing emission from the Shakura-Sunyaev accretion disk, which, thanks to the small mass of the central black hole emerges in the soft X-ray band. However, the observed temperature appears to be too high and requires about ~ 10 times less massive black hole, than $\sim 1 \times 10^5 M_\odot$ derived by Chilingarian et al. (2018) from optical spectroscopy.

The observed soft spectrum of this source may resemble the soft excess observed in AGN (Gierliński, Done, 2004; Done, 2010; Done et al., 2012). However, the soft excess typically appears on top of the hard power-law emission usually observed in AGN. For ID 10487, the hard power-law component seems to be subdominant. All in all, this scenario seems to be less likely and further investigation of this source in X-ray and optical bands is required to solve the puzzle of its soft X-ray spectrum.

The third soft source (ID 33862) has only 24 spectral counts, and precise spectral analysis is hampered. It is located in a radio galaxy FIRST J103837.1+443123 at $z = 0.0124$ and has X-ray luminosity $\sim 2 \times 10^{40}$ erg s^{-1}. The photon index is $\Gamma = 4.5 \pm 1.5$ and black body temperature

[22] https://ztf.snad.space/dr17/view/480206200003099

is $kT = 110 \pm 10$ eV. The $\frac{L_{\rm X,obs}}{L_{\rm X,XRB}}$ is only 1.2, but the soft X-ray spectrum cannot be explained by X-ray binaries. The contribution of the hot gas of ISM is not sufficient to explain the observed luminosity in the 0.5-2 keV energy range in all three soft sources.

4.5.3 ID 45689, 11124 and 49241 – peculiar absorbed sources in dwarf galaxies

ID 45689 is a very luminous source. If the association between the SDSS dwarf (z=0.21) and the eROSITA source is not a chance coincidence, the dwarf has an obscured nucleus. eROSITA spectrum is fit with absorbed power law in the form of PHABS*ZPHABS*ZPO, yielding the intrinsic absorption (ZPHABS) of $N_{\rm H} = 1.4^{+0.8}_{-0.6} \times 10^{22}$ cm^{-2}. The photon index is fixed at 1.9. The unabsorbed luminosity is $L_{\rm X} = (1.4 \pm 0.4) \times 10^{44}$ erg s^{-1}in the 0.3–8 keV band.

To our knowledge, the largest reported luminosity of an AGN in a dwarf galaxy is 10^{44} erg s^{-1}at $z = 2.39$ found by Mezcua et al. 2018 (their cid_1192). Clearly, eROSITA found a quite rare object – in Mezcua et al. 2018; Zou et al. 2023, none of the sources has luminosity above 10^{43} erg s^{-1}at $z < 0.3$. The constraints on the bright end of the luminosity functions of active dwarfs may be important to assess the cosmic evolution of this population to constrain the scenarios of the AGN triggering and lifetime in low-mass black hole mass regime. eROSITA spectrum for this source is shown in Fig. 4.11.

ID 11124 is an obscured source (z=0.003493). It is fit in a similar fashion as ID 45689 above yielding intrinsic absorption of $N_{\rm H} = 0.18^{-0.05}_{+0.06} \times 10^{22}$ cm^{-2} and unabsorbed luminosity of $L_{\rm X} = (1.1 \pm 0.1) \times 10^{40}$ erg s^{-1}. The source seems to be variable: in eRASS 1,3 it has the X-ray flux of $\sim 1.0 \pm 0.2 \times 10^{-12}$ erg s^{-1} cm^{-2}, and in eRASS 2,4,5 the flux is $0.3 \pm 0.15 \times 10^{-12}$ ($R = 4.1$). The spectrum and light curve for this source are shown in Fig. 4.11.

ID 49241 is located in a nearby dwarf galaxy NGC 4395. According to eROSITA data, ID 49241 shows a hard spectrum with a photon index $\Gamma = 0.2 \pm 0.3$. The galaxy is known to have an X-ray source in a nucleus and is active (Moran et al., 2005; Nardini, Risaliti, 2011). X-ray analysis of archival data suggests the presence of variable absorption and changing spectral shape (Kammoun et al., 2019).

4.5.4 Galaxy pairs

There are several dwarf galaxies and/or eROSITA-SDSS matches excluded from the final list of X-ray active dwarfs which are located close to another galaxy/galaxies. It is important to note that we did not perform a *systematic search* for galaxy pairs, but rather found several examples via visual inspection of DESI LIS images of each galaxy's surrounding. Those which we found will usually have Simbad type of 'Galaxy in a Pair of Galaxies', 'Galaxy in a Galaxy cluster' or 'Galaxy in a group of Galaxies'.

We show three examples in Fig. 4.12. The galaxy separations reported below are projected separations and were calculated using the redshift of the Simbad galaxy associated with the eROSITA source.

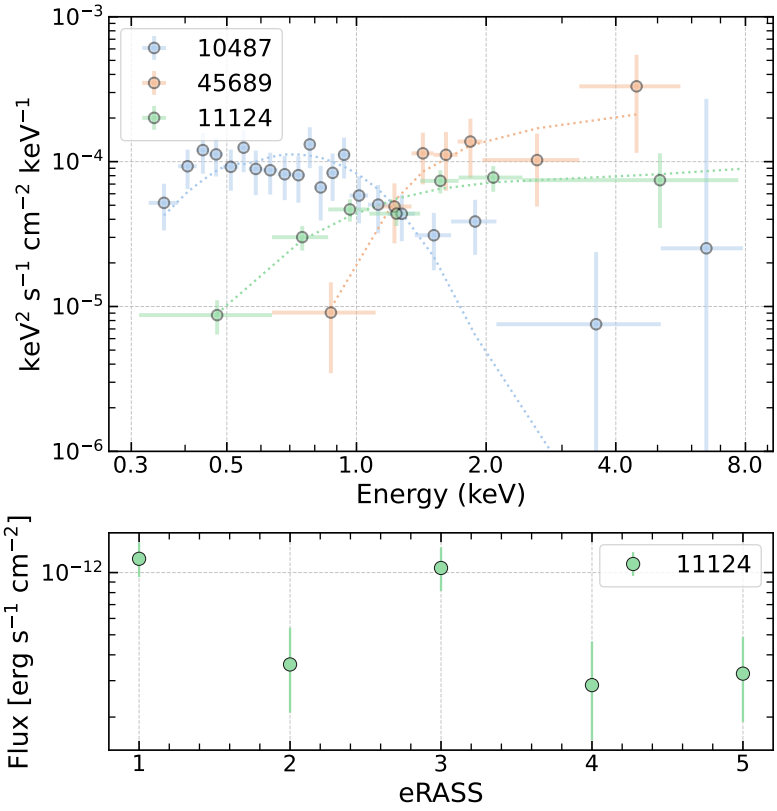

Figure 4.11: X-ray spectra and light curve of a few selected sources discussed individually (ID 10487, 45689, 11124). In the top panel, unfolded eROSITA spectra are shown (rebinned for clarity). A power-law shape with $\Gamma = 2.0$ in this plot would be a horizontal line. In the bottom panel, an X-ray light curve of ID 11124 is shown, as in Fig. 4.3.

The first example is the dwarf ID 28027 and excluded match ID 28024 (likely a massive galaxy) which are located in galaxies UGC 4904 and NGC 2798 respectively, with the projected separation of $\sim$ 40 kpc. NGC 2798, in turn, interacts with galaxy NGC 2799 nearby. It may be the case that this pair is a rare example of 'dual AGN'.

The second instance is excluded source 15414 in galaxy NGC 5218 separated by $\sim$ 50 kpc from NGC 5216. The latter coincides with an eROSITA source not reported in this work. The third example, dwarf 64653, is identified as galaxy UGC 9925, a satellite of NGC 5962 (Mao et al., 2021) some $\sim$ 80 kpc away. eROSITA sees a few sources near the core of NGC 5962, but they are not reported in this work.

Other examples of pairs are ID 11387 (30 kpc projected separation, both galaxies active in X-rays), ID 64321 (6 kpc separation and both active in X-rays), ID 34500 (6 kpc separation), ID 25180 (150 kpc separation), ID 3474 (20 kpc separation). Excluded source ID 29963 is located in one of the interacting galaxy pair MCG+08-26-012 and 2MASX J14122652+4541254 (16 kpc separation).

Some objects are located in a galaxy cluster or group, e.g. for dwarf galaxies those are ID 53431 (an X-ray source known before eROSITA), 16640, 2364, 53431 (a known X-ray source) and 32206; and for rejected matches ID 2356, 17032 and 23630. The latter is close to a gravitational lens candidate, but a follow-up is needed to confirm or exclude this association.

Galaxy mergers are expected to play a significant role in AGN triggering and fuelling mechanisms and the corresponding growth of a massive black hole (Mayer et al., 2010; Allevato et al., 2016). Observational results imply that the AGN activity depends on the separation between pairs (Satyapal et al., 2014; Fu et al., 2018; Dougherty et al., 2023), including the observation of rare dual-AGN (McGurk et al., 2015). There is evidence for the different behaviour observed in absorbed and unabsorbed X-ray AGNs (Guainazzi et al., 2021) with decreasing separations. The large-scale environment of AGN may play a role in determining the AGN triggering (Hopkins et al., 2014; Allevato et al., 2016), and sources located in galaxy groups and clusters may aid further research in this direction if confirmed as AGN. The systematic search of AGN in interacting galaxies is within the scope of future research with eROSITA data.

4.5.5 Ultra-luminous X-ray sources candidates

During the visual inspection of sources, we found three cases when eROSITA clearly detects off-centre X-ray emission in a dwarf galaxy. This happens because the MPA-JHU catalogue sometimes includes several fibre positions for one galaxy, and the eROSITA source may be matched with one of them. The sources in question are ID 2387, 27303 and 30593, their optical images are shown in Fig. 4.13. The sources are removed from the active dwarf catalogue because they are off-centred (sect. 4.3.1). Note that ULXs may be also responsible for *nuclear* X-ray emission of some dwarf galaxies, but these cases are quite difficult to discern from a genuine AGN based on eROSITA data only. None the less, based on the expected frequency of ULXs, we do not anticipate that they dominate our sample of 99 active dwarfs.

X-ray spectra of these sources are consistent with the canonical AGN spectrum (see sect. 4.3.2). ID 2387 and 27303 have luminosities of $\sim 5 \times 10^{39}$ erg s^{-1}, and 30593 has a luminosity of $\sim 10^{40}$ erg s^{-1}.

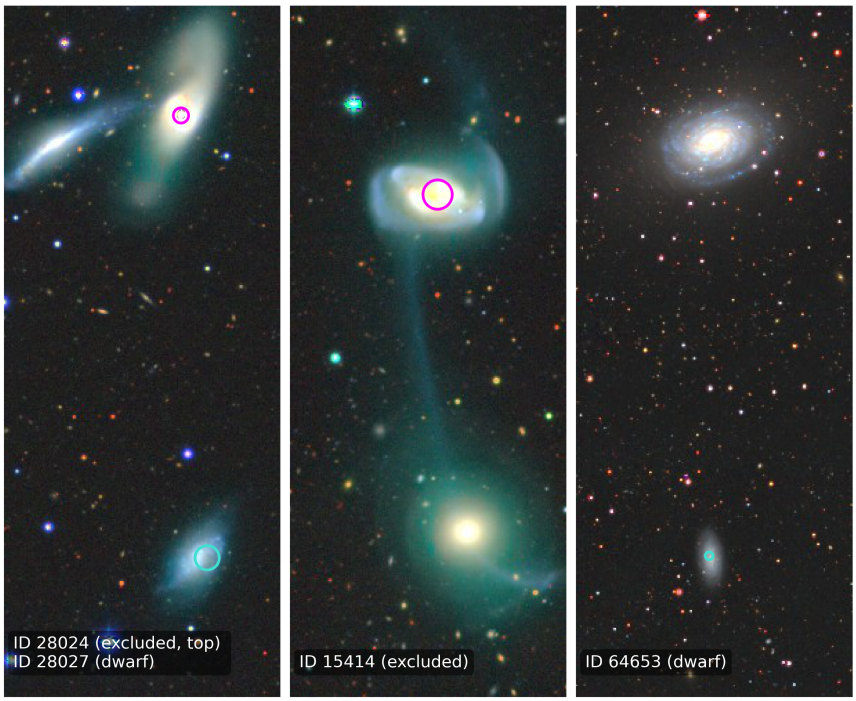

Figure 4.12: As Fig. 4.1, but for three examples of identified X-ray sources in galaxy pairs, see sect. 4.5.4.

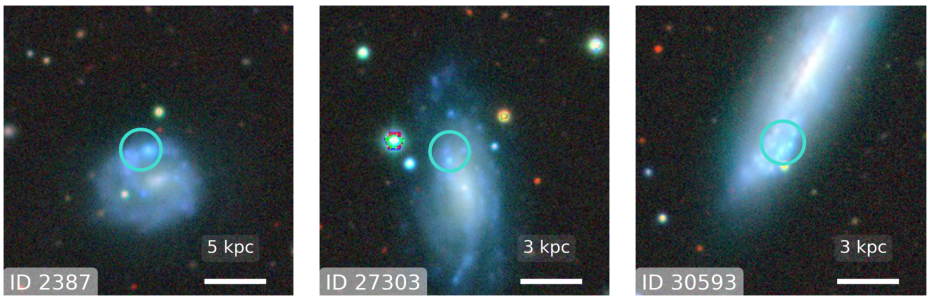

Figure 4.13: As Fig. 4.1, but for ULX candidates in the outskirts of dwarf galaxies, see sect. 4.5.5.

ID	Peculiarity
	Dwarf galaxies
4296	TDE cand. (sect. 4.5.1)
10487	Soft state AGN (sect. 4.5.2)
45689	Obscured AGN (sect. 4.5.3)
28027	Gal. pair (with 28024)
11387	Gal. pair
64321	Gal. pair
34500	Gal. pair
64653	Gal. pair
25180	Gal. pair
3474	Gal. pair
53431	In group
32206	In group
2364	In group
16640	In cluster
	Excluded sources
2387	ULX cand. (sect. 4.5.5)
27303	ULX cand. (sect. 4.5.5)
30539	ULX cand. (sect. 4.5.5)
28024	Gal. pair (with 28027)
15414	Gal. pair
29963	Gal. pair
23630	Grav lens.?
2356	In group
17032	In group

Table 4.1: List of individually discussed/mentioned sources (sect. 4.5)

Ultra-luminous X-ray sources, ULX, (Fabbiano, 1989; Swartz et al., 2004; Kaaret et al., 2017; Fabrika et al., 2021; King et al., 2023) is a kind of an X-ray object which has luminosity over 10^{39} erg s^{-1}(an Eddington luminosity of $10M_{\odot}$ object) and is not (usually) located at the centre of its host galaxy. About 1800 ULX candidates are known so far (Walton et al., 2022). It is suggested that intermediate-mass black holes (IMBH) or super-critically accreting pulsars may be responsible for the phenomena. Even though our search is not a substitute for a systematic ULX survey, the three ULXs found may present a useful sample for the population studies of this kind of object. It is observed that the ULX populations depend on the galaxy morphological type, metallicity, mass and star formation rate (Kovlakas et al., 2020), with dwarfs hosting more ULXs than expected from their SFR (Walton et al., 2011; Plotkin et al., 2014; Kovlakas et al., 2020). Further discussion is much beyond the scope of this chapter. None of our three ULX candidates are found in the catalogue of 1800 ULX candidates of Walton et al..

4.6 Conclusion

We performed a systematic and rigorous search for X-ray signatures of accreting massive black holes in dwarf galaxies from the MPA-JHU catalogue (based on SDSS data). We used the data from the SRG/eROSITA all-sky survey in the Eastern galactic hemisphere. In total, we found 178 matches between the eROSITA source catalogue and low mass galaxies ($M_* < 10^{9.5} M_\odot$) in the MPA-JHU catalogue. We estimate the number of spurious matches as $\sim$ 17 per cent. The initial matches between X-ray sources and dwarf galaxies were conservatively cleaned to achieve high purity of the final catalogue of X-ray active dwarf galaxies, including the removal of quasars and massive galaxies (sect. 4.3.1). As a result, we presented a catalogue of 99 dwarf galaxies with nuclear X-ray activity. Only 14 sources were reported as possible active dwarf candidates in previous studies (sect. 4.4.2).

We performed a detailed analysis of the X-ray properties of objects, including spectral and variability studies (sect. 4.3.2). We estimate the contribution from X-ray binaries and the hot ISM gas to the observed X-ray emission to find that the majority of sources (82/99) are in fact strong candidates for being an AGN in the dwarf galaxy (sect. 4.3.3).

We discussed the host galaxy properties of selected sources (sect. 4.4). Emission line diagnostics proposes that almost all sources are star-forming galaxies, emphasising the importance of X-ray surveys for discovering low-luminosity AGN in low-mass galaxies (sect. 4.4.3). Assuming a relationship between galaxy stellar mass and the mass of the central black hole we estimate that the bulk of sources are accreting at around 1 per cent of the critical accretion rate (sect. 4.4.3).

We estimate the fraction of dwarfs with active nuclei (sect. 4.4.4). We find that the occupation fraction of dwarfs with AGN falls with increasing X-ray luminosity and spans from $\sim 0.01 - 2$ per cent. The AGN fraction increases with host mass, at least for luminosities above 10^{40} erg s^{-1}, from $\sim$ 0.2 per cent to $\sim$ 1 per cent between $8 < \log M_* < 9$ and $9 < \log M_* < 9.5$. We discuss possible selection effects affecting the measured occupation fraction. The measurements of AGN fraction impose a lower limit on the occupation fraction of dwarf galaxies with central black holes.

We present the catalogues with optical and X-ray properties of all 99 X-ray active dwarf galaxies (Appendix C.1, Table C.1). We also present the list of matches which were rejected in the course of the cleaning procedure (Appendix C.2).

We serendipitously discovered several interesting sources. A prominent object is a transient eROSITA source coinciding with a known optical transient. The X-ray spectral shape and variability suggest that this source may be a tidal disruption event hosted by an active dwarf galaxy at $z = 0.048$. This is a novel addition to a few known TDEs in dwarf galaxies selected in X-rays and optical wavelengths.

Another source with a soft X-ray spectrum is fit with thermal emission with a black body temperature of 160 eV. The source spectrum suggests a disc-dominated state of an accreting massive black hole, however, the X-ray spectral fit requires almost an order of magnitude less massive black hole, than inferred from optical spectroscopy.

A few sources with hard spectra are found to be of an obscured nature. One of those is a very luminous and relatively close AGN rivalling the luminosity record holder in dwarf galaxies.

Another obscured source is variable in X-rays on the time scale of 6 months.

We found an array of dwarf galaxies (as well as eROSITA sources from the excluded list of galaxies) which are located in galaxy pairs, groups and clusters. The found projected separations span from $\sim$ 5 to $\sim$ 150 kpc and contain four examples when the X-ray source is visible in both galaxies in a pair. 6 sources are located in compact galaxy groups or clusters of galaxies. In future, a complete eROSITA sample of this kind of object may give important information towards the AGN triggering mechanisms.

We report three ULX (Ultra-luminous X-ray sources) candidates found in three dwarf galaxies. These sources will allow us to better populate the low-mass regime of the vast ULX population and better study the environmental dependencies of the occurrence of this type of object.

This chapter concludes the first part of the thesis. In the next part, we will study accreting neutron stars – X-ray pulsars. The interaction of matter, radiation and magnetic field in these extreme objects can produce a very complicated geometry of accretion flows. We attempt to use reprocessed X-ray radiation to study the geometrical configurations of two X-ray pulsars. The following chapter is devoted to X-ray pulsar V 0332+53.

Part II

Accreting neutron stars

CHAPTER 5

Pulsating iron spectral features in the emission of X-ray pulsar V 0332+53

The contents of this chapter are based on the manuscript originally published in ***Bykov*** *et al. (2021). My contribution to that paper was the data analysis, interpretation and paper writing. All other authors (especially M. Gilfanov and E. Filippova) contributed to the data interpretation and writing and provided me with advice on the data analysis.*

Abstract

We present results of phase- and time-resolved study of iron spectral features in the emission of the Be/X-ray transient pulsar V 0332+53 during its type II outburst in 2004 using archival *RXTE*/PCA data. Coherent pulsations of both fluorescent iron line at ≈ 6.4 keV and neutral iron K-edge at ≈ 7.1 keV have been detected throughout the entire outburst. The pulsating iron K-edge is reported for the first time for this object. Near the peak of the outburst, the 3–12 keV pulse profile shows two deep, $F_{\max}/F_{\min} \sim 2$, and narrow dips of nearly identical shape, separated by exactly $\Delta\phi = 0.5$ in phase. The dip spectra are nearly identical to each other and very similar in shape to the spectra outside the dips. The iron K-edge peaks at the phase intervals corresponding to the dips, although its optical depth $\tau_{\rm K} \sim 0.05$ is by far insufficient to explain the dips. The iron line shows pulsations with a complex pulse profile without any obvious correlation with the total flux or optical depth of the K-edge. Accounting for the component associated with reprocessing of the pulsar emission by the surface of the donor star and circumstellar material, we find a very high pulsation amplitude of the iron line flux, $F_{\max}/F_{\min} \sim 10$. We demonstrate that these properties of V 0332+53 can not be explained by contemporary emission models for accreting X-ray pulsars and speculate about the origin of the observed iron spectral features.

5.1 Introduction

Be/X-ray binaries (BeXRBs) are binary systems harbouring a neutron star and a fast-spinning early-type star with an equatorial circumstellar disc (Reig, 2011). Such objects are known for their transient behaviour in X-rays and show two types of outbursting activity (Reig, 2011). Type I outbursts happen periodically when the neutron star passes a periastron of its eccentric orbit (Okazaki et al., 2002), with the maximum luminosity reaching up to 10^{37}erg s^{-1}. On the other hand, giant (Type II) events are rare, not related to any orbital phase and much brighter than Type I (achieving or even surpassing the Eddington luminosity limit for a neutron star $\sim 10^{38}$ erg s^{-1}). The origin of giant outbursts is not exactly known and is probably related to mass ejection events

from the companion star (Okazaki, Negueruela, 2001). Due to the large range of observed luminosities during type II outbursts, these objects permit exploring the accretion flow's structure around magnetised neutron stars in a broad range of mass accretion rates. Examining the matter distribution close to the neutron star allows for the study of the interaction of matter with high magnetic and radiation fields near the pulsar and the shape of the accretion structures formed as a result of this interaction. Besides, the accretion regimes may change with luminosity, which, in turn, leads to the changes in beaming patterns of the X-ray emission from the accreting neutron star (e.g. Basko, Sunyaev, 1976). Such changes directly affect what an observer sees, hence serving as a probe of the complex physics of magnetised accretion.

In binary systems, some fraction of the primary X-ray emission may be intercepted by the surrounding relatively cold matter which leads to the appearance of the reprocessed emission. This emission, in particular fluorescent iron K_α (2P-1S) line, can serve as a powerful tool to study the spatial distribution and ionisation state of the material around the X-ray sources (Basko et al., 1974; Inoue, 1985; Makishima, 1986; Fabian et al., 1989; George, Fabian, 1991; Gilfanov et al., 1999; Gilfanov, 2010; Tsygankov, Lutovinov, 2010; Giménez-García et al., 2015; Aftab et al., 2019). The energy of this line is $\approx$ 6.4 keV for neutral and low-ionized iron atoms and increases up to $\approx$ 7 keV for H-like iron, whilst the corresponding K-absorption edge energy varies between $\sim$ 7.1 and $\sim$ 9 keV respectively. Iron has a large fluorescent yield ($\sim$30% for low-ionized ions) and its K_α line energy falls in the standard X-ray band, i.e. within the sensitivity range of a plethora of X-ray instruments. The flux, equivalent width (EW) and shape of the iron line depend on the relative location of the X-ray source and the reflecting medium, its area, density, kinematics and ionisation state. For example, significant progress has been made by applying the 'iron line tomography' to the High-Mass X-ray binaries (HMXB) (e.g. Nagase et al., 1992; Day et al., 1993; Giménez-García et al., 2015; Aftab et al., 2019) as well as low mass X-ray binaries (Gilfanov et al., 1999, 2000; Churazov et al., 2001). In HMXB X-ray pulsars, the list of candidates for the fluorescent emission production sites includes all main components of the accretion flow: the accretion column, the accretion stream, the Alfven surface (shell), accretion disc, the stellar wind material, as well as the surface of the massive donor star itself (e.g., Inoue, 1985).

In some HMXB pulsars, the equivalent width of the iron line was shown to vary with the rotational phase of the neutron star. Among others, the pulsating iron line was detected in LMC X-4 (Shtykovsky et al., 2017), Cen X-3 (Day et al., 1993), GX 301-2 (Liu et al., 2018; Zheng et al., 2020), Her X-1 (Choi et al., 1994) and 4U 1538-522 (Hemphill et al., 2014). Interestingly, none of these sources is a BeXRB.

Several models were proposed to explain these variations. It was suggested that variations in the line equivalent width may be caused by the variations in time of the observed columns density of the cold material in the vicinity of the neutron star (e.g. Inoue, 1985; Leahy et al., 1989, and references therein). On the other hand, the pulsating nature of the iron line may indicate that the matter is not distributed symmetrically around the pulsar. In this case, the irradiating flux from the primary varies with the rotation of the pulsar (Inoue, 1985; Day et al., 1993). Shtykovsky et al. (2017) used phase-resolved spectroscopy to study LMC X-4 and concluded that the iron line emission possibly comes from the hot spot on the accretion disc. Studying changes in the emission pattern during the eclipses of the HMXB pulsar Cen X-3 Nagase et al. (1992) found that the 6.4

keV line must be produced fairly close to the neutron star and obtained an upper limit for the distance between the fluorescent matter and the X-ray source of ∼ 1 lt-sec (light second). Later, Kohmura et al. (2001) proposed for this source that the reprocessing site is the accreting matter flowing along the magnetic field lines at the distance of $\approx 1.7 \times 10^8$ cm from the neutron star. Sanjurjo-Ferrín et al. (2021) propose the accretion stream in Cen X-3 as a source of reprocessed neutral iron. Similarly, in GX 301-2 Liu et al. (2018) detected transient pulsations of iron line flux, suggesting that the reprocessing medium might be the accretion stream or the secondary's surface. On the other hand, Zheng et al. (2020) argued that the size of the emission region in this pulsar varies in the range of ∼ 0–40 light seconds, with the average values consistent with the distance from the pulsar to the accretion stream from the secondary star. Endo et al. (2002) found that some fraction of the iron line emission in GX 301-2 originates in the accretion column itself. Recently Yoshida et al. (2017) proposed that the modulation of the iron line intensity may be due to the finite speed of light, and the effect is determined by the size of the reprocessing region.

An important clue for the origin of the iron line may be provided by its evolution during outbursts of transient pulsars. However, the evidence is still incomplete and controversial. In 4U 0115+63, Tsygankov et al. (2007) found that the equivalent width of the iron line decreases with the declining luminosity of the pulsar, which was interpreted as the decrease of the solid angle of the reprocessing material as seen by the primary emission source. For 1A 1118-615, on the contrary, it was shown that the equivalent width of the line was constant during the type II outburst (Nespoli, Reig, 2011).

A promising and so far unexplored venue is the spectroscopy of the iron absorption K-edge. Recently, Yoshida, Kitamoto (2019) proposed the accretion stream from the inner disc onto pulsar (the accretion curtain) as a source of low-ionised fluorescent emission based on the dynamics of iron K-edge absorption in Vela X-1, GX 1+4 and, possibly, in two other pulsars. Their arguments were based on the variations of the K-edge depth as well as the presence of dips in the observed count rate (flux) of the sources related to the eclipse of the emitting region by the accretion column. They suggested that the matter captured by the magnetic field which co-rotates with the neutron star can produce the observed variability in K-edge absorption optical depth. To our knowledge, this is the first and so far the only detection of the variability of the iron absorption edge in accretion-powered X-ray pulsars.

Thus, a wealth of information is provided by the X-ray spectral features associated with iron absorption and fluorescence. This information may help to constrain the geometry of the accretion column, accretion flow and surrounding material and shed further light on the emission mechanisms in accreting X-ray pulsars. In the present chapter, we analyse the behaviour of iron spectral features in Be/X-ray HMXB pulsar V 0332+53 during its type II outburst in 2004.

System V 0332+53

The luminous transient X-ray pulsar V 0332+53 was discovered in 1973 during its bright outburst with a peak intensity of ∼ 1.4 Crab[1] in 3–12 keV energy band (Terrell, Priedhorsky, 1984). The pulsation period of ∼4.4 s and parameters of orbital motion (orbital period of ∼ 34 days and

[1] 1 Crab is approx 2.4×10^{-8} erg s^{-1} cm^{-2}

eccentricity of ∼0.3) were determined later, during the next less prominent outbursts in 1983-1984 (Stella et al., 1985). The optical counterpart was found to be an O8-9Ve star BQ Cam (Honeycutt, Schlegel, 1985). Another outburst of the source was registered in 1989 (Makishima et al., 1990). The significant cyclotron resonance scattering feature (CRSF) at the energy 28.5 keV was detected, which allowed estimating the magnetic field strength to be around $\sim 2.5 \times 10^{12}$ G.

Based on the optical properties of the source the distance to the system was initially estimated to be ∼ 7 kpc (Negueruela et al., 1999). More recently, Rouco Escorial et al. (2019) and Arnason et al. (2021) used Gaia DR2 measurements and derived the distance of $5.1^{+0.9}_{-0.7}$ kpc and $5.1^{+0.8}_{-1.0}$ respectively. We thus note that the majority of initial studies of V 0332+53 adopted the distance of 7 kpc and therefore overestimated the source luminosity by a factor of ∼2, if the true distance to the pulsar is ≈ 5 kpc. In this work, we adopt the Gaia distance of 5.1 kpc.

The next major outburst of V 0332+53 occurred in 2004 and was fully covered by *RXTE* observations. Two CRSF harmonics we detected in the source spectrum, which showed complex evolution in time and with luminosity (see e.g., Kreykenbohm et al., 2005; Tsygankov et al., 2006, 2010; Lutovinov et al., 2015). The observed anti-correlation between the CRSF centroid energy and luminosity during the outburst can be understood either as the changing height of the accretion column (Tsygankov et al., 2006; Mushtukov et al., 2015a), or as a result of reflection of the accretion column emission from the surface of the neutron star (Poutanen et al., 2013; Lutovinov et al., 2015; Mushtukov et al., 2018). The behaviour of the iron line emission was studied succinctly in Tsygankov, Lutovinov (2010). They reported the modulation of iron line flux and equivalent width with the rotation of the pulsar. They also found long-term variability of the equivalent width of the iron line which seemed to correlate with the orbital phase and tentatively interpreted this fact as fluorescence of the material at the surface of the optical companion or its circumstellar disc.

The most recent giant outburst of the source took place in 2015, followed by a mini-outburst in 2016 (Cusumano et al., 2016; Tsygankov et al., 2016; Baum et al., 2017). In Doroshenko et al. (2017); Vybornov et al. (2018) it was found that the above-mentioned anti-correlation between CRSF energy and luminosity breaks at low fluxes, suggesting the change in accretion regimes (from super- to sub-critical, see Basko, Sunyaev, 1976; Mushtukov et al., 2015b). Based on all observational data up to 2015, Doroshenko et al. (2016) obtained the orbital solution of the pulsar which we use in this work (Table 5.1). The evolution of the rotational frequency of V 0332+53 with luminosity proposes that the pulsar is accreting from the disc (Doroshenko et al., 2016; Filippova et al., 2017) and not the wind.

The goal of the present chapter is to utilise the information provided by the spectral features of iron to study the structure of the accretion flow in the vicinity of the neutron star as well as the overall distribution of the circumstellar material in the system V 0332+53. The chapter is based on *RXTE* observations of the type II outburst of the source in 2004. The chapter is structured as follows. The details of *RXTE* data reduction are presented in sect. 5.2. In sect. 5.3.1 we investigate the evolution of the flux and equivalent width of the iron line and of the depth of its K-edge on the time-scales of the outburst. The pulse-phase-resolved modulations of the iron line and K-edge parameters are studied in sect. 5.3.3. In sect. 5.4 we discuss our results and constrain the location of the material responsible for absorption and emission features in the

Table 5.1: Orbital parameters of V 0332+53 (Doroshenko et al., 2016)

Parameter	Value
$P_{\rm orb}$ - orbital period	33.850(1) days
$a\ sin(i)$ - semi-major axis projection on the line of sight	77.81(7) lt s
e - eccentricity	0.3713(8)
ω -longitude of periastron	277.43(5) deg
$T_{\rm PA}$ - periastron time passage	MJD 57157.88(3)

source spectrum. Our conclusions are summarised in sect. 5.5

5.2 Observations and data analysis

During its 2004-2005 type II outburst, V 0332+53 was monitored by *Rossi X-ray Timing Explorer* (*RXTE*) observatory, covering all phases of the outburst. In this work, we use all available *RXTE*/PCA (Proportional Counter Array) spectrometer data between MJD 53336 and MJD 53440, 97 observations in total from proposals 90014, 90089, and 90427.

RXTE/PCA spectrometer (Jahoda et al., 1996) is an array of five proportional counters sensitive in the energy range 3-60 keV. It has a total collecting area of 6400 cm^2 (for all 5 units) and 20% energy resolution at 6 keV (depending on the energy binning of configurations). We reduced *RXTE*/PCA data following the *RXTE* cookbook[2] with the standard FTOOLS/HEASOFT v 6.24 package. Observation-averaged spectra were extracted from the top layer of PCU2 detector (the best calibrated one) in Standard2 data mode, the additional systematic error of 0.25% was added on all channels due to uncertainties in the telescope's response (García et al., 2014). All spectra were fit with XSPEC package (Arnaud, 1996) using χ^2 statistics.

There were 72 observations that had data configuration appropriate for phase-resolved spectroscopy in the energy range 3–12 keV (E_125us_64M_0_1s, B_16ms_{46M_0_49_H; 64M_0_249}. The time of arrival of photons was corrected to solar system barycentre, and the Doppler shift due to orbital motion of a pulsar in the binary was corrected for using orbital parameters from Doroshenko et al. (2016) (see Table 5.1). In the phase-resolved analysis, photons were folded into 16, 12 or 8 phase bins using FASEBIN FTOOLS/HEASOFT task. In the last four observations (90014-01-08-(00-03)), pulsations were not detected, and correspondingly no phase-resolved analysis was performed.

All but three observations during the rising part of the outburst (up to MJD 53360) had E_125us_64M_0_1s configuration (the remaining three were in B_16ms_64M_0_249 data mode). Between MJD 56383 and 53403 (the declining part of the outburst) the data suitable for phase-resolved spectroscopy had B_16ms_46M_0_49_H configuration, and after MJD 53403 it had E_125us_64M_0_1s data mode again. Unfortunately, the E_125us_64M_0_1s configuration in PCU2 has a corrupt channel 10 covering $\sim$ 6.14–6.54 keV energy range, which registers no photons. As these energies are of primary interest for our study we had to exclude observations made

[2] https://heasarc.gsfc.nasa.gov/docs/xte/recipes/cook_book.html

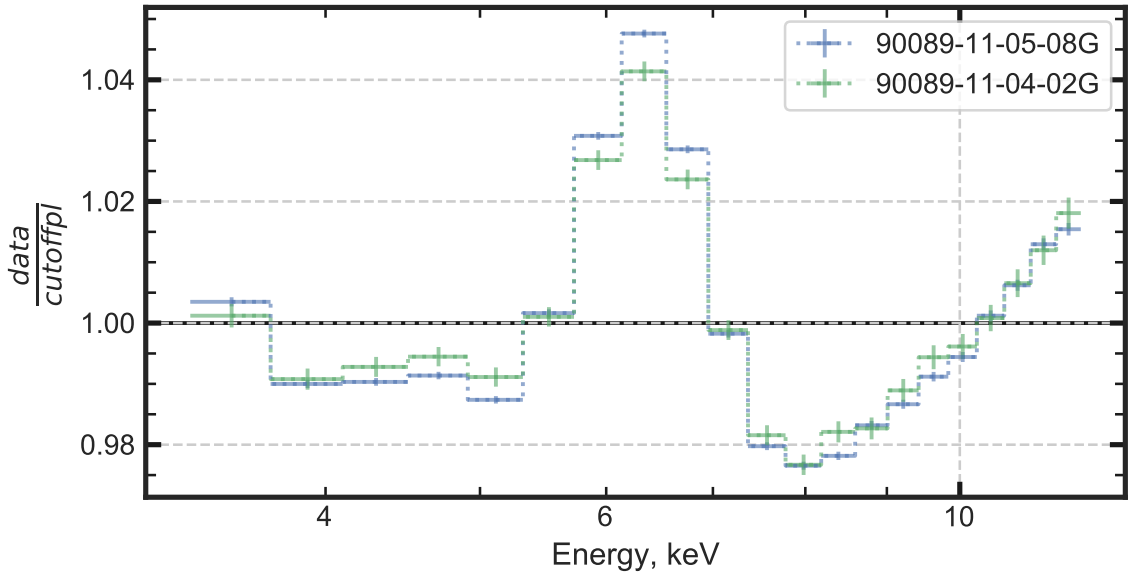

Figure 5.1: The ratio of data to exponentially cutoff power-law in the time-averaged spectra of two observations (90089-11-05-08G, MJD 53365.3 and 90427-01-03-00, MJD 53384.4).

in this configuration from phase-resolved spectroscopy of the iron line. In phase-resolved spectra, a systematic error of 0.4% was added to all channels. The systematic error differs from the one used in Standard2 mode because the data from all three layers of active PCUs were gathered into one event file in these configurations (B_16ms_46M_0_49_H and B_16ms_64M_0_249).

Observations with similar pulse profiles and the same configuration/detectors were combined using FBADD task, and their phase-resolved spectra were combined with ADDSPEC script (see sect. 5.3.3 for details about groups).

All that leaves us with 30 observations and 8 groups where we performed phase-resolved spectroscopy.

5.3 Results

5.3.1 Light curve and long-term spectral evolution

Tsygankov, Lutovinov (2010) reported the presence of a strong iron emission line (EW$\sim 60-100$ eV) in the spectra of V 0332+53. To corroborate this result we plot the ratio of the source spectra obtained in two observations around MJD 53365.3 and 53384.4 to the best-fitting model of a power-law with exponential cutoff (Fig. 5.1). The plot reveals a strong emission feature at ~ 6.4 keV as well as a depression in the spectrum near ~ 7 keV which resembles the behaviour observed in black hole X-ray binaries (e.g. Gilfanov et al., 1999). Similar to the latter, these features can be associated with the fluorescent K-α line and absorption K-edge of low-ionized iron and, possibly, the lower energy part of the Compton reflection bump.

To quantitatively describe iron spectral features we use a model consisting of a power-law with exponential decay (CUTOFFPL in XSPEC package), a Gaussian emission line (GAUSS) and the absorption edge (EDGE), XSPEC formula EDGE*(CUTOFFPL+GAUSS). The line centroid and the energy of the edge were fixed at 6.4 keV and 7.112 keV, respectively. The broadband spectral shape of V 0332+53 is rather complex and to facilitate the description of the continuum with a simple model with a minimal number of free parameters, we decided to limit the energy range for spectral analysis to 3–12 keV.

Making the line centroid energy a free parameter of the fit (model CUTOFFPL+GAUSS), its best-fitting values varied in the $\approx$ 6.35–6.45 keV range. From our experience, this is within the accuracy of the PCA instrument in measuring the centroid energy for the iron line. On the other hand, by fixing the line energy at 6.4 keV and making the energy of the edge a free parameter of the model, we obtained the edge energy consistent with the value of 7.1 keV in all observations. This justifies our choice to freeze these parameters at values expected for the neutral iron.

In HMXBs, emission lines of Fe XXV and Fe XXVI are often observed (Aftab et al., 2019), which can not be resolved at the PCA energy resolution. Unfortunately, no useful CCD data is available for this outburst of V 0332+53. An XMM-Newton observation during the 2015 outburst is quite heavily piled up. However, the consistently good agreement of the line centroid and position of the K-edge with the values expected for neutral iron in all analysed PCA data suggests that the contribution of heavily ionized iron is not significant in this source.

Equivalent hydrogen column density in this source was measured to be of the order of $N_{\rm H} \approx 10^{22}$ cm^{-2} (Tsygankov et al., 2016; Doroshenko et al., 2017). Fixing $N_{\rm H}$ at this value in the spectral fitting lead to poor fit quality with significant deviations at lower energies. Making $N_{\rm H}$ a free parameter of the fit results in the best-fitting values in the $\sim$ (0.2–0.5) $\times 10^{22}$ cm^{-2} range with some variations throughout the outburst. Although some local absorption by circumbinary material is, in principle, possible in a binary system like V 0332+53, insufficient low energy coverage of PCA instrument and systematic uncertainties in its energy response at the low energy end do not permit us to make any reliable statement about the value and time evolution of $N_{\rm H}$. Therefore we chose to exclude interstellar absorption from the spectral model. This does not affect the best-fitting parameters of the continuum model in any significant way. However, absorbing column with $N_{\rm H} \sim 10^{22}$ cm^{-2} and cosmic abundance of iron should produce the iron K-edge with the optical depth of $\sim$ 0.007–0.015, with the exact value depending on the cross-section models and assumed abundance on iron along the line of sight in the direction toward V 0332+53. This value is comparable, within a factor of $\sim$ 2–3, with the measured value of the K-edge depth. However, we clearly see variations of the iron K-edge depth, long-term, throughout the outburst, and short-term, on the time-scales corresponding to the rotation period of the neutron star (Section 5.3.3). This leaves no doubts that most of iron K-edge absorption observed in the spectrum of the V 0332+53 originates in the source itself and not in the interstellar medium (ISM).

In our fits, the spectral width of the line was poorly constrained but had a value typically $\sim$ 0.3 $\pm$ 0.1 keV. Therefore we fixed the width at 0.3 keV, a value similar to the results of Caballero-García et al. (2016); Baum et al. (2017). With applied systematic errors (sect. 5.2) majority of spectra have an acceptable reduced chi-square value (the mean value of $\approx$ 1.1 for 16 dof) However, a few spectra have large values of the reduced chi-square, sometimes exceeding $\sim$ 2. Inspection of these spectra showed that large residuals are observed at the energies below

$\lesssim$ 5 keV. The deviations of data from the model have positive as well as negative signs and can not be universally fixed varying the low energy absorption. Based on our experience of working with PCA data we believe that, most likely, they are related to some calibration uncertainties of the PCA instrument.

Throughout this chapter, all confidence intervals for spectral parameters are calculated for 68% (1σ) confidence level (cl), and upper limits are 90% cl. Table D.1 presents the observation log, configuration and grouping used in phase-resolved spectroscopy, and results of the observation-averaged spectral analysis – reduced chi-square value for the model described above, the 3–12 keV model flux and the value of the equivalent width of the iron line, as well as its intensity.

Fig. 5.2, panel A shows the evolution of the 3–12 keV flux and the iron line flux during the outburst. The outburst started approximately on MJD 53340 (2004 December 1), achieved its peak flux of 3.5×10^{-8} erg s^{-1} cm^{-2} about 20 days later and then started its gradual decline followed by a fairly sharp drop at the end of the outburst around MJD 53430, after which observations of the source were finished. At the end of the outburst, the iron line flux declined faster than the continuum flux, and the line was undetectable in the last six observations.

In Fig. 5.2, panel B the variation of the equivalent width of the iron line with time during the outburst is shown. At the beginning of the outburst, the equivalent width had a value of $\sim$ 65 eV and started to grow until it reached $\sim$ 90 eV at the peak of the outburst. After that, the value of the equivalent width declined to $\sim$ 70 eV until it grew again up to $\sim$ 80 eV in $\sim$ 10 days. At the end of the outburst, the value returned to the initial value of ~50–60 eV. There is a 'cut-off' at the end of the outburst, where the equivalent width drops (EW$<$ 60 eV) in a matter of $\sim$ 5 days. As the equivalent width of the line depends on its assumed spectral width (in our case fixed at 0.3 keV), we also obtained spectral fits for smaller (0.2 keV) and larger (0.4 keV) line widths. We found, as expected, that although this changes slightly the absolute value of the line EW, the overall shape of the EW curve is not affected by the moderate changes in the line width.

In Fig. 5.2, panel B one can see a hint of periodic variations of the line EW with the period of $\approx$ 30 days, consistent with the orbital period of the binary system. This behaviour was earlier reported by Tsygankov, Lutovinov (2010). It could be related to the orbital motion of the system if, for instance, the reprocessing matter was located near the optical companion of the pulsar. In Fig. 5.2, panel B we plot by the dashed line the line-of-sight projected distance from the neutron star to the centre of the companion star. As one can see, the peaks of the line EW roughly coincide with the moments in time when the distance to the companion star is minimal. This suggests that some fraction of the iron line originates on the surface of the donor star or in the material located near it. This will be further discussed in Section 5.4.

We report for the first time variability of the depth of the iron K-edge with time (Fig. 5.2, panel C). At the beginning of the outburst, the iron K-edge was not detected in individual observations with the 90% upper limits typically in the $\sim$ (0.5–1) $\times 10^{-2}$ range. Around the peak of the outburst, the K-edge optical depth was approximately constant at the level of $\approx 0.015 - 0.02$, and started to decline after MJD 53380 becoming undetectable again after MJD 53390 with the upper limit of $\sim (0.5 - 1) \times 10^{-2}$. However, after $\sim$ MJD 53420, approximately after apastron passage, the optical depth of the K-edge increased significantly within about five days to $\sim 10 \times 10^{-2}$ level and then appeared to drop again, although the upper limits are not constraining to fully characterise its behaviour. Interestingly, the iron line was not detected when the K-edge was the

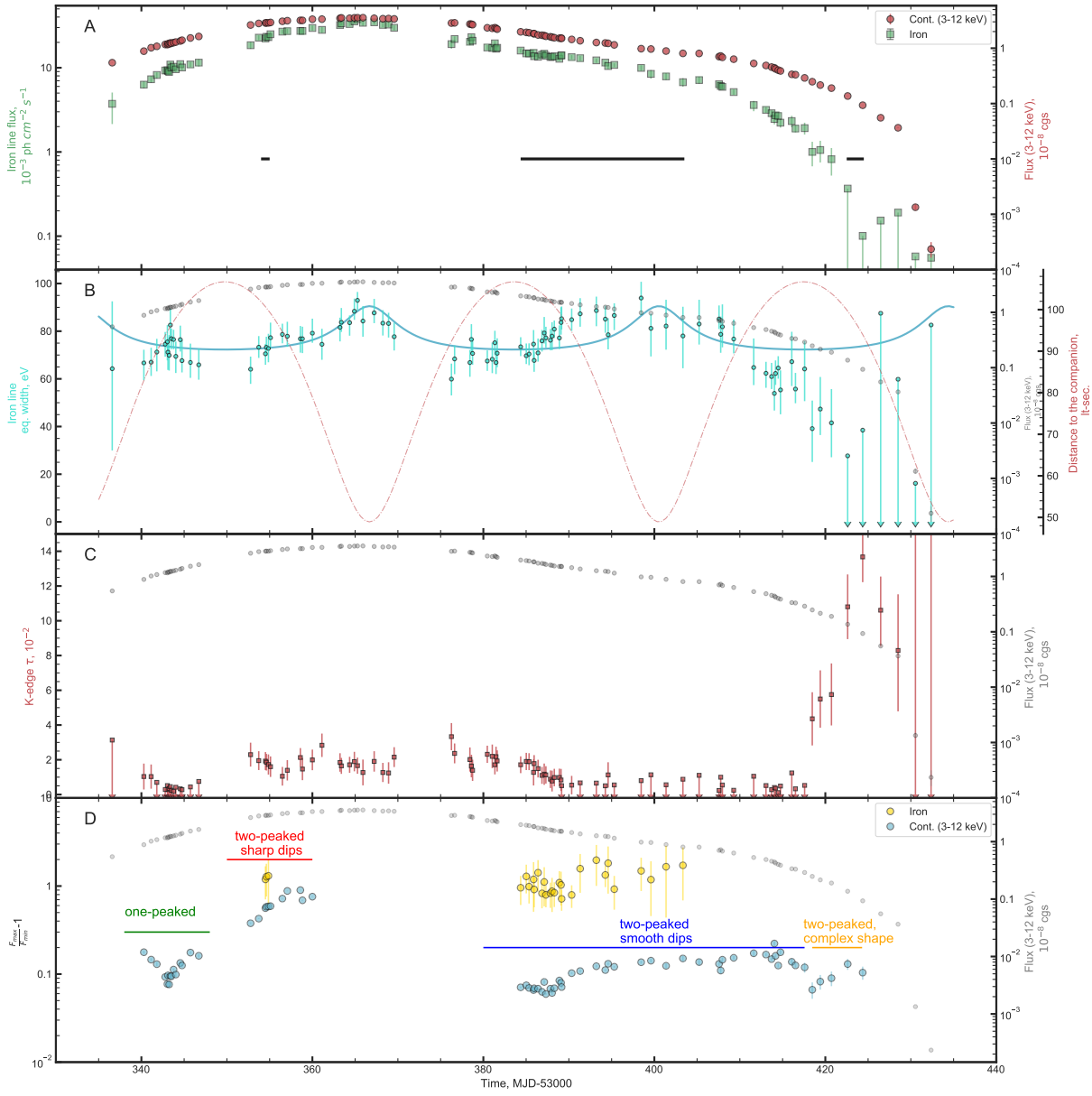

Figure 5.2: **Panel A**: The light curve of V 0332+53 in 2004-2005 outburst. The 3–12 keV flux in units of 10^{-8} erg s^{-1} cm^{-2} is shown as red circles, while the flux of the iron K_α line in units of 10^{-3} phot cm^{-2} s^{-1} is presented by green squares. Horizontal black solid lines indicate the observations during which phase-resolved spectroscopy was carried out. **Panel B**: The evolution with time of the equivalent width of the iron K_α line (cyan circles). The line-of-sight projected distance between the pulsar and the optical companion is plotted with a red dashed-dotted line. The solid cyan line shows the approximation of EW data with the model described by eq. 5.4, see sect. 5.4 for discussion. **Panel C**: Optical depth of the iron K-edge (red squares). **Panel D**: Morphology of pulse profiles in the 3–12 keV energy band. Cyan dots demonstrate the quantity $R = (F_{max} - F_{min})/F_{min}$ for the 3–12 keV pulse profile, and yellow dots show the same but for iron line flux (see sect. 5.3.3). Horizontal lines with the text present an approximate classification of pulse profiles into morphological types (see the description in sect. 5.3.2). For reference, the 3–12 keV flux in units 10^{-8} erg s^{-1} cm^{-2} is shown by grey circles in panels B,C,D.

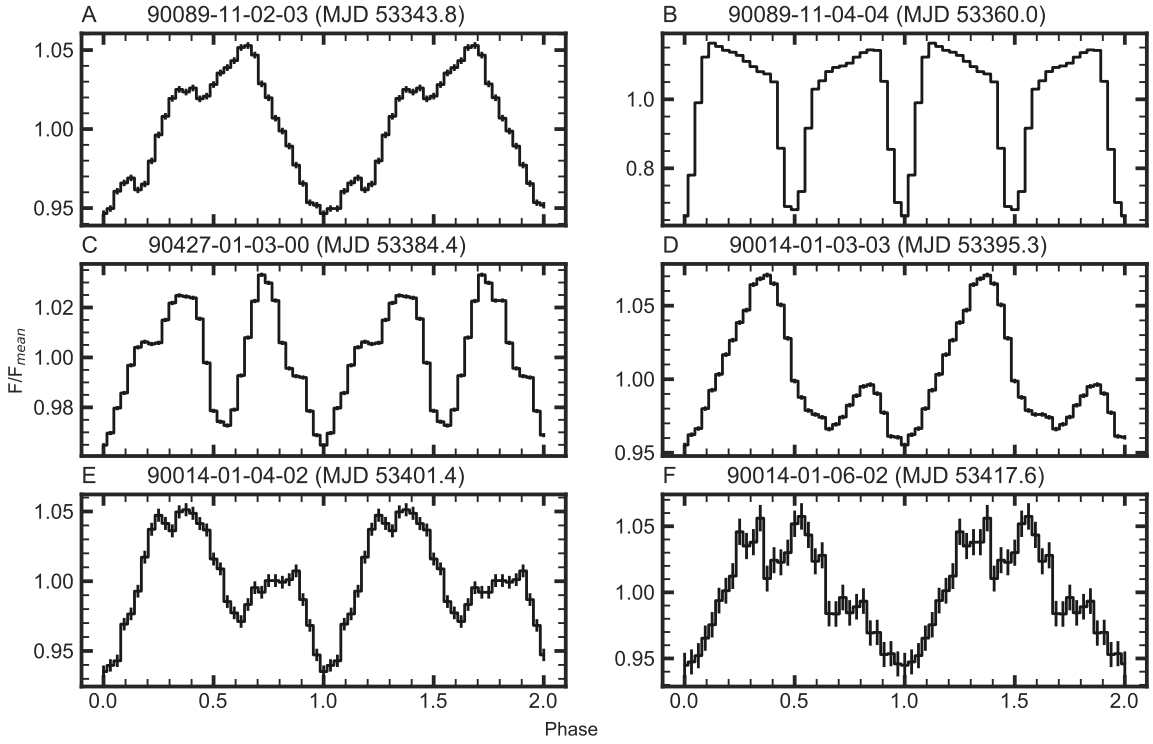

Figure 5.3: Pulse profiles in the 3–12 keV energy range at different stages of the outburst. Panel A shows a single-peaked pulse profile at the beginning of the outburst. The pulse profile shown in panel B was obtained near the peak and displays two strong and narrow dips. Panels C, D and E show the subsequent evolution of the pulse profile during the declining phase of the outburst. Finally, in panel F, near the end of the outburst, the pulse profile had a complex shape, seemingly double-peaked. The individual pulse profiles are not synchronised in phase, but shifted to have the main minimum at phase 0.

deepest. We note that the K-edge depth expected from the interstellar absorption appears to be somewhat higher than the upper limits shown in Fig.5.2, panel C. This disagreement may be a result of calibration uncertainties of *RXTE*/PCA or related to deviations of the iron abundance from the adopted value, as discussed earlier in this section.

5.3.2 Evolution of the pulse profile

For each observation with sufficient time resolution (configurations B_16ms_64M_0_249, B_16ms_46M_0_49
E_125us_64M_0_1s) we measured the pulsation period and obtained binary-motion corrected pulse profiles of counts rate in 3–12 keV energy band [3].

[3]All pulse profiles, phase-resolved spectra best-fitting parameters (including photon index, cutoff energy and reduced chi-square value) can be found at `https://github.com/SergeiDBykov/v0332p53_materials` as well

In the description below we use luminosities measured in the broad energy range 3-100 keV in Tsygankov et al. (2010); Lutovinov et al. (2015), but assuming 5 kpc distance.

The evolution of the shape of the pulse profile followed the pattern typical for transient accreting X-ray pulsars, with complex evolution of pulse profiles in time as described below. Such behaviour has been reported in several pulsars (Tsygankov et al., 2010; Koliopanos, Gilfanov, 2016; Tsygankov et al., 2018; Wilson-Hodge et al., 2018; Lutovinov et al., 2021) and predicted theoretically as a result of the switch of the emission diagram from a pencil beam to fan-shaped beam due to the changes in accretion regime (Gnedin, Sunyaev, 1973; Basko, Sunyaev, 1976; Mushtukov et al., 2015b), although the detailed picture is still debated (e.g. Mushtukov et al., 2018).

At the beginning of the outburst (MJD 53340-50), single-peaked 3–12 keV pulse profiles were observed in virtually every observation. A representative pulse profile of this type is shown in Fig. 5.3, panel A. The pulse profile in this energy range had one broad and somewhat asymmetric peak followed by a similarly broad smooth minimum, the pulsed fraction[4] was $\sim 5\%$. In Tsygankov et al. (2010) it was shown that the pulse profiles in V 0332+53 depend on the energy range, and in harder channels may become double-peaked (e.g. 8–14 keV profile at the rising phase of the outburst is double-peaked). The pulse profile also changes dramatically near the cyclotron line energy (Tsygankov et al., 2010, fig. 6). These aspects of V 0332+53 have been the subject of detailed studies previously (Tsygankov et al., 2006, 2010) and not repeated here.

The transition to the double-peaked profile occurred during the data gap between MJD 53345-53350 at the luminosity level of $\sim 10^{38}$ erg s^{-1}. Near the maximum of outburst, at MJD 53350 – 53360, double-peaked profiles had two strong narrow dips and flat maxima, with the pulsed fraction of nearly $\sim 30\%$, separated in phase by $\Delta\phi \approx 0.5$ (Fig. 5.3, panel B). Interestingly, in two observations 90089-11-04-(03,04) (MJD 53358.8 and 53360.0) pulse profiles had the two dips with the same depth which may suggest some saturation or a full eclipse of the accretion column and the neutron star (see discussion in Section 5.4). The peaks were also fairly equal in flux. Later in the outburst, after the timing data gap in MJD 53360–53385, the breadth of the dips increased and the symmetry between the two peaks (and dips) disappeared (Fig. 5.3, panels C, D, E). The pulsed fraction returned to the initial $\sim 5\%$. The shape of the pulse profile evolved in a complicated manner with its complexity increasing (e.g. Fig. 5.3, panel F) towards the end of the outburst, until luminosities as small as $\sim 1/30$ of the peak luminosity. As we did not detect the transition from the double-peaked pulse profile to the singe-peaked one at the end of the outburst, we can conclude that the singe->double-peaked pulse profile transitions happen at very different luminosities in the beginning and the end of the outburst (hysteresis behaviour).

We summarise the main features of the pulse profile evolution in Fig. 5.2, panel D where show the behaviour of the modulation amplitude $R = F_{\max}/F_{\min} - 1$ and describe the morphology of the pulse profile at different stages of the outburst.

as in the online materials on MNRAS website.

[4]pulsed fraction, PF, defined as $PF = \frac{F_{\max} - F_{\min}}{F_{\max} + F_{\min}}$ where $F_{\max/\min}$ is the maximum/minimum value of flux found in a pulse profile.

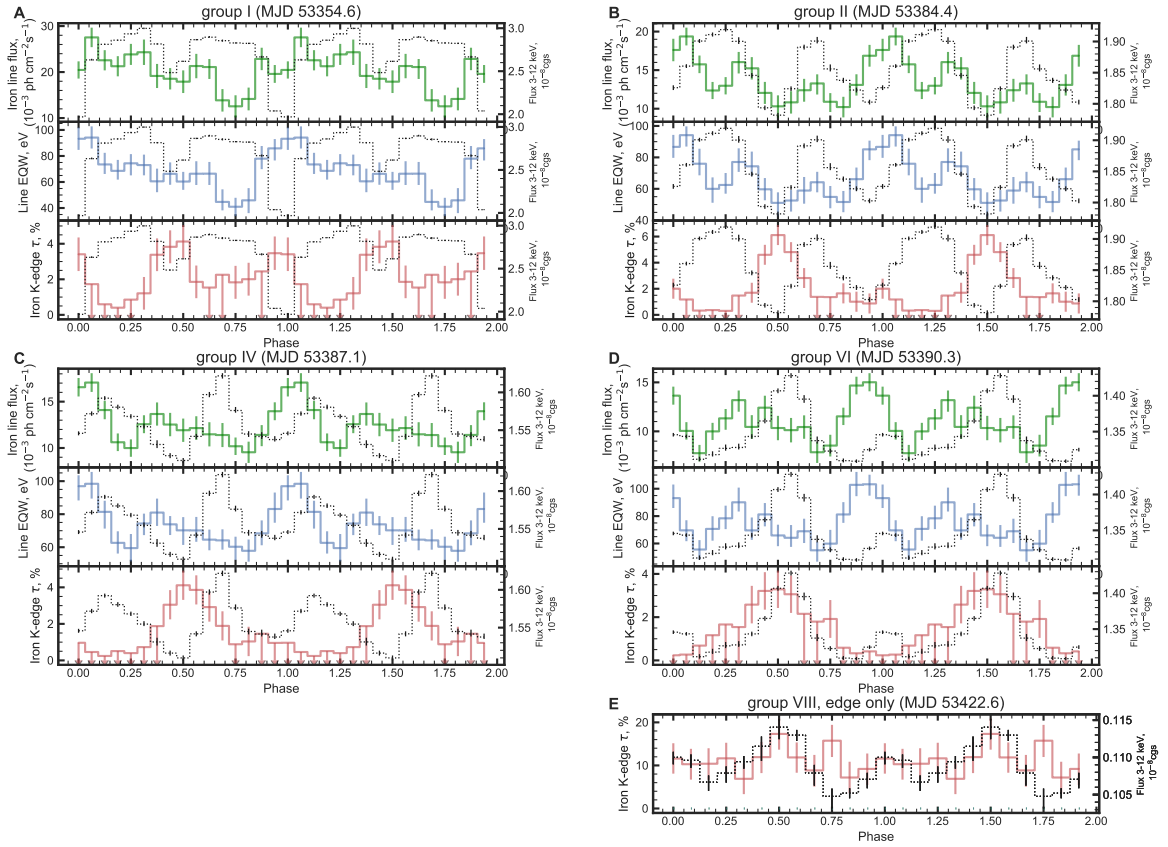

Figure 5.4: Pulse phase dependence of parameters of the phase-resolved spectra for different groups of observations. See Table D.1 for the definition of data groups. On each panel (A, B, C, D) we plot the pulse profile of the flux (3–12 keV) with a dotted black histogram on each sub-panel, the flux of the iron line (green histograms, top sub-panel) and its equivalent width (blue histograms, lower sub-panel), and the optical depth of the iron K-edge as a function of phase (red histograms, bottom sub-panel). **Panel A** shows the group I, the near-maximum part of the outburst (MJD 53350-60). **Panel B, C, D** show groups II, IV and VI from the declining part of the outburst (MJD >53380). In **Panel E** we show the pulse profile of the total flux and K-edge depth for the group VIII, where no iron line was detected in the spectra. All profiles were shifted along the x-axis so that the maximum K-edge optical depth is at phase 0.5.

5.3.3 Phase-resolved Spectroscopy

Only 28 PCA observations were performed in data modes having sufficient time resolution and number of energy channels to permit pulse-phase-resolved spectroscopy of the iron line. In Fig. 5.2, panel A the time intervals covered by these observations are marked by two left-most black horizontal lines. As one can see, no phase-resolved spectroscopy is possible at the peak of the outburst.

The data were divided into seven groups of observations with similar pulse profiles and the same configuration/detectors. The groups cover different parts of the outburst and show different behaviour of the pulse profile and parameters of the phase-resolved spectra (see Table D.1 and Fig. 5.4). The spectrum in each phase bin was fitted in the 3–12 keV band with the model EDGE*(CUTOFFPL+GAUSS) in XSPEC. As suggested by the results of the spectral analysis of average spectra, we fixed the line energy and width at values of 6.4 keV and 0.3 keV respectively, and the edge energy at 7.1 keV (sect. 5.3.1). It should be noted that, unlike fluorescent line energy, the energy of the K-edge depends notably on the ionisation state even for weakly ionised iron (for example increasing from 7.1 keV for Fe I to 7.6 keV for Fe V), however, the higher edge energies seem to be excluded by the results of analysis of average spectra presented in Section 5.3.1.

Results of phase-resolved spectroscopy are shown in Fig. 5.4 where we present variations of parameters of interest with the pulse phase. In particular, we follow a total 3–12 keV flux, shown in each panel by the dashed histogram, flux and equivalent width of the 6.4 keV iron line and the optical depth of the iron K-edge (shown by solid histograms in the top, middle and bottom sub-panels respectively).

One of the most interesting findings of this work is the detection of the variable iron line K-edge whose optical depth varies with the pulse phase. It reveals itself most graphically in data group I. This data group is the closest to the peak of the pulsar light curve in our sample, having the largest luminosity ($\sim 1.7 \times 10^{38}$ erg s^{-1}) among the data sets suitable for phase-resolved spectroscopy. The pulse profile on this date (around MJD 53354.6) shows two rather narrow dips of large (and unequal) amplitude separated by ≈ 0.5 in the pulse phase. In the deeper one of the two, observed flux from the pulsar drops by a factor of ~ 1.5. Comparing with the collection of pulse profiles shown in Fig. 5.3 one may conclude that with further increase of the luminosity, about 5 days later, on MJD 53360, the dips became more narrow and equalised in depth. The luminosity at that time was $\sim 15\%$ larger than in group I. Notably, the dips in the pulse profile appear to be accompanied by the peaks in the iron K-edge (Fig. 5.4, panel A), suggesting that they may be caused by obscuration of the neutron star by, for example, the accretion flow from the inner disc. This possibility is discussed in detail in the next section.

Unfortunately, data around the maximum of the light curve were taken in instrument configurations without 3–12 keV energy coverage. The next (in time) data set suitable for phase-resolved spectroscopy (group II, Fig. 5.4, panel B) was taken a month later, on MJD 53384, when the luminosity was by a factor of ~ 1.6 lower than at the maximum of the light curve and by a factor of ~ 1.5 lower than in the previous data group discussed above (group I). However, it still shows a clear peak in the K-edge depth profile coinciding with one of the two dips in the total flux pulse profile. This trend continues in the following observations, data groups III, IV and V, albeit peaks and dips become broader and progressively more smeared. However, in the last

data set (MJD 53390.3, group VI, Fig. 5.4, panel D) taken near the end of the outburst at the luminosity level of $\sim 0.09 \times 10^{38}$ erg s^{-1}, the pattern changes dramatically and the peaks of the K-edge absorption depth now coincide with the peaks of the total flux. Interestingly, at this point, the K-edge becomes undetectable in the average spectrum.

The iron line flux shows large variations with the pulsed fraction in the $\sim 30\%$ range without evident trends in time and luminosity, see Fig. 5.4. The pulse-profile shape of the line flux has a rather complex shape with several minima and maxima and with less obvious relation to the modulation of the total flux. The equivalent width generally follows the iron line flux because the variability of the line is much larger than the variability of continuum emission, with a typical value of EW of $\sim 50 - 100$ eV. A remarkable property of the iron line spectral features is the lack of correlation between the iron line flux and the depth of its K-edge. This behaviour has important implications on the geometry of the neutral material producing these features which are discussed in sect. 5.4.

After MJD 53420, pulsations were detected only in two observations (90014-01-07-04 and 90014-01-07-00). For phase-resolved spectroscopy, we grouped these two observations into data group VIII. As the iron line was not detected in these data at all, we used the spectral model CUTOFFPL*EDGE which permitted us to carry out phase-resolved spectroscopy despite the missing channel at the energy 6.4 keV in the PCA instrument configuration E_125us_64M_0_1s used in these observations.

We did not detect pulsations of the K-edge optical depth (Fig. 5.4, panel E) in these data. One can see that the behaviour of the K-edge depth pulse profile differs drastically from that observed in previous data groups. In particular, the null hypothesis of the constant depth has a fully acceptable χ^2 value of 7.8 for 11 dof. Assuming a sinusoidal pulse profile with the mean value equal to the K-edge optical depth $\tau_{\rm K}$ measured in the average spectrum in these observations ($\approx 10\%$) we obtained the 90% confidence upper limit on the amplitude of $\tau_{\rm K}$ variations of $\approx 60\%$ of the mean value. Due to the rather limited statistical quality of these data, the upper limit does not seem to be very constraining. However, $\tau_{\rm K}$ pulsations with a pulse profile similar to those observed in data group II or IV can be excluded with high confidence. Indeed, assuming the pulse profile as in panel B in Fig. 5.4 and re-scaling it to give the observed value of the mean K-edge optical depth in group VIII, we obtain the $\chi^2 = 113$ (11 dof) for the null hypothesis of constant $\tau_{\rm K}$.

5.4 Discussion

5.4.1 Summary of observational picture

The findings of this work can be summarised as follows:

1. The 3–12 keV pulse profile evolves throughout the outburst from a single-peaked shape at low luminosity to a double-peaked one at high luminosity. The reverse transition was not observed at low luminosities at the end of the outburst. This behaviour is similar to other accreting transient X-ray pulsars in Be/X systems (Tsygankov et al., 2007; Epili et al., 2017; Wilson-Hodge et al., 2018), its features specific for V 0332+53 have been already

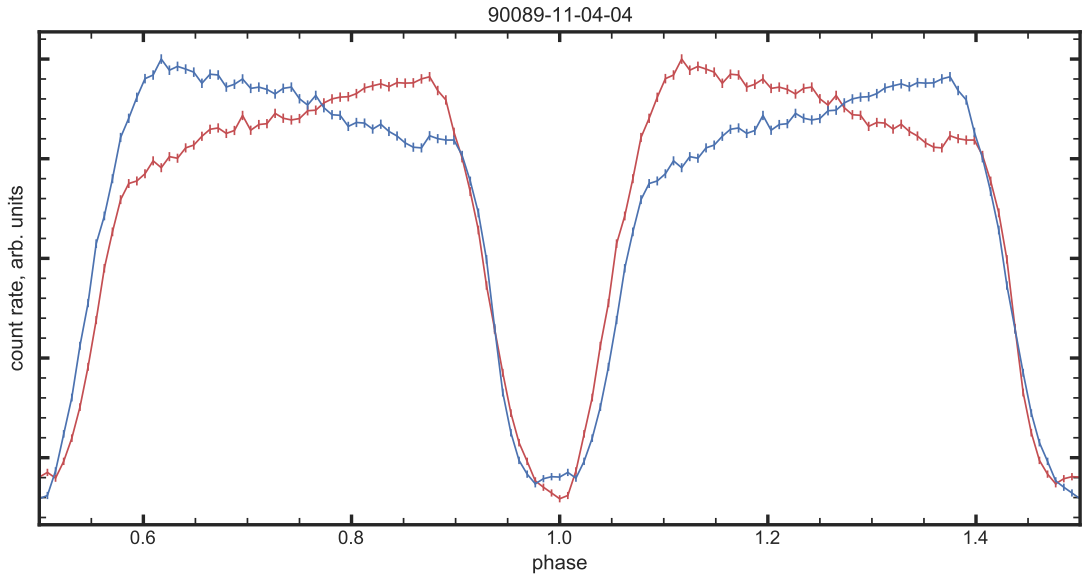

Figure 5.5: Count rate pulse profile in the 3–12 keV range for observation 90089-11-04-04 having maximum luminosity in our data (for which such a profile could be constructed) plotted in 128 phase bins (temporal resolution $\sim$ 0.035 sec). The units along the y-axis are arbitrary. The blue line is the pulse profile, and the red line is the same profile shifted by 0.5 in phase. This plot is intended to demonstrate the striking similarity between the shape and depth of the two dips and the fact that they are separated by nearly exactly $\Delta\phi = 0.5$ in phase.

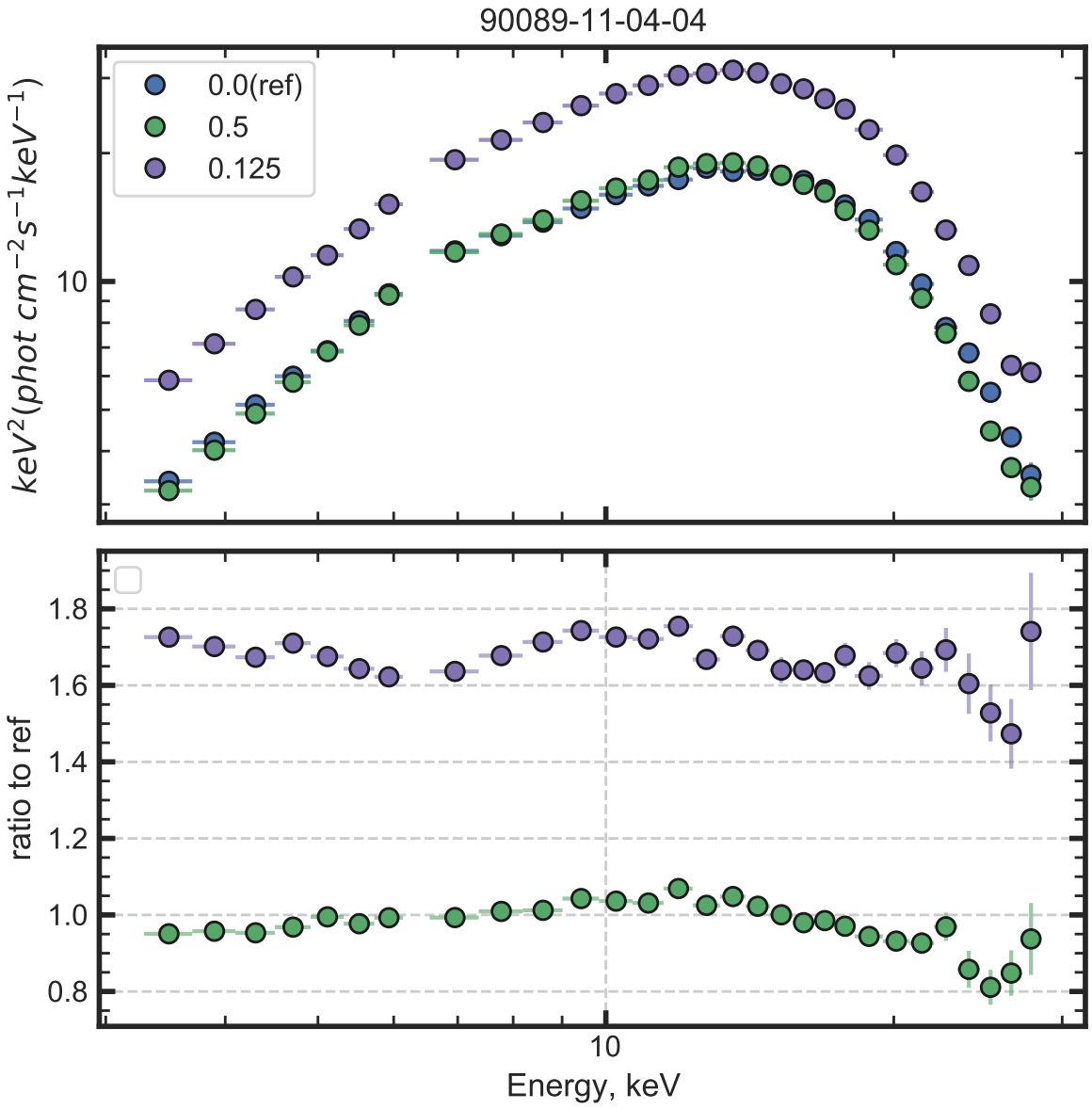

Figure 5.6: Top panel: Unfolded (with CUTOFFPL model) spectra of three phase bins of the pulse profile shown in panel B in Fig. 5.3 and in Fig. 5.5, observation 90089-11-04-04. The chosen phase bins (specified in the legend) correspond to the bottom of the two dips (blue and green circles, phase bins 0/16 and 8/16) and the peak of the pulse profile (magenta circles, phase bin 2/16). Bottom panel: the ratio to the phase 0 spectrum. The data gap at $\sim$ 6.5 keV is due to configuration.

extensively discussed elsewhere, including its behaviour at higher energies (Tsygankov et al., 2006).

2. Outside the peak of the outburst, the pulse profiles in the 3–12 keV band show a moderate modulation at the level of $R = (F_{\max} - F_{\min})/F_{\min} \sim 0.1$–$0.2$. Near the peak of the outburst, the modulation reaches an amplitude of $R \sim 1$ (Fig. 5.2, panel D). Qualitatively, this highly modulated pulse profile can be interpreted as the single peak profile similar to the one observed in the rising part of the light curve (panel A in Fig. 5.3), superimposed on which are two deep and narrow "absorption" features separated by 0.5 in pulse phase. In the declining part of the outburst, the pulse profiles have low modulation ~ 0.1 and a double-peaked shape. Pulse profiles evolve in a complex manner after, possibly having a two-peaked shape until the end of the outburst.

3. The fluorescent iron line at the energy consistent with neutral or weakly ionised iron is detected throughout most of the outburst. On the long time scale, its equivalent width shows possible modulation with the orbital period of the binary (as was noted earlier in Tsygankov, Lutovinov, 2010), varying between $\approx 70 - 90$ eV. Notably, there is a clear cut-off at the end of the outburst, where the equivalent width drops down to $\lesssim 60$ eV on the time-scale of about $\lesssim 5 - 10$ days.

4. The iron line flux pulsates with the rotational period of the pulsar, varying with the amplitude of $R \sim 1$, much larger than oscillations of the total flux. The pulsation amplitude of the iron line flux remains constant through the outburst, where phase-resolved spectroscopy was possible.

5. We detected iron K-edge at the energy 7.1 keV with an optical depth significantly larger than expected from ISM absorption. Its optical depth varies with the pulse phase in a manner approximately anti-correlated with the total flux and also evolves through the outburst. Its long-term variation and presence of pulsations prove that it is mostly caused by the material near the neutron star itself. The presence of pulsating iron K-edge in V 0332+53 was not reported before.

5.4.2 Dips in the pulse profile

The striking feature of the pulse profile at the peak of the outburst is the presence of two nearly identical dips separated in phase by exactly 0.5 (panel B in Fig. 5.3 and Fig. 5.5). The source spectrum in the dips is (i) nearly identical to the spectrum outside the dips and (ii) the spectra in the two dips are nearly identical to each other in shape and normalisation (Fig. 5.5 and 5.6). These properties and the narrowness of the dips suggest that they could be caused by shadowing of the (part of) emission region by some scattering (i.e. ionised) material of moderate optical thickness. They can also arise due to shadowing of the part of the emission region by an opaque material. However, the similarity of dip and off-dip spectra and, in particular, the lack of any strong absorption features in the dip spectra, suggest that the dips can not be produced by neutral or weakly ionised absorbing material of moderate thickness. Similar pulse profiles with very sharp,

luminosity-dependent dip-like features were observed earlier in several accreting X-ray pulsars such as GRO J1008-57 (Naik et al., 2011), EXO 2030+375 (Epili et al., 2017), A0535+262 (Naik et al., 2008; Jaisawal et al., 2021), GX 304-1 (Jaisawal et al., 2016), 2S 1417-624 (Gupta et al., 2018), 4U 1909+07 (Jaisawal et al., 2020) and generally associated with the additional absorption of radiation by matter.

The primary candidate for the obscuring material could be the flow of matter from the inner part of the disc to the pulsar's surface (which is also called the accretion curtain, or accretion channel). Indeed, from the continuity equation one can estimate the electron density n_e in the accretion curtain at radius r as

$$n_{\rm e}(r) = \frac{\dot{M}/2}{v(r)S(r)\mu m_{\rm p}} \tag{5.1}$$

where $\dot{M}/2$ is the accretion rate through one accretion column assuming that there are two opposing streams as expected for the dipole configuration of the magnetic field, $v(r)$ is the velocity of the accreting matter (in the accretion channel it should be close to the free-fall velocity, $v(r) \approx v_{\rm ff}(r) = \sqrt{2GM_{\rm NS}/r}$), $S(r)$ is the area of the flow, μ is the mean molecular weight, n_e is the electron number density and m_p is the proton mass. Expressing the distance from the neutron star to the part of the accretion flow causing obscuration as a fraction of the Alfven radius $r = ar_M$, one can estimate the area of the stream there as $S(r) = 2\pi f d a r_{\rm M}$, where $2\pi f$ is the azimuthal angular size (in radians) of the accretion curtain, $d << r$ is the thickness of the accretion curtain at this radius. With this one can express the Thomson optical depth of the accretion curtain $\tau_{\rm T} = n(r)\sigma_{\rm T} d$ as follows:

$$\tau_{\rm T} = \frac{1}{4\pi f a}\frac{\dot{M}\kappa_{\rm T}}{r_M v_{\rm ff}(a r_{\rm M})} = 0.1 L_{38}^{8/7} R_6^{2/7} M_{\rm NS}^{-10/7} B_{12}^{-2/7} f^{-1} a^{-1/2} \tag{5.2}$$

where $\kappa_{\rm T} = \frac{\sigma_{\rm T}}{\mu m_{\rm p}} = 0.34$ cm^{2}g^{-1} is an electron scattering opacity for solar abundances, $\sigma_{\rm T}$ is an electron scattering cross-section, and the scales are: L_{38} for luminosity in units 10^{38} erg s^{-1}, R_6 for neutron star radius in units 10^6 cm, $M_{\rm NS}$ for neutron star mass in units of solar masses, B_{12} for neutron star magnetic field in units 10^{12} G. The formula for Alfven radius was taken from Frank et al. (2002).

Near the peak of the outburst, the luminosity of V 0332+53 was $\sim 1.9 \times 10^{38}$ erg/s (Lutovinov et al., 2015, but assuming 5 kpc distance); the azimuthal size of the accretion curtain can be estimated from the width of the dips in the pulse profile (panel B in Fig. 5.3) $f \sim 0.2$, the strength of the magnetic filed on the surface was measured at $B = 2.5 \times 10^{12}$ G (see sect. 5.1) and, assuming $a = 0.5$ we obtain

$$\tau_{\rm T} \simeq 0.9 \tag{5.3}$$

We note that this result is close to the one in Mushtukov et al. (2017, equation (3), $\lambda = 0$ and $\tau_{\rm e} = L_{39}^{8/7} B_{12}^{-2/7}$) if we take into account that the azimuthal angle of an accretion channel is not equal to 2π.

Thus, the accretion curtain is sufficiently optically thick to explain the dips in the pulse profile with the amplitude $R \sim 1$, assuming that its material is (nearly) fully ionised. However, the biggest difficulty of this scenario is the presence of two dips separated by almost exactly $\Delta\phi = 0.5$, see

Fig. 5.3, panel B. Assuming that the magnetic field has the dipole geometry, we can not identify a configuration in which two accretion flows could produce two nearly identical dips separated by $\Delta\phi = 0.5$ in phase (Fig. 5.5).

Mushtukov et al. (2018) proposed that the dips in the pulse profile at the highest luminosity are caused by the eclipse of the accretion column by the neutron star itself. They noticed the fact that radiation from the accretion column is strongly beamed towards the surface of the neutron star (Poutanen et al., 2013; Mushtukov et al., 2018). Therefore, during the dip observer receives mainly emission from the eclipsed accretion column on the opposite side, focused by the neutron star serving as a gravitational lens (fig. 6 in Lutovinov et al., 2015). Such a model naturally explains two dips separated in phase by $\Delta\phi = 0.5$. However, in the simplified models considered in Mushtukov et al. (2018), the dips in the pulse profile are not symmetric, having different depths. It remains to be seen whether a more accurate account for the emission diagram of the accretion column can improve this aspect of the model (Mushtukov et al., 2018). We also note that according to the estimations above, the accretion flow from the inner disc presents a substantial obstacle for radiation escaping from the immediate vicinity of a pulsar, even if its azimuthal expansion f is larger than 0.2.

5.4.3 Pulsating K-edge of iron

The instrument configuration did not permit us to perform phase-resolved spectral analysis at the highest luminosities, where the dips were most pronounced. The nearest observation for which this is possible was carried out around MJD 53354.6 about ≈ 6 days earlier. The pulse profile and results of phase-resolved spectral analysis are shown in panel A of Fig. 5.4. The two dips are clearly seen in the pulse profile, albeit of unequal depth and separated in phase by $\Delta\phi \neq 0.5$. Notably, two clear K-edge absorption peaks coincided with the dips in the total flux. The optical depth of the edge is fairly small, $\tau \approx 0.04$, therefore they can not be associated with the material producing the dips. Indeed, considering the accretion curtain as an example, we note that for the solar abundance of cosmic elements, the optical depth of the iron K-edge is $\tau_{\mathrm{Fe-K}} \sim 2\tau_{\mathrm{T}}$. Given our estimate of the Thomson optical depth of the accretion curtain above (eq. 5.2), $\tau_{\mathrm{T}} \sim 1$, this is grossly inconsistent with the observed depth of the K-edge in the phase-resolved spectrum. The K-edge of such small depth could result from an addition of a small fraction of emission reprocessed by neutral material of solar abundance, for example in the accretion disc or on the surface of the neutron star near the accretion column (in the latter case the gravitational redshift should be taken into account). Any such model should also explain the anti-correlation between the total flux and the depth of the K-edge. To add to the complexity of the observational picture, we mention that pulsating K-edge was detected in all analysed data groups after the peak of the light curve, with a rather complicated pulse profile. The lack of correlation between the depth of the edge and flux or equivalent width of the fluorescent iron line suggests that the line and the edge originate in different locations. Indeed, if, for example, the reprocessing neutral material was distributed symmetrically around the primary source, the optical depth of the K-edge should have been correlated with the equivalent width of the fluorescent line. Obviously, our results exclude such simple geometries.

The surge in the K-edge depth near the end of the outburst (Fig. 5.2, panel C) is quite

interesting. The lack of pulsations of the K-edge optical depth during this period suggests that the absorbing material is located sufficiently far from pulsar and, likely, has a different origin, than pulsating K-edge absorption observed in the earlier stages of the outburst. The duration of the K-edge surge, $\sim 10-15$ days, is about $\sim 1/3$–$1/2$ of the orbital period of the binary, suggesting that absorbing material may be associated with some circumbinary material, for example with wind from the donor star. The lack of the fluorescent line of iron in the spectrum during this period further supports the scenario that we are dealing with an absorbing screen. In principle, the spectra in this period may be fitted with a simple absorbed power-law model, with a rather large hydrogen column density, $N_{\rm H} \sim (2.3\text{–}3) \times 10^{22}$ cm^{-2}. With this fit, some residual K-edge absorption was still detected in some of the observations. However, as discussed above, the limited low energy coverage of *RXTE*/PCA did not permit us to make a definitive conclusion. Such absorption enhancements are observed in different X-ray pulsars (e.g. Hemphill et al., 2014; Jaisawal, Naik, 2014; Sanjurjo-Ferrín et al., 2021; Liu et al., 2021; Ji et al., 2021) and usually related to the structures like wind or accretion stream through the inner Lagrange point. To our knowledge, such a clear and isolated episode of increased absorption is detected in the Be/X-ray binary system for the first time.

5.4.4 6.4 keV line

The modulation of the iron line equivalent width with the orbital period of the binary, first noted in (Tsygankov, Lutovinov, 2010, their fig. 2), and its tentative anti-correlation with the distance to the companion star (Fig. 5.2) suggest that some fraction of the iron line flux originates on the surface of the donor star or in the neutral material in its vicinity. In this context, we note that optical studies of V 0332+53 suggested the presence of a circumstellar (decretion) disc (Negueruela et al., 1999; Caballero-García et al., 2016). Although its extent in V 0332+53 is not known, based on typical parameters of such disks in other systems (Coe, Kirk, 2015) we conclude that it can contribute to the fluorescent iron line emission observed from this source.

To estimate the fraction of emission from the donor star and its circumstellar disk we fit the equivalent width curve with the model

$$\mathrm{EW}(t) = \mathrm{EW}_0 + \mathrm{EW}_{\rm star}(t) \tag{5.4}$$

$$\mathrm{EW}_{\rm star}(t) = \frac{N_{star}}{D^2_{\rm star}(t)} \tag{5.5}$$

where $D_{\rm star}(t)$ is the distance from the neutron star to the optical companion, $\mathrm{EW}_{\rm star}(t)$ is the equivalent width of the line produced at or near the optical companion and modulated with the orbital period of the binary and EW_0 represent the rest of the iron line flux. $N_{\rm star}$ is a normalisation factor. This procedure is similar to the one used in Tsygankov, Lutovinov (2010). During the fitting procedure, we ignored the observations without the iron line in spectra (i.e. after approximately MJD 53420). The model employed here ignores possible variations of the emission diagram of the pulsar throughout the outburst, assuming that $\mathrm{EW}_{\rm star}(t)$ is determined only by the solid angle of the companion star as seen from the pulsar. This approximation is sufficient for the purpose of this estimate. Fitting to the data we found $\mathrm{EW}_0 = 67 \pm 2$ eV. The best-fitting model is shown by the solid line in Fig. 5.2, panel B.

Thus, we find that the equivalent width of the iron line from the donor star varies between $\mathrm{EW}_{\min} \approx 5$ and $\mathrm{EW}_{\max} \approx 25$ eV. This is consistent with the expectation (Basko et al., 1974). Indeed, the radius of the donor star in V 0332+53 is probably close to ≈ 21 light sec (nine solar radii) (Negueruela et al., 1999, according to spectral type), the solid angle subtended by the donor star varies in the range $\Delta\Omega/4\pi \approx 0.01$–$0.044$. For an isotropic emission diagram of the primary emission, the equivalent width of the fluorescent line is $\mathrm{EW}_{\max} \times \Delta\Omega/4\pi$ with $\mathrm{EW}_{\max} \sim 1$ keV [5] and will vary between ~ 10 and ≈ 44 eV. The observed values are within a factor of ~ 2 lower which may be understood as the result of the the anisotropy of the emission diagram of the pulsar. The presence of the circumstellar disk around the donor star will further complicate the picture. Furthermore, the fluorescent line flux depends on the inclination of the system which was not taken into account in our simple estimate.

Results of the phase-resolved spectroscopy show that the iron line flux pulsates with the rotation period of the neutron star (Fig. 5.4). Due to the large size of the binary system, $\sim 10^2$ light sec, much larger than the rotation period of the neutron star, ~ 4.4 sec, the pulsating component of the iron line can not originate on (or near) the surface of the donor star. The complex pulse profiles of the line flux and equivalent width suggest that the pulsating part of the iron line must be associated with neutral material located within $\ll 1$ light sec from the neutron star. As estimated above, the total equivalent width of the fluorescent line originating near the neutron star can not exceed $\lesssim 67$ eV. On the other hand, the amplitude of pulsations of the iron line equivalent width is ~ 50–60 eV. Thus, the pulsating component of the fluorescent iron line is very strongly modulated, varying by a factor of $\sim 5 - 10$ with the rotational phase of the pulsar.

Such a strong modulation of the iron line flux seems to be difficult to explain, if the line was originating due to reflection off the accretion disc, because of its large solid angle as seen from the pulsar.

A plausible fluorescence site in the vicinity of the neutron star is the accretion curtain. The solid angle subtended by the two accretion flows as seen from the emission region equals $\Delta\Omega \sim 2 \times \pi/2 \times 2\pi f$, where, as before, $2\pi f$ the azimuthal angular size (in radians) of the accretion curtain. Thus, $\Delta\Omega/4\pi \sim \pi/2 \times f \sim 0.3$, assuming $f \sim 0.2$. Taking into account that the accretion flow is moderately thick (see above), the maximum value of the equivalent width of the line it can produce is a few hundred eV, i.e. it can explain the observed equivalent width of the iron line. As the accretion curtain can have a rather large ratio of its sizes in the azimuthal and radial directions, its rotation can easily explain the large modulation of the iron line, although particular details on the light curve need a much more detailed consideration with the account for the geometry of the accretion flows and the emission diagram of the pulsar.

[5] for moderate optical depth

$$\mathrm{EW}_{\max} = 0.74 \frac{\int_{7.1}^{\infty} I(E)(7.1/E)^{2.8}\mathrm{d}E}{I(E = 6.4keV)} \tau \text{ keV}$$

assuming roughly solar abundance (Churazov et al., 1998, formula 2), where $I(E)$ [phot s^{-1} cm^{-2} keV^{-1}] is the spectrum of a source. For a power-law spectrum with photon index $\Gamma \sim -0.5$ and cutoff energy $E_{\mathrm{cut}} = 7$ keV (parameters typical for V 0332+53) the above formula gives $\mathrm{EW}_{\max} \approx 1.8\tau$ keV. We neglected the effect of CRSF on the flux above 7.1 keV.

5.5 Conclusion

We analysed the data of *RXTE*/PCA observations of V 0332+53 during its type II outburst in 2004. We paid particular attention to the variability of the iron spectral features – the fluorescent line at 6.4 keV and K-edge at 7.1 keV and investigated their evolution on the time scale of the outburst and their pulsations with the pulsar period. Detection of the pulsating iron K-edge in V 0332+53 is reported for the first time in this thesis/corresponding paper.

Both iron line and edge show a complex dependence on the pulse phase which can not be self-consistently accommodated in any of the existing models of emission of accreting pulsars. The most striking of these features are:

1. at high luminosity the pulse profiles in the 3–12 keV band have two deep and narrow dips of $F_{\rm max}/F_{\rm min} \sim 2$ and of nearly identical shape, separated in phase by exactly 0.5. The source spectrum is identical during the two dips and very similar in shape to the spectrum outside the dips.

2. the K-edge peaks at the phase intervals corresponding to the dips, however, the optical depth of the edge $\tau_{\rm K} \sim 0.05$ is by far insufficient to explain the dips.

3. after accounting for the contribution of reflection from the donor star and any circumstellar material which may be present near it, the iron line flux shows pulsations of very large amplitude with the modulation of $F_{\rm max}/F_{\rm min} \sim 10$. The pulse profile of the line flux does not show any easily identifiable correlations with the pulse profiles of the total flux or K-edge depth.

V 0332+53 presents rich and unique opportunities and motivation for further development of theoretical models of emission of accreting neutron stars.

In the next chapter, we will perform reflection emission studies of a unique pulsar Swift J0243.6+6124. This object is very interesting because it is the closest Ultra-Luminous X-ray source discovered. In addition, this pulsar is uniquely placed (in terms of luminosity) between "normal" X-ray pulsars (such as V0332+53 studied in the previous chapter) and very bright Ultra-Luminous X-ray pulsars.

CHAPTER 6

ULX pulsar Swift J0243.6+6124 observations with *NuSTAR* – dominance of reflected emission in the super-Eddington state

The contents of this chapter are based on the manuscript originally published in ***Bykov*** *et al. (2022b). My contribution to that paper was the main idea for the project, selection of an appropriate pulsar, NuSTAR data analysis, interpretation of data and writing. Other authors (especially M. Gilfanov) contributed to the interpretation and writing.*

Abstract

We report the discovery of the bright reflected emission component in the super-Eddington state of the ULX pulsar Swift J0243.6+6124, based on the *NuSTAR* observations of the source during its 2017 outburst. The flux of the reflected emission is weakly variable over the pulsar phase while the direct emission shows significantly larger pulsation amplitude. We propose that in this system the neutron star finds itself in the centre of the well formed by the inner edge of the geometrically thick super-Eddington accretion disc truncated by the magnetic field of the pulsar. The aspect ratio of the well is $H/R \sim 1$. The inner edge of the truncated disc is continuously illuminated by the emission of the accretion column giving rise to the weakly variable reflected emission. As the neutron star rotates, its emission sweeps through the line of sight, giving rise to the pulsating direct emission. From Doppler broadening of the iron line, we measure the truncation radius of the accretion disc $\sim$ 50 $R_{\rm g}$. The inferred dipole component of the magnetic field is consistent with previous estimates favouring a not very strong field. The uniqueness of this system is determined by its moderately super-Eddington accretion rate and the moderate magnetic field so that the inner edge of the truncated geometrically thick accretion disc is seen from the neutron star at a large solid angle.

6.1 Introduction

The X-ray transient Swift J0243.6+6124 was discovered by *Swift* observatory during its 2017 outburst (Cenko et al., 2017). Pulsations with a 9.8 sec period were detected (Kennea et al., 2017), establishing the source as an accreting neutron star and a transient X-ray pulsar (XRP). The outburst lasted $\sim$ 200 days, after which the source transitioned to the regime of flaring activity. The optical counterpart was found to be a Be star (Kouroubatzakis et al., 2017; Reig et al., 2020) confirming that the source belongs to the class of Be X-ray binaries (BeXRB). From *Gaia* data, the distance to the source was estimated to be $6.8^{+1.5}_{-1.1}$ kpc (Bailer-Jones et al., 2018); the mean value of the distance value is adopted below. At the peak of the outburst, the source

reached the luminosity of $\sim 2 \cdot 10^{39}$ erg s^{-1} (bolometric) which exceeds the Eddington limit for a neutron star by a factor of ~ 10 (Tsygankov et al., 2018; Doroshenko et al., 2020), thus placing the source in a cohort of Ultra-Luminous X-ray pulsars (ULX pulsars). Remarkably, it is the first of this kind found in our galaxy.

Due to its uniqueness, X-ray studies of Swift J0243.6+6124 are plentiful. Wilson-Hodge et al. (2018) investigated the spectral and timing behaviour of the pulsar with *Fermi*/GBM and *NICER* telescopes. They found that the pulse profile shows strong evolution and energy dependence, with a transition from single- to double-peaked shape (and vice-versa) as the pulsar brightens (fades). Such behaviour is typical for transient X-ray pulsars and has been predicted theoretically (Basko, Sunyaev, 1975). From the luminosity at which the pulse profile change happens, they estimated the magnetic field of the neutron star to be $B > 10^{13}$ G. However, based on the absence of the propeller effect at the declining phase of the outburst, Tsygankov et al. (2018); Doroshenko et al. (2020) argued that the magnetic field should be smaller. Kong et al. (2022) reported the discovery of the variable cyclotron scattering absorption feature (CSRF) in the spectrum of this pulsar (in the energy range 120–140 keV). The implied magnetic field strength is therefore $\sim 1.6 \times 10^{13}$ G, and it is believed to originate from the non-dipole component of the magnetic field.

Insight-HXMT provided broadband X-ray data with high cadence (Zhang et al., 2019; Kong et al., 2020; Wang et al., 2020). Using these data Doroshenko et al. (2020) reported specific changes in timing and spectral properties of the pulsar. These changes were interpreted as an onset of super-Eddington accretion via the gas pressure-dominated disc and the following transition to the radiation pressure-supported disc (RPD). These results are important since they show that not only do radiation patterns change with pulsar luminosity, but also surrounding matter distribution may evolve in the course of the outburst. The presence of the RPD indicates that the magnetic field may not be very large. This claim is further substantiated by the presence of pulsations and variability of X-ray flux in a quiescent state observed by *NuSTAR* (Doroshenko et al., 2020).

The iron line complex was studied extensively by Jaisawal et al. (2019) using *NICER* and *NuSTAR* data. They detected several bright lines of asymmetric shape in the $6 - 7$ keV range. In particular, data could be fitted with the model consisting of lines at 6.4, 6.7 and 6.98 keV from neutral and ionised iron species. In their model, the 6.4 keV line was very broad (σ up to 1 keV). They interpreted these results that the iron emission is produced in the accretion disc or plasma trapper in the magnetosphere. Tao et al. (2019) also reported the presence of the significant reflection component and relativistic line shapes in Swift J0243.6+6124.

The peak luminosity of Swift J0243.6+6124 lies between 'normal' transient XRPs[1] and bright ULX pulsars. Significant changes in the matter distribution around a magnetised neutron star were predicted to take place at high mass accretion rates (Mushtukov et al., 2017), and Swift J0243.6+6124 may be in the regime where such a transition may happen.

Notwithstanding ample observational data, only one phase-resolved spectroscopic study was done with *NuSTAR* data in the sub-Eddington state of the pulsar (Jaisawal et al., 2018). This chapter aims to fill this gap and is dedicated to the phase-resolved spectroscopy of *NuSTAR* data in the high luminosity state, with particular emphasis on the behaviour of the iron line complex.

[1] such as V 0332+53 presented in chapter 5

In section 6.2 we describe the data reduction and analysis. In sect. 6.3.1 we discuss the timing analysis, in 6.3.2 we describe the results of phase-averaged spectra, and in 6.3.3 we report on the phase-resolved spectroscopy. We discuss our results in sect. 6.4 and conclude in sect. 6.5.

6.2 *NuSTAR* data

NuSTAR (Harrison et al., 2013) is a grazing incidence hard X-ray telescope sensitive in the 3–79 keV energy range with the energy resolution of 4% at 10 keV. It consists of two identical modules: FPMA and FPMB, with data from each being processed separately. In the course of its 2017-2018 type II outburst, Swift J0243.6+6124 was observed with *NuSTAR* five times between MJD 58000 and MJD 58200, observations 9030231900(2,4,6,8) and 90401308001. Observation 90401308001 was excluded due to its short exposure. We add observation 90401308002 of one of the subsequent mini-outbursts (likely Type I outbursts) to our data set. We use the following aliases for observations: 90302319002 – I, 90302319004 – II, 90302319006 – III, 90302319008 – IV, 90401308002 – V. Dates of the observations are the following: I - MJD 58032; II - MJD 58057; III - MJD 58067; IV - MJD 58094; V - MJD 58369.

The *NuSTAR* data reduction was carried out using the HEASOFT v. 6.28 package and *NuSTAR* CALDB files (v117). Standard data-processing tools were used to extract level 2 (NUPIPELINE) and 3 (NUPRODUCTS) products. We choose source and background regions for data extraction: the former is centred on the source position, while the latter is placed as far from the source as possible. Both regions have a circular shape with a 180 arcsec radius. Because of the high count rate in all observations, we set a bitmask "STATUS==b0000xxx00xxxx000" for NUPIPELINE as recommended[2]. All data were barycentred, but the time of arrival of photons is not corrected for the orbital motion of the system due to the lack of orbital solution based on all spin frequency data of the source. Since the on-source time of *NuSTAR* observations is relatively short (a few tens of ks) compared to the orbital period of $\sim$ 30 days this should not present any errors in the timing analysis. Spectra from both modules were simultaneously fit between 4 and 79 keV with XSPEC package (Arnaud, 1996). For phase-resolved spectroscopy photons were folded into 10 phase bins. All *NuSTAR* spectra were grouped to have at least 25 counts per energy bin and χ^2 statistic was used. The error intervals are given for 90% confidence.

6.3 Results

Fig. 6.1 shows the long-term light curve of the source in the 15–50 keV band (*Swift*/BAT data[3]) and the 0.3–10 keV range (*Swift*/XRT data[4]). The main, giant, outburst lasts approx 200 days and is followed by a series of smaller flares (possibly Type I outbursts). Dates of *NuSTAR* observations are marked with vertical lines. All observations except one are taken during the main outburst (I–IV, from left to right), and one during the smaller flare (V, the right-most one in the figure).

[2] `https://heasarc.gsfc.nasa.gov/docs/nustar/analysis/`

[3] `https://swift.gsfc.nasa.gov/results/transients/weak/SwiftJ0243.6p6124/`

[4] reduced from an online tool `https://www.swift.ac.uk/user_objects/`, see Evans et al. (2007)

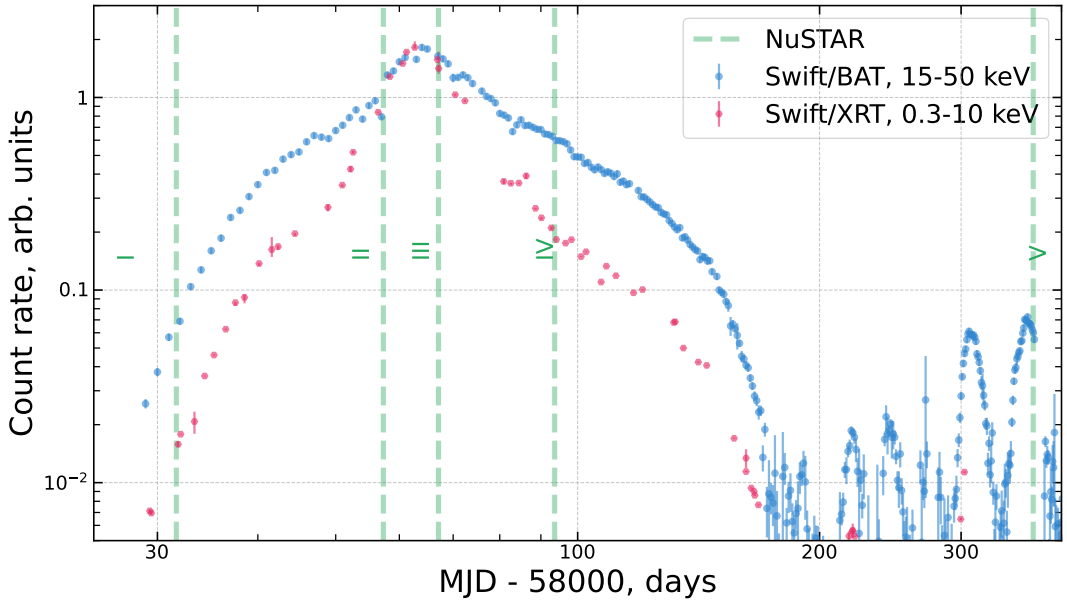

Figure 6.1: *Swift*/BAT and XRT light curves of a source in arbitrary units of count rate (blue and green symbols respectively). *NuSTAR* observations are marked with green vertical lines. Note the time axis in the log scale in units of days after MJD 58000.

The source was in a sub-Eddington state in observations I and V, and in a super-Eddington state in observations II, III and IV (see, e.g., fig. 1 in Wang et al. 2020).

6.3.1 Timing analysis

Pulsations of X-ray flux are detected in all observations. For each observation, we determine the period of the pulsar with EFSEARCH routine, using combined data of both *NuSTAR* detectors. The periods are 9.85425, 9.84435, 9.82340, 9.80105, and 9.7918 seconds for observations I, II, III, IV and V respectively (Solar system barycentre). These values of periods were used for folding the data for pulse profiles and phase-resolved spectroscopy. Due to the lack of a reliable orbital solution for the binary system, no phase connection was made to synchronise pulse profiles between different observations.

In Fig. 6.2 we show the pulse profiles in the 4–79 keV energy range of all five *NuSTAR* observations. Pulse profiles are normalised to the mean count rate (per observation). At the beginning of the outburst (observation I), the pulse profile has a complex shape with multiple minor peaks, but overall the profile is dominated by the one-peak component. The last observation (V) taken during another, minor flare, but in similar brightness, shows a very similar shape. The pulsed fraction PF [5] is $\sim 30\%$ in the considered energy range.

As the source becomes more luminous, the pulse profile changes drastically. In the two

[5] defined as $PF = \frac{\max C - \min C}{\max C + \min C}$ of the pulse profile C

observations where the source was the brightest (II and III), the pulse profiles show a very smooth and symmetric double-peaked shape. In observation II the peaks are roughly equal in amplitude and the pulsed fraction is $\sim 45\%$, whilst in observation III one peak dominates the overall shape and the pulsed fraction is somewhat larger, $\sim 55\%$. In the next observation, IV, the pulse profile features two asymmetric peaks of roughly equal height. The pulsed fraction is $\sim 30\%$. The dependence of PF on the energy of photons may be found in Tao et al. (2019) or Wang et al. (2020). Note that as we did not do phase-connection between individual observations, Fig. 6.2 may not correctly represent how *a particular pulse profile maximum* evolves in time, but rather shows the general evolution of the shape of the pulse profile (see Doroshenko et al., 2020; Jiren et al., 2022).

6.3.2 Phase-average spectral analysis

The X-ray spectra of Swift J0243.6+6124 measured by various observatories have been extensively analysed in the works cited in section 6.1 and the main parameters for common pulsar spectral models have been obtained and discussed. Below we focus on several facts and features, which were not considered in the previous analyses.

A remarkable feature of the spectrum of Swift J0243.6+6124 in the super-Eddington state (observations II, III, IV, the 4–79 keV luminosity of the order of $\sim 10^{39}$ erg s^{-1}) is the presence of strong reflection features, most notably of the fluorescent line of iron. This is illustrated by Fig. 6.3 where the ratio of the *NuSTAR* spectra to a simple power-law model with photon index $\Gamma = 2$ are shown. For these observations, an approximation of the spectrum with the power-law with an exponential cutoff continuum with a superimposed Gaussian line gives the equivalent width of the line 0.9 ± 0.05 keV for the brightest observation. Also quite obvious in the ratio plot are a smeared absorption edge in the $\sim 7 - 15$ keV range and a possible Compton reflection hump at the $\sim 15 - 30$ keV energy domain. All these features are familiar signatures of the reflected emission complicated by photo-ionisation effects and, possibly, by relativistic smearing (Ross, Fabian, 2005).

On the contrary, in the sub-Eddington state (observations I and V) where the source luminosity was $\sim$ few$\times 10^{37}$ erg s^{-1} these features are much less pronounced (Fig. 6.3). Indeed, the equivalent width of the Gaussian line in these observations was 90 ± 5 eV, close to typical values for X-ray binaries in the hard spectral state. During these observations, the source spectrum was quite close to a typical spectrum of an accreting X-ray pulsar (Jaisawal et al., 2018).

In observation IV the source was at the declining part of the light curve (Fig.6.1) and its luminosity was the lowest among the three super-Eddington state observations, $L_X \sim 4 \cdot 10^{38}$ erg s^{-1}. Interestingly, in this observation, the equivalent width of the iron line is large, 0.83 ± 0.02 keV, however, the shape of the continuum is close to sub-Eddington state spectra found in observations I and V (lower panel in Fig. 6.3). It appears that this observation caught the source in transition from super-Eddington to the sub-Eddington state.

Motivated by the ratio plot in Fig. 6.3 we use the following spectral model to describe the emission of the Swift J0243.6+6124 in the super-Eddington regime: PHABS*(RELXILLLP+

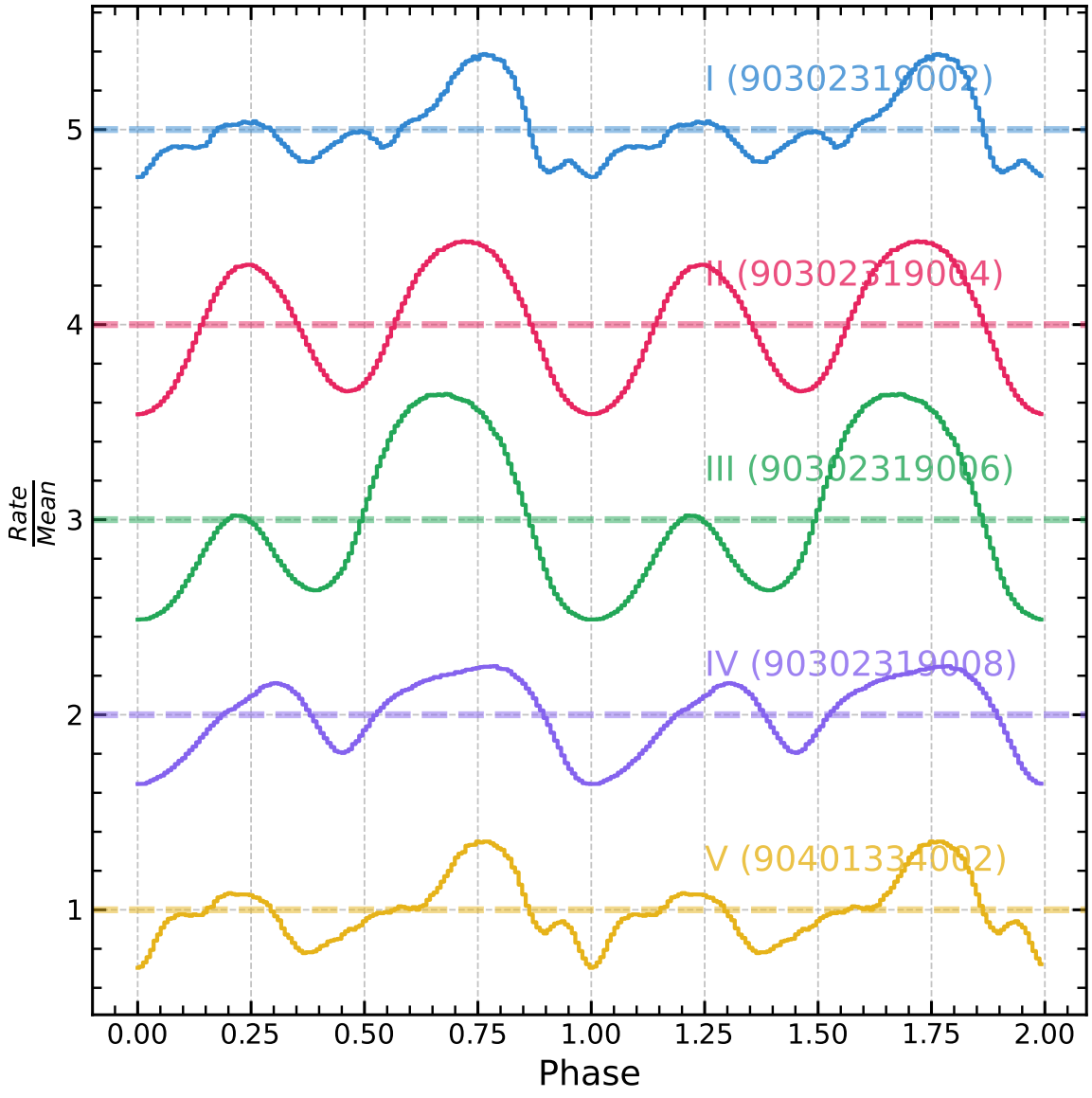

Figure 6.2: Pulse profiles (normalised to mean count rate) in the 4–79 keV energy range. The profiles were offset from each other by 1.0 for readability. The time since the start of the outburst goes from the top to the bottom. All pulse profiles except for the first and the last were taken in the super-Eddington state of the pulsar. Profiles were shifted so that the main minimum is at phase 0.

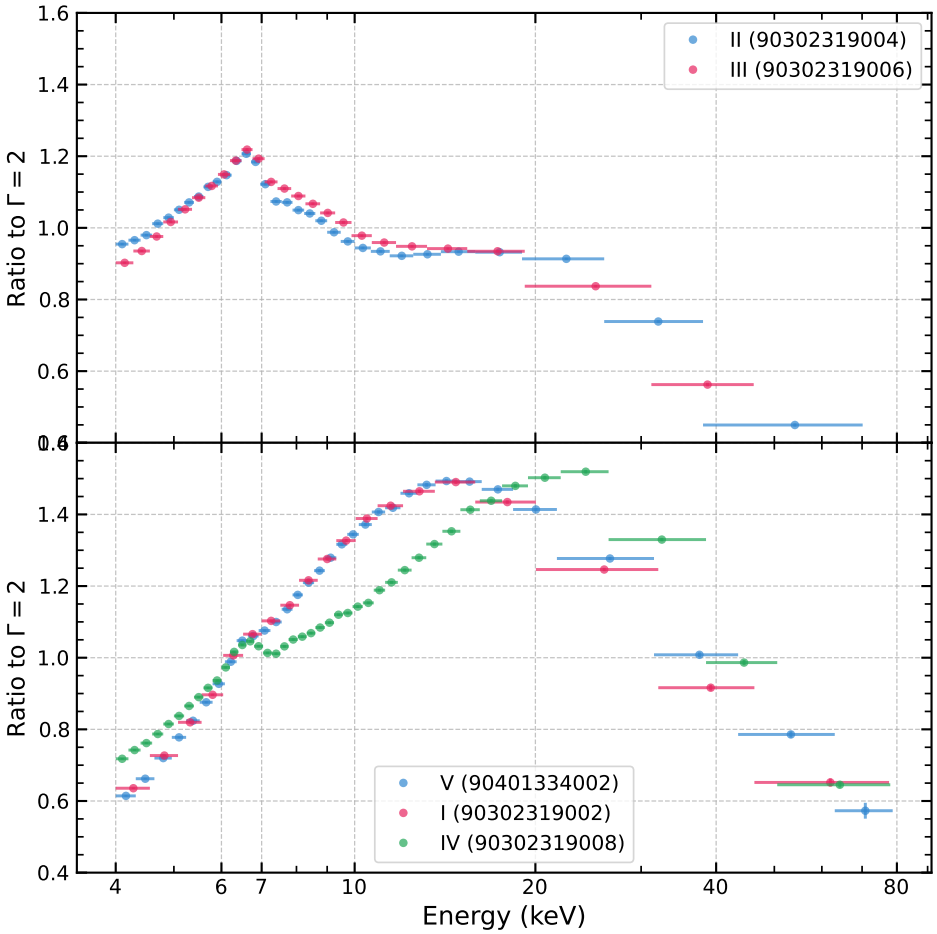

Figure 6.3: The ratio of the *NuSTAR* spectra to the POWERLAW model ($\Gamma = 2$) for observations II and III (upper panel) and observations I, V and IV (lower panel). Only FPMA data are shown.

BBODYRAD). The RELXILLLP[6] (García et al., 2014; Dauser et al., 2016) [v1.4.3] component models reflection of the primary emission (a power law with exponential cutoff) from an accretion disc in lamp-post geometry, with account for possible photo-ionisation of the disc material and relativistic smearing of the reflection spectrum. Previously, such a model, in its RELXILL variant, was successfully applied to the *NICER+NuSTAR* spectra of Swift J0243.6+6124 by Jaisawal et al. (2019). The multiplicative component PHABS takes care of the interstellar absorption. The total Galactic absorption in the direction of the source has the column density of 0.8×10^{22} atoms cm^{-2} [7]. For the sake of fit stability, we fix PHABS parameter at this value. The BBODYRAD component accounts for thermal radiation reported in previous works.

For RELXILLLP, we use the following setup: spin of the object a and its redshift z are both set to 0; iron abundance $A_{\rm Fe}$ is set to 5.0 (Jaisawal et al., 2019); inner disc radius $R_{\rm in}$, power law index Γ, cutoff energy $E_{\rm cut}$ and ionisation parameter $\log \xi$ are free parameters. Outer disc radius was set to $1.1 \times R_{\rm in}$, this choice will be discussed later. Inclination is a free parameter. The height of the lamp-post source h is set to 5 $R_{\rm g}$ (five gravitational radii). Reflection factor $f_{\rm refl}$ controls the amplitude of the reflected component relative to the primary continuum and is a free parameter. $f_{\rm refl}$ is an analogue to the equivalent width of the iron line. The cross-calibration constant is added between FPMA and FPMB spectra. Table 6.1 shows the best-fitting values of parameters in observations II, III, and IV. Fig. 6.4 shows the spectral data and models. For observations I and V, when the source was in the sub-Eddington state, the spectra are adequately approximated by more simple standard pulsar models (Jaisawal et al., 2018) without the need for a significant reflection component. Therefore we focus our attention on the super-Eddington state spectra.

For the super-Eddington state, the reflection model gives fairly consistent values of parameters between three observations. The spectra in the super-Eddington state require large values of reflection fraction $f_{\rm refl} \sim 0.1 - 0.2$ which is not surprising, given the large values of the equivalent width of the iron line obtained in the simple Gaussian fits. Interestingly, the data require both relativistic smearing of the iron line as well as photo-ionisation of the reflector's material with a fairly large ionisation parameter $\log \xi \sim 3.5$ with a typical uncertainty 0.05. The inner radius of the disc $R_{\rm in} \sim 50 - 70\ R_{\rm g}$ corresponds to a circular velocity of approximately 10% of the speed of light for a Keplerian disc. This explains the significant width of the 6.4 keV line reported earlier (Tao et al., 2019; Jaisawal et al., 2019) as well as the presence of the lines of He- and H-like iron. These findings are quite important and will be discussed in the context of the truncated thick disc picture in the following section. The best-fitting model consistently requires fairly low values of the inclination angle of $\approx 10 - 20^\circ$ for all three observations with the errors in $2 - 4^\circ$ range. However, it is worth noting that in the geometry proposed in this chapter, the inclination angle does not have the same straightforward meaning as in the geometry of a lamp post above an accretion disc envisaged in the RELXILLLP model. This is further discussed in Section 4.

As was noted above, in observation IV the source appeared to be in transition from super- to sub-Eddington state. This may explain the harder photon index and smaller reflection amplitude found in this observation (Table 6.1). However, the presence of the reflected component in this spectrum is required with high statistical confidence. Likewise, the relativistic broadening of the

[6] http://www.sternwarte.uni-erlangen.de/~dauser/research/relxill/

[7] https://heasarc.gsfc.nasa.gov/cgi-bin/Tools/w3nh/w3nh.pl, see HI4PI Collaboration et al. (2016)

Component	Parameter	II (90302319004)	III (90302319006)	IV (90302319008)
constant	$C_{\rm FPMA/FPMB}$	0.999 ± 0.001	0.992 ± 0.002	0.999 ± 0.001
relxilllp	$E_{\rm cut}$, keV	20.8 ± 0.5	20.5 ± 0.5	$17.6^{+0.2}_{-0.3}$
	Incl, $^\circ$	18^{+2}_{-3}	10^{+3}_{-4}	16^{+3}_{-2}
	$R_{\rm in}$, $r_{\rm g}$	66 ± 6	53^{+6}_{-5}	51 ± 4
	Photon index	1.27 ± 0.03	1.32 ± 0.03	0.77 ± 0.02
	logξ	$3.47^{+0.04}_{-0.05}$	$3.68^{+0.04}_{-0.03}$	$3.37^{+0.04}_{-0.07}$
	norm	0.45 ± 0.01	0.65 ± 0.02	0.188 ± 0.002
	$f_{\rm refl}$	$0.184^{+0.011}_{-0.010}$	0.24 ± 0.01	0.094 ± 0.009
bbodyrad	kT, keV	1.223 ± 0.008	1.44 ± 0.02	1.07 ± 0.03
	norm	1112^{+52}_{-56}	612^{+91}_{-83}	374^{+26}_{-20}
χ^2/dof		2545.53/2309	2290.51/2170	3224.41/2735
L_{4-79}, 10^{38} erg s^{-1}		7.8	10.1	3.8

Table 6.1: Spectral parameters of *NuSTAR* spectra of Swift J0243.6+6124 in its 2017-2018 outburst for super-Eddington state. The spectral model is described in sect. 6.3.2: PHABS*[RELXILLLP + BBODYRAD]. Luminosity is calculated from unabsorbed flux of CFLUX component in XSPEC. Black body component normalisation *norm* is tied to the radius of emitting areas R (in km) through the distance to the source D (in 10 kpc): $norm = R^2/D^2$.

iron line, expressed in the value of $R_{\rm in}$ parameter, is similar to the other two super-Eddington observations.

Further insights into the geometry of the super-Eddington accretion flow around the magnetised neutron star are provided by the results of pulse phase-resolved spectroscopy.

6.3.3 Phase-resolved spectral analysis

Using the data of three *NuSTAR* observations of the source in the super-Eddington state, we study the evolution of spectral parameters as a function of the rotational phase of the neutron star. To this end, the pulse period is divided into 10 phase bins of equal width, and the spectra are extracted for each phase bin as described in section 6.2. We fit the spectra with the same model as for the phase-averaged case, except that we fix $R_{\rm in}$, $\log\xi$, inclination angle, and parameters of the black body component at the values found for phase-averaged spectra. For all observations and in phase bins we obtained adequate quality of the fit with the reduced χ^2 in the $\chi^2/{\rm dof} \sim 1.1$ range for a typical number of degrees of freedom $\sim 1100 - 1600$. In appendix, the phase dependence of the best-fitting parameters is shown in Fig. E.1, and the representative unfolded spectra in Fig. E.2; the parameters values are presented in Table E.1. Making $\log\xi$ and parameters of the black body component free does not change significantly other parameters of the model and does not affect the interpretation of the results. For simplicity, we do not consider these more sophisticated fits further and focus on our main finding of the presence of a strong reflected component and its behaviour with the pulse phase.

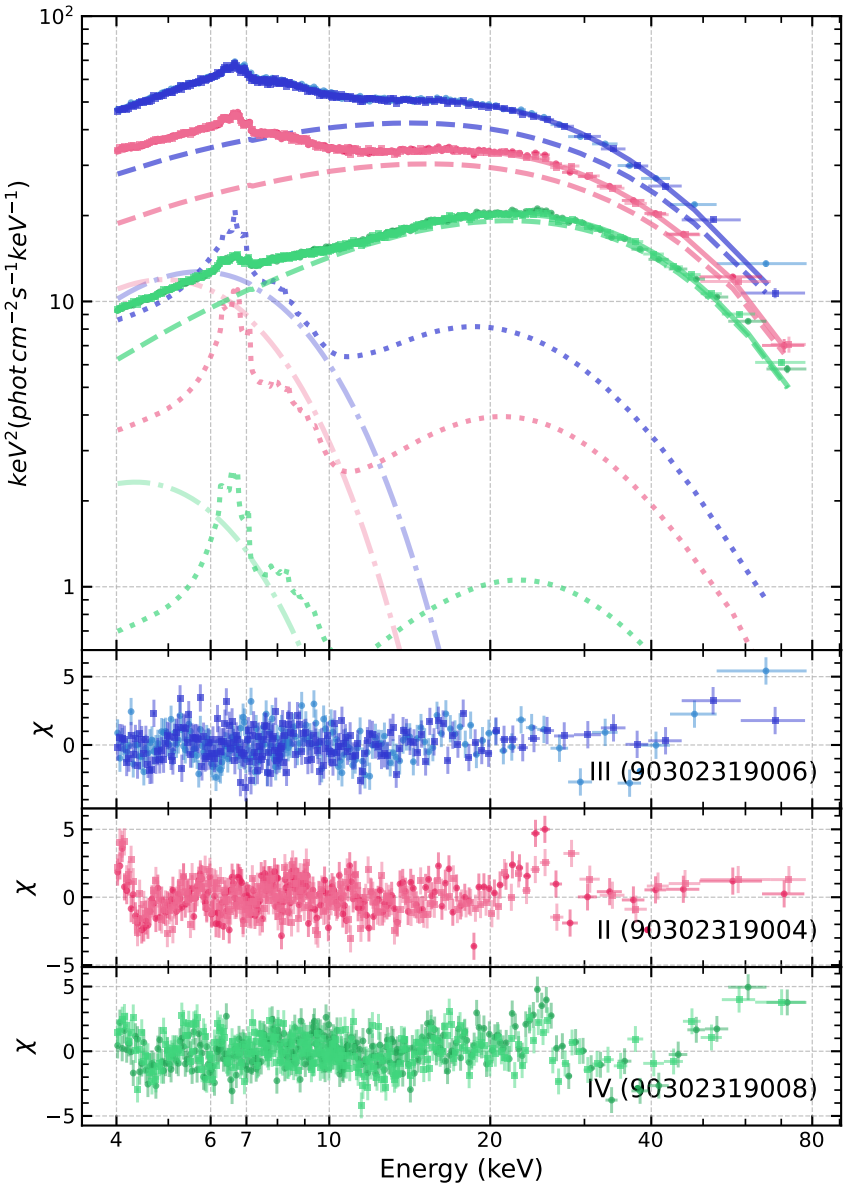

Figure 6.4: Unfolded spectra of the source and its model for observation II-IV. The top subplots show the unfolded spectra from FPMA (circles) and FPMB (squares) which are coloured according to the observation ID. A solid line represents the best-fitting approximation, whose components are also shown: reflection (dotted), power-law continuum (dashed), the thermal radiation (dash-dotted). The lower subplots show the respective residuals from the model. Spectral data were rebinned for plotting purposes.

Using the best-fitting model we compute the flux of reflected and direct emission for each spectrum. We do not compute the uncertainties in those values since it would require computationally-heavy calculations of the parameter chains which is unnecessary because the errors are sufficiently small for the purpose of this work. This is demonstrated by the high accuracy of $f_{\rm refl}$ estimates as well as by the low level of noise in the obtained pulse profiles for the direct and reflected flux. Phase dependence of the direct and reflected flux as well as the total flux and reflection fraction $f_{\rm refl}$ are shown in Fig. 6.5. An immediate conclusion from these plots is that the reflected component is much less variable with the pulse phase than the direct emission. As discussed in the next section, this can be understood in a picture of a rotating neutron star located in the middle of a geometrically thick super-Eddington accretion disc truncated by the magnetic field of the strongly magnetised neutron star. The pulsation amplitude[8] of the direct emission is $\approx 3.5, 5.0, 2.0$ in observations II, III and IV respectively, whereas for the reflected emission the numbers are, respectively, $\approx 1.5, 2.3, 1.3$. The pulsation amplitude for the reflected emission is $\sim 2-3$ times smaller than for the direct emission, which leads to the large pulsations in the reflected fraction $f_{\rm refl}$.

Other parameters of the model show a complex pattern of variations with the pulse phase (Fig. E.1). The spectral hardness and the cut-off energy seem to be slightly correlated with the total pulsar flux, as commonly observed in such objects (e.g. Tsygankov et al., 2017).

The results of the phase-resolved spectral analysis are summarised in Table E.1. In interpreting values of the photon index one should bear in mind that in the RELXILLLP model, the direct emission is modelled as a power law with exponential cut-off. Typical values of the cut-off energy $E_{\rm cut}$ for this source are in the 15-30 keV range. Therefore the actual slope of the spectrum is not well represented by solely the value of the slope Γ, but, rather, by combination of Gamma and $E_{\rm cut}$. Variations of the slope with pulse phase are accompanied by corresponding variations of the $E_{\rm cut}$ so that drastic variations of Γ and $E_{\rm cut}$ from one pulse phase bin to the other do not mean equally drastic variations of the shape of the continuum.

The presence of variations in the strength of the reflected component with the pulsar phase is further illustrated in Fig. 6.6 where the ratio of the spectra in different phase bins to a `cutoffpl` model with the same parameters is shown for several phase bins. One can see that the amplitude of the reflection features is indeed larger in the spectra for which the fit gave larger values of $f_{\rm refl}$.

We find no evidence of the presence of the cyclotron scattering absorption feature (CSRF) in phase-averaged and phase-resolved spectra in the 4–79 keV energy range.

We tried both the lamp-post (RELXILLLP) and corona (RELXILL) models with no noticeable effect on the parameter values. The lamp-post geometry was motivated by the compactness of the accretion column compared to the inner disk radius that we envisaged. We also varied the lamp-post height, tried fixing it to 3, 5, 10 and 40 R_g and found that it did not have any effect on the best-fit values of the parameters except for the normalisation of the RELXILLLP model. Notably, $f_{\rm refl}$ and cutoff energy/photon index did not change. It should be mentioned that both lamp-post and corona models are significant simplifications of the true geometry of the system. However, the agreement between the results we obtained under these geometries suggests that the exact geometry is not the critical parameter.

[8] i.e. $\frac{F_{\rm max}}{F_{\rm min}}$

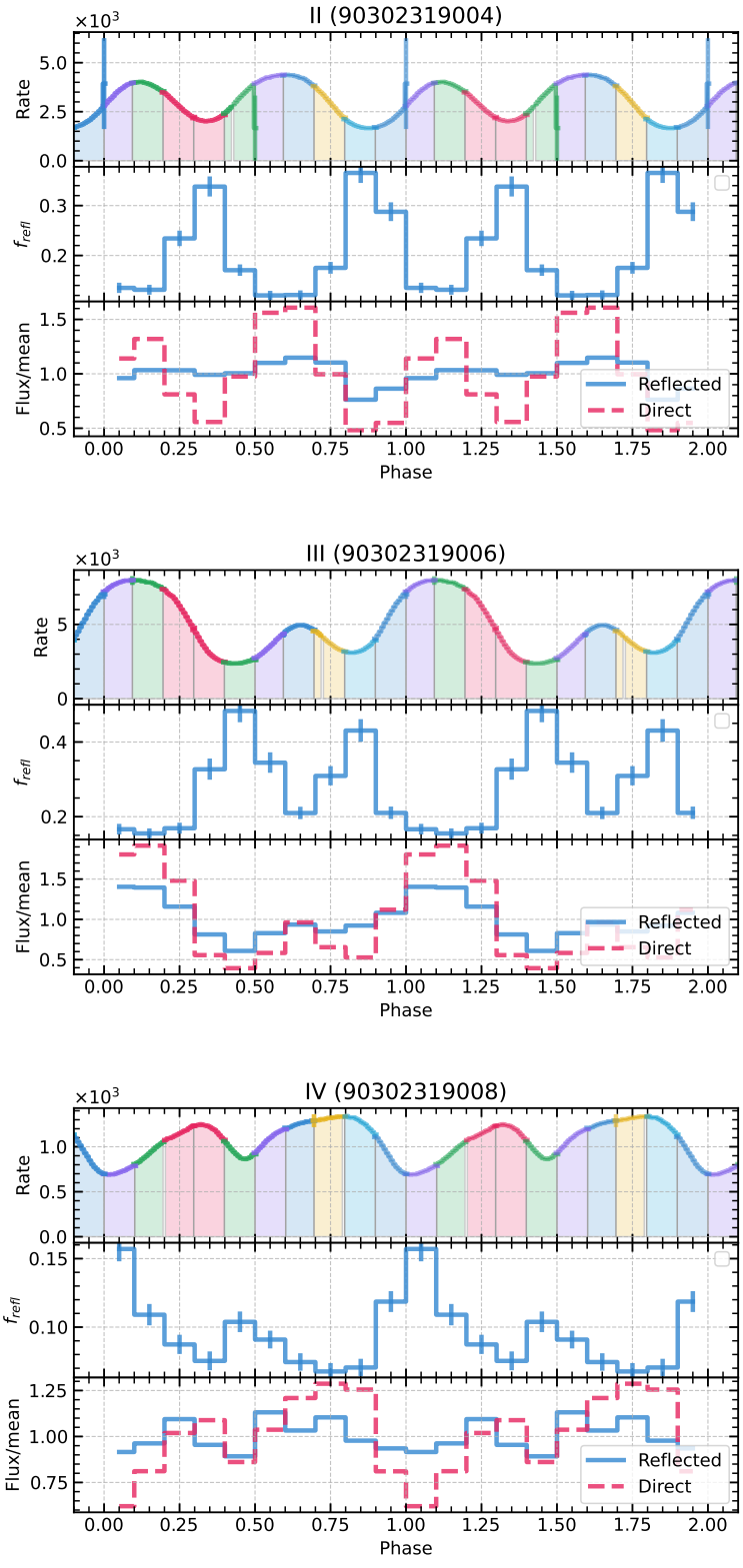

Figure 6.5: The evolution of spectral parameters as the function of pulsar rotation phase for observations II, III, and IV. In each panel from top to bottom subplot: Pulse profile of the count rate in the 4–79 keV energy range; the reflection fraction parameter $f_{\rm refl}$; direct (red, dashed) and reflected(blue, solid) flux (4–50 keV) of the best-fitting model divided by the respective mean flux. All spectral parameters may be found in Fig. E.1

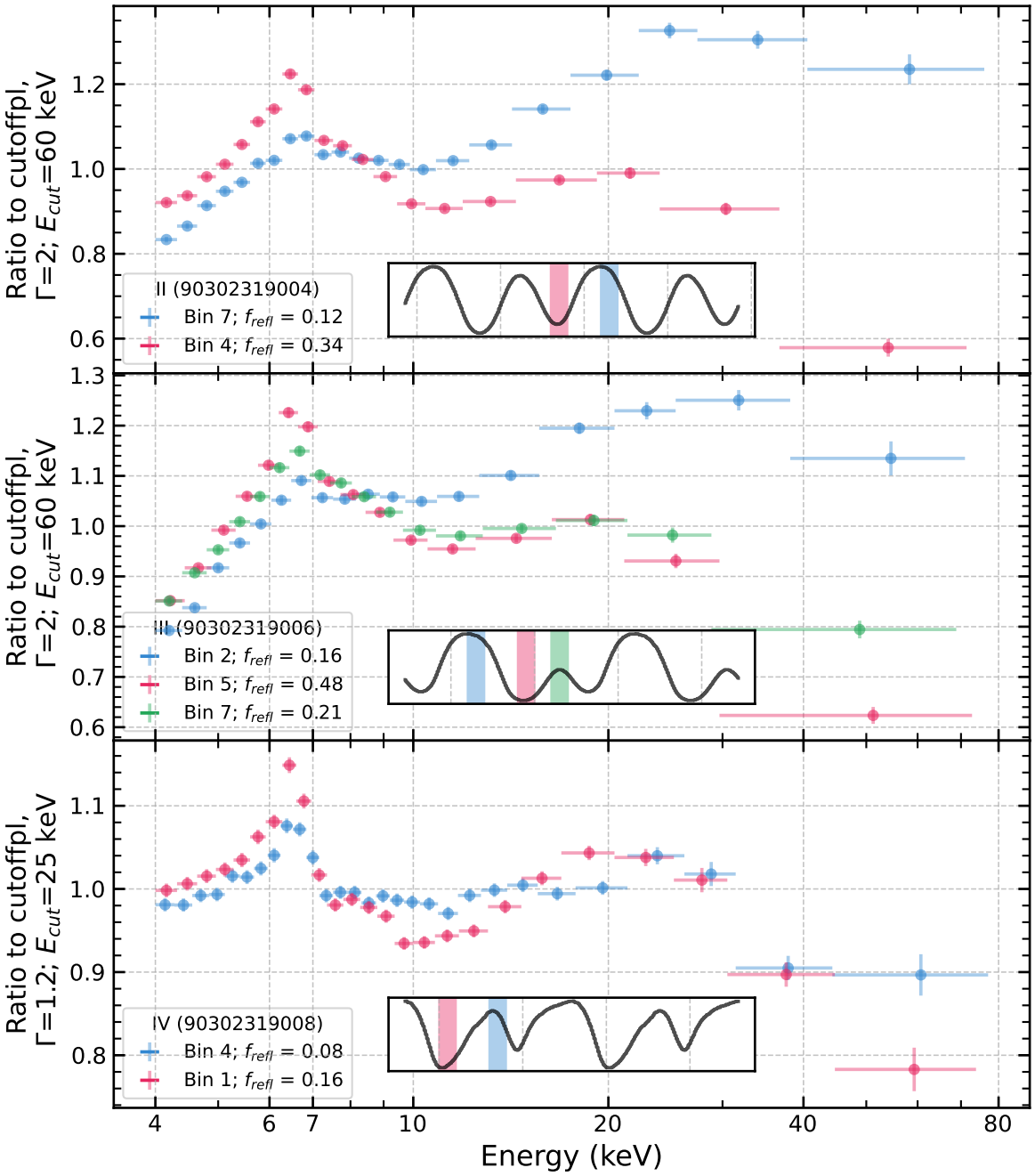

Figure 6.6: The ratio of the spectra collected in specified phase intervals to CUTOFFPL model with fixed parameters. The colour of the spectra corresponds to the colour of a phase bin shown in the pulse profile inset. Data from both detectors are plotted in the figure (square and circle markers). The top panel shows the results for observation II, the middle panel for observation III, and the bottom for observation IV. In the legend of each panel, the value of $f_{\rm refl}$ from the best-fitting model of a bin is shown. Only FPMA data are shown.

6.4 Discussion

The presence of pulsations, i.e. lack of the propeller regime (Illarionov, Sunyaev, 1975) down to the luminosity level of $\sim 3\times10^{34}$ erg s^{-1} found by Doroshenko et al. (2020) implies that the dipole component of the magnetic field is not very strong. Based on this and a few other arguments Doroshenko et al. (2020) estimated the dipole field value of the pulsar $B \sim (3-9)\times10^{12}$ G and coupling constant $\xi \sim 0.1-0.2$ [9]. For such field strengths and super-Eddington luminosity of $L_{\rm X} \approx 10^{39}$ erg s^{-1} at the peak of the light curve one may expect that the pulsar magnetosphere is fairly compact, with $R_{\rm m} \sim 150-500$ km, i.e. $R_{\rm m} \sim 35-120R_{\rm g}$ for a 1.4 $M_\odot$ neutron star (Mushtukov et al., 2017; Tsygankov et al., 2018).

Given a rather small truncation radius, the disc will extend sufficiently close to the compact object, so that a radiation pressure-dominated geometrically thick disc can form near the pulsar magnetosphere in the super-Eddington regime. Using formulae from Shakura, Sunyaev (1973); Mushtukov et al. (2017) one may estimate the H/R at the inner edge of the disc $\left(\frac{H}{R}\right)_{\rm m} = 0.1\frac{L_{\rm X}}{10^{39}}\frac{R_{\rm NS}}{10^6{\rm cm}}\left(\frac{M_{\rm NS}}{M_\odot}\right)^{-1}\left(\frac{R_{\rm m}}{10^8{\rm cm}}\right)^{-1}$, with the parameters normalised to values appropriate for Swift J0243.6+6124. Substituting the values, one obtains $H/R \sim 0.15-0.5$ on the inner edge of the disc. Indeed, Doroshenko et al. (2020), based on the observed transitions in spectral and timing properties of the source, argued that between MJD 58045 and 58098 the inner part of the accretion disc was in the radiation-pressure-dominated regime. All three observations analysed in the present chapter are within this time span.

Truncation of the geometrically thick accretion disc by the magnetic field of the neutron star will form a "well" with the pulsar located in its centre (see the sketch in Fig. 6.7). The inner edge of the "well" will be subject to continuous illumination by X-ray emission from the pulsar (Mushtukov et al., 2021), similar to illumination of the accretion disc in X-ray binaries and active galactic nuclei at more "normal" sub-Eddington accretion rates. However, unlike X-ray binaries at the sub-Eddington accretion rate, the solid angle subtended by the inner edge of the thick accretion disc with $H/R \approx 1$ would be much larger. The solid angle of the inner edge of a disc with aspect ratio $H/R = 1$ is $2\pi\int_{\frac{\pi}{2}-\arctan(H/R)}^{\frac{\pi}{2}+\arctan(H/R)}\sin\theta{\rm d}\theta = 0.7\times4\pi$ sr. Thus, $\Omega/4\pi \sim 0.7$ and the ballpark figure for equivalent width of the fluorescent line of iron is $\sim \frac{\Omega}{4\pi}\times1$ keV ~ 0.7 keV assuming reflection from the optically thick material. This is compatible with the observed equivalent width of the 6.4 keV line of the order of 1 keV (see sect. 6.3.2, also Tao et al., 2019). Similarly, the value of $f_{\rm refl} \sim 0.25$ obtained in the spectral fits corresponds to $\Omega/4\pi \sim 0.2$[10], which is comparable with the value estimated above. We note, however, that this crude estimate assumes an isotropic emission pattern, which is not strictly applicable to a magnetised neutron star.

Furthermore, we note that our best-fitting model predicts the inner radius of the accretion disc $\sim 50-70\ R_{\rm g} \sim (2-3)\times10^7$ cm, with the typical uncertainty of 5 $R_{\rm g}$. This value is controlled by the line profiles in the iron line complex and was determined in the RELXILLLP

[9] the ξ is defined as a parameter relating the magnetospheric radius $R_{\rm m}$ and the Alfven radius $R_{\rm a}$ via $R_{\rm m} = \xi R_{\rm a}$, see, e.g., Mushtukov et al. (2017)

[10] according to the RELXILLLP model, $f_{\rm refl} \sim \frac{\Omega}{4\pi-\Omega}$

model with the account for the Doppler and ionisation effects (both of which contribute to the line broadening). This value of the inner disc radius estimated from the broadening of the line is consistent with the radius of the pulsar magnetosphere $\sim 3 \times 10^7$ cm estimated assuming the (dipole) magnetic field strength of $B = 3 \times 10^{12}$ G and the coupling parameter of $\xi = 0.2$ and (eq. 1 in Mushtukov et al., 2017). This consistency is quite remarkable because the two estimates are based on entirely different physical effects (Doppler effect and disc-magnetosphere interaction) and are independent.

Thus, we hypothesise that the strong reflected emission originates at the inner edge of the thick accretion disc truncated by the magnetic field of the neutron star. The inner edge of the disc is irradiated by hard X-ray emission of an accretion column, as illustrated in Fig. 6.7. The pulsar emission diagram must be sufficiently broad so that the total reflected flux, as seen by the distant observer, does not vary much as the neutron star rotates. As the neutron star rotates, the pulsar beam sweeps through the line of sight giving rise to the direct emission pulsating with a much larger amplitude. These two components, weakly variable reflected emission and more strongly variable direct emission from the pulsar explain the overall behaviour of the pulse with strongly varying reflection fraction. In this picture, the anti-correlation of the reflection fraction and equivalent width of the fluorescent line of iron with the total flux is naturally explained. On the next level of detalisation we may note that, as the pulsar emission is not isotropic, the irradiation pattern varies somewhat as the neutron star rotates, leading to some moderate variations of the reflected flux, which have however smaller fractional amplitude than the direct emission from the pulsar itself.

At the considered luminosity levels, the emission diagram of the pulsar is likely of the fan-like geometry, i.e. sufficiently broad, the pencil beam being subdominant, if any. In this regime, the radiation escapes a super-critical accretion column mostly via its sides, leading to a fan-like emission pattern (Basko, Sunyaev, 1976; Lyubarskii, Syunyaev, 1982; Mushtukov et al., 2015a; Mushtukov, Tsygankov, 2022). Fan-beam naturally produces weakly variable irradiation of the inner disc edge, due to the rather high degree of symmetry of the fan beam as seen from the accretion wall, and, importantly, two-peaked pulse profiles are observed in this state. This is opposite to pencil-beam geometry (expected at smaller accretion rates) when photons escape primarily along the magnetic axis of the pulsar (Gnedin, Sunyaev, 1973) and we expect a one-peaked pulse profile and little irradiation (Koliopanos, Gilfanov, 2016). Variability of the direct emission is caused by the rotation of the fan- and pencil-beam emission components, the latter being sub-dominant at considered luminosities. The suggested picture explains observed behaviour with variable direct emission flux and variable reflection fraction, but significantly less variable reflected flux.

One can estimate the beaming factor of the pulsar comparing reflected and direct flux as follows. Using observation II as an example, the reflected flux in the average spectrum amounts to ~ 2 (in units of 10^{-8} erg s^{-1} cm^{-2}). X-ray albedo varies depending on the ionisation state and incidence angles, but generally, it is greater than ~ 0.3 (Basko et al., 1974; Zycki et al., 1994). Taking into account X-ray albedo we estimate the effective angle-averaged direct emission required to produce observed reflected emission as $\sim 2/0.3 = 6$ (in the same units). The observed direct flux is 12, which is about ~two times higher than the former figure. The ratio of the two flux values gives an estimate of the beaming factor of the order of ~ 2, i.e. beaming of the pulsar

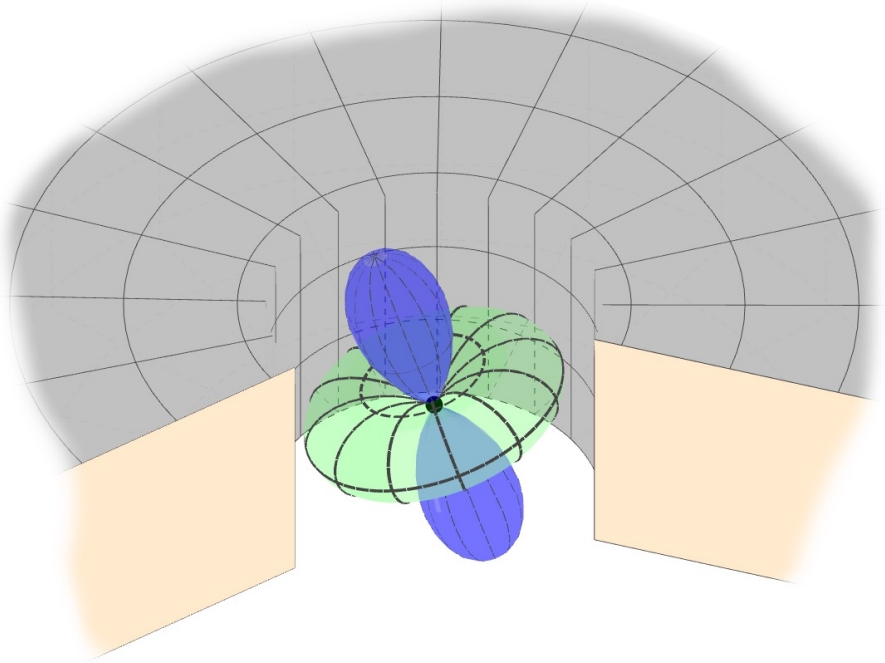

Figure 6.7: The illustration of considered geometry: a **neutron star** (black dot) surrounded by a **thick disc** (grey plane) illuminated by a **pencil beam** (blue cone), and the **fan beam** (green torus). Depending on the orientation of the pulsar and its emission diagram, the visible side of the inner disc may be illuminated differently depending on the rotational phase.

emission is rather weak, and the measured luminosity is fairly close to the real one. Beaming of radiation in X-ray pulsars is discussed, for example, in King, Lasota (2019); Mushtukov et al. (2021).

Outside the outburst peak, at the sub-Eddington accretion rates, the accretion disc returns to the normal geometrically thin state characterised by a rather low reflection fraction, typical for accreting X-ray pulsars, i.e. iron equivalent width $\sim$ 100 eV (e.g. **Bykov** et al., 2021) .

With the advent of X-ray polarimetry instruments (e.g. The Imaging X-ray Polarimetry Explorer, IXPE, Weisskopf et al. (2016)) it may be anticipated that studies of the variability of polarisation and its energy dependence will bring new interesting results. Reflected (reprocesses) emission is expected to have a smaller degree of polarisation than radiation coming from the accretion columns (Basko, Sunyaev, 1975). The degree of polarisation can be used to disentangle the direct pulsar emission from the reflected and/or thermal components, which brings the model-independent way to study the reprocessed emission and hence the matter distribution in such systems.

6.5 Conclusion

We analysed *NuSTAR* data of the Ultra-Luminous X-ray pulsar Swift J0243.6+6124 in the super-Eddington state. In this state, the spectrum of the source shows strong reflection signatures (fluorescent lines of iron with the equivalent width of $\sim$ 1 keV, smeared K-edge and Compton hump) suggesting that the spectrum is dominated by the reflected emission. Pulse phase-resolved spectral analysis using a reflection model demonstrated significant modulation of the reflection fraction $f_{\rm refl}$. However, a more careful look at the data revealed that this modulation is caused by variations of the direct emission, the reflected flux being significantly less variable.

We hypothesised that due to the large accretion rate and relatively moderate dipole magnetic field strength in this pulsar, the configuration is realised when the geometrically thick radiation pressure-dominated accretion disc is truncated close to the neutron star, at the distance of $\sim 50 - 75\ R_{\rm g}$. The inner edge of the truncated accretion disc is filling a large solid angle as seen from the pulsar and is continuously illuminated by the X-ray radiation from the accretion column. The beaming factor of the emission is not large so the radiation has a sufficiently broad fan-like emission diagram, expected at these large luminosities. This gives rise to the strong and weakly variable reflected emission. As the emission from the accretion column sweeps through the line of sight, we see direct emission of the accretion column, which is much more variable.

From the spectral analysis, based on the width of the iron lines and with the account for the photo-ionisation of the material at the inner edge of the accretion disc we estimate its radius to be $\sim 50 - 70\ R_{\rm g}$. This value is remarkably consistent with the magnetospheric radius predicted given the constraints on the neutron star magnetic field strength and coupling parameter.

The uniqueness of this pulsar is explained by the combination of the moderately super-Eddington accretion rate with the moderate magnetic field strength.

This chapter concludes the second part of the thesis. The next chapter is the summary of the finding and conclusion for both parts of this work.

CHAPTER 7

Summary and Conclusion

In this thesis, we studied accreting neutron stars and massive black holes. In this chapter, we briefly re-iterate the results of each paper.

In the **first part of the thesis**, we focus on the actively accreting black holes at the centres of galaxies. The presence of an active galactic nucleus (AGN) plays an important role in the evolution of a host galaxy and its properties. The most powerful AGNs are seen at large distances and can be used for cosmological studies.

In Chapter 2 we explore the feasibility of X-ray-selected samples of AGNs and galaxy clusters of SRG/eROSITA to serve as a cosmological probe. We consider the capacity to detect Baryon Acoustic Oscillations (BAOs) and to constrain cosmological models in the all-sky survey data using the clustering properties of the samples using Fisher Matrices formalism. We take into account that only photometric redshifts will be available for all objects and investigate the impact of their quality on the forecast.

- Redshift rms scatter parameter σ_0 has much more influence on the quality of cosmological forecast than the fraction of catastrophic errors $f_{\rm fail}$.

- It would be doable to detect BAOs with a significance of detection on the $\sim 5-6\sigma$ for AGNs and $\sim 4-5\sigma$ for clusters of galaxies.

- Cosmological constraints from X-ray data without priors (from independent experiments) achieves accuracy $\sim 5-25\%$, and $\sim 0.5-10\%$ with priors. Joining the constraints from AGNs and clusters of galaxies reduces the errors by a factor of ~ 1.5. Limiting the survey duration or area still produces competitive precision.

- Cosmological constraints are competitive with the constraints of operating and planned cosmological surveys. eROSITA-based mass function of galaxy clusters is a less powerful probe compared to the clustering of AGNs and clusters for all studied parameters except matter density $\Omega_{\rm m}$.

- It would be possible to detect small-scale clustering of AGNs in the eFEDS and Lockman Hole eROSITA surveys performed during the Performance verification phase of the observatory.

Chapter 3 presents a method for the identification of X-ray sources in optical wavelengths. This is one of the most crucial steps needed to take full advantage of X-ray data – the correct identification allows us to classify an X-ray object (e.g. star, galaxy, or AGN) and estimate its redshift (distance). We use SRG/eROSITA data in the Lockman Hole region to probe the method.

- Our model is based on artificial neural networks which separate photometric attributes of the optical counterparts of X-ray sources and field sources. Models are trained on the data from the Chandra observatory and DESI LIS sources. The entire set of photometric attributes is transformed into one number with those networks.
- In the Lockman Hole region we assemble a validation set of eROSITA X-ray objects with known counterparts, using data from Chandra and XMM-Newton. This validation set is used to estimate and calibrate the performance of our method, and also to calibrate the positional uncertainties of the catalogue.
- We combine the outputs of the neural network with the positional information of the sources in a Bayesian way. The quality of the identification procedure achieves purity and completeness of 95% for the whole catalogue. For bright sub-sample of X-ray sources, the accuracy is even higher. We also report on the quality metrics for the selection of hostless sources (i.e. sources which do not have an optical counterpart).

Chapter 4 report on the catalogue of dwarf galaxies with active cores compiled with the help of SRG/eROSITA data. Cores of active dwarf galaxies are powered by black holes less massive than their quasar counterparts. Such black holes are essential for studying the formation mechanisms of massive black holes.

- We formulate systematic and stringent criteria for the search of X-ray emission from accreting black holes in dwarf galaxies of the MPA-JHU catalogue (derived from SDSS). We removed sporadic matches with quasars, massive galaxies or stars with the help of external catalogues. The resulting catalogue contains 99 dwarf galaxies with X-ray activity in the central regions.
- We analysed X-ray spectra and variability of the sample in detail. We estimate the expected X-ray emission coming from the X-ray binaries and hot interstellar gas in each dwarf. In 82/99 sources the only plausible explanation of X-ray emission is the accretion onto the massive black hole.
- We analyse the properties of host galaxies of active dwarfs and compare them with the parent dwarf population. Emission line diagnostic fails to identify almost all sources as an AGN, instead indicating that they are star-forming galaxies. We estimate the critical accretion rate for dwarfs and find that the majority of sources are accreting on the level of around $1/100$th of the critical (Eddington) accretion rate.
- We calculate the fraction of dwarf galaxies with actively accreting black holes. We find that the AGN fraction spans the values between $\sim 10^{-4}...10^{-2}$ and drops with the increase in X-ray luminosity. AGN fraction also depends on the stellar mass – AGN fraction is larger for galaxies with larger mass. We discuss that the measurements of AGN fractions pose a lower limit on the abundance of massive black holes in low-mass galaxies.

Moreover, the sheer amount of data used in Chapter 4 allowed us to serendipitously discover several X-ray sources with surprising properties.

- We found a transient eROSITA source coinciding with a dwarf galaxy and an optical transient. X-ray spectra and temporal evolution propose that the source may be a tidal disruption event (TDE) in a dwarf galaxy at $z = 0.048$. This adds to a population of a few known TDEs in dwarf galaxies.

- We report on an X-ray source with a thermal spectrum of X-ray emission. The spectrum suggests a disc-dominated state of the system but the black hole mass required by the X-ray spectral fits are order of magnitude less than that inferred from the optical spectrum.

- Sources with absorbed X-ray spectra are found. One of those is a dwarf galaxy with the highest X-ray luminosity recorded in the literature. Another obscured AGN in a dwarf galaxy is variable on the 6-month time scale.

- We discovered a list of galaxies which are located in galaxy pairs (i.e. on the small distance of $\sim 5 - 150$ kpc from another member of a pair). Notably, in four found pairs both members seem to be X-ray active. Such objects are important for studying the AGN triggering mechanism and environment.

- We report three Ultra-luminous X-ray sources (ULX) candidates found in three dwarf galaxies. Those might be of interest for investigations of the host galaxies of ULXs.

In the **second part of this work**, we studied the spectral and timing properties of pulsars in Be X-ray binary systems. We showed that the reprocessed emission (iron K_α line, absorption edge, reflected spectrum), which is almost omnipresent in accreting pulsars, can effectively constrain the geometry of accretion flows. We demonstrate it in the case of two X-ray pulsars.

In Chapter 5 we analysed X-ray spectral and timing data of V 0332+53 during its accretion outburst in 2004. We focused on tracing the variability of the iron spectral features - fluorescent line and absorption edge with the pulsar rotation phase. Iron spectral features depend on the pulse phase in a complicated manner. We argue that the observational picture cannot be self-consistently explained by any of the existing models of emission of accreting pulsars and their geometrical configuration. We list the following important findings:

- In the peak of luminosity, the pulse profile shows two significant and narrow brightness dips of identical shape, separated by the 180-degree rotation of a neutron star.

- The K-edge feature of the spectrum related to neutral absorption apexes at the phase intervals corresponding to the dips. The optical depth necessary for the observed K-edge peak is by a large factor smaller than needed to explain the dips.

- Part of the reflected emission is coming from the donor star and circumstellar material around it. Taking this emission into account and comparing it with the observed pulsations of the iron line, we show that the variable part of the line intensity shows modulation with a large amplitude (by a factor of 10). The line intensity does not show obvious correlations with the brightness profile and the K-edge depth variability.

In Chapter 6 we performed spectral and timing analysis of the Ultra-Luminous X-ray pulsar Swift J0243.6+6124 during its super-Eddington outburst phase.

- The source has a strong reprocessed (reflected) component with a significant iron line, K-edge and Compton hump. Pulse phase-resolved spectral analysis demonstrates significant variations in the fraction of reflected emission in the total spectrum.
- Using a physically-motivated reflection model we show that the modulations of the reflected fractions are driven mainly by the variable direct neutron star emission, whereas the reflected spectrum shows less strong variations. From the Doppler broadening of the iron line, we estimate the inner radius of the reflective material.
- We propose a model where the pulsar is located at the centre of a well, formed by a geometrically thick super-critical accretion disc truncated by the pulsar's magnetic field of moderate value. The inner sides of the structure are irradiated by the accretion column's radiation and produce reflected emission.
- Broad emission diagram of the accretion columns creates a relatively constant irradiation flux, forcing the reflected component to not vary significantly, whereas the direct emission is strongly modulated by the pulsar's rotation.

V 0332+53, Swift J0243 and other X-ray pulsars with significant reprocessed emission provide prosperous opportunities for the development of theoretical models of emission of accreting neutron stars and the geometry of accretion flows around them.

APPENDIX A

Fisher formalism and the MCMC method for cosmological forecast

This appendix is made for Chapter 2.

There are conditions to be met for the Fisher analysis to yield realistic constraints on the parameters of the model. One such condition is that the posterior probability distribution is a multi-dimensional Gaussian distribution. This is clearly not the case for cosmological models since there are non-linear degeneracies in the parameters. However, one might hope that the resulting errors would be small so that the linear approximation holds and the Fisher matrix method indeed produces a sound forecast.

To test the method, we made a Fisher forecast for the case of AGN (eRASS8, $f_{\rm sky} = 0.658$) with follow-up quality $\sigma_0 = 0.03$ and $f_{\rm fail} = 0.1$ and priors 0.05 on h and 0.01 on $n_{\rm s}$. Then, we used COBAYA[1] code for Bayesian analysis in Cosmology (Torrado, Lewis, 2019, 2021) and their implementation of the MCMC (Monte Carlo Markov Chain) Metropolis sampler (Lewis, Bridle, 2002) to probe the posterior. We assumed a Gaussian likelihood with appropriate priors and made 'data' from our data vector, loaded a covariance matrix, and then ran chains until the convergence. In Fig. A.1, we visualise the probability contours of two methods and in Table A.1, we compare the marginalised 68% credible intervals. One can see that under our assumptions the Fisher forecast produces contours and errors consistent with the result of the full MCMC treatment of the problem. Based on the results of this and other similar tests we chose to use the Fisher matrix formalism, which is significantly computationally faster than MCMC, as our baseline tool.

[1] https://cobaya.readthedocs.io

Method	$\Omega_{\rm c}$	$\Omega_{\rm b}$	h	$n_{\rm s}$	σ_8
MCMC	$0.250^{+0.013}_{-0.014}$	$\left(49.9^{+6.3}_{-6.1}\right) \times 10^{-3}$	$0.696^{+0.045}_{-0.038}$	$\left(959.4^{+10.3}_{-10.0}\right) \times 10^{-3}$	$\left(800.1^{+4.0}_{-4.5}\right) \times 10^{-3}$
Fisher	$0.250^{+0.013}_{-0.013}$	$\left(50.0^{+6.0}_{-6.0}\right) \times 10^{-3}$	$0.700^{+0.041}_{-0.041}$	$\left(960.0^{+9.8}_{-9.8}\right) \times 10^{-3}$	$\left(800.0^{+4.0}_{-4.0}\right) \times 10^{-3}$

Table A.1: Table corresponding to Fig. A.1. The values of the mean of the parameters and corresponding marginalised errors are shown for the MCMC method and the Fisher forecast.

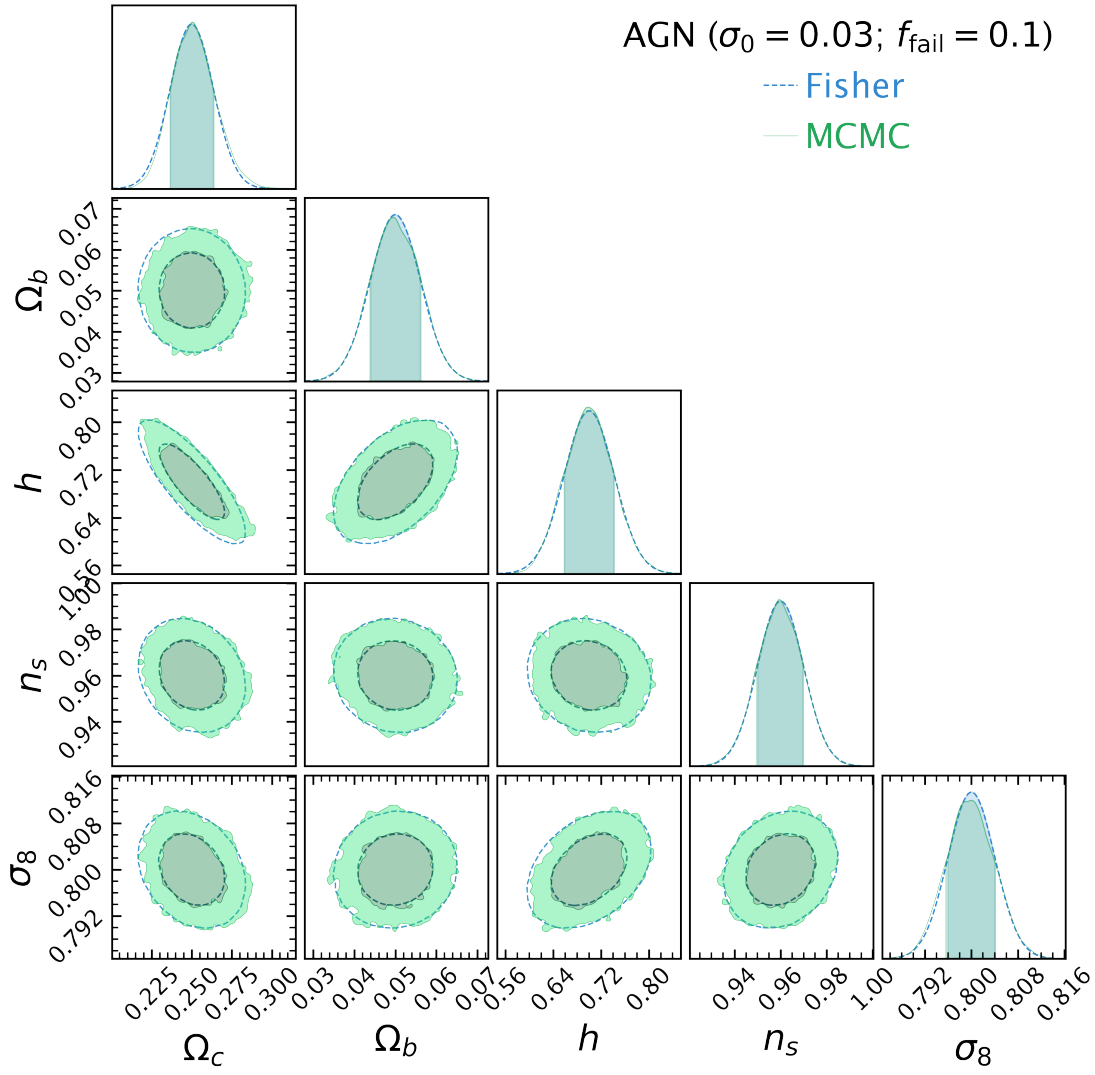

Figure A.1: Error ellipses of cosmological parameter estimation from the angular power spectra for the case of AGNs ($\sigma_0 = 0.03$, $f_{\text{fail}} = 0.1$) with priors. Blue dashed ellipses are the result of the Fisher forecast, whilst the shaded regions show the result of MCMC sampling done in COBAYA. Darker areas correspond to the 68% probability contour and the lighter areas to 95%. On the diagonal of the plot grid, the marginalised histograms of the corresponding parameter are shown. The Fisher formalism provides a forecast in good agreement with the MCMC results.

APPENDIX B

Small-scale clustering simulations forecast

This appendix is made for Chapter 2.

To create a field of sources on the sky we use HEALPix `synfast` command and the Poisson sampling of the density field. In the first step, we generate the angular power spectrum of sources in particular redshift range as described in sect. 2.4. We use a non-linear matter power spectrum calculated with *halofit* (Takahashi et al., 2012) model in the CCL library. Then we use `synfast` command form HEALPy library to create an overdensity Gaussian field $\delta_{\rm AGN}$ with the power spectra equal to the input APS of sources. In the next step, we multiply the density field $1+\delta_{\rm AGN}$ by the expected AGN number per pixel and Poisson-sample the density field. If the density field has a negative value we assign its density to zero (it happens in less than 5% of pixels). If the Poisson-sampled pixel has a value ≥ 2 we assign it to 1 (it happens in less than 0.5% pixels of Poisson source maps). Such pixel replacements affect slightly the APS of the source map, but for our simple computation, this should not alter the small-scale clustering dramatically. We use `NSIDE` of 4096 with pixel resolution $\approx 10^{-2}$ deg. With such a source map of all sky, we divide its full area into several non-overlapping rectangular areas with dimensions 4×5 deg (to simulate Lockman Hole survey, 101 rectangles) and 20×7 deg (to simulate eFEDS, 21 rectangles). We then measure the angular correlation functions (ACF) of sources with TreeCorr[1] (Jarvis et al., 2004) package and write down the resulting ACF. Finally, we find the mean and standard deviation of the ACF measurements in logarithmic bins between 3×10^{-2} deg and ~ 1 deg. The results are presented in Fig. 2.8. The significance of the signal was measured after the inversion of the covariance matrix found in simulations.

[1] `https://rmjarvis.github.io/TreeCorr/_build/html/index.html`

APPENDIX C

Active dwarf galaxies catalogue description

C.1 Catalogue of dwarfs

This appendix is made for Chapter 4. Accompanying text files can be found on the MNRAS website after the online publication of the paper.

In the accompanying text file DWARFS.CSV one finds the catalogue of 99 X-ray selected dwarfs. It has 99 rows and 67 columns. Columns include the relevant identification information; positional information (optical/X-ray coordinates, separations); host galaxy properties - redshift, mass, star formation rate, expected X-ray binaries population, emission line intensities relevant for the BPT diagram; object identification according to SIMBAD; X-ray information - detection likelihood, positional errors, source counts, X-ray luminosities in several bands, variability parameter, fiducial spectral model. When possible, errors are provided for either 68% or 90% intervals. The header of the file explains every column.

Table C.1 presents a quick-look subset of columns for all 82 dwarfs with $\frac{L_{\rm X,obs}}{L_{\rm X,XRB}} > 3$. Namely, optical and X-ray coordinates, host properties (redshift, stellar mass, star formation rate), X-ray luminosity, and its ratio to the expected XRB contribution.

In the attached pdf file DWARFS_STAMPS.PDF an image of every dwarf can be found (as in Fig. 4.1).

C.2 Catalogue of excluded sources

In the accompanying text file REJECTED.CSV one may find the catalogue of 79 eROSITA sources which were cleaned in sect. 4.3.1 with the appropriate rejection reason. The structure of the catalogue is similar to that of 99 dwarfs but without XRB population, emission line intensities, X-ray luminosities (only fluxes) and variability parameter[1].

Some examples of excluded sources are shown in Fig. C.1 with the reason for exclusion marked. All images can be found in the attached pdf file EXCLUDED_STAMPS.PDF (as in Fig. 4.1).

[1]X-ray spectral analysis was not performed for excluded sources

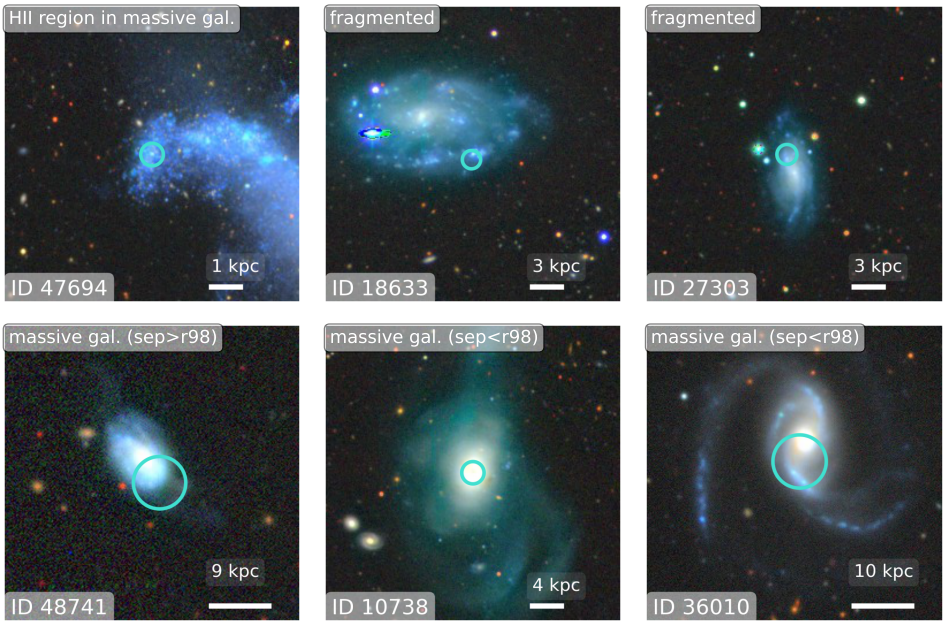

Figure C.1: As Fig. 4.1, but for galaxies which were cleaned during the cross-match process. Each galaxy has an ID on the bottom left, and the reason for exclusion on the top left. All except 10738 and 36010 were removed after visual inspection, and 10738 and 36010 were removed automatically as per massive galaxy within r_{98} criterion. 27303 is a notable example of a dwarf galaxy with an eROSITA source in the outskirts.

Table C.1: SRG/eROSITA–SDSS catalogue of dwarf galaxies with nuclear X-ray activity

ID[(1)]	RA[(2)]	DEC[(3)]	Simbad[(4)]	z[(5)]	ID_X[(6)]	RA_X[(7)]	DEC_X[(8)]	σ_X[(9)]	M_*, $M_\odot$[(10)]	$L_{X,0.3-8}$ erg s^{-1}[(11)]	$\frac{L_{X,0.5-8}}{L_{X,XRB}}$[(12)]
2349	253.88911	63.24213	NGC 6275	0.023	SRGe J165533.6+631432	253.88992	63.24216	5.8	$2.1^{+1.1}_{-0.4} \times 10^9$	$3.4 \pm 0.7 \times 10^{40}$	3.1
2364	253.90256	64.01973	SDSSCGB 51726.2	0.023	SRGe J165536.2+640107	253.90074	64.01858	5.6	$5.5^{+2.2}_{-1.6} \times 10^7$	$1.7 \pm 0.7 \times 10^{40}$	302.4
2506	262.31793	59.56275	SDSS J172916.31+593346.0	0.018	SRGe J172915.7+593345	262.31561	59.5625	6.4	$2.0^{+0.34}_{-0.24} \times 10^8$	$1.3 \pm 0.4 \times 10^{40}$	19.9
2556	262.07526	60.94234	UGC 10880	0.013	SRGe J172817.5+605630	262.07297	60.9416	8.5	$1.22^{+0.5}_{-0.21} \times 10^6$	$5.8 \pm 1.7 \times 10^{39}$	5×10^3
2595	257.75494	56.90007	SDSS J171101.19+565400.2	0.028	SRGe J171101.4+565401	257.75573	56.90038	7.2	$6.9^{+1.6}_{-0.9} \times 10^8$	$2.3 \pm 1.1 \times 10^{40}$	24.6
3474	7.71736	0.52872	LEDA 1881	0.019	SRGe J003051.9+003149	7.71617	0.53035	10.8	$1.13^{+0.21}_{-0.13} \times 10^9$	$2.2 \pm 1.5 \times 10^{40}$	7.9
4296	38.44556	-1.02454	SDSS J023346.93-010128.3	0.049	SRGe J023346.8-010129	38.44505	-1.02478	5.0	$2.9^{+1.0}_{-0.6} \times 10^9$	$2.01 \pm 0.28 \times 10^{42}$	385.6
5545	29.86125	14.83424	LEDA 1468320	7.0×10^{-3}	SRGe J015926.8+145002	29.86185	14.83388	5.4	$2.52^{+0.5}_{-0.33} \times 10^8$	$4.1 \pm 0.9 \times 10^{40}$	123.5
7394	195.00429	66.87216	-	0.048	SRGe J130000.5+665216	195.00222	66.871	5.4	$2.1^{+0.5}_{-0.35} \times 10^9$	$1.14 \pm 0.17 \times 10^{42}$	543.2
9225	143.50993	55.23978	Mrk 116B	2.6×10^{-3}	SRGe J093402.0+551427	143.5085	55.24084	5.6	$1.098^{+0.6}_{-0.03} \times 10^6$	$5.0 \pm 0.9 \times 10^{39}$	11.9
10487	233.60663	4.1352	[RGG2013] 123	0.04	SRGe J153425.5+040806	233.60638	4.13505	5.0	$2.5 \pm 0.7 \times 10^9$	$9.3 \pm 1.2 \times 10^{41}$	222.0
10619	173.33403	63.27942	UGC 6534	4.1×10^{-3}	SRGe J113320.8+631646	173.33667	63.2795	11.3	$2.5^{+0.7}_{-0.4} \times 10^6$	$2.5 \pm 1.1 \times 10^{39}$	1.9×10^3
11048	233.80957	57.51482	2MASX J15351422+5730529	0.01	SRGe J153513.7+573053	233.80694	57.51461	6.1	$6.1^{+1.6}_{-0.9} \times 10^8$	$7.6 \pm 2.3 \times 10^{39}$	11.8
11092	233.36633	53.51831	SDSS J153327.91+533105.9	0.087	SRGe J153326.8+533105	233.36171	53.51814	10.1	$1.8^{+1.4}_{-0.6} \times 10^9$	$4.2 \pm 1.8 \times 10^{41}$	21.1
11124	234.2674	55.26406	SDSS J153704.18+551550.5	3.5×10^{-3}	SRGe J153704.5+551550	234.26857	55.26376	5.0	$7.7^{+1.5}_{-1.2} \times 10^6$	$1.79 \pm 0.17 \times 10^{40}$	113.8
11195	237.02917	55.719	NVSS J154806+554305	0.04	SRGe J154806.7+554307	237.02774	55.71859	10.2	$2.1^{+0.7}_{-0.4} \times 10^7$	$9.0 \pm 3.5 \times 10^{40}$	255.1
11289	242.79799	48.33444	2MASX J16111153+4820036	9.4×10^{-3}	SRGe J161111.5+482005	242.79792	48.33472	6.7	$3.4^{+0.7}_{-0.4} \times 10^8$	$6.9 \pm 1.9 \times 10^{39}$	5.0
11291	243.02216	48.8183	-	0.02	SRGe J161205.4+484905	243.02259	48.8181	7.0	$1.88^{+0.31}_{-0.21} \times 10^8$	$2.7 \pm 0.9 \times 10^{40}$	44.3
11530	249.91254	43.29555	MCG+07-34-128	0.016	SRGe J163938.9+431741	249.91211	43.29459	12.2	$1.94^{+0.4}_{-0.25} \times 10^9$	$1.5 \pm 0.6 \times 10^{40}$	5.2
11568	250.23807	44.94012	[VV2003c] J164057.1+445624	0.018	SRGe J164056.8+445620	250.23652	44.93901	8.7	$8.0^{+1.5}_{-1.3} \times 10^7$	$1.2 \pm 0.6 \times 10^{40}$	29.9
11569	250.68242	45.71156	LEDA 2269311	0.015	SRGe J164243.4+454244	250.68074	45.71209	10.1	$1.2^{+0.26}_{-0.16} \times 10^8$	$2.1 \pm 0.6 \times 10^{40}$	39.5
11622	254.62193	40.95593	SDSS J165829.26+405721.5	0.028	SRGe J165829.7+405721	254.62361	40.95597	12.5	$4.2^{+0.6}_{-0.5} \times 10^8$	$8.6 \pm 2.2 \times 10^{40}$	69.2
11958	356.44275	-8.78514	LEDA 999228	0.056	SRGe J234545.4-084707	356.43932	-8.7854	12.6	$2.16^{+0.5}_{-0.28} \times 10^9$	$3.6 \pm 2.0 \times 10^{41}$	69.1
12509	26.14118	-8.7731	MCG-02-05-039	0.03	SRGe J014433.6-084630	26.14016	-8.77513	10.3	$2.91^{+0.4}_{-0.3} \times 10^9$	$10 \pm 4. \times 10^{40}$	9.1
12608	32.92161	-9.30599	NGC 853	5.0×10^{-3}	SRGe J021141.3-091817	32.92202	-9.30458	11.2	$3.4^{+0.5}_{-0.4} \times 10^6$	$3.3 \pm 1.0 \times 10^{39}$	454.7
13693	336.8779	-9.66499	LEDA 988084	5.7×10^{-3}	SRGe J222730.9-093959	336.87871	-9.66634	7.2	$2.6^{+0.7}_{-0.4} \times 10^7$	$8.8 \pm 3.1 \times 10^{39}$	13.2
15429	206.67245	59.82294	MCG+10-20-028	6.2×10^{-3}	SRGe J134641.8+594925	206.67409	59.82353	8.9	$5.1^{+1.3}_{-1.0} \times 10^8$	$3.7 \pm 1.5 \times 10^{39}$	15.2
15677	232.06538	52.84361	-	0.019	SRGe J152816.3+525041	232.06794	52.84466	8.7	$2.6^{+0.7}_{-0.4} \times 10^8$	$1.9 \pm 1.3 \times 10^{40}$	38.1
16640	42.39076	0.04646	LEDA 1155772	0.186	SRGe J024933.7+000245	42.39057	0.0458	11.3	$1.3^{+1.5}_{-0.8} \times 10^8$	$1.22 \pm 0.28 \times 10^{43}$	4.5×10^5
18466	151.82887	47.00639	UGC 5451	2.4×10^{-3}	SRGe J100718.9+470020	151.82873	47.00552	9.6	$1.2^{+0.28}_{-0.2} \times 10^8$	$1.1 \pm 0.4 \times 10^{39}$	16.4
18549	164.24457	50.14062	2MASX J10565868+5008256	4.6×10^{-3}	SRGe J105658.8+500828	164.24494	50.14115	6.7	$1.06^{+0.4}_{-0.17} \times 10^8$	$5.6 \pm 1.5 \times 10^{39}$	23.3
18900	187.5442	52.76308	LEDA 2423061	0.06	SRGe J123011.3+524543	187.54727	52.76196	8.5	$2.6^{+1.3}_{-0.4} \times 10^9$	$5.9 \pm 2.3 \times 10^{41}$	157.7
19521	158.13281	54.40104	Mrk 33	9.8×10^{-3}	SRGe J103232.0+542401	158.13351	54.40027	8.1	$9.5^{+4.0}_{-1.7} \times 10^8$	$4.2 \pm 0.8 \times 10^{40}$	18.6
20701	158.5423	58.06363	Mrk 1434	7.5×10^{-3}	SRGe J103410.1+580347	158.54189	58.0631	5.9	$1.0^{+0.5}_{-0.04} \times 10^7$	$1.5 \pm 0.5 \times 10^{40}$	41.0
20867	171.68462	59.15545	IC 691	5.5×10^{-3}	SRGe J112644.4+590921	171.68514	59.15595	8.0	$9.3^{+4.0}_{-1.6} \times 10^8$	$1.37 \pm 0.26 \times 10^{40}$	4.9
20929	176.93875	59.88667	MCG+10-17-072	4.3×10^{-3}	SRGe J114745.9+595304	176.94125	59.88458	10.0	$1.7^{+0.8}_{-0.4} \times 10^8$	$2.4 \pm 1.0 \times 10^{39}$	5.5
20944	184.00491	59.50806	Mrk 1468	0.015	SRGe J121601.4+593024	184.00592	59.50675	8.4	$2.0^{+0.7}_{-0.4} \times 10^9$	$2.3 \pm 0.5 \times 10^{41}$	62.3
21021	186.27255	61.15314	SDSS J122505.40+610911.7	2.3×10^{-3}	SRGe J122505.3+610912	186.27217	61.15329	6.8	$8.5^{+2.4}_{-0.5} \times 10^6$	$1.27 \pm 0.31 \times 10^{39}$	3.7
21115	197.96373	60.24735	UGC 8282	0.011	SRGe J131151.3+601455	197.96392	60.24863	8.4	$3.3^{+0.5}_{-0.4} \times 10^8$	$1.5 \pm 0.6 \times 10^{40}$	26.5
22648	167.01215	53.61681	UGC 6182	4.1×10^{-3}	SRGe J110803.3+533700	167.01393	53.61657	9.1	$1.17^{+0.26}_{-0.16} \times 10^6$	$4.4 \pm 1.6 \times 10^{39}$	1.9×10^3
22933	183.35844	54.60879	SDSS J121326.03+543631.7	8.0×10^{-3}	SRGe J121325.9+543632	183.35809	54.60893	7.3	$2.43^{+0.4}_{-0.28} \times 10^7$	$1.5 \pm 0.4 \times 10^{40}$	161.7
23630	320.71609	-0.99672	SDSS J212252.00-005949.4	0.184	SRGe J212252.0-005957	320.71659	-0.99911	9.3	$2.82^{+0.5}_{-0.32} \times 10^9$	$1.8 \pm 0.5 \times 10^{43}$	859.9

Continued on next page

Table C.1: SRG/eROSITA–SDSS catalogue of dwarf galaxies with nuclear X-ray activity

ID[(1)]	RA[(2)]	DEC[(3)]	Simbad[(4)]	z[(5)]	ID$_X$[(6)]	RA$_X$[(7)]	DEC$_X$[(8)]	σ_X[(9)]	M_*, $M_\odot$[(10)]	$L_{X,0.3-8}$ erg s^{-1}[(11)]	$\frac{L_{X,0.5-8}}{L_{X,XRB}}$[(12)]
25180	214.87833	51.92448	MCG+09-23-060	0.029	SRGe J141931.2+515528	214.88	51.92432	7.4	$2.76^{+0.5}_{-0.35} \times 10^9$	$1.36 \pm 0.34 \times 10^{41}$	87.8
25337	228.05357	47.27519	LEDA 87385	0.053	SRGe J151212.9+471635	228.05386	47.27634	8.7	$1.31^{+0.4}_{-0.26} \times 10^9$	$2.3 \pm 0.8 \times 10^{41}$	3.8
27238	227.16699	52.45378	Mrk 846	0.011	SRGe J150840.4+522713	227.16818	52.45371	6.9	$1.90^{+0.5}_{-0.28} \times 10^9$	$4.7 \pm 1.2 \times 10^{40}$	19.5
28027	139.34045	41.91099	UGC 4904	5.6×10^{-3}	SRGe J091721.1+415439	139.33812	41.91083	8.8	$1.09^{+0.28}_{-0.12} \times 10^6$	$6.3 \pm 2.5 \times 10^{39}$	9.9×10^3
30754	180.76497	56.91676	LEDA 2551818	0.019	SRGe J120303.9+565500	180.76619	56.91658	7.0	$2.7^{+0.7}_{-0.5} \times 10^9$	$1.16 \pm 0.26 \times 10^{41}$	79.1
30769	182.85503	58.75883	SBSG 1209+590	0.011	SRGe J121124.6+584540	182.85253	58.76102	9.4	$3.9^{+0.5}_{-0.4} \times 10^8$	$1.7 \pm 0.6 \times 10^{40}$	8.5
30874	200.21776	57.64159	NGC 5109	7.0×10^{-3}	SRGe J132053.1+573833	200.22106	57.64258	8.1	$1.1^{+1.1}_{-0.7} \times 10^9$	$7.4 \pm 2.3 \times 10^{39}$	20.6
30902	201.47424	57.25445	Mrk 66	0.021	SRGe J132554.2+571518	201.47571	57.25493	10.2	$1.90^{+0.21}_{-0.18} \times 10^9$	$5.7 \pm 2.3 \times 10^{40}$	7.2
31794	216.3376	39.53958	UGC 9242	5.5×10^{-3}	SRGe J142521.3+393223	216.33894	39.5397	9.4	$2.9^{+0.6}_{-0.4} \times 10^8$	$2.8 \pm 1.0 \times 10^{39}$	6.7
32206	166.28383	44.74646	[BKD2008] WR 276	0.022	SRGe J110508.3+444455	166.28462	44.74856	9.3	$4.9^{+0.6}_{-0.7} \times 10^8$	$7.3 \pm 2.9 \times 10^{40}$	3.4
32658	206.99294	39.38945	LEDA 2148943	9.3×10^{-3}	SRGe J134758.2+392325	206.99243	39.39034	8.8	$9.4^{+2.1}_{-1.2} \times 10^7$	$5.4 \pm 2.7 \times 10^{39}$	32.5
33466	253.33936	23.08278	SDSS J165321.44+230458.0	0.036	SRGe J165321.9+230500	253.34143	23.08311	9.8	$3.0^{+0.7}_{-0.4} \times 10^9$	$1.5 \pm 0.7 \times 10^{41}$	38.8
34306	177.55119	42.0745	UGC 6805	3.9×10^{-3}	SRGe J115012.4+420427	177.5515	42.07431	10.1	$4.1^{+1.0}_{-0.7} \times 10^8$	$2.1 \pm 0.9 \times 10^{39}$	4.9
34500	181.94214	43.12635	NGC 4117	4.7×10^{-3}	SRGe J120746.3+430733	181.94302	43.12581	9.7	$2.2^{+0.5}_{-0.4} \times 10^9$	$2.7 \pm 1.2 \times 10^{39}$	4.9
37144	41.71429	-0.48567	-	0.044	SRGe J024651.9-002909	41.71637	-0.48585	8.4	$1.3^{+2.0}_{-1.9} \times 10^9$	$2.0 \pm 0.9 \times 10^{41}$	746.5
39439	215.28319	35.29539	MCG+06-32-004	0.012	SRGe J142108.6+351741	215.28596	35.29464	9.8	$2.9^{+1.5}_{-0.4} \times 10^8$	$1.2 \pm 0.5 \times 10^{40}$	3.3
39591	230.56068	31.47515	Mrk 850	7.3×10^{-3}	SRGe J152214.7+312832	230.56111	31.47566	6.5	$2.2^{+1.4}_{-0.7} \times 10^7$	$7.5 \pm 1.9 \times 10^{39}$	13.7
39731	242.73491	23.99648	SDSS J161056.37+235947.3	0.033	SRGe J161056.1+235950	242.73375	23.99715	8.0	$1.4^{+1.7}_{-1.0} \times 10^9$	$1.6 \pm 0.5 \times 10^{41}$	527.9
39846	49.62766	40.50241	LEDA 2166728	0.026	SRGe J031830.3+403004	49.62641	40.50113	10.4	$1.01^{+0.18}_{-0.12} \times 10^9$	$9. \pm 4. \times 10^{40}$	51.8
41568	229.95583	8.07313	SDSS J151949.39+080423.2	0.042	SRGe J151949.8+080428	229.95769	8.07432	7.9	$1.83^{+0.4}_{-0.28} \times 10^9$	$2.4 \pm 0.9 \times 10^{41}$	111.7
43461	137.56142	59.95417	UGC 4808	4.4×10^{-3}	SRGe J091015.0+595710	137.56234	59.95288	6.5	$2.7^{+0.6}_{-0.5} \times 10^8$	$7.5 \pm 1.6 \times 10^{39}$	115.3
44628	231.65569	6.99491	2MASS J15263736+0659417	0.038	SRGe J152637.5+065942	231.65612	6.99489	5.0	$2.6^{+0.9}_{-0.7} \times 10^9$	$5.02 \pm 0.26 \times 10^{42}$	777.2
45689	313.08316	0.05463	-	0.211	SRGe J205220.2+000319	313.08396	0.05528	6.7	$5.^{+25}_{-5.} \times 10^8$	$9.1 \pm 1.9 \times 10^{43}$	8.6×10^5
47785	203.8987	29.21744	UGC 8578	4.1×10^{-3}	SRGe J133535.6+291306	203.89854	29.21821	5.0	$1.45^{+0.29}_{-0.26} \times 10^6$	$6.6 \pm 1.1 \times 10^{39}$	1.5×10^3
49241	186.45361	33.54687	NGC 4395	1.0×10^{-3}	SRGe J122548.6+333247	186.45266	33.54625	7.2	$2.5^{+0.7}_{-0.5} \times 10^7$	$1.04 \pm 0.28 \times 10^{39}$	191.9
49754	196.48788	32.839	LEDA 2014266	0.018	SRGe J130557.6+325013	196.49004	32.83702	14.0	$6.7^{+1.0}_{-0.7} \times 10^8$	$3.0 \pm 1.5 \times 10^{40}$	17.7
50706	176.60869	34.85195	Mrk 429	5.8×10^{-3}	SRGe J114625.8+345105	176.60744	34.85128	14.8	$2.6^{+0.6}_{-0.4} \times 10^7$	$3.5 \pm 2.0 \times 10^{39}$	53.4
50842	205.80479	36.74931	2MASX J13431319+3644574	0.02	SRGe J134313.2+364455	205.80521	36.74859	5.9	$1.87^{+0.70}_{-0.34} \times 10^9$	$1.71 \pm 0.24 \times 10^{41}$	25.4
50909	201.08405	36.59609	Mrk 451	0.016	SRGe J132419.9+363552	201.08301	36.59783	11.1	$2.2^{+1.2}_{-0.6} \times 10^9$	$8.1 \pm 3.2 \times 10^{40}$	6.9
51004	200.30437	31.22184	UGC 8392	0.017	SRGe J132113.0+311303	200.30419	31.21747	16.1	$2.9^{+0.6}_{-0.4} \times 10^9$	$10 \pm 4. \times 10^{40}$	91.8
52047	217.16235	30.63451	Z 163-59	0.013	SRGe J142838.7+303809	217.16116	30.63569	9.7	$1.43^{+0.4}_{-0.26} \times 10^9$	$5.1 \pm 1.7 \times 10^{40}$	33.4
52077	217.22009	27.8344	2MASS J14285283+2750037	0.016	SRGe J142852.8+275005	217.2198	27.83462	8.8	$1.12^{+0.23}_{-0.14} \times 10^9$	$1.4 \pm 0.8 \times 10^{40}$	7.2
52695	227.23254	25.73327	UGC 9739	7.3×10^{-3}	SRGe J150856.4+254359	227.23492	25.73296	11.3	$7.4^{+1.2}_{-0.7} \times 10^7$	$5.1 \pm 1.8 \times 10^{39}$	24.1
53431	241.38271	17.80728	2XMM J160531.8+174825	0.032	SRGe J160531.8+174824	241.38247	17.80677	6.9	$1.64^{+0.4}_{-0.31} \times 10^9$	$2.8 \pm 0.7 \times 10^{41}$	224.9
57825	162.58224	48.33294	-	0.098	SRGe J105019.2+481958	162.58002	48.33282	11.0	$7.5^{+2.7}_{-1.2} \times 10^8$	$1.1 \pm 0.6 \times 10^{42}$	258.3
63593	213.63451	17.98318	ECO 2507	0.024	SRGe J141432.4+175900	213.63489	17.98327	9.5	$1.43^{+0.17}_{-0.15} \times 10^8$	$5.6 \pm 2.3 \times 10^{40}$	9.9
63898	233.69412	12.44725	LEDA 3091021	9.0×10^{-3}	SRGe J153446.8+122654	233.69496	12.44838	9.1	$9.6^{+1.2}_{-0.9} \times 10^7$	$1.4 \pm 0.4 \times 10^{40}$	37.6
64321	233.64713	15.20097	NGC 5954	7.5×10^{-3}	SRGe J153435.1+151203	233.64612	15.20094	9.0	$7.9^{+7.0}_{-3.0} \times 10^6$	$1.08 \pm 0.31 \times 10^{40}$	40.5
64653	234.13292	16.44037	UGC 9925	0.011	SRGe J153632.1+162628	234.13383	16.44113	5.6	$6.8^{+1.7}_{-1.2} \times 10^8$	$4.4 \pm 0.8 \times 10^{40}$	163.3
65319	240.86063	19.16268	Mrk 296	0.016	SRGe J160326.5+190940	240.86027	19.16108	7.7	$2.1^{+2.1}_{-1.3} \times 10^9$	$2.1 \pm 0.9 \times 10^{40}$	22.7

Continued on next page

Table C.1: SRG/eROSITA–SDSS catalogue of dwarf galaxies with nuclear X-ray activity

ID(1)	RA(2)	DEC(3)	Simbad(4)	z(5)	ID_X(6)	RA_X(7)	DEC_X(8)	σ_X(9)	M_*, $M_\odot$(10)	$L_{X,0.3-8}$ erg s^{-1}(11)	$\frac{L_{X,0.5-8}}{L_{X,XRB}}$(12)

(1) - ID from this paper; (2,3) - SDSS fibre position in deg, (4) Galaxy name from Simbad; (5) redshift; (6,7,8) eROSITA name, coordinates (in deg); (9) eROSITA positional error, radius of the 98% probability circle in arcsec ; (10) Stellar mass (solar masses); (11) X-ray luminosity in the 0.3–8 keV energy range (erg/s); (12) ratio of the observed X-ray luminosity to the expected X-ray binary emission (0.5–8 keV).

APPENDIX D

RXTE/PCA observation log for V 0332+53

This appendix is made for Chapter 5.

Table D.1 shows an observation log of RXTE/PCA, data used in this work (Group number, Observation ID, exposure, time and configuration used in phase-resolved spectroscopy), and the main parameters of spectral fits: reduced chi-squared value (11 dof), flux and equivalent width of the iron line, and flux in 3–12 keV band, and the intensity of the iron line.

Table D.1: The log of RXTE/PCA observations of the 2004-2005 outburst of V 0332+53.

Gr.	ObsID	Time MJD	Exposure s	Configuration*	χ^2_{red}	Eq. width eV	Flux (3-12 keV) $10^{-9}\times$ erg cm^{-2} s^{-1}	Iron line int 10^{-3} phot cm^{-2} s^{-1}
-	90089-11-01-00	53336.6	160	-	1.06	64^{+28}_{-34}	$5.48^{+0.05}_{-0.03}$	$3.7^{+1.3}_{-1.6}$
-	90089-11-01-02	53340.3	2688	-	0.93	67^{+6}_{-7}	8.85 ± 0.02	6.3 ± 0.6
-	90089-11-01-03	53341.1	2912	-	0.78	67 ± 6	10.20 ± 0.02	7.3 ± 0.7
-	90089-11-01-04	53341.8	1760	-	0.54	71^{+6}_{-8}	$10.82^{+0.02}_{-0.01}$	$8.2^{+0.6}_{-0.8}$
-	90089-11-02-00	53342.8	11584	-	1.49	75 ± 5	11.70 ± 0.01	9.3 ± 0.4
-	90089-11-02-05	53343.0	1712	-	1.52	76^{+7}_{-8}	11.62 ± 0.02	9.3 ± 0.7
-	90089-11-02-06	53343.1	2288	-	1.51	71^{+6}_{-7}	12.06 ± 0.02	9.1 ± 0.6
-	90089-11-02-01	53343.2	2000	-	1.43	70^{+8}_{-6}	11.96 ± 0.02	8.9 ± 0.6
-	90089-11-02-02	53343.4	1424	-	1.88	83^{+7}_{-6}	12.44 ± 0.02	10.9 ± 0.7
-	90089-11-02-03G	53343.5	10400	-	1.86	77 ± 4	12.28 ± 0.01	10.0 ± 0.5
-	90089-11-02-03	53343.8	11680	-	2.07	77 ± 4	12.63 ± 0.01	10.3 ± 0.5
-	90089-11-02-07	53344.0	1824	-	1.51	69^{+6}_{-7}	12.92 ± 0.02	9.6 ± 0.7
-	90089-11-02-04	53344.5	2816	-	1.48	76^{+6}_{-5}	13.50 ± 0.02	11.0 ± 0.6
-	90089-11-02-10	53344.7	1936	-	2.19	68^{+9}_{-5}	13.96 ± 0.02	10.1 ± 0.7
-	90089-11-02-09	53345.7	2000	-	2.59	67^{+8}_{-6}	$15.31^{+0.03}_{-0.02}$	10.9 ± 0.8
-	90089-11-02-08	53346.7	1408	-	0.66	66^{+7}_{-6}	16.32 ± 0.03	11.5 ± 1.2
-	90089-11-03-03	53352.8	1152	-	1.15	64^{+5}_{-6}	26.30 ± 0.05	18.5 ± 1.8
-	90089-11-03-04	53353.7	3168	-	0.87	73^{+5}_{-4}	28.04 ± 0.04	22.7 ± 1.5
I	90089-11-03-00G	53354.5	4416	X	0.67	71^{+4}_{-5}	28.60 ± 0.04	22.3 ± 1.5
I	90089-11-03-01G	53354.6	10768	X	0.48	73 ± 4	28.76 ± 0.04	23.3 ± 1.4
I	90089-11-03-02	53354.9	2128	X	0.78	73 ± 6	28.68 ± 0.04	23.1 ± 1.6
-	90089-11-03-05	53355.1	1904	-	0.63	77^{+6}_{-5}	29.21 ± 0.04	25.0 ± 1.7
-	90089-11-04-00G	53356.5	3008	-	0.63	79 ± 4	30.68 ± 0.04	26.8 ± 1.6
-	90089-11-04-01	53357.1	1808	-	0.90	78^{+6}_{-4}	31.40 ± 0.05	27.2 ± 1.8
-	90089-11-04-02G	53358.6	2672	-	0.54	77^{+5}_{-6}	31.83 ± 0.04	27.3 ± 1.7
-	90089-11-04-03	53358.8	1216	-	0.66	77^{+5}_{-6}	31.82 ± 0.05	27.3 ± 2.0
-	90089-11-04-04	53360.0	1600	-	0.98	79^{+6}_{-4}	33.42 ± 0.05	29.6 ± 2.0
-	90089-11-04-05	53361.1	944	-	0.76	75 ± 7	33.52 ± 0.06	28.2 ± 2.3
-	90089-11-05-00G	53363.2	2768	-	0.89	82^{+4}_{-6}	34.77 ± 0.05	32.2 ± 1.9
-	90089-22-01-00G	53363.4	20544	-	0.39	84^{+6}_{-4}	35.32 ± 0.04	33.6 ± 1.7
-	90089-22-01-01G	53364.4	21792	-	0.58	84^{+3}_{-5}	34.78 ± 0.04	33.0 ± 1.6
-	90089-11-05-01	53364.9	1968	-	0.65	88^{+5}_{-4}	35.36 ± 0.05	35.5 ± 2.0
-	90089-11-05-08G	53365.3	15392	-	0.59	93 ± 4	35.55 ± 0.04	37.6 ± 1.7
-	90089-11-05-02	53365.9	624	-	0.63	84^{+6}_{-7}	35.59 ± 0.07	34.2 ± 2.7
-	90427-01-01-00G	53367.2	1584	-	1.03	88^{+6}_{-4}	34.78 ± 0.05	34.6 ± 2.1
-	90427-01-01-01	53368.2	2240	-	0.82	83 ± 5	34.10 ± 0.05	32.3 ± 1.9
-	90427-01-01-02	53368.9	1264	-	0.37	83^{+4}_{-6}	34.38 ± 0.05	32.6 ± 2.2
-	90427-01-01-03	53369.6	1872	-	0.67	78 ± 6	33.84 ± 0.05	29.8 ± 2.0
-	90427-01-02-02	53376.3	688	-	1.39	60^{+6}_{-7}	28.48 ± 0.06	19.1 ± 2.2
-	90427-01-02-03	53376.6	2240	-	0.94	68 ± 6	28.76 ± 0.04	22.0 ± 1.6
-	90014-01-01-00	53378.4	1040	-	0.98	67^{+5}_{-6}	27.33 ± 0.05	20.3 ± 1.9
-	90014-01-01-06	53378.6	1344	-	0.54	77 ± 6	27.09 ± 0.05	23.1 ± 1.7
-	90014-01-01-07	53378.7	1744	-	0.76	71^{+6}_{-5}	26.62 ± 0.04	20.9 ± 1.6
-	90014-01-01-03	53380.5	8144	-	0.76	67 ± 4	23.38 ± 0.03	17.4 ± 1.1
-	90014-01-01-02	53381.0	1376	-	1.23	68^{+7}_{-6}	22.87 ± 0.04	17.2 ± 1.5
-	90014-01-01-01	53381.3	3280	-	1.12	75 ± 5	23.48 ± 0.03	19.5 ± 1.3
-	90014-01-01-04	53381.5	2784	-	0.52	67 ± 5	22.81 ± 0.03	16.8 ± 1.3
-	90014-01-01-05	53381.6	2176	-	0.54	71 ± 6	22.12 ± 0.04	17.2 ± 1.3
II	90427-01-03-00	53384.4	13152	Y	0.66	73 ± 4	19.79 ± 0.02	16.0 ± 0.9
II	90427-01-03-01	53385.0	9776	Y	0.68	70^{+5}_{-3}	19.34 ± 0.02	14.8 ± 0.9
II	90427-01-03-02	53385.3	12272	Y	1.02	70^{+4}_{-5}	19.04 ± 0.02	14.7 ± 0.9
-	90014-01-02-03	53385.9	1200	Y	1.26	75^{+6}_{-7}	18.34 ± 0.04	15.0 ± 1.3
III	90427-01-03-14G	53385.9	12512	Y	0.70	68^{+4}_{-5}	18.39 ± 0.02	13.7 ± 0.9
III	90014-01-02-00	53386.4	8240	Y	0.76	71^{+6}_{-4}	17.36 ± 0.02	13.5 ± 0.9
III	90427-01-03-05	53386.9	12944	Y	0.94	76^{+5}_{-4}	17.18 ± 0.02	14.3 ± 0.8

-	90014-01-02-10	53387.1	2784	Y	0.92	79^{+7}_{-4}	16.92 ± 0.03	14.7 ± 1.0
IV	90427-01-03-06	53387.3	10880	Y	1.17	77^{+5}_{-4}	16.46 ± 0.02	13.9 ± 0.8
IV	90427-01-03-07	53387.8	9632	Y	1.10	76^{+5}_{-4}	16.07 ± 0.02	13.4 ± 0.8
IV	90014-01-02-08	53388.0	3264	Y	1.31	78 ± 6	15.82 ± 0.02	13.5 ± 0.9
V	90427-01-03-09	53388.3	10912	Y	1.06	81 ± 4	15.48 ± 0.02	13.7 ± 0.8
V	90427-01-03-11	53388.9	9744	Y	0.67	77 ± 5	15.16 ± 0.02	12.8 ± 0.8
-	90014-01-02-15	53389.1	2672	Y	1.11	84^{+6}_{-5}	15.28 ± 0.03	14.0 ± 0.9
V	90427-01-03-12	53389.2	9664	Y	0.85	85 ± 5	15.07 ± 0.02	$14.0^{+0.7}_{-0.8}$
VI	90014-01-02-13	53390.3	7056	Y	1.35	85 ± 5	14.43 ± 0.02	$13.3^{+0.7}_{-0.8}$
VI	90014-01-03-00	53391.3	2336	Y	1.28	87^{+7}_{-5}	$13.65^{+0.02}_{-0.01}$	$13.0^{+0.8}_{-0.9}$
VI	90014-01-03-01	53393.2	2768	Y	1.08	89^{+6}_{-7}	$12.68^{+0.02}_{-0.01}$	$12.2^{+0.6}_{-0.8}$
VII	90014-01-03-020	53394.3	13568	Y	0.98	85 ± 6	$12.44^{+0.02}_{-0.01}$	$11.5^{+0.3}_{-0.6}$
VII	90014-01-03-02	53394.6	2032	Y	0.98	79^{+7}_{-6}	12.26 ± 0.02	10.5 ± 0.9
VII	90014-01-03-03	53395.3	6192	Y	1.08	87^{+5}_{-6}	11.50 ± 0.01	$10.8^{+0.5}_{-0.6}$
-	90014-01-04-00	53398.5	1904	Y	1.03	94 ± 7	9.81 ± 0.02	10.0 ± 0.8
-	90014-01-04-01	53399.6	784	Y	0.73	81^{+6}_{-12}	9.67 ± 0.03	$8.5^{+0.9}_{-1.0}$
-	90014-01-04-02	53401.4	944	Y	1.23	82^{+11}_{-10}	8.90 ± 0.02	7.9 ± 0.7
-	90014-01-04-03	53403.3	624	Y	1.14	78^{+12}_{-14}	$8.08^{+0.03}_{-0.02}$	6.7 ± 0.8
-	90014-01-05-00	53405.2	848	-	0.83	83^{+10}_{-9}	$8.05^{+0.03}_{-0.02}$	7.1 ± 0.7
-	90014-01-05-01	53407.6	7376	-	1.87	85^{+6}_{-4}	7.05 ± 0.01	6.4 ± 0.3
-	90014-01-05-04	53407.8	1472	-	0.82	79^{+7}_{-8}	7.24 ± 0.02	6.1 ± 0.7
-	90014-01-05-05	53408.0	1920	-	1.12	82 ± 9	$6.84^{+0.02}_{-0.01}$	5.9 ± 0.4
-	90014-01-05-02	53409.3	2864	-	2.59	77^{+8}_{-6}	6.34 ± 0.01	5.1 ± 0.4
-	90014-01-05-06	53411.6	1040	-	0.76	65^{+12}_{-7}	$5.31^{+0.02}_{-0.01}$	$3.6^{+0.4}_{-0.6}$
-	90427-01-04-00	53413.1	5616	-	1.52	62^{+5}_{-6}	4.88 ± 0.01	3.2 ± 0.2
-	90427-01-04-04	53413.7	6016	-	1.62	61^{+6}_{-5}	4.56 ± 0.01	2.9 ± 0.2
-	90014-01-06-00	53414.0	1200	-	1.04	54^{+8}_{-7}	4.43 ± 0.01	2.5 ± 0.3
-	90427-01-04-02	53414.2	11392	-	1.67	62 ± 5	4.24 ± 0.01	2.7 ± 0.2
-	90427-01-04-03	53414.5	6736	-	1.46	65^{+5}_{-4}	4.02 ± 0.00	2.7 ± 0.2
-	90427-01-04-05	53414.8	2128	-	1.94	55^{+8}_{-10}	3.89 ± 0.01	$2.2^{+0.2}_{-0.3}$
-	90014-01-06-01	53416.1	1872	-	1.06	67^{+13}_{-10}	3.37 ± 0.01	2.3 ± 0.4
-	90427-01-04-01	53416.5	5264	-	0.97	56^{+7}_{-6}	$3.32^{+0.00}_{-0.01}$	1.9 ± 0.2
-	90014-01-06-02	53417.6	1248	-	1.21	64^{+12}_{-14}	2.91 ± 0.01	1.9 ± 0.3
-	90014-01-06-03	53418.5	1616	-	0.73	39^{+12}_{-14}	2.49 ± 0.01	1.0 ± 0.3
-	90014-01-07-01	53419.4	1568	-	1.56	47^{+13}_{-11}	2.16 ± 0.01	1.1 ± 0.3
-	90014-01-07-03	53420.7	1504	-	1.48	42 ± 14	1.90 ± 0.01	0.8 ± 0.3
VIII	90014-01-07-04	53422.6	1888	Z	1.20	< 27	1.37 ± 0.01	< 0.4
VIII	90014-01-07-00	53424.4	2864	Z	0.61	< 38	0.93 ± 0.00	< 0.1
-	90014-01-08-00	53426.5	2384	-	0.76	< 87	0.55 ± 0.01	< 0.2
-	90014-01-08-01	53428.5	2160	-	1.19	< 60	0.37 ± 0.01	< 0.2
-	90014-01-08-02	53430.5	1968	-	0.69	< 16	0.01 ± 0.00	< 0.1
-	90014-01-08-03	53432.4	2176	-	0.32	< 83	0.00 ± 0.00	< 0.1

*: X is for B_16ms_64M_0_249_H configuration, Y is for B_16ms_46M_0_49_H, Z is for E_125us_64M_0_1s

APPENDIX E

Spectral parameters of Swift J0243.6+6124

This appendix is made for Chapter 6.
Fig. E.1 shows the phase-resolved parameters of the reflection model in three observations of Swift J0243.6+6124, see text in sect. 6.3.3 for details. Fig. E.2 shows the best-fitting spectral models for different phase bins (highlighted in each panel) for the phase-resolved spectroscopy.

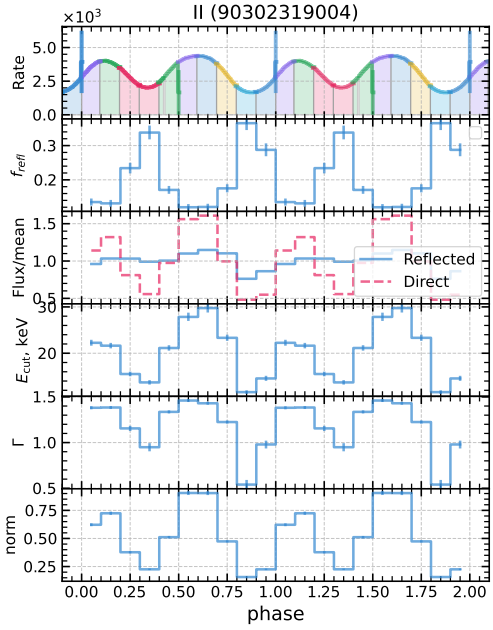

(a) Observation II

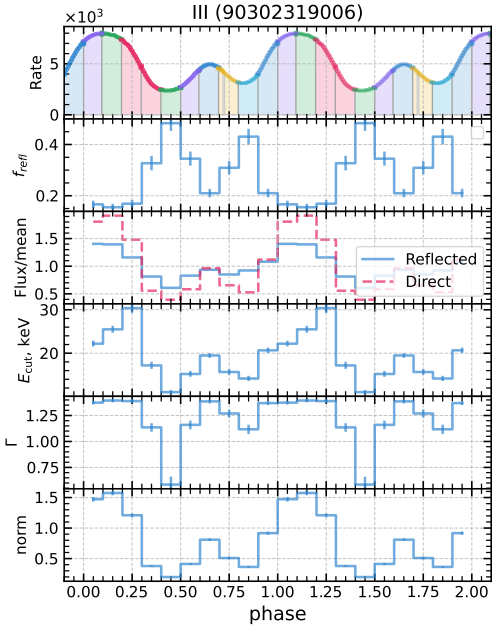

(b) Observation III

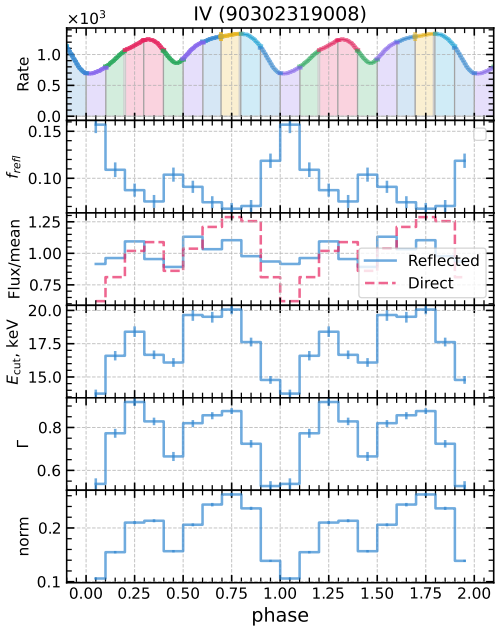

(c) Observation IV

Figure E.1: The evolution of spectral parameters as the function of pulsar rotation phase for observations II, III and IV. In each panel from top to bottom subplot: Pulse profile of the count rate in the 4–79 keV energy range; the reflection fraction parameter $f_{\rm refl}$; direct (red, dashed) and reflected(blue, solid) flux (4–50 keV) of best-fitting model divided by the respective mean flux; e-folding energy of the continuum $E_{\rm cut}$; Photon index Γ; normalisation of RELXILLLP model. Two phase intervals are plotted. In Fig. 6.5 only the top three panels of this figure are shown for each observation.

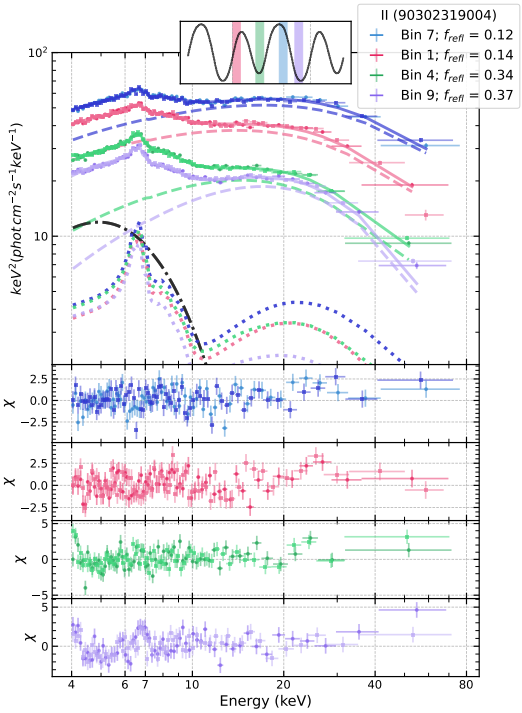

(a) Observation II

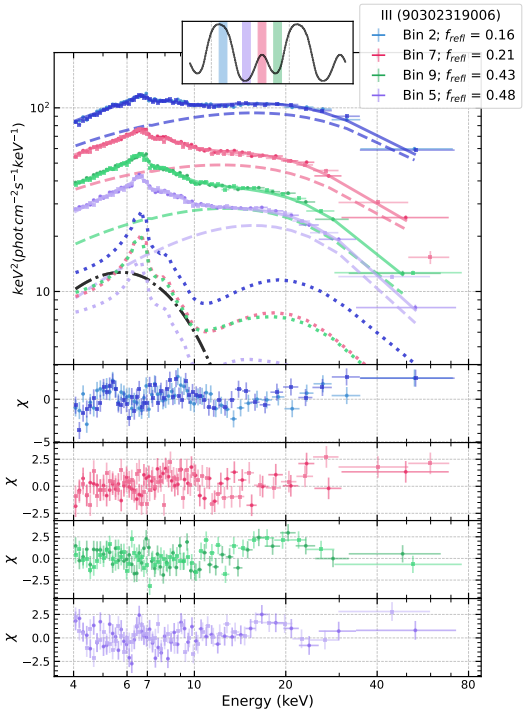

(b) Observation III

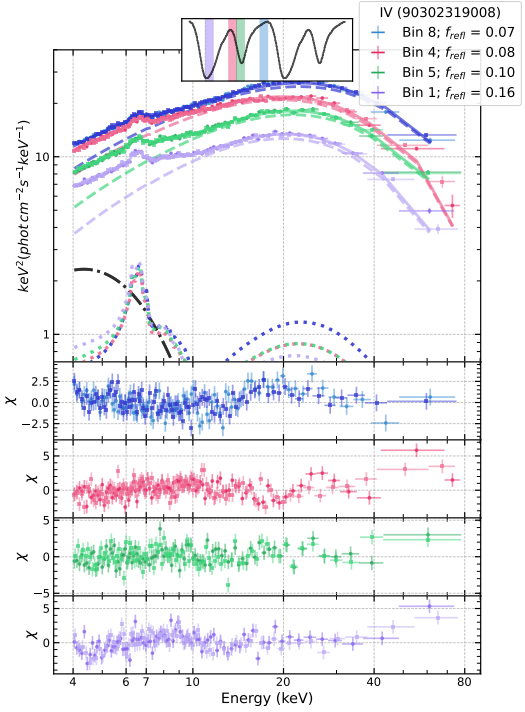

(c) Observation IV

Figure E.2: As in Fig. 6.4 but for spectra of different rotational phases in observation II, III and IV (colour of the spectrum corresponds to the colour of a phase-bin in the pulse profile inset). In the legend, the reflected fraction $f_{\rm frac}$ of the RELXILLLP model is shown for a given bin.

phase	$f_{\rm refl}$	$F_{\rm refl}$ (10^{-8} erg cm^{-1}s^{-1})	$F_{\rm dir}$ (10^{-8} erg cm^{-1}s^{-1})	$E_{\rm cut}$, keV	Γ	norm
II (90302319004)						
0.05	0.14 ± 0.01	1.46	13.0	$22.3^{+0.7}_{-0.6}$	1.38 ± 0.02	0.62 ± 0.01
0.15	0.131 ± 0.010	1.57	15.0	21.6 ± 0.6	1.38 ± 0.02	0.72 ± 0.01
0.25	0.23 ± 0.02	1.57	9.2	15.5 ± 0.5	1.16 ± 0.03	0.38 ± 0.01
0.35	0.34 ± 0.02	1.50	6.3	13.7 ± 0.5	0.95 ± 0.04	0.225 ± 0.007
0.45	0.17 ± 0.01	1.52	11.1	21.1 ± 0.6	1.34 ± 0.02	0.51 ± 0.01
0.55	0.120 ± 0.009	1.67	17.7	27.8 ± 0.9	1.46 ± 0.02	0.90 ± 0.02
0.65	0.121 ± 0.009	1.74	18.3	29.7 ± 1.0	1.43 ± 0.02	0.90 ± 0.02
0.75	0.18 ± 0.01	1.67	11.3	$23.3^{+0.7}_{-0.6}$	1.22 ± 0.02	0.474 ± 0.010
0.85	0.37 ± 0.02	1.16	5.5	11.6 ± 0.4	0.54 ± 0.05	$0.157^{+0.005}_{-0.004}$
0.95	0.29 ± 0.02	1.31	6.2	$14.6^{+0.6}_{-0.5}$	0.98 ± 0.04	0.225 ± 0.007
III (90302319006)						
0.05	0.17 ± 0.01	4.92	30.9	22.2 ± 0.7	1.37 ± 0.02	1.47 ± 0.04
0.15	0.16 ± 0.01	4.88	32.8	25.5 ± 0.8	1.39 ± 0.02	1.57 ± 0.04
0.25	0.17 ± 0.01	4.06	25.3	30 ± 1	1.39 ± 0.02	1.21 ± 0.03
0.35	0.33 ± 0.03	2.85	9.5	17.2 ± 0.8	1.14 ± 0.04	0.38 ± 0.02
0.45	0.48 ± 0.03	2.13	6.7	11.0 ± 0.5	0.58 ± 0.08	0.198 ± 0.008
0.55	0.34 ± 0.03	2.90	10.0	$15.2^{+0.7}_{-0.6}$	1.16 ± 0.04	0.41 ± 0.02
0.65	0.21 ± 0.02	3.28	16.5	$19.5^{+0.6}_{-0.5}$	1.39 ± 0.02	0.81 ± 0.02
0.75	0.31 ± 0.03	2.98	11.2	$15.7^{+0.7}_{-0.6}$	1.27 ± 0.04	0.51 ± 0.02
0.85	0.43 ± 0.03	3.23	9.0	14.2 ± 0.6	$1.12^{+0.04}_{-0.05}$	0.36 ± 0.02
0.95	0.21 ± 0.02	3.79	19.2	20.7 ± 0.6	1.37 ± 0.02	0.92 ± 0.03
IV (90302319008)						
0.05	0.157 ± 0.009	0.33	3.7	13.8 ± 0.3	0.54 ± 0.03	0.106 ± 0.002
0.15	0.109 ± 0.008	0.35	4.8	$16.6^{+0.4}_{-0.3}$	0.77 ± 0.02	0.155 ± 0.002
0.25	0.087 ± 0.007	0.40	6.1	18.4 ± 0.4	0.92 ± 0.02	0.210 ± 0.003
0.35	0.075 ± 0.007	0.34	6.5	16.7 ± 0.3	0.83 ± 0.02	0.213 ± 0.003
0.45	$0.104^{+0.008}_{-0.007}$	0.32	5.1	16.1 ± 0.3	0.67 ± 0.02	0.157 ± 0.002
0.55	$0.091^{+0.007}_{-0.006}$	0.41	6.2	19.7 ± 0.4	$0.82^{+0.01}_{-0.02}$	0.206 ± 0.003
0.65	0.074 ± 0.006	0.37	7.2	19.5 ± 0.4	$0.86^{+0.01}_{-0.02}$	$0.244^{+0.003}_{-0.004}$
0.75	0.068 ± 0.006	0.40	7.7	20.1 ± 0.4	0.88 ± 0.01	0.262 ± 0.003
0.85	0.071 ± 0.006	0.35	7.5	17.6 ± 0.3	0.72 ± 0.02	0.236 ± 0.003
0.95	0.119 ± 0.008	0.34	4.8	14.8 ± 0.3	0.53 ± 0.02	0.139 ± 0.002

Table E.1: Spectral parameters of all ten phase-bins of Swift J0243.6+6124 in phase-resolved analysis in three observations. The modelling details are described in sect. 6.3.3. The position of zero-phase is arbitrary.

Bibliography

Abbott T. M. C., Aguena M., Alarcon A., Allam S., Alves O., Amon A., Andrade-Oliveira F., Annis J., Avila S., Bacon D., Baxter E., Bechtol K., Becker M. R., Bernstein G. M., Bhargava S., Birrer S., Blazek J., Brandao-Souza A., Bridle S. L., Brooks D., Buckley-Geer E., Burke D. L., Camacho H., Campos A., Carnero Rosell A., Carrasco Kind M., Carretero J., Castander F. J., Cawthon R., Chang C., Chen A., Chen R., Choi A., Conselice C., Cordero J., Costanzi M., Crocce M., da Costa L. N., da Silva Pereira M. E., Davis C., Davis T. M., De Vicente J., DeRose J., Desai S., Di Valentino E., Diehl H. T., Dietrich J. P., Dodelson S., Doel P., Doux C., Drlica-Wagner A., Eckert K., Eifler T. F., Elsner F., Elvin-Poole J., Everett S., Evrard A. E., Fang X., Farahi A., Fernandez E., Ferrero I., Ferté A., Fosalba P., Friedrich O., Frieman J., García-Bellido J., Gatti M., Gaztanaga E., Gerdes D. W., Giannantonio T., Giannini G., Gruen D., Gruendl R. A., Gschwend J., Gutierrez G., Harrison I., Hartley W. G., Herner K., Hinton S. R., Hollowood D. L., Honscheid K., Hoyle B., Huff E. M., Huterer D., Jain B., James D. J., Jarvis M., Jeffrey N., Jeltema T., Kovacs A., Krause E., Kron R., Kuehn K., Kuropatkin N., Lahav O., Leget P. F., Lemos P., Liddle A. R., Lidman C., Lima M., Lin H., MacCrann N., Maia M. A. G., Marshall J. L., Martini P., McCullough J., Melchior P., Mena-Fernández J., Menanteau F., Miquel R., Mohr J. J., Morgan R., Muir J., Myles J., Nadathur S., Navarro-Alsina A., Nichol R. C., Ogando R. L. C., Omori Y., Palmese A., Pandey S., Park Y., Paz-Chinchón F., Petravick D., Pieres A., Plazas Malagón A. A., Porredon A., Prat J., Raveri M., Rodriguez-Monroy M., Rollins R. P., Romer A. K., Roodman A., Rosenfeld R., Ross A. J., Rykoff E. S., Samuroff S., Sánchez C., Sanchez E., Sanchez J., Sanchez Cid D., Scarpine V., Schubnell M., Scolnic D., Secco L. F., Serrano S., Sevilla-Noarbe I., Sheldon E., Shin T., Smith M., Soares-Santos M., Suchyta E., Swanson M. E. C., Tabbutt M., Tarle G., Thomas D., To C., Troja A., Troxel M. A., Tucker D. L., Tutusaus I., Varga T. N., Walker A. R., Weaverdyck N., Wechsler R., Weller J., Yanny B., Yin B., Zhang Y., Zuntz J., DES Collaboration . Dark Energy Survey Year 3 results: Cosmological constraints from galaxy clustering and weak lensing // Phys. Rev. D. I 2022a. 105, 2. 023520.

Abbott T. M. C., Aguena M., Allam S., Amon A., Andrade-Oliveira F., Asorey J., Avila S., Bernstein G. M., Bertin E., Brandao-Souza A., Brooks D., Burke D. L., Calcino J., Camacho H., Carnero Rosell A., Carollo D., Carrasco Kind M., Carretero J., Castander F. J., Cawthon R., Chan K. C., Choi A., Conselice C., Costanzi M., Crocce M., da Costa L. N., Pereira M. E. S., Davis T. M., De Vicente J., Desai S., Diehl H. T., Doel P., Eckert K., Elvin-Poole J., Everett S., Evrard A. E., Fang X., Ferrero I., Ferté A., Flaugher B., Fosalba P., García-Bellido J., Gaztanaga E., Gerdes D. W., Giannantonio T., Glazebrook K., Gomes D., Gruen D., Gruendl R. A., Gschwend J., Gutierrez G., Hinton S. R., Hollowood D. L., Honscheid K., Huterer D., Jain B., James D. J., Jeltema T., Kokron N., Krause E., Kuehn K., Lahav O., Lewis G. F., Lidman C., Lima M., Lin H., Maia M. A. G., Malik U., Martini P., Melchior P., Mena-Fernández J., Menanteau F., Miquel R., Mohr J. J., Morgan R., Muir J., Myles J., Möller A., Palmese A., Paz-Chinchón F., Percival W. J., Pieres A., Plazas Malagón A. A., Porredon A., Prat J., Reil K., Rodriguez-Monroy M., Romer A. K., Roodman A., Rosenfeld R., Ross A. J., Sanchez E., Sanchez Cid D., Scarpine V., Serrano S., Sevilla-Noarbe I., Sheldon E., Smith M., Soares-Santos M., Suchyta

E., Swanson M. E. C., Tarle G., Thomas D., To C., Troxel M. A., Tucker B. E., Tucker D. L., Tutusaus I., Uddin S. A., Varga T. N., Weller J., Wilkinson R. D., DES Collaboration . Dark Energy Survey Year 3 results: A 2.7% measurement of baryon acoustic oscillation distance scale at redshift 0.835 // Phys. Rev. D. II 2022b. 105, 4. 043512.

Aftab Nafisa, Paul Biswajit, Kretschmar Peter. X-Ray Reprocessing: Through the Eclipse Spectra of High-mass X-Ray Binaries with XMM-Newton // ApJS. VIII 2019. 243, 2. 29.

Aird J., Coil A. L., Georgakakis A. X-rays across the galaxy population - II. The distribution of AGN accretion rates as a function of stellar mass and redshift. // MNRAS. I 2018. 474. 1225–1249.

Aird J., Coil A. L., Georgakakis A., Nandra K., Barro G., Pérez-González P. G. The evolution of the X-ray luminosity functions of unabsorbed and absorbed AGNs out to z∼ 5 // MNRAS. VIII 2015. 451, 2. 1892–1927.

Aird J., Nandra K., Laird E. S., Georgakakis A., Ashby M. L. N., Barmby P., Coil A. L., Huang J. S., Koekemoer A. M., Steidel C. C., Willmer C. N. A. The evolution of the hard X-ray luminosity function of AGN // MNRAS. II 2010. 401, 4. 2531–2551.

Aird James, Coil Alison L., Moustakas John, Blanton Michael R., Burles Scott M., Cool Richard J., Eisenstein Daniel J., Smith M. Stephen M., Wong Kenneth C., Zhu Guangtun. PRIMUS: The Dependence of AGN Accretion on Host Stellar Mass and Color // ApJ. II 2012. 746, 1. 90.

Alam Shadab, Albareti Franco D., Allende Prieto Carlos, Anders F., Anderson Scott F., Anderton Timothy, Andrews Brett H., Armengaud Eric, Aubourg Éric, Bailey Stephen, al. et. The Eleventh and Twelfth Data Releases of the Sloan Digital Sky Survey: Final Data from SDSS-III // ApJS. VII 2015. 219, 1. 12.

Alam Shadab, Ata Metin, Bailey Stephen, Beutler Florian, Bizyaev Dmitry, Blazek Jonathan A., Bolton Adam S., Brownstein Joel R., Burden Angela, Chuang Chia-Hsun, Comparat Johan, Cuesta Antonio J., Dawson Kyle S., Eisenstein Daniel J., Escoffier Stephanie, Gil-Marín Héctor, Grieb Jan Niklas, Hand Nick, Ho Shirley, Kinemuchi Karen, Kirkby David, Kitaura Francisco, Malanushenko Elena, Malanushenko Viktor, Maraston Claudia, McBride Cameron K., Nichol Robert C., Olmstead Matthew D., Oravetz Daniel, Padmanabhan Nikhil, Palanque-Delabrouille Nathalie, Pan Kaike, Pellejero-Ibanez Marcos, Percival Will J., Petitjean Patrick, Prada Francisco, Price-Whelan Adrian M., Reid Beth A., Rodríguez-Torres Sergio A., Roe Natalie A., Ross Ashley J., Ross Nicholas P., Rossi Graziano, Rubiño-Martín Jose Alberto, Saito Shun, Salazar-Albornoz Salvador, Samushia Lado, Sánchez Ariel G., Satpathy Siddharth, Schlegel David J., Schneider Donald P., Scóccola Claudia G., Seo Hee-Jong, Sheldon Erin S., Simmons Audrey, Slosar Anže, Strauss Michael A., Swanson Molly E. C., Thomas Daniel, Tinker Jeremy L., Tojeiro Rita, Magaña Mariana Vargas, Vazquez Jose Alberto, Verde Licia, Wake David A., Wang Yuting, Weinberg David H., White Martin, Wood-Vasey W. Michael, Yèche Christophe, Zehavi Idit, Zhai Zhongxu, Zhao Gong-Bo. The clustering of galaxies in

the completed SDSS-III Baryon Oscillation Spectroscopic Survey: cosmological analysis of the DR12 galaxy sample // MNRAS. IX 2017. 470, 3. 2617–2652.

Alam Shadab, Aubert Marie, Avila Santiago, Balland Christophe, Bautista Julian E., Bershady Matthew A., Bizyaev Dmitry, Blanton Michael R., Bolton Adam S., Bovy Jo, Brinkmann Jonathan, Brownstein Joel R., Burtin Etienne, Chabanier Solène, Chapman Michael J., Choi Peter Doohyun, Chuang Chia-Hsun, Comparat Johan, Cousinou Marie-Claude, Cuceu Andrei, Dawson Kyle S., de la Torre Sylvain, de Mattia Arnaud, Agathe Victoria de Sainte, des Bourboux Hélion du Mas, Escoffier Stephanie, Etourneau Thomas, Farr James, Font-Ribera Andreu, Frinchaboy Peter M., Fromenteau Sebastien, Gil-Marín Héctor, Le Goff Jean-Marc, Gonzalez-Morales Alma X., Gonzalez-Perez Violeta, Grabowski Kathleen, Guy Julien, Hawken Adam J., Hou Jiamin, Kong Hui, Parker James, Klaene Mark, Kneib Jean-Paul, Lin Sicheng, Long Daniel, Lyke Brad W., de la Macorra Axel, Martini Paul, Masters Karen, Mohammad Faizan G., Moon Jeongin, Mueller Eva-Maria, Muñoz-Gutiérrez Andrea, Myers Adam D., Nadathur Seshadri, Neveux Richard, Newman Jeffrey A., Noterdaeme Pasquier, Oravetz Audrey, Oravetz Daniel, Palanque-Delabrouille Nathalie, Pan Kaike, Paviot Romain, Percival Will J., Pérez-Ràfols Ignasi, Petitjean Patrick, Pieri Matthew M., Prakash Abhishek, Raichoor Anand, Ravoux Corentin, Rezaie Mehdi, Rich James, Ross Ashley J., Rossi Graziano, Ruggeri Rossana, Ruhlmann-Kleider Vanina, Sánchez Ariel G., Sánchez F. Javier, Sánchez-Gallego José R., Sayres Conor, Schneider Donald P., Seo Hee-Jong, Shafieloo Arman, Slosar Anže, Smith Alex, Stermer Julianna, Tamone Amelie, Tinker Jeremy L., Tojeiro Rita, Vargas-Magaña Mariana, Variu Andrei, Wang Yuting, Weaver Benjamin A., Weijmans Anne-Marie, Yèche Christophe, Zarrouk Pauline, Zhao Cheng, Zhao Gong-Bo, Zheng Zheng. Completed SDSS-IV extended Baryon Oscillation Spectroscopic Survey: Cosmological implications from two decades of spectroscopic surveys at the Apache Point Observatory // Phys. Rev. D. IV 2021. 103, 8. 083533.

Alexander D. M., Hickox R. C. What drives the growth of black holes? // New Astron. Rev.. VI 2012. 56, 4. 93–121.

Allen Steven W., Evrard August E., Mantz Adam B. Cosmological Parameters from Observations of Galaxy Clusters // ARA&A. IX 2011. 49, 1. 409–470.

Allevato V., Civano F., Finoguenov A., Marchesi S., Shankar F., Zamorani G., Hasinger G., Salvato M., Miyaji T., Gilli R., Cappelluti N., Brusa M., Suh H., Lanzuisi G., Trakhtenbrot B., Griffiths R., Vignali C., Schawinski K., Karim A. The Chandra COSMOS Legacy Survey: Clustering of X-Ray-selected AGNs at $2.9 \leq z \leq 5.5$ Using Photometric Redshift Probability Distribution Functions // ApJ. XI 2016. 832, 1. 70.

Allevato V., Finoguenov A., Cappelluti N., Miyaji T., Hasinger G., Salvato M., Brusa M., Gilli R., Zamorani G., Shankar F., James J. B., McCracken H. J., Bongiorno A., Merloni A., Peacock J. A., Silverman J., Comastri A. The XMM-Newton Wide Field Survey in the COSMOS Field: Redshift Evolution of AGN Bias and Subdominant Role of Mergers in Triggering Moderate-luminosity AGNs at Redshifts up to 2.2 // ApJ. VIII 2011. 736, 2. 99.

Allevato V., Viitanen A., Finoguenov A., Civano F., Suh H., Shankar F., Bongiorno A., Ferrara A., Gilli R., Miyaji T., Marchesi S., Cappelluti N., Salvato M. Chandra COSMOS Legacy Survey: Clustering dependence of Type 2 active galactic nuclei on host galaxy properties // A&A. XII 2019. 632. A88.

Ananna Tonima Tasnim, Salvato Mara, LaMassa Stephanie, Urry C. Megan, Cappelluti Nico, Cardamone Carolin, Civano Francesca, Farrah Duncan, Gilfanov Marat, Glikman Eilat, Hamilton Mark, Kirkpatrick Allison, Lanzuisi Giorgio, Marchesi Stefano, Merloni Andrea, Nandra Kirpal, Natarajan Priyamvada, Richards Gordon T., Timlin John. AGN Populations in Large-volume X-Ray Surveys: Photometric Redshifts and Population Types Found in the Stripe 82X Survey // ApJ. XI 2017. 850, 1. 66.

Ananna Tonima Tasnim, Treister Ezequiel, Urry C. Megan, Ricci C., Kirkpatrick Allison, LaMassa Stephanie, Buchner Johannes, Civano Francesca, Tremmel Michael, Marchesi Stefano. The Accretion History of AGNs. I. Supermassive Black Hole Population Synthesis Model // ApJ. II 2019. 871, 2. 240.

Angus C. R., Baldassare V. F., Mockler B., Foley R. J., Ramirez-Ruiz E., Raimundo S. I., French K. D., Auchettl K., Pfister H., Gall C., Hjorth J., Drout M. R., Alexander K. D., Dimitriadis G., Hung T., Jones D. O., Rest A., Siebert M. R., Taggart K., Terreran G., Tinyanont S., Carroll C. M., DeMarchi L., Earl N., Gagliano A., Izzo L., Villar V. A., Zenati Y., Arendse N., Cold C., de Boer T. J. L., Chambers K. C., Coulter D. A., Khetan N., Lin C. C., Magnier E. A., Rojas-Bravo C., Wainscoat R. J., Wojtak R. A fast-rising tidal disruption event from a candidate intermediate-mass black hole // Nature Astronomy. XII 2022. 6. 1452–1463.

Antonucci Robert. Unified models for active galactic nuclei and quasars. // ARA&A. I 1993. 31. 473–521.

Arnason R. M., Papei H., Barmby P., Bahramian A., Gorski M. D. Distances to Galactic X-ray Binaries with Gaia DR2 // arXiv e-prints. II 2021. arXiv:2102.02615.

Arnaud K. A. XSPEC: The First Ten Years // Astronomical Data Analysis Software and Systems V. 101. I 1996. 17. (Astronomical Society of the Pacific Conference Series).

Astropy Collaboration , Price-Whelan A. M., Sipőcz B. M., Günther H. M., Lim P. L., Crawford S. M., Conseil S., Shupe D. L., Craig M. W., Dencheva N., Ginsburg A., Vand erPlas J. T., Bradley L. D., Pérez-Suárez D., de Val-Borro M., Aldcroft T. L., Cruz K. L., Robitaille T. P., Tollerud E. J., Ardelean C., Babej T., Bach Y. P., Bachetti M., Bakanov A. V., Bamford S. P., Barentsen G., Barmby P., Baumbach A., Berry K. L., Biscani F., Boquien M., Bostroem K. A., Bouma L. G., Brammer G. B., Bray E. M., Breytenbach H., Buddelmeijer H., Burke D. J., Calderone G., Cano Rodríguez J. L., Cara M., Cardoso J. V. M., Cheedella S., Copin Y., Corrales L., Crichton D., D'Avella D., Deil C., Depagne É., Dietrich J. P., Donath A., Droettboom M., Earl N., Erben T., Fabbro S., Ferreira L. A., Finethy T., Fox R. T., Garrison L. H., Gibbons S. L. J., Goldstein D. A., Gommers R., Greco J. P., Greenfield P., Groener A. M., Grollier F., Hagen A., Hirst P., Homeier D., Horton A. J., Hosseinzadeh G., Hu L., Hunkeler

J. S., Ivezić Ž., Jain A., Jenness T., Kanarek G., Kendrew S., Kern N. S., Kerzendorf W. E., Khvalko A., King J., Kirkby D., Kulkarni A. M., Kumar A., Lee A., Lenz D., Littlefair S. P., Ma Z., Macleod D. M., Mastropietro M., McCully C., Montagnac S., Morris B. M., Mueller M., Mumford S. J., Muna D., Murphy N. A., Nelson S., Nguyen G. H., Ninan J. P., Nöthe M., Ogaz S., Oh S., Parejko J. K., Parley N., Pascual S., Patil R., Patil A. A., Plunkett A. L., Prochaska J. X., Rastogi T., Reddy Janga V., Sabater J., Sakurikar P., Seifert M., Sherbert L. E., Sherwood-Taylor H., Shih A. Y., Sick J., Silbiger M. T., Singanamalla S., Singer L. P., Sladen P. H., Sooley K. A., Sornarajah S., Streicher O., Teuben P., Thomas S. W., Tremblay G. R., Turner J. E. H., Terrón V., van Kerkwijk M. H., de la Vega A., Watkins L. L., Weaver B. A., Whitmore J. B., Woillez J., Zabalza V., Astropy Contributors . The Astropy Project: Building an Open-science Project and Status of the v2.0 Core Package // AJ. IX 2018. 156, 3. 123.

Auchettl Katie, Ramirez-Ruiz Enrico, Guillochon James. A Comparison of the X-Ray Emission from Tidal Disruption Events with those of Active Galactic Nuclei // ApJ. I 2018. 852, 1. 37.

Bailer-Jones C. A. L., Rybizki J., Fouesneau M., Mantelet G., Andrae R. Estimating Distance from Parallaxes. IV. Distances to 1.33 Billion Stars in Gaia Data Release 2 // AJ. VIII 2018. 156, 2. 58.

Baldassare Vivienne F., Geha Marla, Greene Jenny. A Search for Optical AGN Variability in 35,000 Low-mass Galaxies with the Palomar Transient Factory // ApJ. VI 2020. 896, 1. 10.

Baldassare Vivienne F., Reines Amy E., Gallo Elena, Greene Jenny E. X-ray and Ultraviolet Properties of AGNs in Nearby Dwarf Galaxies // ApJ. II 2017. 836, 1. 20.

Baldwin J. A., Phillips M. M., Terlevich R. Classification parameters for the emission-line spectra of extragalactic objects. // PASP. II 1981. 93. 5–19.

Barai Paramita, de Gouveia Dal Pino Elisabete M. Intermediate-mass black hole growth and feedback in dwarf galaxies at high redshifts // MNRAS. VIII 2019. 487, 4. 5549–5563.

Basko M. M., Sunyaev R. A. Radiative transfer in a strong magnetic field and accreting X-ray pulsars. // A&A. IX 1975. 42, 3. 311–321.

Basko M. M., Sunyaev R. A. The limiting luminosity of accreting neutron stars with magnetic fields. // MNRAS. V 1976. 175. 395–417.

Basko M. M., Sunyaev R. A., Titarchuk L. G. Reflection and reprocessing of X-ray source radiation by the atmosphere of the normal star in a binary system. // A&A. III 1974. 31. 249–263.

Baum Zachary A., Cherry Michael L., Rodi James. Observations of V0332+53 during the 2015 outburst using Fermi/GBM, MAXI, Swift and INTEGRAL // MNRAS. VI 2017. 467, 4. 4424–4430.

Bautista Julian E., Paviot Romain, Vargas Magaña Mariana, de la Torre Sylvain, Fromenteau Sebastien, Gil-Marín Hector, Ross Ashley J., Burtin Etienne, Dawson Kyle S., Hou Jiamin, Kneib

Jean-Paul, de Mattia Arnaud, Percival Will J., Rossi Graziano, Tojeiro Rita, Zhao Cheng, Zhao Gong-Bo, Alam Shadab, Brownstein Joel, Chapman Michael J., Choi Peter D., Chuang Chia-Hsun, Escoffier Stéphanie, de la Macorra Axel, du Mas des Bourboux Hélion, Mohammad Faizan G., Moon Jeongin, Müller Eva-Maria, Nadathur Seshadri, Newman Jeffrey A., Schneider Donald, Seo Hee-Jong, Wang Yuting. The completed SDSS-IV extended Baryon Oscillation Spectroscopic Survey: measurement of the BAO and growth rate of structure of the luminous red galaxy sample from the anisotropic correlation function between redshifts 0.6 and 1 // MNRAS. I 2021. 500, 1. 736–762.

Bellm Eric C., Kulkarni Shrinivas R., Graham Matthew J., Dekany Richard, Smith Roger M., Riddle Reed, Masci Frank J., Helou George, Prince Thomas A., Adams Scott M., Barbarino C., Barlow Tom, Bauer James, Beck Ron, Belicki Justin, Biswas Rahul, Blagorodnova Nadejda, Bodewits Dennis, Bolin Bryce, Brinnel Valery, Brooke Tim, Bue Brian, Bulla Mattia, Burruss Rick, Cenko S. Bradley, Chang Chan-Kao, Connolly Andrew, Coughlin Michael, Cromer John, Cunningham Virginia, De Kishalay, Delacroix Alex, Desai Vandana, Duev Dmitry A., Eadie Gwendolyn, Farnham Tony L., Feeney Michael, Feindt Ulrich, Flynn David, Franckowiak Anna, Frederick S., Fremling C., Gal-Yam Avishay, Gezari Suvi, Giomi Matteo, Goldstein Daniel A., Golkhou V. Zach, Goobar Ariel, Groom Steven, Hacopians Eugean, Hale David, Henning John, Ho Anna Y. Q., Hover David, Howell Justin, Hung Tiara, Huppenkothen Daniela, Imel David, Ip Wing-Huen, Ivezić Željko, Jackson Edward, Jones Lynne, Juric Mario, Kasliwal Mansi M., Kaspi S., Kaye Stephen, Kelley Michael S. P., Kowalski Marek, Kramer Emily, Kupfer Thomas, Landry Walter, Laher Russ R., Lee Chien-De, Lin Hsing Wen, Lin Zhong-Yi, Lunnan Ragnhild, Giomi Matteo, Mahabal Ashish, Mao Peter, Miller Adam A., Monkewitz Serge, Murphy Patrick, Ngeow Chow-Choong, Nordin Jakob, Nugent Peter, Ofek Eran, Patterson Maria T., Penprase Bryan, Porter Michael, Rauch Ludwig, Rebbapragada Umaa, Reiley Dan, Rigault Mickael, Rodriguez Hector, van Roestel Jan, Rusholme Ben, van Santen Jakob, Schulze S., Shupe David L., Singer Leo P., Soumagnac Maayane T., Stein Robert, Surace Jason, Sollerman Jesper, Szkody Paula, Taddia F., Terek Scott, Van Sistine Angela, van Velzen Sjoert, Vestrand W. Thomas, Walters Richard, Ward Charlotte, Ye Quan-Zhi, Yu Po-Chieh, Yan Lin, Zolkower Jeffry. The Zwicky Transient Facility: System Overview, Performance, and First Results // PASP. I 2019. 131, 995. 018002.

Belvedersky M. I., Bykov S. D., Gilfanov M. R. SRG/eROSITA Survey in the Lockman Hole: Classification of X-ray Sources // Astronomy Letters. XII 2022a. 48, 12. 755–766.

Belvedersky M. I., Meshcheryakov A. V., Medvedev P. S., Gilfanov M. R. SRGz: Building an Optical Cross-Match Model for the X-ray SRG/eROSITA Sources Using the Lockman Hole Data // Astronomy Letters. II 2022b. 48, 2. 109–125.

Bethe H. A., Wilson J. R. Revival of a stalled supernova shock by neutrino heating // ApJ. VIII 1985. 295. 14–23.

Beutler Florian, Blake Chris, Colless Matthew, Jones D. Heath, Staveley-Smith Lister, Campbell Lachlan, Parker Quentin, Saunders Will, Watson Fred. The 6dF Galaxy Survey: baryon acoustic oscillations and the local Hubble constant // MNRAS. X 2011. 416, 4. 3017–3032.

Birchall Keir L., Watson M. G., Aird J. X-ray detected AGN in SDSS dwarf galaxies // MNRAS. II 2020. 492, 2. 2268–2284.

Birchall Keir L., Watson M. G., Aird J., Starling R. L. C. The incidence of X-ray selected AGN in nearby galaxies // MNRAS. III 2022. 510, 3. 4556–4572.

Blake Chris, Kazin Eyal A., Beutler Florian, Davis Tamara M., Parkinson David, Brough Sarah, Colless Matthew, Contreras Carlos, Couch Warrick, Croom Scott, Croton Darren, Drinkwater Michael J., Forster Karl, Gilbank David, Gladders Mike, Glazebrook Karl, Jelliffe Ben, Jurek Russell J., Li I. Hui, Madore Barry, Martin D. Christopher, Pimbblet Kevin, Poole Gregory B., Pracy Michael, Sharp Rob, Wisnioski Emily, Woods David, Wyder Ted K., Yee H. K. C. The WiggleZ Dark Energy Survey: mapping the distance-redshift relation with baryon acoustic oscillations // MNRAS. XII 2011. 418, 3. 1707–1724.

Borisov Viktor, Meshcheryakov Alex, Gerasimov Sergey, RU eROSITA catalog group . Probabilistic photo-z machine learning models for X-ray sky surveys // arXiv e-prints. VII 2021. arXiv:2107.01891.

Brandt W. N., Alexander D. M. Cosmic X-ray surveys of distant active galaxies. The demographics, physics, and ecology of growing supermassive black holes // A&ARv. I 2015. 23. 1.

Brandt W. N., Hasinger G. Deep Extragalactic X-Ray Surveys // ARA&A. IX 2005. 43, 1. 827–859.

Brinchmann J., Charlot S., White S. D. M., Tremonti C., Kauffmann G., Heckman T., Brinkmann J. The physical properties of star-forming galaxies in the low-redshift Universe // MNRAS. VII 2004. 351, 4. 1151–1179.

Brunner H., Liu T., Lamer G., Georgakakis A., Merloni A., Brusa M., Bulbul E., Dennerl K., Friedrich S., Liu A., Maitra C., Nandra K., Ramos-Ceja M. E., Sanders J. S., Stewart I. M., Boller T., Buchner J., Clerc N., Comparat J., Dwelly T., Eckert D., Finoguenov A., Freyberg M., Ghirardini V., Gueguen A., Haberl F., Kreykenbohm I., Krumpe M., Osterhage S., Pacaud F., Predehl P., Reiprich T. H., Robrade J., Salvato M., Santangelo A., Schrabback T., Schwope A., Wilms J. The eROSITA Final Equatorial Depth Survey (eFEDS). X-ray catalogue // A&A. V 2022a. 661. A1.

Brunner H., Liu T., Lamer G., Georgakakis A., Merloni A., Brusa M., Bulbul E., Dennerl K., Friedrich S., Liu A., Maitra C., Nandra K., Ramos-Ceja M. E., Sanders J. S., Stewart I. M., Boller T., Buchner J., Clerc N., Comparat J., Dwelly T., Eckert D., Finoguenov A., Freyberg M., Ghirardini V., Gueguen A., Haberl F., Kreykenbohm I., Krumpe M., Osterhage S., Pacaud F., Predehl P., Reiprich T. H., Robrade J., Salvato M., Santangelo A., Schrabback T., Schwope A., Wilms J. The eROSITA Final Equatorial Depth Survey (eFEDS). X-ray catalogue // A&A. V 2022b. 661. A1.

Brusa M., Comastri A., Gilli R., Hasinger G., Iwasawa K., Mainieri V., Mignoli M., Salvato M., Zamorani G., Bongiorno A., Cappelluti N., Civano F., Fiore F., Merloni A., Silverman J.,

Trump J., Vignali C., Capak P., Elvis M., Ilbert O., Impey C., Lilly S. High-Redshift Quasars in the COSMOS Survey: The Space Density of z > 3 X-Ray Selected QSOs // ApJ. III 2009. 693, 1. 8–22.

Brusa M., Zamorani G., Comastri A., Hasinger G., Cappelluti N., Civano F., Finoguenov A., Mainieri V., Salvato M., Vignali C., Elvis M., Fiore F., Gilli R., Impey C. D., Lilly S. J., Mignoli M., Silverman J., Trump J., Urry C. M., Bender R., Capak P., Huchra J. P., Kneib J. P., Koekemoer A., Leauthaud A., Lehmann I., Massey R., Matute I., McCarthy P. J., McCracken H. J., Rhodes J., Scoville N. Z., Taniguchi Y., Thompson D. The XMM-Newton Wide-Field Survey in the COSMOS Field. III. Optical Identification and Multiwavelength Properties of a Large Sample of X-Ray-Selected Sources // ApJS. IX 2007. 172, 1. 353–367.

Bruzual G., Charlot S. Stellar population synthesis at the resolution of 2003 // MNRAS. X 2003. 344, 4. 1000–1028.

Buchner Johannes, Boller Thomas, Bogensberger David, Malyali Adam, Nandra Kirpal, Wilms Joern, Dwelly Tom, Liu Teng. Systematic evaluation of variability detection methods for eROSITA // A&A. V 2022. 661. A18.

Buchner Johannes, Georgakakis Antonis, Nandra Kirpal, Brightman Murray, Menzel Marie-Luise, Liu Zhu, Hsu Li-Ting, Salvato Mara, Rangel Cyprian, Aird James, Merloni Andrea, Ross Nicholas. Obscuration-dependent Evolution of Active Galactic Nuclei // ApJ. IV 2015. 802, 2. 89.

Budavári Tamás, Loredo Thomas J. Probabilistic Record Linkage in Astronomy: Directional Cross-Identification and Beyond // Annual Review of Statistics and Its Application. IV 2015. 2, 1. 113–139.

Budavári Tamás, Szalay Alexander S. Probabilistic Cross-Identification of Astronomical Sources // ApJ. V 2008. 679, 1. 301–309.

Burke Colin J., Shen Yue, Liu Xin, Natarajan Priyamvada, Caplar Neven, Bellovary Jillian M., Wang Z. Franklin. Dwarf AGNs from variability for the origins of seeds (DAVOS): Intermediate-mass black hole demographics from optical synoptic surveys // MNRAS. I 2023. 518, 2. 1880–1904.

Burrows David N., Hill J. E., Nousek J. A., Kennea J. A., Wells A., Osborne J. P., Abbey A. F., Beardmore A., Mukerjee K., Short A. D. T., Chincarini G., Campana S., Citterio O., Moretti A., Pagani C., Tagliaferri G., Giommi P., Capalbi M., Tamburelli F., Angelini L., Cusumano G., Bräuninger H. W., Burkert W., Hartner G. D. The Swift X-Ray Telescope // Space Sci. Rev.. X 2005. 120, 3-4. 165–195.

***Bykov S.**, Gilfanov M., Sunyaev R.* Forecasts for cosmological measurements based on the angular power spectra of AGN and clusters of galaxies in the SRG/eROSITA all-sky survey // A&A. I 2023. 669. A61.

***Bykov S. D.**, Belvedersky M. I., Gilfanov M. R.* Optical Cross-Match of SRG/eROSITA X-ray Sources Using the Deep Lockman Hole Survey as an Example // Astronomy Letters. XI 2022a. 48, 11. 653–664.

***Bykov S. D.**, Filippova E. V., Gilfanov M. R., Tsygankov S. S., Lutovinov A. A., Molkov S. V.* Pulsating iron spectral features in the emission of X-ray pulsar V 0332+53 // MNRAS. IX 2021. 506, 2. 2156–2169.

***Bykov S. D.**, Gilfanov M. R., Sunyaev R. A.* SRG/eROSITA catalogue of X-ray active SDSS dwarf galaxies // Monthly Notices of the Royal Astronomical Society. 1 2024. 527, 2. 1962–1981.

***Bykov S. D.**, Gilfanov M. R., Tsygankov S. S., Filippova E. V.* ULX pulsar Swift J0243.6+6124 observations with NuSTAR: dominance of reflected emission in the super-Eddington state // MNRAS. X 2022b. 516, 2. 1601–1611.

Caballero-García M. D., Camero-Arranz A., Özbey Arabacı M., Zurita C., Suso J., Gutiérrez-Soto J., Beklen E., Kiaeerad F., Garrido R., Hudec R. Activity from the Be/X-ray binary system V0332+53 during its intermediate-luminosity outburst in 2008 // A&A. V 2016. 589. A9.

Calabrò A., Amorín R., Fontana A., Pérez-Montero E., Lemaux B. C., Ribeiro B., Bardelli S., Castellano M., Contini T., De Barros S., Garilli B., Grazian A., Guaita L., Hathi N. P., Koekemoer A. M., Le Fèvre O., Maccagni D., Pentericci L., Schaerer D., Talia M., Tasca L. A. M., Zucca E. Characterization of star-forming dwarf galaxies at $0.1 \lesssim z \lesssim 0.9$ in VUDS: probing the low-mass end of the mass-metallicity relation // A&A. V 2017. 601. A95.

Canal R., Gutiérrez J. The possible white dwarf-neutron star connection // White dwarfs. 214. 1997. 49. (Astrophysics and Space Science Library).

Cappelluti N., Ajello M., Burlon D., Krumpe M., Miyaji T., Bonoli S., Greiner J. Active Galactic Nuclei Clustering in the Local Universe: An Unbiased Picture from Swift-BAT // ApJ. VI 2010. 716, 2. L209–L213.

Cappelluti N., Allevato V., Finoguenov A. Clustering of X-Ray-Selected AGN // Advances in Astronomy. I 2012. 2012. 853701.

Cappelluti Nico, Li Yanxia, Ricarte Angelo, Agarwal Bhaskar, Allevato Viola, Tasnim Ananna Tonima, Ajello Marco, Civano Francesca, Comastri Andrea, Elvis Martin, Finoguenov Alexis, Gilli Roberto, Hasinger Günther, Marchesi Stefano, Natarajan Priyamvada, Pacucci Fabio, Treister E., Urry C. Megan. The Chandra COSMOS Legacy Survey: Energy Spectrum of the Cosmic X-Ray Background and Constraints on Undetected Populations // ApJ. III 2017. 837, 1. 19.

Carroll Bradley W., Ostlie Dale A. An Introduction to Modern Astrophysics. 1996.

Cash W. Parameter estimation in astronomy through application of the likelihood ratio. // ApJ. III 1979. 228. 939–947.

Cenko S. B., Barthelmy S. D., D'Avanzo P., Kennea J. A., Lien A. Y., Marshall F. E., Palmer D. M., Siegel M. H., Tohuvavohu A. GRB 171003A: Swift detection of a burst or a Galactic Transient. // GRB Coordinates Network. I 2017. 21960. 1.

Cerda-Duran Pablo, Elias-Rosa Nancy. Neutron Stars Formation and Core Collapse Supernovae // Astrophysics and Space Science Library. 457. 2018. 1. (Astrophysics and Space Science Library).

Chen C. T. J., Brandt W. N., Luo B., Ranalli P., Yang G., Alexander D. M., Bauer F. E., Kelson D. D., Lacy M., Nyland K., Tozzi P., Vito F., Cirasuolo M., Gilli R., Jarvis M. J., Lehmer B. D., Paolillo M., Schneider D. P., Shemmer O., Smail I., Sun M., Tanaka M., Vaccari M., Vignali C., Xue Y. Q., Banerji M., Chow K. E., Häußler B., Norris R. P., Silverman J. D., Trump J. R. The XMM-SERVS survey: new XMM-Newton point-source catalogue for the XMM-LSS field // MNRAS. VIII 2018. 478, 2. 2132–2163.

Chilingarian Igor V., Katkov Ivan Yu., Zolotukhin Ivan Yu., Grishin Kirill A., Beletsky Yuri, Boutsia Konstantina, Osip David J. A Population of Bona Fide Intermediate-mass Black Holes Identified as Low-luminosity Active Galactic Nuclei // ApJ. VIII 2018. 863, 1. 1.

Chisari Nora Elisa, Alonso David, Krause Elisabeth, Leonard C. Danielle, Bull Philip, Neveu Jérémy, Villarreal Antonio, Singh Sukhdeep, McClintock Thomas, Ellison John, Du Zilong, Zuntz Joe, Mead Alexander, Joudaki Shahab, Lorenz Christiane S., Tröster Tilman, Sanchez Javier, Lanusse Francois, Ishak Mustapha, Hlozek Renée, Blazek Jonathan, Campagne Jean-Eric, Almoubayyed Husni, Eifler Tim, Kirby Matthew, Kirkby David, Plaszczynski Stéphane, Slosar Anže, Vrastil Michal, Wagoner Erika L., LSST Dark Energy Science Collaboration . Core Cosmology Library: Precision Cosmological Predictions for LSST // ApJS. V 2019. 242, 1. 2.

Choi C. S., Nagase F., Makino F., Dotani T., Kitamoto S., Takahama S. Iron Line Intensity Variations of Hercules X-1 over the Pulse Phase and the 35 Day Cycle // ApJ. XII 1994. 437. 449.

Churazov E., Gilfanov M., Revnivtsev M. Soft state of Cygnus X-1: stable disc and unstable corona // MNRAS. III 2001. 321, 4. 759–766.

Churazov E., Sunyaev R., Gilfanov M., Forman W., Jones C. The 6.4-keV fluorescent iron line from cluster cooling flows // MNRAS. VII 1998. 297, 4. 1274–1278.

Coe Dan. Fisher Matrices and Confidence Ellipses: A Quick-Start Guide and Software // arXiv e-prints. VI 2009. arXiv:0906.4123.

Coe M. J., Kirk J. Catalogue of Be/X-ray binary systems in the Small Magellanic Cloud: X-ray, optical and IR properties // MNRAS. IX 2015. 452, 1. 969–977.

Coil Alison L., Georgakakis Antonis, Newman Jeffrey A., Cooper Michael C., Croton Darren, Davis Marc, Koo David C., Laird Elise S., Nandra Kirpal, Weiner Benjamin J., Willmer

Christopher N. A., Yan Renbin. AEGIS: The Clustering of X-Ray Active Galactic Nucleus Relative to Galaxies at z ∼1 // ApJ. VIII 2009. 701, 2. 1484–1499.

Cole Shaun, Percival Will J., Peacock John A., Norberg Peder, Baugh Carlton M., Frenk Carlos S., Baldry Ivan, Bland-Hawthorn Joss, Bridges Terry, Cannon Russell, Colless Matthew, Collins Chris, Couch Warrick, Cross Nicholas J. G., Dalton Gavin, Eke Vincent R., De Propris Roberto, Driver Simon P., Efstathiou George, Ellis Richard S., Glazebrook Karl, Jackson Carole, Jenkins Adrian, Lahav Ofer, Lewis Ian, Lumsden Stuart, Maddox Steve, Madgwick Darren, Peterson Bruce A., Sutherland Will, Taylor Keith. The 2dF Galaxy Redshift Survey: power-spectrum analysis of the final data set and cosmological implications // MNRAS. IX 2005. 362, 2. 505–534.

Comparat J., Merloni A., Salvato M., Nandra K., Boller T., Georgakakis A., Finoguenov A., Dwelly T., Buchner J., Del Moro A., Clerc N., Wang Y., Zhao G., Prada F., Yepes G., Brusa M., Krumpe M., Liu T. Active galactic nuclei and their large-scale structure: an eROSITA mock catalogue // MNRAS. VIII 2019. 487, 2. 2005–2029.

Crocce M., Gaztañaga E., Cabré A., Carnero A., Sánchez E. Clustering of photometric luminous red galaxies - I. Growth of structure and baryon acoustic feature // MNRAS. XI 2011. 417, 4. 2577–2591.

Crummy J., Fabian A. C., Gallo L., Ross R. R. An explanation for the soft X-ray excess in active galactic nuclei // MNRAS. II 2006. 365, 4. 1067–1081.

Cusumano G., La Parola V., D'Aì A., Segreto A., Tagliaferri G., Barthelmy S. D., Gehrels N. An unexpected drop in the magnetic field of the X-ray pulsar V0332+53 after the bright outburst occurred in 2015 // MNRAS. VII 2016. 460, 1. L99–L103.

Dauser T., García J., Walton D. J., Eikmann W., Kallman T., McClintock J., Wilms J. Normalizing a relativistic model of X-ray reflection. Definition of the reflection fraction and its implementation in relxill // A&A. V 2016. 590. A76.

Day C. S. R., Nagase F., Asai K., Takeshima T. The Discovery of Pulsed Iron Line Emission from Centaurus X-3 // ApJ. V 1993. 408. 656.

Dey Arjun, Schlegel David J., Lang Dustin, Blum Robert, Burleigh Kaylan, Fan Xiaohui, Findlay Joseph R., Finkbeiner Doug, Herrera David, Juneau Stéphanie, Landriau Martin, Levi Michael, McGreer Ian, Meisner Aaron, Myers Adam D., Moustakas John, Nugent Peter, Patej Anna, Schlafly Edward F., Walker Alistair R., Valdes Francisco, Weaver Benjamin A., Yèche Christophe, Zou Hu, Zhou Xu, Abareshi Behzad, Abbott T. M. C., Abolfathi Bela, Aguilera C., Alam Shadab, Allen Lori, Alvarez A., Annis James, Ansarinejad Behzad, Aubert Marie, Beechert Jacqueline, Bell Eric F., BenZvi Segev Y., Beutler Florian, Bielby Richard M., Bolton Adam S., Briceño César, Buckley-Geer Elizabeth J., Butler Karen, Calamida Annalisa, Carlberg Raymond G., Carter Paul, Casas Ricard, Castander Francisco J., Choi Yumi, Comparat Johan, Cukanovaite Elena, Delubac Timothée, DeVries Kaitlin, Dey Sharmila, Dhungana

Govinda, Dickinson Mark, Ding Zhejie, Donaldson John B., Duan Yutong, Duckworth Christopher J., Eftekharzadeh Sarah, Eisenstein Daniel J., Etourneau Thomas, Fagrelius Parker A., Farihi Jay, Fitzpatrick Mike, Font-Ribera Andreu, Fulmer Leah, Gänsicke Boris T., Gaztanaga Enrique, George Koshy, Gerdes David W., Gontcho Satya Gontcho A., Gorgoni Claudio, Green Gregory, Guy Julien, Harmer Diane, Hernandez M., Honscheid Klaus, Huang Lijuan Wendy, James David J., Jannuzi Buell T., Jiang Linhua, Joyce Richard, Karcher Armin, Karkar Sonia, Kehoe Robert, Kneib Jean-Paul, Kueter-Young Andrea, Lan Ting-Wen, Lauer Tod R., Le Guillou Laurent, Le Van Suu Auguste, Lee Jae Hyeon, Lesser Michael, Perreault Levasseur Laurence, Li Ting S., Mann Justin L., Marshall Robert, Martínez-Vázquez C. E., Martini Paul, du Mas des Bourboux Hélion, McManus Sean, Meier Tobias Gabriel, Ménard Brice, Metcalfe Nigel, Muñoz-Gutiérrez Andrea, Najita Joan, Napier Kevin, Narayan Gautham, Newman Jeffrey A., Nie Jundan, Nord Brian, Norman Dara J., Olsen Knut A. G., Paat Anthony, Palanque-Delabrouille Nathalie, Peng Xiyan, Poppett Claire L., Poremba Megan R., Prakash Abhishek, Rabinowitz David, Raichoor Anand, Rezaie Mehdi, Robertson A. N., Roe Natalie A., Ross Ashley J., Ross Nicholas P., Rudnick Gregory, Safonova Sasha, Saha Abhijit, Sánchez F. Javier, Savary Elodie, Schweiker Heidi, Scott Adam, Seo Hee-Jong, Shan Huanyuan, Silva David R., Slepian Zachary, Soto Christian, Sprayberry David, Staten Ryan, Stillman Coley M., Stupak Robert J., Summers David L., Sien Tie Suk, Tirado H., Vargas-Magaña Mariana, Vivas A. Katherina, Wechsler Risa H., Williams Doug, Yang Jinyi, Yang Qian, Yapici Tolga, Zaritsky Dennis, Zenteno A., Zhang Kai, Zhang Tianmeng, Zhou Rongpu, Zhou Zhimin. Overview of the DESI Legacy Imaging Surveys // AJ. V 2019. 157, 5. 168.

Di Matteo Tiziana, Springel Volker, Hernquist Lars. Energy input from quasars regulates the growth and activity of black holes and their host galaxies // Nature. II 2005. 433, 7026. 604–607.

Dodelson Scott. Modern cosmology. 2003.

Donato D., Cenko S. B., Covino S., Troja E., Pursimo T., Cheung C. C., Fox O., Kutyrev A., Campana S., Fugazza D., Landt H., Butler N. R. A Tidal Disruption Event in a nearby Galaxy Hosting an Intermediate Mass Black Hole // ApJ. II 2014. 781, 2. 59.

Done Chris. Observational characteristics of accretion onto black holes // arXiv e-prints. VIII 2010. arXiv:1008.2287.

Done Chris, Davis S. W., Jin C., Blaes O., Ward M. Intrinsic disc emission and the soft X-ray excess in active galactic nuclei // MNRAS. III 2012. 420, 3. 1848–1860.

Dong Ruobing, Greene Jenny E., Ho Luis C. X-Ray Properties of Intermediate-mass Black Holes in Active Galaxies. III. Spectral Energy Distribution and Possible Evidence for Intrinsically X-Ray-weak Active Galactic Nuclei // ApJ. XII 2012. 761, 1. 73.

Doroshenko V., Tsygankov S., Santangelo A. Orbital parameters of V 0332+53 from 2015 giant outburst data // A&A. V 2016. 589. A72.

Doroshenko V., Zhang S. N., Santangelo A., Ji L., Tsygankov S., Mushtukov A., Qu L. J., Zhang S., Ge M. Y., Chen Y. P., Bu Q. C., Cao X. L., Chang Z., Chen G., Chen L., Chen T. X., Chen Y., Chen Y. B., Cui W., Cui W. W., Deng J. K., Dong Y. W., Du Y. Y., Fu M. X., Gao G. H., Gao H., Gao M., Gu Y. D., Guan J., Guo C. C., Han D. W., Hu W., Huang Y., Huo J., Jia S. M., Jiang L. H., Jiang W. C., Jin J., Jin Y. J., Kong L. D., Li B., Li C. K., Li G., Li M. S., Li T. P., Li W., Li X., Li X. B., Li X. F., Li Y. G., Li Z. J., Li Z. W., Liang X. H., Liao J. Y., Liu C. Z., Liu G. Q., Liu H. W., Liu S. Z., Liu X. J., Liu Y., Liu Y. N., Lu B., Lu F. J., Lu X. F., Luo T., Ma X., Meng B., Nang Y., Nie J. Y., Ou G., Sai N., Shang R. C., Song L. M., Song X. Y., Sun L., Tan Y., Tao L., Tuo Y. L., Wang G. F., Wang J., Wang W. S., Wang Y. S., Wen X. Y., Wu B. B., Wu M., Xiao G. C., Xiong S. L., Xu H., Xu Y. P., Yang Y. R., Yang J. W., Yang S., Yang Y. J., Zhang A. M., Zhang C. L., Zhang C. M., Zhang F., Zhang H. M., Zhang J., Zhang Q., Zhang T., Zhang W., Zhang W. C., Zhang W. Z., Zhang Y., Zhang Y., Zhang Y. F., Zhang Y. J., Zhang Z., Zhang Z. L., Zhao H. S., Zhao J. L., Zhao X. F., Zheng S. J., Zhu Y., Zhu Y. X., Zou C. L., Zhang R. L. Hot disc of the Swift J0243.6+6124 revealed by Insight-HXMT // MNRAS. I 2020. 491, 2. 1857–1867.

Doroshenko Victor, Tsygankov Sergey S., Mushtukov Alexand er A., Lutovinov Alexander A., Santangelo Andrea, Suleimanov Valery F., Poutanen Juri. Luminosity dependence of the cyclotron line and evidence for the accretion regime transition in V 0332+53 // MNRAS. IV 2017. 466, 2. 2143–2150.

Dougherty Sean L., Harrison C. M., Kocevski Dale D., Rosario D. J. Obscured AGN enhancement in galaxy pairs at cosmic noon: evidence from a probabilistic treatment of photometric redshifts // MNRAS. V 2023.

Duras F., Bongiorno A., Ricci F., Piconcelli E., Shankar F., Lusso E., Bianchi S., Fiore F., Maiolino R., Marconi A., Onori F., Sani E., Schneider R., Vignali C., La Franca F. Universal bolometric corrections for active galactic nuclei over seven luminosity decades // A&A. IV 2020. 636. A73.

Ebisawa Ken, Mitsuda Kazuhisa, Hanawa Tomoyuki. Application of a General Relativistic Accretion Disk Model to LMC X-1, LMC X-3, X1608-522, and X1636-536 // ApJ. I 1991. 367. 213.

Ebrero J., Mateos S., Stewart G. C., Carrera F. J., Watson M. G. High-precision multi-band measurements of the angular clustering of X-ray sources // A&A. VI 2009. 500, 2. 749–762.

Eisenstein Daniel J., Hu Wayne. Baryonic Features in the Matter Transfer Function // ApJ. III 1998. 496, 2. 605–614.

Eisenstein Daniel J., Zehavi Idit, Hogg David W., Scoccimarro Roman, Blanton Michael R., Nichol Robert C., Scranton Ryan, Seo Hee-Jong, Tegmark Max, Zheng Zheng, Anderson Scott F., Annis Jim, Bahcall Neta, Brinkmann Jon, Burles Scott, Castander Francisco J., Connolly Andrew, Csabai Istvan, Doi Mamoru, Fukugita Masataka, Frieman Joshua A., Glazebrook Karl, Gunn James E., Hendry John S., Hennessy Gregory, Ivezić Zeljko, Kent

Stephen, Knapp Gillian R., Lin Huan, Loh Yeong-Shang, Lupton Robert H., Margon Bruce, McKay Timothy A., Meiksin Avery, Munn Jeffery A., Pope Adrian, Richmond Michael W., Schlegel David, Schneider Donald P., Shimasaku Kazuhiro, Stoughton Christopher, Strauss Michael A., SubbaRao Mark, Szalay Alexander S., Szapudi István, Tucker Douglas L., Yanny Brian, York Donald G. Detection of the Baryon Acoustic Peak in the Large-Scale Correlation Function of SDSS Luminous Red Galaxies // ApJ. XI 2005. 633, 2. 560–574.

Elyiv A., Clerc N., Plionis M., Surdej J., Pierre M., Basilakos S., Chiappetti L., Gandhi P., Gosset E., Melnyk O., Pacaud F. Angular correlation functions of X-ray point-like sources in the full exposure XMM-LSS field // A&A. I 2012. 537. A131.

Endo Takao, Ishida Manabu, Masai Kuniaki, Kunieda Hideyo, Inoue Hajime, Nagase Fumiaki. Broadening of Nearly Neutral Iron Emission Line of GX 301-2 Observed with ASCA // ApJ. VIII 2002. 574, 2. 879–898.

Epili Prahlad, Naik Sachindra, Jaisawal Gaurava K., Gupta Shivangi. Decade long RXTE monitoring observations of Be/X-ray binary pulsar EXO 2030+375 // MNRAS. XII 2017. 472, 3. 3455–3466.

Estrada Juan, Sefusatti Emiliano, Frieman Joshua A. The Correlation Function of Optically Selected Galaxy Clusters in the Sloan Digital Sky Survey // ApJ. II 2009. 692, 1. 265–282.

Euclid Collaboration , Blanchard A., Camera S., Carbone C., Cardone V. F., Casas S., Clesse S., Ilić S., Kilbinger M., Kitching T., Kunz M., Lacasa F., Linder E., Majerotto E., Markovič K., Martinelli M., Pettorino V., Pourtsidou A., Sakr Z., Sánchez A. G., Sapone D., Tutusaus I., Yahia-Cherif S., Yankelevich V., Andreon S., Aussel H., Balaguera-Antolínez A., Baldi M., Bardelli S., Bender R., Biviano A., Bonino D., Boucaud A., Bozzo E., Branchini E., Brau-Nogue S., Brescia M., Brinchmann J., Burigana C., Cabanac R., Capobianco V., Cappi A., Carretero J., Carvalho C. S., Casas R., Castander F. J., Castellano M., Cavuoti S., Cimatti A., Cledassou R., Colodro-Conde C., Congedo G., Conselice C. J., Conversi L., Copin Y., Corcione L., Coupon J., Courtois H. M., Cropper M., Da Silva A., de la Torre S., Di Ferdinando D., Dubath F., Ducret F., Duncan C. A. J., Dupac X., Dusini S., Fabbian G., Fabricius M., Farrens S., Fosalba P., Fotopoulou S., Fourmanoit N., Frailis M., Franceschi E., Franzetti P., Fumana M., Galeotta S., Gillard W., Gillis B., Giocoli C., Gómez-Alvarez P., Graciá-Carpio J., Grupp F., Guzzo L., Hoekstra H., Hormuth F., Israel H., Jahnke K., Keihanen E., Kermiche S., Kirkpatrick C. C., Kohley R., Kubik B., Kurki-Suonio H., Ligori S., Lilje P. B., Lloro I., Maino D., Maiorano E., Marggraf O., Martinet N., Marulli F., Massey R., Medinaceli E., Mei S., Mellier Y., Metcalf B., Metge J. J., Meylan G., Moresco M., Moscardini L., Munari E., Nichol R. C., Niemi S., Nucita A. A., Padilla C., Paltani S., Pasian F., Percival W. J., Pires S., Polenta G., Poncet M., Pozzetti L., Racca G. D., Raison F., Renzi A., Rhodes J., Romelli E., Roncarelli M., Rossetti E., Saglia R., Schneider P., Scottez V., Secroun A., Sirri G., Stanco L., Starck J. L., Sureau F., Tallada-Crespí P., Tavagnacco D., Taylor A. N., Tenti M., Tereno I., Toledo-Moreo R., Torradeflot F., Valenziano L., Vassallo T., Verdoes Kleijn G. A., Viel M., Wang Y., Zacchei A., Zoubian J., Zucca E. Euclid preparation. VII. Forecast validation for Euclid cosmological probes // A&A. X 2020. 642. A191.

Evans Ian N., Primini Francis A., Glotfelty Kenny J., Anderson Craig S., Bonaventura Nina R., Chen Judy C., Davis John E., Doe Stephen M., Evans Janet D., Fabbiano Giuseppina, Galle Elizabeth C., Gibbs II Danny G., Grier John D., Hain Roger M., Hall Diane M., Harbo Peter N., He Xiangqun Helen, Houck John C., Karovska Margarita, Kashyap Vinay L., Lauer Jennifer, McCollough Michael L., McDowell Jonathan C., Miller Joseph B., Mitschang Arik W., Morgan Douglas L., Mossman Amy E., Nichols Joy S., Nowak Michael A., Plummer David A., Refsdal Brian L., Rots Arnold H., Siemiginowska Aneta, Sundheim Beth A., Tibbetts Michael S., Van Stone David W., Winkelman Sherry L., Zografou Panagoula. The Chandra Source Catalog // ApJS. VII 2010. 189, 1. 37–82.

Evans P. A., Beardmore A. P., Page K. L., Tyler L. G., Osborne J. P., Goad M. R., O'Brien P. T., Vetere L., Racusin J., Morris D., Burrows D. N., Capalbi M., Perri M., Gehrels N., Romano P. An online repository of Swift/XRT light curves of γ-ray bursts // A&A. VII 2007. 469, 1. 379–385.

Fabbiano G. X-rays from normal galaxies. // ARA&A. I 1989. 27. 87–138.

Fabian A. C., Rees M. J., Stella L., White N. E. X-ray fluorescence from the inner disc in Cygnus X-1. // MNRAS. V 1989. 238. 729–736.

Fabrika S. N., Atapin K. E., Vinokurov A. S., Sholukhova O. N. Ultraluminous X-Ray Sources // Astrophysical Bulletin. I 2021. 76, 1. 6–38.

Fanidakis N., Baugh C. M., Benson A. J., Bower R. G., Cole S., Done C., Frenk C. S., Hickox R. C., Lacey C., Del P. Lagos C. The evolution of active galactic nuclei across cosmic time: what is downsizing? // MNRAS. II 2012. 419, 4. 2797–2820.

Ferrarese Laura, Merritt David. A Fundamental Relation between Supermassive Black Holes and Their Host Galaxies // ApJ. VIII 2000. 539, 1. L9–L12.

Ferré-Mateu A., Mezcua M., Barrows R. S. A search for active galactic nuclei in low-mass compact galaxies // MNRAS. X 2021. 506, 4. 4702–4714.

Filippova E. V., Mereminskiy I. A., Lutovinov A. A., Molkov S. V., Tsygankov S. S. Radius of the neutron star magnetosphere during disk accretion // Astronomy Letters. XI 2017. 43, 11. 706–729.

Fotopoulou S., Buchner J., Georgantopoulos I., Hasinger G., Salvato M., Georgakakis A., Cappelluti N., Ranalli P., Hsu L. T., Brusa M., Comastri A., Miyaji T., Nandra K., Aird J., Paltani S. The 5-10 keV AGN luminosity function at 0.01 < z < 4.0 // A&A. III 2016. 587. A142.

Frank Juhan, King Andrew, Raine Derek J. Accretion Power in Astrophysics: Third Edition. 2002.

Fu Hai, Steffen Joshua L., Gross Arran C., Dai Y. Sophia, Isbell Jacob W., Lin Lihwai, Wake David, Xue Rui, Bizyaev Dmitry, Pan Kaike. SDSS-IV MaNGA: Galaxy Pair Fraction and Correlated Active Galactic Nuclei // ApJ. IV 2018. 856, 2. 93.

Galeev A. A., Rosner R., Vaiana G. S. Structured coronae of accretion disks. // ApJ. IV 1979. 229. 318–326.

García Javier A., McClintock Jeffrey E., Steiner James F., Remillard Ronald A., Grinberg Victoria. An Empirical Method for Improving the Quality of RXTE PCA Spectra // ApJ. X 2014. 794, 1. 73.

Ge Lingsong, Paltani Stéphane, Eckert Dominique, Salvato Mara. Reconstructing AGN X-ray spectral parameter distributions with Bayesian methods. II. Population inference // A&A. XI 2022. 667. A153.

Gehrels N., Chincarini G., Giommi P., Mason K. O., Nousek J. A., Wells A. A., White N. E., Barthelmy S. D., Burrows D. N., Cominsky L. R., Hurley K. C., Marshall F. E., Mészáros P., Roming P. W. A., Angelini L., Barbier L. M., Belloni T., Campana S., Caraveo P. A., Chester M. M., Citterio O., Cline T. L., Cropper M. S., Cummings J. R., Dean A. J., Feigelson E. D., Fenimore E. E., Frail D. A., Fruchter A. S., Garmire G. P., Gendreau K., Ghisellini G., Greiner J., Hill J. E., Hunsberger S. D., Krimm H. A., Kulkarni S. R., Kumar P., Lebrun F., Lloyd-Ronning N. M., Markwardt C. B., Mattson B. J., Mushotzky R. F., Norris J. P., Osborne J., Paczynski B., Palmer D. M., Park H. S., Parsons A. M., Paul J., Rees M. J., Reynolds C. S., Rhoads J. E., Sasseen T. P., Schaefer B. E., Short A. T., Smale A. P., Smith I. A., Stella L., Tagliaferri G., Takahashi T., Tashiro M., Townsley L. K., Tueller J., Turner M. J. L., Vietri M., Voges W., Ward M. J., Willingale R., Zerbi F. M., Zhang W. W. The Swift Gamma-Ray Burst Mission // ApJ. VIII 2004. 611, 2. 1005–1020.

Georgakakis A., Aird J., Buchner J., Salvato M., Menzel M. L., Brandt W. N., McGreer I. D., Dwelly T., Mountrichas G., Koki C., Georgantopoulos I., Hsu L. T., Merloni A., Liu Z., Nandra K., Ross N. P. The X-ray luminosity function of active galactic nuclei in the redshift interval z=3-5 // MNRAS. X 2015. 453, 2. 1946–1964.

Georgakakis A., Nandra K., Laird E. S., Aird J., Trichas M. A new method for determining the sensitivity of X-ray imaging observations and the X-ray number counts // MNRAS. VIII 2008. 388, 3. 1205–1213.

George I. M., Fabian A. C. X-ray reflection from cold matter in Active Galactic Nuclei and X-ray binaries. // MNRAS. III 1991. 249. 352.

Gezari Suvi. Tidal Disruption Events // ARA&A. IX 2021. 59. 21–58.

Ghosh P., Lamb F. K. Accretion by rotating magnetic neutron stars. III. Accretion torques and period changes in pulsating X-ray sources. // ApJ. XI 1979. 234. 296–316.

Gianolli V. E., Kim D. E., Bianchi S., Agís-González B., Madejski G., Marin F., Marinucci A., Matt G., Middei R., Petrucci P. O., Soffitta P., Tagliacozzo D., Tombesi F., Ursini F., Barnouin T., De Rosa A., Di Gesu L., Ingram A., Loktev V., Panagiotou C., Podgorny J., Poutanen J., Puccetti S., Ratheesh A., Veledina A., Zhang W., Agudo I., Antonelli L. A., Bachetti M., Baldini L., Baumgartner W. H., Bellazzini R., Bongiorno S. D., Bonino R., Brez A., Bucciantini N.,

Capitanio F., Castellano S., Cavazzuti E., Chen C. T., Ciprini S., Costa E., Del Monte E., Di Lalla N., Di Marco A., Donnarumma I., Doroshenko V., Dovčiak M., Ehlert S. R., Enoto T., Evangelista Y., Fabiani S., Ferrazzoli R., García J. A., Gunji S., Heyl J., Iwakiri W., Jorstad S. G., Kaaret P., Karas V., Kislat F., Kitaguchi T., Kolodziejczak J. J., Krawczynski H., La Monaca F., Latronico L., Liodakis I., Maldera S., Manfreda A., Marscher A. P., Marshall H. L., Massaro F., Mitsuishi I., Mizuno T., Muleri F., Negro M., Ng C. Y., O'Dell S. L., Omodei N., Oppedisano C., Papitto A., Pavlov G. G., Peirson A. L., Perri M., Pesce-Rollins M., Pilia M., Possenti A., Ramsey B. D., Rankin J., Roberts O. J., Romani R. W., Sgrò C., Slane P., Spandre G., Swartz D. A., Tamagawa T., Tavecchio F., Taverna R., Tawara Y., Tennant A. F., Thomas N. E., Trois A., Tsygankov S. S., Turolla R., Vink J., Weisskopf M. C., Wu K., Xie F., Zane S. Uncovering the geometry of the hot X-ray corona in the Seyfert galaxy NGC 4151 with IXPE // MNRAS. VIII 2023. 523, 3. 4468–4476.

Gierliński Marek, Done Chris. Is the soft excess in active galactic nuclei real? // MNRAS. III 2004. 349, 1. L7–L11.

Gil-Marín Héctor, Bautista Julián E., Paviot Romain, Vargas-Magaña Mariana, de la Torre Sylvain, Fromenteau Sebastien, Alam Shadab, Ávila Santiago, Burtin Etienne, Chuang Chia-Hsun, Dawson Kyle S., Hou Jiamin, de Mattia Arnaud, Mohammad Faizan G., Müller Eva-Maria, Nadathur Seshadri, Neveux Richard, Percival Will J., Raichoor Anand, Rezaie Mehdi, Ross Ashley J., Rossi Graziano, Ruhlmann-Kleider Vanina, Smith Alex, Tamone Amélie, Tinker Jeremy L., Tojeiro Rita, Wang Yuting, Zhao Gong-Bo, Zhao Cheng, Brinkmann Jonathan, Brownstein Joel R., Choi Peter D., Escoffier Stephanie, de la Macorra Axel, Moon Jeongin, Newman Jeffrey A., Schneider Donald P., Seo Hee-Jong, Vivek Mariappan. The Completed SDSS-IV extended Baryon Oscillation Spectroscopic Survey: measurement of the BAO and growth rate of structure of the luminous red galaxy sample from the anisotropic power spectrum between redshifts 0.6 and 1.0 // MNRAS. X 2020. 498, 2. 2492–2531.

Gilfanov M. X-Ray Emission from Black-Hole Binaries // Lecture Notes in Physics, Berlin Springer Verlag. 794. 2010. 17.

Gilfanov M., Churazov E., Revnivtsev M. Reflection and noise in Cygnus X-1 // A&A. XII 1999. 352. 182–188.

Gilfanov M., Churazov E., Revnivtsev M. Frequency-resolved spectroscopy of Cyg X-1: fast variability of the reflected emission in the soft state // MNRAS. VIII 2000. 316, 4. 923–928.

Gilfanov Marat, Fabbiano Giuseppina, Lehmer Bret, Zezas Andreas. X-Ray Binaries in External Galaxies // Handbook of X-ray and Gamma-ray Astrophysics. Singapore: Springer Nature Singapore, 2022. 1–38.

Gilli R., Comastri A., Hasinger G. The synthesis of the cosmic X-ray background in the Chandra and XMM-Newton era // A&A. II 2007. 463, 1. 79–96.

Gilli R., Daddi E., Zamorani G., Tozzi P., Borgani S., Bergeron J., Giacconi R., Hasinger G., Mainieri V., Norman C., Rosati P., Szokoly G., Zheng W. The spatial clustering of X-ray

selected AGN and galaxies in the Chandra Deep Field South and North // A&A. II 2005. 430. 811–825.

Gilli R., Zamorani G., Miyaji T., Silverman J., Brusa M., Mainieri V., Cappelluti N., Daddi E., Porciani C., Pozzetti L., Civano F., Comastri A., Finoguenov A., Fiore F., Salvato M., Vignali C., Hasinger G., Lilly S., Impey C., Trump J., Capak P., McCracken H., Scoville N., Taniguchi Y., Carollo C. M., Contini T., Kneib J. P., Le Fevre O., Renzini A., Scodeggio M., Bardelli S., Bolzonella M., Bongiorno A., Caputi K., Cimatti A., Coppa G., Cucciati O., de La Torre S., de Ravel L., Franzetti P., Garilli B., Iovino A., Kampczyk P., Knobel C., Kovač K., Lamareille F., Le Borgne J. F., Le Brun V., Maier C., Mignoli M., Pellò R., Peng Y., Perez Montero E., Ricciardelli E., Tanaka M., Tasca L., Tresse L., Vergani D., Zucca E., Abbas U., Bottini D., Cappi A., Cassata P., Fumana M., Guzzo L., Leauthaud A., Maccagni D., Marinoni C., Memeo P., Meneux B., Oesch P., Scaramella R., Walcher J. The spatial clustering of X-ray selected AGN in the XMM-COSMOS field // A&A. I 2009. 494, 1. 33–48.

Giménez-García A., Torrejón J. M., Eikmann W., Martínez-Núñez S., Oskinova L. M., Rodes-Roca J. J., Bernabéu G. An XMM-Newton view of FeKα in high-mass X-ray binaries // A&A. IV 2015. 576. A108.

Gnedin Yu. N., Sunyaev R. A. The Beaming of Radiation from an Accreting Magnetic Neutron Star and the X-ray Pulsars // A&A. I 1973. 25. 233.

Górski K. M., Hivon E., Banday A. J., Wandelt B. D., Hansen F. K., Reinecke M., Bartelmann M. HEALPix: A Framework for High-Resolution Discretization and Fast Analysis of Data Distributed on the Sphere // ApJ. IV 2005. 622. 759–771.

Greene Jenny E., Ho Luis C. A New Sample of Low-Mass Black Holes in Active Galaxies // ApJ. XI 2007. 670, 1. 92–104.

Greene Jenny E., Strader Jay, Ho Luis C. Intermediate-Mass Black Holes // ARA&A. VIII 2020. 58. 257–312.

Grimm H. J., Gilfanov M., Sunyaev R. High-mass X-ray binaries as a star formation rate indicator in distant galaxies // MNRAS. III 2003. 339, 3. 793–809.

Guainazzi Matteo, De Rosa Alessandra, Bianchi Stefano, Husemann Bernd, Bogdanovic Tamara, Komossa Stefanie, Loiseau Nora, Paragi Zsolt, Pérez-Torres Miguel, Piconcelli Enrico, Vignali Cristian. An XMM-Newton study of active-inactive galaxy pairs // MNRAS. VI 2021. 504, 1. 393–405.

Gupta Shivangi, Naik Sachindra, Jaisawal Gaurava K., Epili Prahlad R. Spectral and timing studies of 2S 1417-624 during a giant outburst // MNRAS. X 2018. 479, 4. 5612–5619.

HI4PI Collaboration , Ben Bekhti N., Flöer L., Keller R., Kerp J., Lenz D., Winkel B., Bailin J., Calabretta M. R., Dedes L., Ford H. A., Gibson B. K., Haud U., Janowiecki S., Kalberla P. M. W., Lockman F. J., McClure-Griffiths N. M., Murphy T., Nakanishi H., Pisano D. J.,

Staveley-Smith L. HI4PI: A full-sky H I survey based on EBHIS and GASS // A&A. X 2016. 594. A116.

Haardt F., Maraschi L. A Two-Phase Model for the X-Ray Emission from Seyfert Galaxies // ApJ. X 1991. 380. L51.

Haardt Francesco, Maraschi Laura. X-Ray Spectra from Two-Phase Accretion Disks // ApJ. VIII 1993. 413. 507.

Harris Charles R., Millman K. Jarrod, Walt Stéfan J. van der, Gommers Ralf, Virtanen Pauli, Cournapeau David, Wieser Eric, Taylor Julian, Berg Sebastian, Smith Nathaniel J., Kern Robert, Picus Matti, Hoyer Stephan, Kerkwijk Marten H. van, Brett Matthew, Haldane Allan, Río Jaime Fernández del, Wiebe Mark, Peterson Pearu, Gérard-Marchant Pierre, Sheppard Kevin, Reddy Tyler, Weckesser Warren, Abbasi Hameer, Gohlke Christoph, Oliphant Travis E. Array programming with NumPy // Nature. IX 2020. 585, 7825. 357–362.

Harrison C. M., Costa T., Tadhunter C. N., Flütsch A., Kakkad D., Perna M., Vietri G. AGN outflows and feedback twenty years on // Nature Astronomy. II 2018. 2. 198–205.

Harrison Christopher. Observational constraints on the influence of active galactic nuclei on the evolution of galaxies (PhD thesis). IX 2014.

Harrison Fiona A., Craig William W., Christensen Finn E., Hailey Charles J., Zhang William W., Boggs Steven E., Stern Daniel, Cook W. Rick, Forster Karl, Giommi Paolo, Grefenstette Brian W., Kim Yunjin, Kitaguchi Takao, Koglin Jason E., Madsen Kristin K., Mao Peter H., Miyasaka Hiromasa, Mori Kaya, Perri Matteo, Pivovaroff Michael J., Puccetti Simonetta, Rana Vikram R., Westergaard Niels J., Willis Jason, Zoglauer Andreas, An Hongjun, Bachetti Matteo, Barrière Nicolas M., Bellm Eric C., Bhalerao Varun, Brejnholt Nicolai F., Fuerst Felix, Liebe Carl C., Markwardt Craig B., Nynka Melania, Vogel Julia K., Walton Dominic J., Wik Daniel R., Alexander David M., Cominsky Lynn R., Hornschemeier Ann E., Hornstrup Allan, Kaspi Victoria M., Madejski Greg M., Matt Giorgio, Molendi Silvano, Smith David M., Tomsick John A., Ajello Marco, Ballantyne David R., Baloković Mislav, Barret Didier, Bauer Franz E., Blandford Roger D., Brandt W. Niel, Brenneman Laura W., Chiang James, Chakrabarty Deepto, Chenevez Jerome, Comastri Andrea, Dufour Francois, Elvis Martin, Fabian Andrew C., Farrah Duncan, Fryer Chris L., Gotthelf Eric V., Grindlay Jonathan E., Helfand David J., Krivonos Roman, Meier David L., Miller Jon M., Natalucci Lorenzo, Ogle Patrick, Ofek Eran O., Ptak Andrew, Reynolds Stephen P., Rigby Jane R., Tagliaferri Gianpiero, Thorsett Stephen E., Treister Ezequiel, Urry C. Megan. The Nuclear Spectroscopic Telescope Array (NuSTAR) High-energy X-Ray Mission // ApJ. VI 2013. 770, 2. 103.

Hasinger G., Miyaji T., Schmidt M. Luminosity-dependent evolution of soft X-ray selected AGN. New Chandra and XMM-Newton surveys // A&A. X 2005. 441, 2. 417–434.

He J. S., Dou L. M., Ai Y. L., Shu X. W., Jiang N., Wang T. G., Zhang F. B., Shen R. F. Long-term X-ray evolution of SDSS J134244.4+053056.1. A more than 18 year-old, long-lived IMBH-TDE candidate // A&A. VIII 2021. 652. A15.

Heckman Timothy M., Best Philip N. The Coevolution of Galaxies and Supermassive Black Holes: Insights from Surveys of the Contemporary Universe // ARA&A. VIII 2014. 52. 589–660.

Hemphill Paul B., Rothschild Richard E., Markowitz Alex, Fürst Felix, Pottschmidt Katja, Wilms Jörn. A Clumpy Stellar Wind and Luminosity-dependent Cyclotron Line Revealed by the First Suzaku Observation of the High-mass X-Ray Binary 4U 1538-522 // ApJ. IX 2014. 792, 1. 14.

Hickox Ryan C., Alexander David M. Obscured Active Galactic Nuclei // ARA&A. IX 2018. 56. 625–671.

Hickox Ryan C., Myers Adam D., Brodwin Mark, Alexander David M., Forman William R., Jones Christine, Murray Stephen S., Brown Michael J. I., Cool Richard J., Kochanek Christopher S., Dey Arjun, Jannuzi Buell T., Eisenstein Daniel, Assef Roberto J., Eisenhardt Peter R., Gorjian Varoujan, Stern Daniel, Le Floc'h Emeric, Caldwell Nelson, Goulding Andrew D., Mullaney James R. Clustering of Obscured and Unobscured Quasars in the Boötes Field: Placing Rapidly Growing Black Holes in the Cosmic Web // ApJ. IV 2011. 731, 2. 117.

Hills J. G. Possible power source of Seyfert galaxies and QSOs // Nature. III 1975. 254, 5498. 295–298.

Honeycutt R. K., Schlegel E. M. Spectrophotometry of the probable optical counterpart of the transient X-ray sourve V 0332+53. // PASP. IV 1985. 97. 300–302.

Hong Tao, Han J. L., Wen Z. L. A Detection of Baryon Acoustic Oscillations from the Distribution of Galaxy Clusters // ApJ. VIII 2016. 826, 2. 154.

Hopkins Philip F., Hernquist Lars, Cox Thomas J., Di Matteo Tiziana, Robertson Brant, Springel Volker. A Unified, Merger-driven Model of the Origin of Starbursts, Quasars, the Cosmic X-Ray Background, Supermassive Black Holes, and Galaxy Spheroids // ApJS. III 2006. 163, 1. 1–49.

Hopkins Philip F., Hernquist Lars, Cox Thomas J., Kereš Dušan. A Cosmological Framework for the Co-Evolution of Quasars, Supermassive Black Holes, and Elliptical Galaxies. I. Galaxy Mergers and Quasar Activity // ApJS. IV 2008. 175, 2. 356–389.

Hopkins Philip F., Kocevski Dale D., Bundy Kevin. Do we expect most AGN to live in discs? // MNRAS. XI 2014. 445, 1. 823–834.

Hou Jiamin, Sánchez Ariel G., Ross Ashley J., Smith Alex, Neveux Richard, Bautista Julian, Burtin Etienne, Zhao Cheng, Scoccimarro Román, Dawson Kyle S., de Mattia Arnaud, de la Macorra Axel, du Mas des Bourboux Hélion, Eisenstein Daniel J., Gil-Marín Héctor, Lyke Brad W., Mohammad Faizan G., Mueller Eva-Maria, Percival Will J., Rossi Graziano, Vargas Magaña Mariana, Zarrouk Pauline, Zhao Gong-Bo, Brinkmann Jonathan, Brownstein Joel R., Chuang Chia-Hsun, Myers Adam D., Newman Jeffrey A., Schneider Donald P., Vivek M. The completed SDSS-IV extended Baryon Oscillation Spectroscopic Survey: BAO and RSD measurements from anisotropic clustering analysis of the quasar sample in configuration space between redshift 0.8 and 2.2 // MNRAS. I 2021. 500, 1. 1201–1221.

Hunter J. D. Matplotlib: A 2D graphics environment // Computing in Science & Engineering. 2007. 9, 3. 90–95.

Hütsi G. Acoustic oscillations in the SDSS DR4 luminous red galaxy sample power spectrum // A&A. IV 2006. 449, 3. 891–902.

Hütsi Gert. Power spectrum of the maxBCG sample: detection of acoustic oscillations using galaxy clusters // MNRAS. II 2010. 401, 4. 2477–2489.

Hütsi Gert, Gilfanov Marat, Kolodzig Alexander, Sunyaev Rashid. Probing large-scale structure with large samples of X-ray selected AGN. I. Baryonic acoustic oscillations // A&A. XII 2014. 572. A28.

Hwang Hsiang-Chih, Zakamska Nadia L. Lifetime of short-period binaries measured from their Galactic kinematics // MNRAS. IV 2020. 493, 2. 2271–2286.

Illarionov A. F., Sunyaev R. A. Why the Number of Galactic X-ray Stars Is so Small? // A&A. II 1975. 39. 185.

Inoue H. TENMA Observations of Bright Binary X-Ray Sources // Space Sci. Rev.. II 1985. 40, 1-2. 317–338.

Jahoda Keith, Swank Jean H., Giles Alan B., Stark Michael J., Strohmayer Tod, Zhang Weiping, Morgan Edward H. In-orbit performance and calibration of the Rossi X-ray Timing Explorer (RXTE) Proportional Counter Array (PCA) // Proc. SPIE. 2808. 1996. 59–70. (Society of Photo-Optical Instrumentation Engineers (SPIE) Conference Series).

Jaisawal Gaurava K., Naik Sachindra. Investigation of iron emission lines in the eclipsing high mass X-ray binary pulsar OAO_1657-415 // Bulletin of the Astronomical Society of India. IX 2014. 42. 147–164.

Jaisawal Gaurava K., Naik Sachindra, Chenevez Jérôme. Understanding the spectral and timing behaviour of a newly discovered transient X-ray pulsar Swift J0243.6+6124 // MNRAS. III 2018. 474, 4. 4432–4437.

Jaisawal Gaurava K., Naik Sachindra, Epili Prahlad. Suzaku view of the Be/X-ray binary pulsar GX 304-1 during Type I X-ray outbursts // MNRAS. IV 2016. 457, 3. 2749–2760.

Jaisawal Gaurava K., Naik Sachindra, Epili Prahlad R., Chhotaray Birendra, Jana Arghajit, Agrawal P. C. AstroSat observations of eclipsing high mass X-ray binary pulsar OAO 1657-415 // arXiv e-prints. I 2021. arXiv:2101.00815.

Jaisawal Gaurava K., Naik Sachindra, Ho Wynn C. G., Kumari Neeraj, Epili Prahlad, Vasilopoulos Georgios. Revisiting the spectral and timing properties of 4U 1909+07 with NuSTAR and Astrosat // MNRAS. XI 2020. 498, 4. 4830–4838.

Jaisawal Gaurava K., Wilson-Hodge Colleen A., Fabian Andrew C., Naik Sachindra, Chakrabarty Deepto, Kretschmar Peter, Ballantyne David R., Ludlam Renee M., Chenevez Jérôme, Altamirano Diego, Arzoumanian Zaven, Fürst Felix, Gendreau Keith C., Guillot Sebastien, Malacaria Christian, Miller Jon M., Stevens Abigail L., Wolff Michael T. An Evolving Broad Iron Line from the First Galactic Ultraluminous X-Ray Pulsar Swift J0243.6+6124 // ApJ. XI 2019. 885, 1. 18.

Jansen F., Lumb D., Altieri B., Clavel J., Ehle M., Erd C., Gabriel C., Guainazzi M., Gondoin P., Much R., Munoz R., Santos M., Schartel N., Texier D., Vacanti G. XMM-Newton observatory. I. The spacecraft and operations // A&A. I 2001. 365. L1–L6.

Jarvis M., Bernstein G., Jain B. The skewness of the aperture mass statistic // MNRAS. VII 2004. 352, 1. 338–352.

Ji L., Doroshenko V., Suleimanov V., Santangelo A., Orlandini M., Liu J., Ducci L., Zhang S. N., Nabizadeh A., Gavran D., Zhang S., Ge M. Y., Li X. B., Tao L., Bu Q. C., Qu J. L., Lu F. J., Chen L., Song L. M., Li T. P., Xu Y. P., Cao X. L., Chen Y., Liu C. Z., Cai C., Chang Z., Chen T. X., Chen Y. P., Cui W. W., Du Y. Y., Gao G. H., Gao H., Gu Y. D., Guan J., Guo C. C., Han D. W., Huang Y., Huo J., Jia S. M., Jiang W. C., Jin J., Kong L. D., Li B., Li C. K., Li G., Li W., Li X., Li X. F., Li Z. W., Liang X. H., Liao J. Y., Liu B. S., Liu H. X., Liu H. W., Liu X. J., Lu X. F., Luo Q., Luo T., Ma R. C., Ma X., Meng B., Nang Y., Nie J. Y., Ou G., Ren X. Q., Sai N., Song X. Y., Sun L., Tan Y., Tuo Y. L., Wang C., Wang L. J., Wang P. J., Wang W. S., Wang Y. S., Wen X. Y., Wu B. Y., Wu B. B., Wu M., Xiao G. C., Xiao S., Xiong S. L., Yang R. J., Yang S., Yang Yan-Ji, Yang Yi-Jung, Yi Q. B., Yin Q. Q., You Y., Zhang F., Zhang H. M., Zhang J., Zhang P., Zhang W., Zhang W. C., Zhang Yi, Zhang Y. F., Zhang Y. H., Zhao H. S., Zhao X. F., Zheng S. J., Zheng Y. G., Zhou D. K. X-ray reprocessing in accreting pulsar GX 301-2 observed with Insight-HXMT // MNRAS. II 2021. 501, 2. 2522–2530.

Jiren Liu, Jenke Peter A, Long Ji, Shuang-Nan Zhang, Shu Zhang, Mingyu Ge, Jinyuan Liao, Xiaobo Li, Liming Song. Super-Eddington accretion of the first Galactic Ultra-luminous X-ray pulsar Swift J0243.6+6124 // arXiv e-prints. III 2022. arXiv:2203.12227.

Kaaret Philip, Feng Hua, Roberts Timothy P. Ultraluminous X-Ray Sources // ARA&A. VIII 2017. 55, 1. 303–341.

Kaiser Nick. Clustering in real space and in redshift space // MNRAS. VII 1987. 227. 1–21.

Kammoun E. S., Nardini E., Zoghbi A., Miller J. M., Cackett E. M., Gallo E., Reynolds M. T., Risaliti G., Barret D., Brandt W. N., Brenneman L. W., Kaastra J. S., Koss M., Lohfink A. M., Mushotzky R. F., Raymond J., Stern D. The Nature of the Broadband X-Ray Variability in the Dwarf Seyfert Galaxy NGC 4395 // ApJ. XII 2019. 886, 2. 145.

Kauffmann Guinevere, Heckman Timothy M., Tremonti Christy, Brinchmann Jarle, Charlot Stéphane, White Simon D. M., Ridgway Susan E., Brinkmann Jon, Fukugita Masataka, Hall Patrick B., Ivezić Željko, Richards Gordon T., Schneider Donald P. The host galaxies of active galactic nuclei // MNRAS. XII 2003a. 346, 4. 1055–1077.

Kauffmann Guinevere, Heckman Timothy M., White Simon D. M., Charlot Stéphane, Tremonti Christy, Brinchmann Jarle, Bruzual Gustavo, Peng Eric W., Seibert Mark, Bernardi Mariangela, Blanton Michael, Brinkmann Jon, Castander Francisco, Csábai Istvan, Fukugita Masataka, Ivezic Zeljko, Munn Jeffrey A., Nichol Robert C., Padmanabhan Nikhil, Thakar Aniruddha R., Weinberg David H., York Donald. Stellar masses and star formation histories for 10^5 galaxies from the Sloan Digital Sky Survey // MNRAS. V 2003b. 341, 1. 33–53.

Kennea J. A., Lien A. Y., Krimm H. A., Cenko S. B., Siegel M. H. Swift J0243.6+6124: Swift discovery of an accreting NS transient // The Astronomer's Telegram. X 2017. 10809. 1.

Kewley L. J., Dopita M. A., Sutherland R. S., Heisler C. A., Trevena J. Theoretical Modeling of Starburst Galaxies // ApJ. VII 2001. 556, 1. 121–140.

Khorunzhev G. A., Sazonov S. Yu., Medvedev P. S., Gilfanov M. R., Atapin K. E., Belinski A. A., Vozyakova O. V., Dodin A. V., Safonov B. S., Tatarnikov A. M., Bikmaev I. F., Burenin R. A., Dodonov S. N., Eselevich M. V., Zaznobin I. A., Krivonos R. A., Uklein R. I., Postnov K. A., Sunyaev R. A. Search for Tidal Disruption Events Based on the SRG/eROSITA Survey with Subsequent Optical Spectroscopy // Astronomy Letters. XII 2022. 48, 12. 767–789.

King Andrew, Lasota Jean-Pierre. No magnetars in ULXs // MNRAS. V 2019. 485, 3. 3588–3594.

King Andrew, Lasota Jean-Pierre, Middleton Matthew. Ultraluminous X-ray sources // New Astron. Rev.. VI 2023. 96. 101672.

Kohmura T., Kitamoto S., Torii K. Delayed Iron Lines in Centaurus X-3 // ApJ. XII 2001. 562, 2. 943–949.

Koliopanos Filippos, Gilfanov Marat. Luminosity-dependent change of the emission diagram in the X-ray pulsar 4U 1626-67 // MNRAS. III 2016. 456, 4. 3535–3541.

Kolodzig Alexander, Gilfanov Marat, Hütsi Gert, Sunyaev Rashid. AGN and QSOs in the eROSITA All-Sky Survey. II. The large-scale structure // A&A. X 2013a. 558. A90.

Kolodzig Alexander, Gilfanov Marat, Hütsi Gert, Sunyaev Rashid. Can AGN and galaxy clusters explain the surface brightness fluctuations of the cosmic X-ray background? // MNRAS. IV 2017. 466, 3. 3035–3059.

Kolodzig Alexander, Gilfanov Marat, Hütsi Gert, Sunyaev Rashid. Studying the ICM in clusters of galaxies via surface brightness fluctuations of the cosmic X-ray background // MNRAS. II 2018. 473, 4. 4653–4671.

Kolodzig Alexander, Gilfanov Marat, Sunyaev Rashid, Sazonov Sergey, Brusa Marcella. AGN and QSOs in the eROSITA All-Sky Survey. I. Statistical properties // A&A. X 2013b. 558. A89.

Kong L. D., Zhang S., Chen Y. P., Zhang S. N., Ji L., Doroshenko V., Wang P. J., Tao L., Ge M. Y., Liu C. Z., Song L. M., Lu F. J., Qu J. L., Li T. P., Xu Y. P., Cao X. L., Chen Y., Bu Q. C., Cai C., Chang Z., Chen G., Chen L., Chen T. X., Chen Y. B., Cui W., Cui W. W., Deng J. K., Dong Y. W., Du Y. Y., Fu M. X., Gao G. H., Gao H., Gao M., Gu Y. D., Guan J., Guo C. C., Han D. W., Huang Y., Huo J., Jia S. M., Jiang L. H., Jiang W. C., Jin J., Jin Y. J., Li B., Li C. K., Li G., Li M. S., Li W., Li X., Li X. B., Li X. F., Li Y. G., Li Z. W., Liang X. H., Liao J. Y., Liu B. S., Liu G. Q., Liu H. W., Liu X. J., Liu Y. N., Lu B., Lu X. F., Luo Q., Luo T., Ma X., Meng B., Nang Y., Nie J. Y., Ou G., Sai N., Shang R. C., Song X. Y., Sun L., Tan Y., Tuo Y. L., Wang C., Wang G. F., Wang J., Wang L. J., Wang W. S., Wang Y. S., Wen X. Y., Wu B. B., Wu B. Y., Wu M., Xiao G. C., Xiao S., Xiong S. L., Xu H., Yang J. W., Yang S., Yang Y. J., Yang Y. J., Yi Q. B., Yin Q. Q., You Y., Zhang A. M., Zhang C. M., Zhang F., Zhang H. M., Zhang J., Zhang T., Zhang W. C., Zhang W., Zhang W. Z., Zhang Y., Zhang Y. F., Zhang Y. J., Zhang Y., Zhang Z., Zhang Z., Zhang Z. L., Zhao H. S., Zhao X. F., Zheng S. J., Zheng Y. G., Zhou D. K., Zhou J. F., Zhu Y. X., Zhuang R. L. Two Complete Spectral Transitions of Swift J0243.6+6124 Observed by Insight-HXMT // ApJ. X 2020. 902, 1. 18.

Kong Ling-Da, Zhang Shu, Zhang Shuang-Nan, Ji Long, Doroshenko Victor, Santangelo Andrea, Chen Yu-Peng, Lu Fang-Jun, Ge Ming-Yu, Wang Peng-Ju, Tao Lian, Qu Jin-Lu, Li Ti-Pei, Liu Cong-Zhan, Liao Jin-Yuan, Chang Zhi, Peng Jing-Qiang, Shui Qing-Cang. Insight-HXMT Discovery of the Highest-energy CRSF from the First Galactic Ultraluminous X-Ray Pulsar Swift J0243.6+6124 // ApJ. VII 2022. 933, 1. L3.

Kormendy John, Ho Luis C. Coevolution (Or Not) of Supermassive Black Holes and Host Galaxies // ARA&A. VIII 2013. 51, 1. 511–653.

Kouroubatzakis K., Reig P., Andrews J.,) A. Zezas. The optical counterpart to the new accreting pulsar Swift J0243.6+6124 is a Be star // The Astronomer's Telegram. X 2017. 10822. 1.

Koutoulidis L., Georgantopoulos I., Mountrichas G., Plionis M., Georgakakis A., Akylas A., Rovilos E. Dependence of clustering of X-ray AGN on obscuration // MNRAS. XII 2018. 481, 3. 3063–3069.

Kovlakas K., Zezas A., Andrews J. J., Basu-Zych A., Fragos T., Hornschemeier A., Lehmer B., Ptak A. A census of ultraluminous X-ray sources in the local Universe // MNRAS. XI 2020. 498, 4. 4790–4810.

Kreykenbohm I., Mowlavi N., Produit N., Soldi S., Walter R., Dubath P., Lubiński P., Türler M., Coburn W., Santangelo A., Rothschild R. E., Staubert R. INTEGRAL observation of V 0332+53 in outburst // A&A. IV 2005. 433, 3. L45–L48.

Kroupa Pavel. On the variation of the initial mass function // MNRAS. IV 2001. 322, 2. 231–246.

Krumpe Mirko, Miyaji Takamitsu, Coil Alison L., Aceves Hector. The Spatial Clustering of ROSAT All-Sky Survey Active Galactic Nuclei. III. Expanded Sample and Comparison with Optical Active Galactic Nuclei // ApJ. II 2012. 746, 1. 1.

Krumpe Mirko, Miyaji Takamitsu, Coil Alison L., Aceves Hector. Spatial clustering and halo occupation distribution modelling of local AGN via cross-correlation measurements with 2MASS galaxies // MNRAS. II 2018. 474, 2. 1773–1786.

Lagos Claudia Del P., Cora Sofía A., Padilla Nelson D. Effects of AGN feedback on ΛCDM galaxies // MNRAS. VIII 2008. 388, 2. 587–602.

Latimer Lilikoi J., Reines Amy E., Bogdan Akos, Kraft Ralph. The AGN Fraction in Dwarf Galaxies from eROSITA: First Results and Future Prospects // ApJ. XII 2021. 922, 2. L40.

Leahy D. A., Matsuoka M., Kawai N., Makino F. Iron line fluorescence models for GX 301-2. // MNRAS. II 1989. 236. 603–610.

Lehmer B. D., Alexander D. M., Bauer F. E., Brandt W. N., Goulding A. D., Jenkins L. P., Ptak A., Roberts T. P. A Chandra Perspective on Galaxy-wide X-ray Binary Emission and its Correlation with Star Formation Rate and Stellar Mass: New Results from Luminous Infrared Galaxies // ApJ. XI 2010. 724, 1. 559–571.

Lehmer B. D., Xue Y. Q., Brandt W. N., Alexander D. M., Bauer F. E., Brusa M., Comastri A., Gilli R., Hornschemeier A. E., Luo B., Paolillo M., Ptak A., Shemmer O., Schneider D. P., Tozzi P., Vignali C. The 4 Ms Chandra Deep Field-South Number Counts Apportioned by Source Class: Pervasive Active Galactic Nuclei and the Ascent of Normal Galaxies // ApJ. VI 2012. 752, 1. 46.

Lemons Sean M., Reines Amy E., Plotkin Richard M., Gallo Elena, Greene Jenny E. An X-Ray Selected Sample of Candidate Black Holes in Dwarf Galaxies // ApJ. V 2015. 805, 1. 12.

Lewis Antony, Bridle Sarah. Cosmological parameters from CMB and other data: A Monte Carlo approach // Phys. Rev. D. XI 2002. 66, 10. 103511.

Lewis Antony, Challinor Anthony. CAMB: Code for Anisotropies in the Microwave Background. II 2011. ascl:1102.026.

Lin Dacheng, Guillochon James, Komossa S., Ramirez-Ruiz Enrico, Irwin Jimmy A., Maksym W. Peter, Grupe Dirk, Godet Olivier, Webb Natalie A., Barret Didier, Zauderer B. Ashley, Duc Pierre-Alain, Carrasco Eleazar R., Gwyn Stephen D. J. A likely decade-long sustained tidal disruption event // Nature Astronomy. II 2017. 1. 0033.

Liu Jiren, Ji Long, Jenke Peter A., Doroshenko Victor, Liao Zhenxuan, Li Xiaobo, Zhang Shuangnan, Orlandini Mauro, Ge Mingyu, Zhang Shu, Santangelo Andrea. Disk versus wind accretion in X-ray pulsar GX 301-2 // MNRAS. IV 2021.

Liu Jiren, Soria Roberto, Qiao Erlin, Liu Jifeng. Discovery of a pulsating Fe K α line in GX 301-2 // MNRAS. XI 2018. 480, 4. 4746–4753.

Liu Teng, Buchner Johannes, Nandra Kirpal, Merloni Andrea, Dwelly Tom, Sanders Jeremy S., Salvato Mara, Arcodia Riccardo, Brusa Marcella, Wolf Julien, Georgakakis Antonis, Boller Thomas, Krumpe Mirko, Lamer Georg, Waddell Sophia, Urrutia Tanya, Schwope Axel, Robrade Jan, Wilms Jörn, Dauser Thomas, Comparat Johan, Toba Yoshiki, Ichikawa Kohei, Iwasawa Kazushi, Shen Yue, Medel Hector Ibarra. The eROSITA Final Equatorial-Depth Survey (eFEDS). The AGN catalog and its X-ray spectral properties // A&A. V 2022a. 661. A5.

Liu Teng, Merloni Andrea, Comparat Johan, Nandra Kirpal, Sanders Jeremy, Lamer Georg, Buchner Johannes, Dwelly Tom, Freyberg Michael, Malyali Adam, Georgakakis Antonis, Salvato Mara, Brunner Hermann, Brusa Marcella, Klein Matthias, Ghirardini Vittorio, Clerc Nicolas, Pacaud Florian, Bulbul Esra, Liu Ang, Schwope Axel, Robrade Jan, Wilms Jörn, Dauser Thomas, Ramos-Ceja Miriam E., Reiprich Thomas H., Boller Thomas, Wolf Julien. Establishing the X-ray source detection strategy for eROSITA with simulations // A&A. V 2022b. 661. A27.

Lockman F. J., Jahoda K., McCammon D. The Structure of Galactic H i in Directions of Low Total Column Density // ApJ. III 1986. 302. 432.

Loeb Abraham, Rasio Frederic A. Collapse of Primordial Gas Clouds and the Formation of Quasar Black Holes // ApJ. IX 1994. 432. 52.

Loureiro Arthur, Moraes Bruno, Abdalla Filipe B., Cuceu Andrei, McLeod Michael, Whiteway Lorne, Balan Sreekumar T., Benoit-Lévy Aurélien, Lahav Ofer, Manera Marc, Rollins Richard P., Xavier Henrique S. Cosmological measurements from angular power spectra analysis of BOSS DR12 tomography // MNRAS. V 2019. 485, 1. 326–355.

Luo B., Brandt W. N., Xue Y. Q., Brusa M., Alexander D. M., Bauer F. E., Comastri A., Koekemoer A., Lehmer B. D., Mainieri V., Rafferty D. A., Schneider D. P., Silverman J. D., Vignali C. Identifications and Photometric Redshifts of the 2 Ms Chandra Deep Field-South Sources // ApJS. IV 2010. 187, 2. 560–580.

Luo B., Brandt W. N., Xue Y. Q., Lehmer B., Alexander D. M., Bauer F. E., Vito F., Yang G., Basu-Zych A. R., Comastri A., Gilli R., Gu Q. S., Hornschemeier A. E., Koekemoer A., Liu T., Mainieri V., Paolillo M., Ranalli P., Rosati P., Schneider D. P., Shemmer O., Smail I., Sun M., Tozzi P., Vignali C., Wang J. X. The Chandra Deep Field-South Survey: 7 Ms Source Catalogs // ApJS. I 2017. 228, 1. 2.

Lusso Elisabeta, Valiante Rosa, Vito Fabio. The Dawn of Black Holes // Handbook of X-ray and Gamma-ray Astrophysics. Singapore: Springer Nature Singapore, 2022. 1–61.

Lutovinov A., Tsygankov S., Molkov S., Doroshenko V., Mushtukov A., Arefiev V., Lapshov I., Tkachenko A., Pavlinsky M. SRG/ART-XC and NuSTAR observations of the X-ray pulsar GRO J1008-57 in the lowest luminosity state // arXiv e-prints. III 2021. arXiv:2103.05728.

Lutovinov A. A., Tsygankov S. S., Suleimanov V. F., Mushtukov A. A., Doroshenko V., Nagirner D. I., Poutanen J. Transient X-ray pulsar V 0332+53: pulse-phase-resolved spectroscopy and the reflection model // MNRAS. IV 2015. 448, 3. 2175–2186.

Lyke Brad W., Higley Alexandra N., McLane J. N., Schurhammer Danielle P., Myers Adam D., Ross Ashley J., Dawson Kyle, Chabanier Solène, Martini Paul, Busca Nicolás G., Mas des Bourboux Hélion du, Salvato Mara, Streblyanska Alina, Zarrouk Pauline, Burtin Etienne, Anderson Scott F., Bautista Julian, Bizyaev Dmitry, Brandt W. N., Brinkmann Jonathan, Brownstein Joel R., Comparat Johan, Green Paul, de la Macorra Axel, Muñoz Gutiérrez Andrea, Hou Jiamin, Newman Jeffrey A., Palanque-Delabrouille Nathalie, Pâris Isabelle, Percival Will J., Petitjean Patrick, Rich James, Rossi Graziano, Schneider Donald P., Smith Alexander, Vivek M., Weaver Benjamin Alan. The Sloan Digital Sky Survey Quasar Catalog: Sixteenth Data Release // ApJS. IX 2020. 250, 1. 8.

Lynden-Bell D. Galactic Nuclei as Collapsed Old Quasars // Nature. VIII 1969. 223, 5207. 690–694.

Lyubarskii Y. E., Syunyaev R. A. Comptonization in a Radiation Dominated Shock and the Spectra of X-Ray Pulsars // Soviet Astronomy Letters. VI 1982. 8. 330–335.

Madau Piero, Rees Martin J. Massive Black Holes as Population III Remnants // ApJ. IV 2001. 551, 1. L27–L30.

Magdziarz Pawel, Zdziarski Andrzej A. Angle-dependent Compton reflection of X-rays and gamma-rays // MNRAS. IV 1995. 273, 3. 837–848.

Makishima K. Iron Lines from Galactic and Extragalactic X-ray Sources // The Physics of Accretion onto Compact Objects. 266. 1986. 249.

Makishima K., Mihara T., Ishida M., Ohashi T., Sakao T., Tashiro M., Tsuru T., Kii T., Makino F., Murakami T., Nagase F., Tanaka Y., Kunieda H., Tawara Y., Kitamoto S., Miyamoto S., Yoshida A., Turner M. J. L. Discovery of a Prominent Cyclotron Absorption Feature from the Transient X-Ray Pulsar X0331+53 // ApJ. XII 1990. 365. L59.

Maksym W. P., Ulmer M. P., Eracleous M. C., Guennou L., Ho L. C. A tidal flare candidate in Abell 1795 // MNRAS. XI 2013. 435, 3. 1904–1927.

Maksym W. Peter, Lin Dacheng, Irwin Jimmy A. RBS 1032: A Tidal Disruption Event in Another Dwarf Galaxy? // ApJ. IX 2014. 792, 2. L29.

Malanchev Konstantin, Kornilov Matwey V., Pruzhinskaya Maria V., Ishida Emille E. O., Aleo Patrick D., Korolev Vladimir S., Lavrukhina Anastasia, Russeil Etienne, Sreejith Sreevarsha, Volnova Alina A., Voloshina Anastasiya, Krone-Martins Alberto. The SNAD Viewer: Everything You Want to Know about Your Favorite ZTF Object // PASP. II 2023. 135, 1044. 024503.

Manzano-King Christina M., Canalizo Gabriela, Sales Laura V. AGN-Driven Outflows in Dwarf Galaxies // ApJ. X 2019. 884, 1. 54.

Mao Yao-Yuan, Geha Marla, Wechsler Risa H., Weiner Benjamin, Tollerud Erik J., Nadler Ethan O., Kallivayalil Nitya. The SAGA Survey. II. Building a Statistical Sample of Satellite Systems around Milky Way-like Galaxies // ApJ. II 2021. 907, 2. 85.

Marchesi S., Civano F., Elvis M., Salvato M., Brusa M., Comastri A., Gilli R., Hasinger G., Lanzuisi G., Miyaji T., Treister E., Urry C. M., Vignali C., Zamorani G., Allevato V., Cappelluti N., Cardamone C., Finoguenov A., Griffiths R. E., Karim A., Laigle C., LaMassa S. M., Jahnke K., Ranalli P., Schawinski K., Schinnerer E., Silverman J. D., Smolcic V., Suh H., Trakhtenbrot B. The Chandra COSMOS Legacy survey: optical/IR identifications // ApJ. I 2016. 817, 1. 34.

Marleau Francine R., Clancy Dominic, Habas Rebecca, Bianconi Matteo. Infrared signature of active massive black holes in nearby dwarf galaxies // A&A. VI 2017. 602. A28.

Marulli F., Veropalumbo A., Sereno M., Moscardini L., Pacaud F., Pierre M., Plionis M., Cappi A., Adami C., Alis S., Altieri B., Birkinshaw M., Ettori S., Faccioli L., Gastaldello F., Koulouridis E., Lidman C., Le Fèvre J. P., Maurogordato S., Poggianti B., Pompei E., Sadibekova T., Valtchanov I. The XXL Survey. XVI. The clustering of X-ray selected galaxy clusters at z 0.3 // A&A. XI 2018. 620. A1.

Mateos S., Warwick R. S., Carrera F. J., Stewart G. C., Ebrero J., Della Ceca R., Caccianiga A., Gilli R., Page M. J., Treister E., Tedds J. A., Watson M. G., Lamer G., Saxton R. D., Brunner H., Page C. G. High precision X-ray log N - log S distributions: implications for the obscured AGN population // A&A. XII 2008. 492, 1. 51–69.

Mayer L., Kazantzidis S., Escala A., Callegari S. Direct formation of supermassive black holes via multi-scale gas inflows in galaxy mergers // Nature. VIII 2010. 466, 7310. 1082–1084.

McConnell Nicholas J., Ma Chung-Pei. Revisiting the Scaling Relations of Black Hole Masses and Host Galaxy Properties // ApJ. II 2013. 764, 2. 184.

McGurk R. C., Max C. E., Medling A. M., Shields G. A., Comerford J. M. Spatially Resolved Imaging and Spectroscopy of Candidate Dual Active Galactic Nuclei // ApJ. IX 2015. 811, 1. 14.

Medvedev P. S., Gilfanov M. R., Sazonov S. Yu., Sunyaev R. A., Khorunzhev G. A. Highly Variable Active Galactic Nuclei in the SRG/eROSITA Sky Survey: I. The Constriction of a Sample and the Catalog of Objects Detected in a Low State // Astronomy Letters. XII 2022. 48, 12. 735–754.

Mereminskiy I. A., Sazonov S. Yu., Krivonos R. A., Karachentsev I. D. Search for AGNs in Dwarf Galaxies in the the M81 Field with INTEGRAL Data // Astronomy Letters. I 2023. 49, 1. 1–8.

Merloni A., Predehl P., Becker W., Böhringer H., Boller T., Brunner H., Brusa M., Dennerl K., Freyberg M., Friedrich P., Georgakakis A., Haberl F., Hasinger G., Meidinger N., Mohr J., Nandra K., Rau A., Reiprich T. H., Robrade J., Salvato M., Santangelo A., Sasaki M., Schwope A., Wilms J., German eROSITA Consortium the. eROSITA Science Book: Mapping the Structure of the Energetic Universe // arXiv e-prints. IX 2012. arXiv:1209.3114.

Mezcua M., Civano F., Marchesi S., Suh H., Fabbiano G., Volonteri M. Intermediate-mass black holes in dwarf galaxies out to redshift ~2.4 in the Chandra COSMOS-Legacy Survey // MNRAS. VIII 2018. 478, 2. 2576–2591.

Mezcua Mar. Observational evidence for intermediate-mass black holes // International Journal of Modern Physics D. I 2017. 26, 11. 1730021.

Mezcua Mar, Siudek Malgorzata, Suh Hyewon, Valiante Rosa, Spinoso Daniele, Bonoli Silvia. Overmassive Black Holes in Dwarf Galaxies Out to z 0.9 in the VIPERS Survey // ApJ. I 2023. 943, 1. L5.

Mineo S., Gilfanov M., Sunyaev R. X-ray emission from star-forming galaxies - I. High-mass X-ray binaries // MNRAS. I 2012a. 419, 3. 2095–2115.

Mineo S., Gilfanov M., Sunyaev R. X-ray emission from star-forming galaxies - II. Hot interstellarmedium // MNRAS. XI 2012b. 426, 3. 1870–1883.

Miyaji T., Hasinger G., Salvato M., Brusa M., Cappelluti N., Civano F., Puccetti S., Elvis M., Brunner H., Fotopoulou S., Ueda Y., Griffiths R. E., Koekemoer A. M., Akiyama M., Comastri A., Gilli R., Lanzuisi G., Merloni A., Vignali C. Detailed Shape and Evolutionary Behavior of the X-Ray Luminosity Function of Active Galactic Nuclei // ApJ. V 2015. 804, 2. 104.

Miyaji Takamitsu, Hasinger Günther, Schmidt Maarten. Soft X-ray AGN luminosity function from it ROSAT surveys. I. Cosmological evolution and contribution to the soft X-ray background // A&A. I 2000. 353. 25–40.

Molina Mallory, Reines Amy E., Latimer Lilikoi J., Baldassare Vivienne, Salehirad Sheyda. A Sample of Massive Black Holes in Dwarf Galaxies Detected via [Fe X] Coronal Line Emission: Active Galactic Nuclei and/or Tidal Disruption Events // ApJ. XII 2021. 922, 2. 155.

Moran Edward C., Eracleous Michael, Leighly Karen M., Chartas George, Filippenko Alexei V., Ho Luis C., Blanco Philip R. Extreme X-Ray Behavior of the Low-Luminosity Active Nucleus in NGC 4395 // AJ. V 2005. 129, 5. 2108–2118.

Moresco Michele, Veropalumbo Alfonso, Marulli Federico, Moscardini Lauro, Cimatti Andrea. C^3: Cluster Clustering Cosmology. II. First Detection of the Baryon Acoustic Oscillations Peak in the Three-point Correlation Function of Galaxy Clusters // ApJ. X 2021. 919, 2. 144.

Moretti A., Vattakunnel S., Tozzi P., Salvaterra R., Severgnini P., Fugazza D., Haardt F., Gilli R. Spectrum of the unresolved cosmic X-ray background: what is unresolved 50 years after its discovery // A&A. XII 2012. 548. A87.

Mountrichas G., Georgakakis A. The clustering of X-ray-selected active galactic nuclei at z= 0.1 // MNRAS. II 2012. 420, 1. 514–525.

Mountrichas G., Georgakakis A., Menzel M. L., Fanidakis N., Merloni A., Liu Z., Salvato M., Nandra K. The clustering amplitude of X-ray-selected AGN at z ∼ 0.8: evidence for a negative dependence on accretion luminosity // MNRAS. IV 2016. 457, 4. 4195–4204.

Mushtukov Alexander, Tsygankov Sergey. Acctering strongly magnetised neutron stars: X-ray Pulsars // arXiv e-prints. IV 2022. arXiv:2204.14185.

Mushtukov Alexander A., Portegies Zwart Simon, Tsygankov Sergey S., Nagirner Dmitrij I., Poutanen Juri. Pulsating ULXs: large pulsed fraction excludes strong beaming // MNRAS. II 2021. 501, 2. 2424–2429.

Mushtukov Alexander A., Suleimanov Valery F., Tsygankov Sergey S., Ingram Adam. Optically thick envelopes around ULXs powered by accreating neutron stars // MNRAS. V 2017. 467, 1. 1202–1208.

Mushtukov Alexander A., Suleimanov Valery F., Tsygankov Sergey S., Poutanen Juri. On the maximum accretion luminosity of magnetized neutron stars: connecting X-ray pulsars and ultraluminous X-ray sources // MNRAS. XII 2015a. 454, 3. 2539–2548.

Mushtukov Alexander A., Suleimanov Valery F., Tsygankov Sergey S., Poutanen Juri. The critical accretion luminosity for magnetized neutron stars // MNRAS. II 2015b. 447, 2. 1847–1856.

Mushtukov Alexander A., Verhagen Patrick A., Tsygankov Sergey S., van der Klis Michiel, Lutovinov Alexander A., Larchenkova Tatiana I. On the radiation beaming of bright X-ray pulsars and constraints on neutron star mass-radius relation // MNRAS. III 2018. 474, 4. 5425–5436.

Nagase F., Corbet R. H. D., Day C. S. R., Inoue H., Takeshima T., Yoshida K., Mihara T. GINGA Observations of Centaurus X-3 // ApJ. IX 1992. 396. 147.

Naik S., Dotani T., Terada Y., Nakajima M., Mihara T., Suzuki M., Makishima K., Sudoh K., Kitamoto S., Nagase F., Enoto T., Takahashi H. Broadband X-Ray Spectroscopy of A0535+262 with Suzaku // ApJ. I 2008. 672, 1. 516–523.

Naik Sachindra, Paul Biswajit, Kachhara Chetan, Vadawale Santosh V. Suzaku observation of the transient X-ray pulsar GRO J1008-57 // MNRAS. V 2011. 413, 1. 241–248.

Narayan Ramesh, Yi Insu. Advection-dominated Accretion: Underfed Black Holes and Neutron Stars // ApJ. X 1995. 452. 710.

Nardini E., Risaliti G. The effects of X-ray absorption variability in NGC 4395 // MNRAS. XI 2011. 417, 4. 2571–2576.

Navarro Julio F., Frenk Carlos S., White Simon D. M. The Structure of Cold Dark Matter Halos // ApJ. V 1996. 462. 563.

Navarro Julio F., Frenk Carlos S., White Simon D. M. A Universal Density Profile from Hierarchical Clustering // ApJ. XII 1997. 490, 2. 493–508.

Naylor Tim, Broos Patrick S., Feigelson Eric D. Bayesian Matching for X-Ray and Infrared Sources in the MYStIX Project // ApJS. XII 2013. 209, 2. 30.

Negueruela I., Roche P., Fabregat J., Coe M. J. The Be/X-ray transient V0332+53: evidence for a tilt between the orbit and the equatorial plane? // MNRAS. VIII 1999. 307, 3. 695–702.

Nespoli E., Reig P. Discovery of a quasi-periodic oscillation in the X-ray pulsar 1A 1118-615: correlated spectral and aperiodic variability // A&A. II 2011. 526. A7.

Netzer Hagai. Revisiting the Unified Model of Active Galactic Nuclei // ARA&A. VIII 2015. 53. 365–408.

Neustadt J. M. M., Holoien T. W. S., Kochanek C. S., Auchettl K., Brown J. S., Shappee B. J., Pogge R. W., Dong Subo, Stanek K. Z., Tucker M. A., Bose S., Chen Ping, Ricci C., Vallely P. J., Prieto J. L., Thompson T. A., Coulter D. A., Drout M. R., Foley R. J., Kilpatrick C. D., Piro A. L., Rojas-Bravo C., Buckley D. A. H., Gromadzki M., Dimitriadis G., Siebert M. R., Do A., Huber M. E., Payne A. V. To TDE or not to TDE: the luminous transient ASASSN-18jd with TDE-like and AGN-like qualities // MNRAS. V 2020. 494, 2. 2538–2560.

Neveux Richard, Burtin Etienne, de Mattia Arnaud, Smith Alex, Ross Ashley J., Hou Jiamin, Bautista Julian, Brinkmann Jonathan, Chuang Chia-Hsun, Dawson Kyle S., Gil-Marín Héctor, Lyke Brad W., de la Macorra Axel, du Mas des Bourboux Hélion, Mohammad Faizan G., Müller Eva-Maria, Myers Adam D., Newman Jeffrey A., Percival Will J., Rossi Graziano, Schneider Donald, Vivek M., Zarrouk Pauline, Zhao Cheng, Zhao Gong-Bo. The completed SDSS-IV extended Baryon Oscillation Spectroscopic Survey: BAO and RSD measurements from the anisotropic power spectrum of the quasar sample between redshift 0.8 and 2.2 // MNRAS. XI 2020. 499, 1. 210–229.

Okazaki A. T., Bate M. R., Ogilvie G. I., Pringle J. E. Viscous effects on the interaction between the coplanar decretion disc and the neutron star in Be/X-ray binaries // MNRAS. XII 2002. 337, 3. 967–980.

Okazaki A. T., Negueruela I. Origin of the X-ray Activity of Be/X-ray Binaries // X-ray Astronomy 2000. 234. 2001. 281. (Astronomical Society of the Pacific Conference Series).

Padmanabhan Nikhil, Schlegel David J., Seljak Uroš, Makarov Alexey, Bahcall Neta A., Blanton Michael R., Brinkmann Jonathan, Eisenstein Daniel J., Finkbeiner Douglas P., Gunn James E., Hogg David W., Ivezić Željko, Knapp Gillian R., Loveday Jon, Lupton Robert H., Nichol Robert C., Schneider Donald P., Strauss Michael A., Tegmark Max, York Donald G. The clustering of luminous red galaxies in the Sloan Digital Sky Survey imaging data // MNRAS. VII 2007. 378, 3. 852–872.

Padmanabhan Nikhil, Xu Xiaoying, Eisenstein Daniel J., Scalzo Richard, Cuesta Antonio J., Mehta Kushal T., Kazin Eyal. A 2 per cent distance to z = 0.35 by reconstructing baryon acoustic oscillations - I. Methods and application to the Sloan Digital Sky Survey // MNRAS. XII 2012. 427, 3. 2132–2145.

Padovani P., Alexander D. M., Assef R. J., De Marco B., Giommi P., Hickox R. C., Richards G. T., Smolčić V., Hatziminaoglou E., Mainieri V., Salvato M. Active galactic nuclei: what's in a name? // A&ARv. VIII 2017. 25, 1. 2.

Page M. J., Carrera F. J. An improved method of constructing binned luminosity functions // MNRAS. I 2000. 311, 2. 433–440.

Pardo K., Goulding A. D., Greene J. E., Somerville R. S., Gallo E., Hickox R. C., Miller B. P., Reines A. E., Silverman J. D. X-Ray Detected Active Galactic Nuclei in Dwarf Galaxies at 0 < z < 1 // ApJ. XI 2016. 831, 2. 203.

Pavlinsky M., Tkachenko A., Levin V., Alexandrovich N., Arefiev V., Babyshkin V., Batanov O., Bodnar Yu., Bogomolov A., Bubnov A., Buntov M., Burenin R., Chelovekov I., Chen C. T., Drozdova T., Ehlert S., Filippova E., Frolov S., Gamkov D., Garanin S., Garin M., Glushenko A., Gorelov A., Grebenev S., Grigorovich S., Gureev P., Gurova E., Ilkaev R., Katasonov I., Krivchenko A., Krivonos R., Korotkov F., Kudelin M., Kuznetsova M., Lazarchuk V., Lomakin I., Lapshov I., Lipilin V., Lutovinov A., Mereminskiy I., Molkov S., Nazarov V., Oleinikov V., Pikalov E., Ramsey B. D., Roiz I., Rotin A., Ryadov A., Sankin E., Sazonov S., Sedov D., Semena A., Semena N., Serbinov D., Shirshakov A., Shtykovsky A., Shvetsov A., Sunyaev R., Swartz D. A., Tambov V., Voron V., Yaskovich A. The ART-XC telescope on board the SRG observatory // A&A. VI 2021. 650. A42.

Peebles P. J. E., Yu J. T. Primeval Adiabatic Perturbation in an Expanding Universe // ApJ. XII 1970. 162. 815.

Percival Will J., Reid Beth A., Eisenstein Daniel J., Bahcall Neta A., Budavari Tamas, Frieman Joshua A., Fukugita Masataka, Gunn James E., Ivezić Željko, Knapp Gillian R., Kron Richard G., Loveday Jon, Lupton Robert H., McKay Timothy A., Meiksin Avery, Nichol Robert C., Pope Adrian C., Schlegel David J., Schneider Donald P., Spergel David N., Stoughton Chris, Strauss Michael A., Szalay Alexander S., Tegmark Max, Vogeley Michael S., Weinberg David H., York Donald G., Zehavi Idit. Baryon acoustic oscillations in the Sloan Digital Sky Survey Data Release 7 galaxy sample // MNRAS. II 2010. 401, 4. 2148–2168.

Pillepich Annalisa, Porciani Cristiano, Reiprich Thomas H. The X-ray cluster survey with eRosita: forecasts for cosmology, cluster physics and primordial non-Gaussianity // MNRAS. V 2012. 422, 1. 44–69.

Pineau F. X., Derriere S., Motch C., Carrera F. J., Genova F., Michel L., Mingo B., Mints A., Nebot Gómez-Morán A., Rosen S. R., Ruiz Camuñas A. Probabilistic multi-catalogue positional cross-match // A&A. I 2017. 597. A89.

Planck Collaboration , Aghanim N., Akrami Y., Ashdown M., Aumont J., Baccigalupi C., Ballardini M., Banday A. J., Barreiro R. B., Bartolo N., Basak S., Battye R., Benabed K., Bernard J. P., Bersanelli M., Bielewicz P., Bock J. J., Bond J. R., Borrill J., Bouchet F. R., Boulanger F., Bucher M., Burigana C., Butler R. C., Calabrese E., Cardoso J. F., Carron J., Challinor A., Chiang H. C., Chluba J., Colombo L. P. L., Combet C., Contreras D., Crill B. P., Cuttaia F., de Bernardis P., de Zotti G., Delabrouille J., Delouis J. M., Di Valentino E., Diego J. M., Doré O., Douspis M., Ducout A., Dupac X., Dusini S., Efstathiou G., Elsner F., Enßlin T. A., Eriksen H. K., Fantaye Y., Farhang M., Fergusson J., Fernandez-Cobos R., Finelli F., Forastieri F., Frailis M., Fraisse A. A., Franceschi E., Frolov A., Galeotta S., Galli S., Ganga K., Génova-Santos R. T., Gerbino M., Ghosh T., González-Nuevo J., Górski K. M., Gratton S., Gruppuso A., Gudmundsson J. E., Hamann J., Handley W., Hansen F. K., Herranz D., Hildebrandt S. R., Hivon E., Huang Z., Jaffe A. H., Jones W. C., Karakci A., Keihänen E., Keskitalo R., Kiiveri K., Kim J., Kisner T. S., Knox L., Krachmalnicoff N., Kunz M., Kurki-Suonio H., Lagache G., Lamarre J. M., Lasenby A., Lattanzi M., Lawrence C. R., Le Jeune M., Lemos P., Lesgourgues J., Levrier F., Lewis A., Liguori M., Lilje P. B., Lilley M., Lindholm V., López-Caniego M., Lubin P. M., Ma Y. Z., Macías-Pérez J. F., Maggio G., Maino D., Mandolesi N., Mangilli A., Marcos-Caballero A., Maris M., Martin P. G., Martinelli M., Martínez-González E., Matarrese S., Mauri N., McEwen J. D., Meinhold P. R., Melchiorri A., Mennella A., Migliaccio M., Millea M., Mitra S., Miville-Deschênes M. A., Molinari D., Montier L., Morgante G., Moss A., Natoli P., Nørgaard-Nielsen H. U., Pagano L., Paoletti D., Partridge B., Patanchon G., Peiris H. V., Perrotta F., Pettorino V., Piacentini F., Polastri L., Polenta G., Puget J. L., Rachen J. P., Reinecke M., Remazeilles M., Renzi A., Rocha G., Rosset C., Roudier G., Rubiño-Martín J. A., Ruiz-Granados B., Salvati L., Sandri M., Savelainen M., Scott D., Shellard E. P. S., Sirignano C., Sirri G., Spencer L. D., Sunyaev R., Suur-Uski A. S., Tauber J. A., Tavagnacco D., Tenti M., Toffolatti L., Tomasi M., Trombetti T., Valenziano L., Valiviita J., Van Tent B., Vibert L., Vielva P., Villa F., Vittorio N., Wandelt B. D., Wehus I. K., White M., White S. D. M., Zacchei A., Zonca A. Planck 2018 results. VI. Cosmological parameters // A&A. IX 2020. 641. A6.

Plionis M., Koutoulidis L., Koulouridis E., Moscardini L., Lidman C., Pierre M., Adami C., Chiappetti L., Faccioli L., Fotopoulou S., Pacaud F., Paltani S. The XXL Survey. XXXII. Spatial clustering of the XXL-S AGN // A&A. XI 2018. 620. A17.

Plotkin Richard. M., Gallo Elena, Miller Brendan P., Baldassare Vivienne F., Treu Tommaso, Woo Jong-Hak. An Environmental Study of the Ultraluminous X-Ray Source Population in Early-type Galaxies // ApJ. I 2014. 780, 1. 6.

Pounds K. A., Nandra K., Stewart G. C., George I. M., Fabian A. C. X-ray reflection from cold matter in the nuclei of active galaxies // Nature. III 1990. 344, 6262. 132–133.

Poutanen Juri, Mushtukov Alexander A., Suleimanov Valery F., Tsygankov Sergey S., Nagirner Dmitrij I., Doroshenko Victor, Lutovinov Alexand er A. A Reflection Model for the Cyclotron Lines in the Spectra of X-Ray Pulsars // ApJ. XI 2013. 777, 2. 115.

Powell M. C., Cappelluti N., Urry C. M., Koss M., Finoguenov A., Ricci C., Trakhtenbrot B., Allevato V., Ajello M., Oh K., Schawinski K., Secrest N. The Swift/BAT AGN Spectroscopic

Survey. IX. The Clustering Environments of an Unbiased Sample of Local AGNs // ApJ. V 2018. 858, 2. 110.

Predehl P., Andritschke R., Arefiev V., Babyshkin V., Batanov O., Becker W., Böhringer H., Bogomolov A., Boller T., Borm K., Bornemann W., Bräuninger H., Brüggen M., Brunner H., Brusa M., Bulbul E., Buntov M., Burwitz V., Burkert W., Clerc N., Churazov E., Coutinho D., Dauser T., Dennerl K., Doroshenko V., Eder J., Emberger V., Eraerds T., Finoguenov A., Freyberg M., Friedrich P., Friedrich S., Fürmetz M., Georgakakis A., Gilfanov M., Granato S., Grossberger C., Gueguen A., Gureev P., Haberl F., Hälker O., Hartner G., Hasinger G., Huber H., Ji L., Kienlin A. v., Kink W., Korotkov F., Kreykenbohm I., Lamer G., Lomakin I., Lapshov I., Liu T., Maitra C., Meidinger N., Menz B., Merloni A., Mernik T., Mican B., Mohr J., Müller S., Nandra K., Nazarov V., Pacaud F., Pavlinsky M., Perinati E., Pfeffermann E., Pietschner D., Ramos-Ceja M. E., Rau A., Reiffers J., Reiprich T. H., Robrade J., Salvato M., Sanders J., Santangelo A., Sasaki M., Scheuerle H., Schmid C., Schmitt J., Schwope A., Shirshakov A., Steinmetz M., Stewart I., Strüder L., Sunyaev R., Tenzer C., Tiedemann L., Trümper J., Voron V., Weber P., Wilms J., Yaroshenko V. The eROSITA X-ray telescope on SRG // A&A. III 2021. 647. A1.

Pringle J. E. Accretion discs in astrophysics // ARA&A. I 1981. 19. 137–162.

Prokopenko I. G., Gilfanov M. R. Normal galaxies in the all-sky survey by the eROSITA X-ray telescope of the Spectrum-X-Gamma observatory // Astronomy Letters. V 2009. 35, 5. 294–304.

Raichoor Anand, de Mattia Arnaud, Ross Ashley J., Zhao Cheng, Alam Shadab, Avila Santiago, Bautista Julian, Brinkmann Jonathan, Brownstein Joel R., Burtin Etienne, Chapman Michael J., Chuang Chia-Hsun, Comparat Johan, Dawson Kyle S., Dey Arjun, du Mas des Bourboux Hélion, Elvin-Poole Jack, Gonzalez-Perez Violeta, Gorgoni Claudio, Kneib Jean-Paul, Kong Hui, Lang Dustin, Moustakas John, Myers Adam D., Müller Eva-Maria, Nadathur Seshadri, Newman Jeffrey A., Percival Will J., Rezaie Mehdi, Rossi Graziano, Ruhlmann-Kleider Vanina, Schlegel David J., Schneider Donald P., Seo Hee-Jong, Tamone Amélie, Tinker Jeremy L., Tojeiro Rita, Vivek M., Yèche Christophe, Zhao Gong-Bo. The completed SDSS-IV extended Baryon Oscillation Spectroscopic Survey: large-scale structure catalogues and measurement of the isotropic BAO between redshift 0.6 and 1.1 for the Emission Line Galaxy Sample // MNRAS. I 2021. 500, 3. 3254–3274.

Ranalli P., Koulouridis E., Georgantopoulos I., Fotopoulou S., Hsu L. T., Salvato M., Comastri A., Pierre M., Cappelluti N., Carrera F. J., Chiappetti L., Clerc N., Gilli R., Iwasawa K., Pacaud F., Paltani S., Plionis E., Vignali C. The 2-10 keV unabsorbed luminosity function of AGN from the LSS, CDFS, and COSMOS surveys // A&A. V 2016. 590. A80.

Rees Martin J. Tidal disruption of stars by black holes of 10^6-10^8 solar masses in nearby galaxies // Nature. VI 1988. 333, 6173. 523–528.

Reig P., Fabregat J., Alfonso-Garzón J. Optical counterpart to Swift J0243.6+6124 // A&A. VIII 2020. 640. A35.

Reig Pablo. Be/X-ray binaries // Ap&SS. III 2011. 332, 1. 1–29.

Reines Amy E. Hunting for massive black holes in dwarf galaxies // Nature Astronomy. I 2022. 6. 26–34.

Reines Amy E., Condon James J., Darling Jeremy, Greene Jenny E. A New Sample of (Wandering) Massive Black Holes in Dwarf Galaxies from High-resolution Radio Observations // ApJ. I 2020. 888, 1. 36.

Reines Amy E., Greene Jenny E., Geha Marla. Dwarf Galaxies with Optical Signatures of Active Massive Black Holes // ApJ. X 2013. 775, 2. 116.

Reines Amy E., Sivakoff Gregory R., Johnson Kelsey E., Brogan Crystal L. An actively accreting massive black hole in the dwarf starburst galaxy Henize2-10 // Nature. II 2011. 470, 7332. 66–68.

Reines Amy E., Volonteri Marta. Relations between Central Black Hole Mass and Total Galaxy Stellar Mass in the Local Universe // ApJ. XI 2015. 813, 2. 82.

Remillard Ronald A., McClintock Jeffrey E. X-Ray Properties of Black-Hole Binaries // ARA&A. IX 2006. 44, 1. 49–92.

Reynolds Christopher S. Measuring Black Hole Spin Using X-Ray Reflection Spectroscopy // Space Sci. Rev.. IX 2014. 183, 1-4. 277–294.

Reynolds Christopher S., Fabian Andrew C. Broad Iron-Kα Emission Lines as a Diagnostic of Black Hole Spin // ApJ. III 2008. 675, 2. 1048–1056.

Ross Ashley J., Samushia Lado, Howlett Cullan, Percival Will J., Burden Angela, Manera Marc. The clustering of the SDSS DR7 main Galaxy sample - I. A 4 per cent distance measure at z = 0.15 // MNRAS. V 2015. 449, 1. 835–847.

Ross R. R., Fabian A. C. A comprehensive range of X-ray ionized-reflection models // MNRAS. III 2005. 358, 1. 211–216.

Rouco Escorial A., Wijnands R., Ootes L. S., Degenaar N., Snelders M., Kaper L., Cackett E. M., Homan J. Quiescent X-ray variability in the neutron star Be/X-ray transient GRO J1750-27 // A&A. X 2019. 630. A105.

Salim Samir, Rich R. Michael, Charlot Stéphane, Brinchmann Jarle, Johnson Benjamin D., Schiminovich David, Seibert Mark, Mallery Ryan, Heckman Timothy M., Forster Karl, Friedman Peter G., Martin D. Christopher, Morrissey Patrick, Neff Susan G., Small Todd, Wyder Ted K., Bianchi Luciana, Donas José, Lee Young-Wook, Madore Barry F., Milliard Bruno, Szalay Alex S., Welsh Barry Y., Yi Sukyoung K. UV Star Formation Rates in the Local Universe // ApJS. XII 2007. 173, 2. 267–292.

Salvato M., Buchner J., Budavári T., Dwelly T., Merloni A., Brusa M., Rau A., Fotopoulou S., Nandra K. Finding counterparts for all-sky X-ray surveys with NWAY: a Bayesian algorithm for cross-matching multiple catalogues // MNRAS. II 2018. 473, 4. 4937–4955.

Salvato M., Wolf J., Dwelly T., Georgakakis A., Brusa M., Merloni A., Liu T., Toba Y., Nandra K., Lamer G., Buchner J., Schneider C., Freund S., Rau A., Schwope A., Nishizawa A., Klein M., Arcodia R., Comparat J., Musiimenta B., Nagao T., Brunner H., Malyali A., Finoguenov A., Anderson S., Shen Y., Ibarra-Medel H., Trump J., Brandt W. N., Urry C. M., Rivera C., Krumpe M., Urrutia T., Miyaji T., Ichikawa K., Schneider D. P., Fresco A., Boller T., Haase J., Brownstein J., Lane R. R., Bizyaev D., Nitschelm C. The eROSITA Final Equatorial-Depth Survey (eFEDS). Identification and characterization of the counterparts to point-like sources // A&A. V 2022. 661. A3.

Sanjurjo-Ferrín G., Torrejón J. M., Postnov K., Oskinova L., Rodes-Roca J. J., Bernabeu G. X-ray variability of the HMXB Cen X-3: evidence for inhomogeneous accretion flows // MNRAS. III 2021. 501, 4. 5892–5909.

Sartori Lia F., Schawinski Kevin, Treister Ezequiel, Trakhtenbrot Benny, Koss Michael, Shirazi Maryam, Oh Kyuseok. The search for active black holes in nearby low-mass galaxies using optical and mid-IR data // MNRAS. XII 2015. 454, 4. 3722–3742.

Satyapal Shobita, Ellison Sara L., McAlpine William, Hickox Ryan C., Patton David R., Mendel J. Trevor. Galaxy pairs in the Sloan Digital Sky Survey - IX. Merger-induced AGN activity as traced by the Wide-field Infrared Survey Explorer // MNRAS. VI 2014. 441, 2. 1297–1304.

Saxton R., Komossa S., Auchettl K., Jonker P. G. X-Ray Properties of TDEs // Space Sci. Rev.. VII 2020. 216, 5. 85.

Saxton R. D., Read A. M., Esquej P., Komossa S., Dougherty S., Rodriguez-Pascual P., Barrado D. A tidal disruption-like X-ray flare from the quiescent galaxy SDSS J120136.02+300305.5 // A&A. V 2012. 541. A106.

Sazonov S., Gilfanov M., Medvedev P., Yao Y., Khorunzhev G., Semena A., Sunyaev R., Burenin R., Lyapin A., Meshcheryakov A., Uskov G., Zaznobin I., Postnov K. A., Dodin A. V., Belinski A. A., Cherepashchuk A. M., Eselevich M., Dodonov S. N., Grokhovskaya A. A., Kotov S. S., Bikmaev I. F., Zhuchkov R. Ya, Gumerov R. I., van Velzen S., Kulkarni S. First tidal disruption events discovered by SRG/eROSITA: X-ray/optical properties and X-ray luminosity function at z < 0.6 // MNRAS. XII 2021. 508, 3. 3820–3847.

Schönherr G., Wilms J., Kretschmar P., Kreykenbohm I., Santangelo A., Rothschild R. E., Coburn W., Staubert R. A model for cyclotron resonance scattering features // A&A. IX 2007. 472, 2. 353–365.

Seo Hee-Jong, Ho Shirley, White Martin, Cuesta Antonio J., Ross Ashley J., Saito Shun, Reid Beth, Padmanabhan Nikhil, Percival Will J., de Putter Roland, Schlegel David J., Eisenstein Daniel J., Xu Xiaoying, Schneider Donald P., Skibba Ramin, Verde Licia, Nichol Robert C.,

Bizyaev Dmitry, Brewington Howard, Brinkmann J., Nicolaci da Costa Luiz Alberto, Gott III J. Richard, Malanushenko Elena, Malanushenko Viktor, Oravetz Dan, Palanque-Delabrouille Nathalie, Pan Kaike, Prada Francisco, Ross Nicholas P., Simmons Audrey, de Simoni Fernando, Shelden Alaina, Snedden Stephanie, Zehavi Idit. Acoustic Scale from the Angular Power Spectra of SDSS-III DR8 Photometric Luminous Galaxies // ApJ. XII 2012. 761, 1. 13.

Sereno Mauro, Veropalumbo Alfonso, Marulli Federico, Covone Giovanni, Moscardini Lauro, Cimatti Andrea. New constraints on σ_8 from a joint analysis of stacked gravitational lensing and clustering of galaxy clusters // MNRAS. VI 2015. 449, 4. 4147–4161.

Shakura N. I., Sunyaev R. A. Black holes in binary systems. Observational appearance. // A&A. I 1973. 24. 337–355.

Shakura N. I., Sunyaev R. A. The theory of an accretion disk/ neutron star boundary layer // Advances in Space Research. I 1988. 8, 2-3. 135–140.

Shtykovskiy P., Gilfanov M. High-mass X-ray binaries in the Small Magellanic Cloud: the luminosity function // MNRAS. IX 2005. 362, 3. 879–890.

Shtykovsky A. E., Lutovinov A. A., Arefiev V. A., Molkov S. V., Tsygankov S. S., Revnivtsev M. G. NuSTAR observations of the X-ray pulsar LMC X-4: A constraint on the magnetic field and tomography of the system in the fluorescent iron line // Astronomy Letters. III 2017. 43, 3. 175–185.

Sibgatullin N. R., Sunyaev R. A. Energy Release During Disk Accretion onto a Rapidly Rotating Neutron Star // Astronomy Letters. XI 2000. 26. 699–724.

Silk Joseph. Feedback by Massive Black Holes in Gas-rich Dwarf Galaxies // ApJ. IV 2017. 839, 1. L13.

Simon P. How accurate is Limber's equation? // A&A. X 2007. 473, 3. 711–714.

Springel Volker, White Simon D. M., Jenkins Adrian, Frenk Carlos S., Yoshida Naoki, Gao Liang, Navarro Julio, Thacker Robert, Croton Darren, Helly John, Peacock John A., Cole Shaun, Thomas Peter, Couchman Hugh, Evrard August, Colberg Jörg, Pearce Frazer. Simulations of the formation, evolution and clustering of galaxies and quasars // Nature. VI 2005. 435, 7042. 629–636.

Stella L., White N. E., Davelaar J., Parmar A. N., Blissett R. J., van der Klis M. The discovery of 4.4 second X-ray pulsations from the rapidly variable X-ray transient V 0332+53. // ApJ. I 1985. 288. L45–L49.

Suh Hyewon, Civano Francesca, Trakhtenbrot Benny, Shankar Francesco, Hasinger Günther, Sanders David B., Allevato Viola. No Significant Evolution of Relations between Black Hole Mass and Galaxy Total Stellar Mass Up to z ~ 2.5 // ApJ. I 2020. 889, 1. 32.

Sukhbold Tuguldur, Ertl T., Woosley S. E., Brown Justin M., Janka H. T. Core-collapse Supernovae from 9 to 120 Solar Masses Based on Neutrino-powered Explosions // ApJ. IV 2016. 821, 1. 38.

Sunyaev R., Arefiev V., Babyshkin V., Bogomolov A., Borisov K., Buntov M., Brunner H., Burenin R., Churazov E., Coutinho D., Eder J., Eismont N., Freyberg M., Gilfanov M., Gureyev P., Hasinger G., Khabibullin I., Kolmykov V., Komovkin S., Krivonos R., Lapshov I., Levin V., Lomakin I., Lutovinov A., Medvedev P., Merloni A., Mernik T., Mikhailov E., Molodtsov V., Mzhelsky P., Müller S., Nandra K., Nazarov V., Pavlinsky M., Poghodin A., Predehl P., Robrade J., Sazonov S., Scheuerle H., Shirshakov A., Tkachenko A., Voron V. SRG X-ray orbital observatory. Its telescopes and first scientific results // A&A. XII 2021. 656. A132.

Sunyaev R. A., Titarchuk L. G. Comptonization of X-Rays in Plasma Clouds - Typical Radiation Spectra // A&A. VI 1980. 86. 121.

Sunyaev R. A., Truemper J. Hard X-ray spectrum of CYG X-1 // Nature. VI 1979. 279. 506–508.

Sunyaev R. A., Zeldovich Ya. B. Small-Scale Fluctuations of Relic Radiation // Ap&SS. IV 1970. 7, 1. 3–19.

Sutherland Will, Saunders Will. On the likelihood ratio for source identification. // MNRAS. XII 1992. 259. 413–420.

Swartz Douglas A., Ghosh Kajal K., Tennant Allyn F., Wu Kinwah. The Ultraluminous X-Ray Source Population from the Chandra Archive of Galaxies // ApJS. X 2004. 154, 2. 519–539.

Takahashi Ryuichi, Sato Masanori, Nishimichi Takahiro, Taruya Atsushi, Oguri Masamune. Revising the Halofit Model for the Nonlinear Matter Power Spectrum // ApJ. XII 2012. 761, 2. 152.

Tao Lian, Feng Hua, Zhang Shuangnan, Bu Qingcui, Zhang Shu, Qu Jinlu, Zhang Yue. Super-Eddington Accretion onto the Galactic Ultraluminous X-Ray Pulsar Swift J0243.6+6124 // ApJ. III 2019. 873, 1. 19.

Tegmark Max. How to measure CMB power spectra without losing information // Phys. Rev. D. V 1997. 55, 10. 5895–5907.

Tegmark Max, Blanton Michael R., Strauss Michael A., Hoyle Fiona, Schlegel David, Scoccimarro Roman, Vogeley Michael S., Weinberg David H., Zehavi Idit, Berlind Andreas, Budavari Tamás, Connolly Andrew, Eisenstein Daniel J., Finkbeiner Douglas, Frieman Joshua A., Gunn James E., Hamilton Andrew J. S., Hui Lam, Jain Bhuvnesh, Johnston David, Kent Stephen, Lin Huan, Nakajima Reiko, Nichol Robert C., Ostriker Jeremiah P., Pope Adrian, Scranton Ryan, Seljak Uroš, Sheth Ravi K., Stebbins Albert, Szalay Alexander S., Szapudi István, Verde Licia, Xu Yongzhong, Annis James, Bahcall Neta A., Brinkmann J., Burles Scott, Castander Francisco J., Csabai Istvan, Loveday Jon, Doi Mamoru, Fukugita Masataka, Gott III J. Richard, Hennessy Greg, Hogg David W., Ivezić Željko, Knapp Gillian R., Lamb Don Q., Lee Brian C.,

Lupton Robert H., McKay Timothy A., Kunszt Peter, Munn Jeffrey A., O'Connell Liam, Peoples John, Pier Jeffrey R., Richmond Michael, Rockosi Constance, Schneider Donald P., Stoughton Christopher, Tucker Douglas L., Vanden Berk Daniel E., Yanny Brian, York Donald G., SDSS Collaboration . The Three-Dimensional Power Spectrum of Galaxies from the Sloan Digital Sky Survey // ApJ. V 2004. 606, 2. 702–740.

Tegmark Max, Taylor Andy N., Heavens Alan F. Karhunen-Loève Eigenvalue Problems in Cosmology: How Should We Tackle Large Data Sets? // ApJ. V 1997. 480, 1. 22–35.

Terrell J., Priedhorsky W. C. The 1973 X-ray transient V 0332+53. // ApJ. X 1984. 285. L15–L18.

Tinker Jeremy, Kravtsov Andrey V., Klypin Anatoly, Abazajian Kevork, Warren Michael, Yepes Gustavo, Gottlöber Stefan, Holz Daniel E. Toward a Halo Mass Function for Precision Cosmology: The Limits of Universality // ApJ. XII 2008. 688, 2. 709–728.

Tinker Jeremy L., Robertson Brant E., Kravtsov Andrey V., Klypin Anatoly, Warren Michael S., Yepes Gustavo, Gottlöber Stefan. The Large-scale Bias of Dark Matter Halos: Numerical Calibration and Model Tests // ApJ. XII 2010. 724, 2. 878–886.

Titarchuk Lev. Generalized Comptonization Models and Application to the Recent High-Energy Observations // ApJ. X 1994. 434. 570.

Torrado Jesús, Lewis Antony. Cobaya: Bayesian analysis in cosmology. X 2019. ascl:1910.019.

Torrado Jesús, Lewis Antony. Cobaya: code for Bayesian analysis of hierarchical physical models // J. Cosmology Astropart. Phys.. V 2021. 2021, 5. 057.

Tremonti Christy A., Heckman Timothy M., Kauffmann Guinevere, Brinchmann Jarle, Charlot Stéphane, White Simon D. M., Seibert Mark, Peng Eric W., Schlegel David J., Uomoto Alan, Fukugita Masataka, Brinkmann Jon. The Origin of the Mass-Metallicity Relation: Insights from 53,000 Star-forming Galaxies in the Sloan Digital Sky Survey // ApJ. X 2004. 613, 2. 898–913.

Truemper J. The ROSAT mission // Advances in Space Research. I 1982. 2, 4. 241–249.

Tsygankov S., Lutovinov A. Iron line emission from X-ray pulsars: physical conditions and geometry of the system // arXiv e-prints. II 2010. arXiv:1002.1898.

Tsygankov S. S., Doroshenko V., Lutovinov A. A., Mushtukov A. A., Poutanen J. SMC X-3: the closest ultraluminous X-ray source powered by a neutron star with non-dipole magnetic field // A&A. IX 2017. 605. A39.

Tsygankov S. S., Lutovinov A. A., Churazov E. M., Sunyaev R. A. V0332+53 in the outburst of 2004-2005: luminosity dependence of the cyclotron line and pulse profile // MNRAS. IX 2006. 371, 1. 19–28.

Tsygankov S. S., Lutovinov A. A., Churazov E. M., Sunyaev R. A. 4U 0115+63 from RXTE and INTEGRAL data: Pulse profile and cyclotron line energy // Astronomy Letters. VI 2007. 33, 6. 368–384.

Tsygankov S. S., Lutovinov A. A., Doroshenko V., Mushtukov A. A., Suleimanov V., Poutanen J. Propeller effect in two brightest transient X-ray pulsars: 4U 0115+63 and V 0332+53 // A&A. VIII 2016. 593. A16.

Tsygankov S. S., Lutovinov A. A., Serber A. V. Completing the puzzle of the 2004-2005 outburst in V0332+53: the brightening phase included // MNRAS. I 2010. 401, 3. 1628–1635.

Tsygankov Sergey S., Doroshenko Victor, Mushtukov Alexander A., Lutovinov Alexander A., Poutanen Juri. On the magnetic field of the first Galactic ultraluminous X-ray pulsar Swift J0243.6+6124 // MNRAS. IX 2018. 479, 1. L134–L138.

Tsygankov Sergey S., Doroshenko Victor, Poutanen Juri, Heyl Jeremy, Mushtukov Alexander A., Caiazzo Ilaria, Di Marco Alessandro, Forsblom Sofia V., González-Caniulef Denis, Klawin Moritz, La Monaca Fabio, Malacaria Christian, Marshall Herman L., Muleri Fabio, Ng Mason, Suleimanov Valery F., Sunyaev Rashid A., Turolla Roberto, Agudo Iván, Antonelli Lucio A., Bachetti Matteo, Baldini Luca, Baumgartner Wayne H., Bellazzini Ronaldo, Bianchi Stefano, Bongiorno Stephen D., Bonino Raffaella, Brez Alessandro, Bucciantini Niccolò, Capitanio Fiamma, Castellano Simone, Cavazzuti Elisabetta, Ciprini Stefano, Costa Enrico, De Rosa Alessandra, Del Monte Ettore, Di Gesu Laura, Di Lalla Niccolò, Donnarumma Immacolata, Dovčiak Michal, Ehlert Steven R., Enoto Teruaki, Evangelista Yuri, Fabiani Sergio, Ferrazzoli Riccardo, Garcia Javier A., Gunji Shuichi, Hayashida Kiyoshi, Iwakiri Wataru, Jorstad Svetlana G., Karas Vladimir, Kitaguchi Takao, Kolodziejczak Jeffery J., Krawczynski Henric, Latronico Luca, Liodakis Ioannis, Maldera Simone, Manfreda Alberto, Marin Frédéric, Marinucci Andrea, Marscher Alan P., Matt Giorgio, Mitsuishi Ikuyuki, Mizuno Tsunefumi, Ng Chi-Yung, O'Dell Stephen L., Omodei Nicola, Oppedisano Chiara, Papitto Alessandro, Pavlov George G., Peirson Abel L., Perri Matteo, Pesce-Rollins Melissa, Petrucci Pierre-Olivier, Pilia Maura, Possenti Andrea, Puccetti Simonetta, Ramsey Brian D., Rankin John, Ratheesh Ajay, Romani Roger W., Sgrò Carmelo, Slane Patrick, Soffitta Paolo, Spandre Gloria, Tamagawa Toru, Tavecchio Fabrizio, Taverna Roberto, Tawara Yuzuru, Tennant Allyn F., Thomas Nicholas E., Tombesi Francesco, Trois Alessio, Vink Jacco, Weisskopf Martin C., Wu Kinwah, Xie Fei, Zane Silvia, IXPE Collaboration . The X-Ray Polarimetry View of the Accreting Pulsar Cen X-3 // ApJ. XII 2022. 941, 1. L14.

Ueda Yoshihiro, Akiyama Masayuki, Hasinger Günther, Miyaji Takamitsu, Watson Michael G. Toward the Standard Population Synthesis Model of the X-Ray Background: Evolution of X-Ray Luminosity and Absorption Functions of Active Galactic Nuclei Including Compton-thick Populations // ApJ. V 2014. 786, 2. 104.

Ueda Yoshihiro, Akiyama Masayuki, Ohta Kouji, Miyaji Takamitsu. Cosmological Evolution of the Hard X-Ray Active Galactic Nucleus Luminosity Function and the Origin of the Hard X-Ray Background // ApJ. XII 2003. 598, 2. 886–908.

Urry C. Megan, Padovani Paolo. Unified Schemes for Radio-Loud Active Galactic Nuclei // PASP. IX 1995. 107. 803.

Viitanen A., Allevato V., Finoguenov A., Shankar F., Gilli R., Lanzuisi G., Vito F. Large-scale clustering of buried X-ray AGN: Trends in AGN obscuration and redshift evolution // A&A. VI 2023. 674. A214.

Vikhlinin A., Burenin R. A., Ebeling H., Forman W. R., Hornstrup A., Jones C., Kravtsov A. V., Murray S. S., Nagai D., Quintana H., Voevodkin A. Chandra Cluster Cosmology Project. II. Samples and X-Ray Data Reduction // ApJ. II 2009a. 692, 2. 1033–1059.

Vikhlinin A., Kravtsov A. V., Burenin R. A., Ebeling H., Forman W. R., Hornstrup A., Jones C., Murray S. S., Nagai D., Quintana H., Voevodkin A. Chandra Cluster Cosmology Project III: Cosmological Parameter Constraints // ApJ. II 2009b. 692, 2. 1060–1074.

Virtanen Pauli, Gommers Ralf, Oliphant Travis E., Haberland Matt, Reddy Tyler, Cournapeau David, Burovski Evgeni, Peterson Pearu, Weckesser Warren, Bright Jonathan, van der Walt Stéfan J., Brett Matthew, Wilson Joshua, Millman K. Jarrod, Mayorov Nikolay, Nelson Andrew R. J., Jones Eric, Kern Robert, Larson Eric, Carey C J, Polat İlhan, Feng Yu, Moore Eric W., VanderPlas Jake, Laxalde Denis, Perktold Josef, Cimrman Robert, Henriksen Ian, Quintero E. A., Harris Charles R., Archibald Anne M., Ribeiro Antônio H., Pedregosa Fabian, van Mulbregt Paul, SciPy 1.0 Contributors . SciPy 1.0: Fundamental Algorithms for Scientific Computing in Python // Nature Methods. 2020. 17. 261–272.

Vito F., Gilli R., Vignali C., Comastri A., Brusa M., Cappelluti N., Iwasawa K. The hard X-ray luminosity function of high-redshift ($3 < z \lesssim 5$) active galactic nuclei // MNRAS. XII 2014. 445, 4. 3557–3574.

Voges W., Aschenbach B., Boller Th., Bräuninger H., Briel U., Burkert W., Dennerl K., Englhauser J., Gruber R., Haberl F., Hartner G., Hasinger G., Kürster M., Pfeffermann E., Pietsch W., Predehl P., Rosso C., Schmitt J. H. M. M., Trümper J., Zimmermann H. U. The ROSAT all-sky survey bright source catalogue // A&A. IX 1999. 349. 389–405.

Volonteri Marta. Formation of supermassive black holes // A&ARv. VII 2010. 18, 3. 279–315.

Voss Rasmus, Gilfanov Marat, Sivakoff Gregory R., Kraft Ralph P., Jordán Andrés, Raychaudhury Somak, Birkinshaw Mark, Brassington Nicola J., Croston Judith H., Evans Daniel A., Forman William R., Hardcastle Martin J., Harris William E., Jones Christine, Juett Adrienne M., Murray Stephen S., Sarazin Craig L., Woodley Kristin A., Worrall Diana M. Luminosity Functions of LMXBs in Centaurus a: Globular Clusters Versus the Field // ApJ. VIII 2009. 701, 1. 471–480.

Vybornov V., Doroshenko V., Staubert R., Santangelo A. Changes in the cyclotron line energy on short and long timescales in V 0332+53 // A&A. III 2018. 610. A88.

Walton D. J., Mackenzie A. D. A., Gully H., Patel N. R., Roberts T. P., Earnshaw H. P., Mateos S. A multimission catalogue of ultraluminous X-ray source candidates // MNRAS. I 2022. 509, 2. 1587–1604.

Walton D. J., Roberts T. P., Mateos S., Heard V. 2XMM ultraluminous X-ray source candidates in nearby galaxies // MNRAS. IX 2011. 416, 3. 1844–1861.

Wang P. J., Kong L. D., Zhang S., Chen Y. P., Zhang S. N., Qu J. L., Ji L., Tao L., Ge M. Y., Lu F. J., Chen L., Song L. M., Li T. P., Xu Y. P., Cao X. L., Chen Y., Liu C. Z., Bu Q. C., Cai C., Chang Z., Chen G., Chen T. X., Chen Y. B., Cui W., Cui W. W., Deng J. K., Dong Y. W., Du Y. Y., Fu M. X., Gao G. H., Gao H., Gao M., Gu Y. D., Guan J., Guo C. C., Han D. W., Huang Y., Huo J., Jia S. M., Jiang L. H., Jiang W. C., Jin J., Jin Y. J., Li B., Li C. K., Li G., Li M. S., Li W., Li X., Li X. B., Li X. F., Li Y. G., Li Z. W., Liang X. H., Liao J. Y., Liu B. S., Liu G. Q., Liu H. W., Liu X. J., Liu Y. N., Lu B., Lu X. F., Luo Q., Luo T., Ma X., Meng B., Nang Y., Nie J. Y., Ou G., Sai N., Shang R. C., Song X. Y., Sun L., Tan Y., Tuo Y. L., Wang C., Wang G. F., Wang J., Wang L. J., Wang W. S., Wang Y. S., Wen X. Y., Wu B. Y., Wu B. B., Wu M., Xiao G. C., Xiao S., Xiong S. L., Yang J. W., Yang S., Yang Yan Ji, Yang Yi Jung, Yi Q. B., Yin Q. Q., You Y., Zhang A. M., Zhang C. M., Zhang F., Zhang H. M., Zhang J., Zhang T., Zhang W. C., Zhang W., Zhang W. Z., Zhang Y., Zhang Y. F., Zhang Y. J., Zhang Y., Zhang Zhao, Zhang Zhi, Zhang Z. L., Zhao H. S., Zhao X. F., Zheng S. J., Zheng Y. G., Zhou D. K., Zhou J. F., Zhu Y. X., Zhu Y., Zhuang R. L. Insight-HXMT observations of Swift J0243.6+6124: the evolution of RMS pulse fractions at super-Eddington luminosity // MNRAS. X 2020. 497, 4. 5498–5506.

Ward Charlotte, Gezari Suvi, Nugent Peter, Bellm Eric C., Dekany Richard, Drake Andrew, Duev Dmitry A., Graham Matthew J., Kasliwal Mansi M., Kool Erik C., Masci Frank J., Riddle Reed L. Variability-selected Intermediate-mass Black Hole Candidates in Dwarf Galaxies from ZTF and WISE // ApJ. IX 2022. 936, 2. 104.

Watson M. G., Schröder A. C., Fyfe D., Page C. G., Lamer G., Mateos S., Pye J., Sakano M., Rosen S., Ballet J., Barcons X., Barret D., Boller T., Brunner H., Brusa M., Caccianiga A., Carrera F. J., Ceballos M., Della Ceca R., Denby M., Denkinson G., Dupuy S., Farrell S., Fraschetti F., Freyberg M. J., Guillout P., Hambaryan V., Maccacaro T., Mathiesen B., McMahon R., Michel L., Motch C., Osborne J. P., Page M., Pakull M. W., Pietsch W., Saxton R., Schwope A., Severgnini P., Simpson M., Sironi G., Stewart G., Stewart I. M., Stobbart A. M., Tedds J., Warwick R., Webb N., West R., Worrall D., Yuan W. The XMM-Newton serendipitous survey. V. The Second XMM-Newton serendipitous source catalogue // A&A. I 2009. 493, 1. 339–373.

Webb N. A., Coriat M., Traulsen I., Ballet J., Motch C., Carrera F. J., Koliopanos F., Authier J., de la Calle I., Ceballos M. T., Colomo E., Chuard D., Freyberg M., Garcia T., Kolehmainen M., Lamer G., Lin D., Maggi P., Michel L., Page C. G., Page M. J., Perea-Calderon J. V., Pineau F. X., Rodriguez P., Rosen S. R., Santos Lleo M., Saxton R. D., Schwope A., Tomás L., Watson M. G., Zakardjian A. The XMM-Newton serendipitous survey. IX. The fourth XMM-Newton serendipitous source catalogue // A&A. IX 2020. 641. A136.

Weisskopf M. C., Brinkman B., Canizares C., Garmire G., Murray S., Van Speybroeck L. P. An Overview of the Performance and Scientific Results from the Chandra X-Ray Observatory // PASP. I 2002. 114, 791. 1–24.

Weisskopf Martin C., Ramsey Brian, O'Dell Stephen, Tennant Allyn, Elsner Ronald, Soffitta Paolo, Bellazzini Ronaldo, Costa Enrico, Kolodziejczak Jeffrey, Kaspi Victoria, Muleri Fabio, Marshall Herman, Matt Giorgio, Romani Roger. The Imaging X-ray Polarimetry Explorer (IXPE) // Space Telescopes and Instrumentation 2016: Ultraviolet to Gamma Ray. 9905. VII 2016. 990517. (Society of Photo-Optical Instrumentation Engineers (SPIE) Conference Series).

Wenger M., Ochsenbein F., Egret D., Dubois P., Bonnarel F., Borde S., Genova F., Jasniewicz G., Laloë S., Lesteven S., Monier R. The SIMBAD astronomical database. The CDS reference database for astronomical objects // A&AS. IV 2000. 143. 9–22.

Wilson-Hodge Colleen A., Malacaria Christian, Jenke Peter A., Jaisawal Gaurava K., Kerr Matthew, Wolff Michael T., Arzoumanian Zaven, Chakrabarty Deepto, Doty John P., Gendreau Keith C., Guillot Sebastien, Ho Wynn C. G., LaMarr Beverly, Markwardt Craig B., Özel Feryal, Prigozhin Gregory Y., Ray Paul S., Ramos-Lerate Mercedes, Remillard Ronald A., Strohmayer Tod E., Vezie Michael L., Wood Kent S., NICER Science Team . NICER and Fermi GBM Observations of the First Galactic Ultraluminous X-Ray Pulsar Swift J0243.6+6124 // ApJ. VIII 2018. 863, 1. 9.

Wolf J., Nandra K., Salvato M., Liu T., Buchner J., Brusa M., Hoang D. N., Moss V., Arcodia R., Brüggen M., Comparat J., de Gasperin F., Georgakakis A., Hotan A., Lamer G., Merloni A., Rau A., Rottgering H. J. A., Shimwell T. W., Urrutia T., Whiting M., Williams W. L. First constraints on the AGN X-ray luminosity function at z 6 from an eROSITA-detected quasar // A&A. III 2021. 647. A5.

Woods Tyrone E., Agarwal Bhaskar, Bromm Volker, Bunker Andrew, Chen Ke-Jung, Chon Sunmyon, Ferrara Andrea, Glover Simon C. O., Haemmerlé Lionel, Haiman Zoltán, Hartwig Tilman, Heger Alexander, Hirano Shingo, Hosokawa Takashi, Inayoshi Kohei, Klessen Ralf S., Kobayashi Chiaki, Koliopanos Filippos, Latif Muhammad A., Li Yuexing, Mayer Lucio, Mezcua Mar, Natarajan Priyamvada, Pacucci Fabio, Rees Martin J., Regan John A., Sakurai Yuya, Salvadori Stefania, Schneider Raffaella, Surace Marco, Tanaka Takamitsu L., Whalen Daniel J., Yoshida Naoki. Titans of the early Universe: The Prato statement on the origin of the first supermassive black holes // Publ. Astron. Soc. Australia. VIII 2019. 36. e027.

Woosley Stan, Janka Thomas. The physics of core-collapse supernovae // Nature Physics. XII 2005. 1, 3. 147–154.

Yao Yuhan, Ravi Vikram, Gezari Suvi, van Velzen Sjoert, Lu Wenbin, Schulze Steve, Somalwar Jean J., Kulkarni S. R., Hammerstein Erica, Nicholl Matt, Graham Matthew J., Perley Daniel A., Cenko S. Bradley, Stein Robert, Ricarte Angelo, Chadayammuri Urmila, Quataert Eliot, Bellm Eric C., Bloom Joshua S., Dekany Richard, Drake Andrew J., Groom Steven L.,

Mahabal Ashish A., Prince Thomas A., Riddle Reed, Rusholme Ben, Sharma Yashvi, Sollerman Jesper, Yan Lin. Tidal Disruption Event Demographics with the Zwicky Transient Facility: Volumetric Rates, Luminosity Function, and Implications for the Local Black Hole Mass Function // arXiv e-prints. III 2023. arXiv:2303.06523.

Yoshida Yuki, Kitamoto Shunji. The Modulating Optical Depth of the Photoelectric Absorption Edge with a Pulse Phase in Accretion-powered X-Ray Pulsars // ApJ. VIII 2019. 880, 2. 101.

Yoshida Yuki, Kitamoto Shunji, Hoshino Akio. The Intensity Modulation of the Fluorescent Line by a Finite Light Speed Effect in Accretion-powered X-Ray Pulsars // ApJ. XI 2017. 849, 2. 116.

Yuan Feng, Narayan Ramesh. Hot Accretion Flows Around Black Holes // ARA&A. VIII 2014. 52. 529–588.

Yungelson L. R., Kuranov A. G. Merging white dwarfs and SN Ia // arXiv e-prints. X 2016. arXiv:1610.07230.

Zabludoff Ann, Arcavi Iair, LaMassa Stephanie, Perets Hagai B., Trakhtenbrot Benny, Zauderer B. Ashley, Auchettl Katie, Dai Jane L., French K. Decker, Hung Tiara, Kara Erin, Lodato Giuseppe, Maksym W. Peter, Qin Yujing, Ramirez-Ruiz Enrico, Roth Nathaniel, Runnoe Jessie C., Wevers Thomas. Distinguishing Tidal Disruption Events from Impostors // Space Sci. Rev.. VI 2021. 217, 4. 54.

Zhang Yue, Ge MingYu, Song LiMing, Zhang ShuangNan, Qu JinLu, Zhang Shu, Doroshenko Victor, Tao Lian, Ji Long, Güngör Can, Santangelo Andrea, Shi ChangSheng, Chang Zhi, Chen Gang, Chen Li, Chen TianXiang, Chen Yong, Chen YiBao, Cui Wei, Cui WeiWei, Deng JingKang, Dong YongWei, Du YuanYuan, Fu MinXue, Gao GuanHua, Gao He, Gao Min, Gu YuDong, Guan Ju, Guo ChengCheng, Han DaWei, Hu Wei, Huang Yue, Huo Jia, Jia ShuMei, Jiang LuHua, Jiang WeiChun, Jin Jing, Jin YongJie, Li Bing, Li ChengKui, Li Gang, Li MaoShun, Li Wei, Li Xian, Li XiaoBo, Li XuFang, Li YanGuo, Li ZiJian, Li ZhengWei, Liang XiaoHua, Liao JinYuan, Liu CongZhan, Liu GuoQing, Liu HongWei, Liu ShaoZhen, Liu XiaoJing, Liu Yuan, Liu YiNong, Lu Bo, Lu XueFeng, Luo Tao, Ma Xiang, Meng Bin, Nang Yi, Nie JianYin, Ou Ge, Sai Na, Sun Liang, Tan Ying, Tao WenHui, Tuo YouLi, Wang GuoFeng, Wang HuanYu, Wang Juan, Wang WenShuai, Wang YuSa, Wen XiangYang, Wu BoBing, Wu Mei, Xiao GuangCheng, Xiong ShaoLin, Xu He, Xu YuPeng, Yan LinLi, Yang JiaWei, Yang Sheng, Yang YanJi, Zhang AiMei, Zhang ChunLei, Zhang ChengMo, Zhang Fan, Zhang HongMei, Zhang Juan, Zhang Tong, Zhang Wei, Zhang WanChang, Zhang WenZhao, Zhang Yi, Zhang YiFei, Zhang YongJie, Zhang Zhao, Zhang ZiLiang, Zhao HaiSheng, Zhao JianLing, Zhao XiaoFan, Zheng ShiJie, Zhu Yue, Zhu YuXuan, Zou ChangLin, Insight-HXMT Collaboration . Insight-HXMT Observations of Swift J0243.6+6124 during Its 2017-2018 Outburst // ApJ. VII 2019. 879, 1. 61.

Zheng Xueying, Liu Jiren, Gou Lijun. The spatial distribution of circumstellar material of the wind-fed system GX 301-2 // MNRAS. II 2020. 491, 4. 4802–4806.

Zonca Andrea, Singer Leo, Lenz Daniel, Reinecke Martin, Rosset Cyrille, Hivon Eric, Gorski Krzysztof. healpy: equal area pixelization and spherical harmonics transforms for data on the sphere in Python // Journal of Open Source Software. III 2019. 4, 35. 1298.

Zou Fan, Brandt W. N., Ni Qingling, Zhu Shifu, Alexander David M., Bauer Franz E., Chen Chien-Ting J., Luo Bin, Sun Mouyuan, Vignali Cristian, Vito Fabio, Xue Yongquan, Yan Wei. Identification and Characterization of a Large Sample of Distant Active Dwarf Galaxies in XMM-SERVS // ApJ. VI 2023. 950, 2. 136.

Zubovas Kastytis. Tidal disruption events can power the observed AGN in dwarf galaxies // MNRAS. II 2019. 483, 2. 1957–1969.

Zycki Piotr T., Krolik Julian H., Zdziarski Andrzej A., Kallman Timothy R. X-Ray Reflection from Photoionized Media in Active Galactic Nuclei // ApJ. XII 1994. 437. 597.

de Mattia Arnaud, Ruhlmann-Kleider Vanina, Raichoor Anand, Ross Ashley J., Tamone Amélie, Zhao Cheng, Alam Shadab, Avila Santiago, Burtin Etienne, Bautista Julian, Beutler Florian, Brinkmann Jonathan, Brownstein Joel R., Chapman Michael J., Chuang Chia-Hsun, Comparat Johan, du Mas des Bourboux Hélion, Dawson Kyle S., de la Macorra Axel, Gil-Marín Héctor, Gonzalez-Perez Violeta, Gorgoni Claudio, Hou Jiamin, Kong Hui, Lin Sicheng, Nadathur Seshadri, Newman Jeffrey A., Mueller Eva-Maria, Percival Will J., Rezaie Mehdi, Rossi Graziano, Schneider Donald P., Tiwari Prabhakar, Vivek M., Wang Yuting, Zhao Gong-Bo. The completed SDSS-IV extended Baryon Oscillation Spectroscopic Survey: measurement of the BAO and growth rate of structure of the emission line galaxy sample from the anisotropic power spectrum between redshift 0.6 and 1.1 // MNRAS. III 2021. 501, 4. 5616–5645.

du Mas des Bourboux Hélion, Rich James, Font-Ribera Andreu, de Sainte Agathe Victoria, Farr James, Etourneau Thomas, Le Goff Jean-Marc, Cuceu Andrei, Balland Christophe, Bautista Julian E., Blomqvist Michael, Brinkmann Jonathan, Brownstein Joel R., Chabanier Solène, Chaussidon Edmond, Dawson Kyle, González-Morales Alma X., Guy Julien, Lyke Brad W., de la Macorra Axel, Mueller Eva-Maria, Myers Adam D., Nitschelm Christian, Muñoz Gutiérrez Andrea, Palanque-Delabrouille Nathalie, Parker James, Percival Will J., Pérez-Ràfols Ignasi, Petitjean Patrick, Pieri Matthew M., Ravoux Corentin, Rossi Graziano, Schneider Donald P., Seo Hee-Jong, Slosar Anže, Stermer Julianna, Vivek M., Yèche Christophe, Youles Samantha. The Completed SDSS-IV Extended Baryon Oscillation Spectroscopic Survey: Baryon Acoustic Oscillations with Lyα Forests // ApJ. X 2020. 901, 2. 153.

team The pandas development. pandas-dev/pandas: Pandas. II 2020.

van Velzen Sjoert, Gezari Suvi, Hammerstein Erica, Roth Nathaniel, Frederick Sara, Ward Charlotte, Hung Tiara, Cenko S. Bradley, Stein Robert, Perley Daniel A., Taggart Kirsty, Foley Ryan J., Sollerman Jesper, Blagorodnova Nadejda, Andreoni Igor, Bellm Eric C., Brinnel Valery, De Kishalay, Dekany Richard, Feeney Michael, Fremling Christoffer, Giomi Matteo, Golkhou V. Zach, Graham Matthew J., Ho Anna. Y. Q., Kasliwal Mansi M., Kilpatrick Charles D., Kulkarni Shrinivas R., Kupfer Thomas, Laher Russ R., Mahabal Ashish, Masci

Frank J., Miller Adam A., Nordin Jakob, Riddle Reed, Rusholme Ben, van Santen Jakob, Sharma Yashvi, Shupe David L., Soumagnac Maayane T. Seventeen Tidal Disruption Events from the First Half of ZTF Survey Observations: Entering a New Era of Population Studies // ApJ. II 2021a. 908, 1. 4.

van Velzen Sjoert, Stein Robert, Gilfanov Marat, Kowalski Marek, Hayasaki Kimitake, Reusch Simeon, Yao Yuhan, Garrappa Simone, Franckowiak Anna, Gezari Suvi, Nordin Jakob, Fremling Christoffer, Sharma Yashvi, Yan Lin, Kool Erik C., Stern Daniel, Veres Patrik M., Sollerman Jesper, Medvedev Pavel, Sunyaev Rashid, Bellm Eric C., Dekany Richard G., Duev Dimitri A., Graham Matthew J., Kasliwal Mansi M., Kulkarni Shrinivas R., Laher Russ R., Riddle Reed L., Rusholme Ben. Establishing accretion flares from massive black holes as a major source of high-energy neutrinos // arXiv e-prints. XI 2021b. arXiv:2111.09391.

Data and Software Acknowledgements

This work is based on observations with the eROSITA telescope onboard the SRG observatory. The SRG observatory was built by Roskosmos in the interests of the Russian Academy of Sciences represented by its Space Research Institute (IKI) in the framework of the Russian Federal Space Program, with the participation of the Deutsches Zentrum für Luft-und Raumfahrt (DLR). The SRG/eROSITA X-ray telescope was built by a consortium of German Institutes led by MPE, and supported by DLR. The SRG spacecraft was designed, built, launched and is operated by the Lavochkin Association and its subcontractors. The science data are downlinked via the Deep Space Network Antennae in Bear Lakes, Ussurijsk, and Baykonur, funded by Roskosmos. The eROSITA data used in this work were processed using the eSASS software system developed by the German eROSITA consortium and proprietary data reduction and analysis software developed by the Russian eROSITA Consortium.

This work used the data of the Sloan Digital Sky Survey. Funding for the Sloan Digital Sky Survey V has been provided by the Alfred P. Sloan Foundation, the Heising-Simons Foundation, the National Science Foundation, and the Participating Institutions. SDSS acknowledges support and resources from the Center for High-Performance Computing at the University of Utah. The SDSS web site is `www.sdss.org`. SDSS is managed by the Astrophysical Research Consortium for the Participating Institutions of the SDSS Collaboration, including the Carnegie Institution for Science, Chilean National Time Allocation Committee (CNTAC) ratified researchers, the Gotham Participation Group, Harvard University, Heidelberg University, The Johns Hopkins University, L'Ecole polytechnique federale de Lausanne (EPFL), Leibniz-Institut fuer Astrophysik Potsdam (AIP), Max-Planck-Institut fuer Astronomie (MPIA Heidelberg), Max-Planck-Institut fuer Extraterrestrische Physik (MPE), Nanjing University, National Astronomical Observatories of China (NAOC), New Mexico State University, The Ohio State University, Pennsylvania State University, Smithsonian Astrophysical Observatory, Space Telescope Science Institute (STScI), the Stellar Astrophysics Participation Group, Universidad Nacional Autónoma de México, University of Arizona, University of Colorado Boulder, University of Illinois at Urbana-Champaign, University of Toronto, University of Utah, University of Virginia, Yale University, and Yunnan University.

We are grateful to the Swift observatory team for approving a ToO observation 19205 of a TDE candidate from Chapter 4. This work made use of data supplied by the UK Swift Science Data Centre at the University of Leicester.

We are grateful for the NuSTAR and RXTE data to the High Energy Astrophysics Science Archive Research Center (HEASARC) Online Service [1] provided by the NASA/Goddard Space Flight Center.

Software (in no particular order): CAMB (Lewis, Challinor, 2011), CCL (Chisari et al., 2019), NumPy (Harris et al., 2020), Matplotlib (Hunter, 2007), SciPy (Virtanen et al., 2020), Pandas(team pandas development, 2020), ChainConsumer [2], COBAYA (Torrado, Lewis, 2021), AstroPy (Astropy Collaboration et al., 2018), HEALPix [3] (Górski et al., 2005), HEALPy (Zonca

[1] `https://heasarc.gsfc.nasa.gov/cgi-bin/W3Browse/w3browse.pl`

[2] `https://samreay.github.io/ChainConsumer/index.html`

[3] `https://sourceforge.net/projects/healpix/`

et al., 2019), HEASoft [4], Keras[5], TensorFlow[6], scikit-learn[7].

[4] https://heasarc.gsfc.nasa.gov/docs/software/heasoft/
[5] https://keras.io
[6] https://www.tensorflow.org
[7] https://scikit-learn.org/stable/

Personal Acknowledgements

I would like to express my heartfelt appreciation to my thesis advisors, Marat Gilfanov and Rashid Sunyaev. Their expertise and mentorship have been invaluable. I am grateful for the freedom I was given in the topics I want to explore and the techniques I want to use. Not only did Marat provide me with valuable insights and criticism but also encouraged me to explore and apply new methods. Marat's very keen sense of data and physics always helped me with very complicated tasks, saving me days and weeks of work. Marat is very understanding and supportive, debating with him about various topics was the best part of my PhD – mainly because the correct solution usually followed. Rashid's kindness and openness to various topics were essential for the success of this thesis. Rashid's very broad knowledge of modern astrophysics (and science in general) was one of the drivers of my work. I am especially grateful to Marat and Rashid for their advice and support of my future career plans.

I am also indebted to the members of my thesis committees, both MPA's thesis committee and the PhD defence committee at LMU. PhD path was very smooth and almost free of bureaucracy with the help of directors, secretaries and IT of MPA and IMPRS. I extend my appreciation to the MPA/MPE faculty and staff who have contributed to my educational experience and exposure to very useful seminars and colloquia. The academic resources, facilities, and opportunities provided by the Max Planck Society have been indispensable and I could not recommend it more. Many thanks to my colleagues, students and postdocs at MPA, MPE, USM and ESO for creating a wonderful scientific environment, whether it's about morning coffee or Christmas dinner.

My family and my partner deserve a special mention for their tenacious support and love. I thank my parents and my sister for their unwavering faith in me. My deepest gratefulness goes to my partner, Elvira, who has been my pillar of strength and guiding light on this journey. Elvira has provided endless encouragement, understanding and motivation when I needed it the most. This thesis is as much about a testament to their support as it is about my academic enterprises. Спасибо.

Thank you, from the bottom of my heart.
SB